Polyoxometalates For Energy Storage Applications

Jack Oliver Mitchinson

A thesis presented for the degree of
Doctor of Philosophy

School of Natural and Environmental Sciences
Newcastle University
September 2022

Contents

Acknowledgements

I would like to thank and acknowledge the Stimming group members and the friends I made along the way. Their ongoing dedication to the pursuit of science has been a source of inspiration, and this project would not have been possible without them.

I want to thank Jochen Friedl, particularly, for his brilliant guidance in the early stages of this project.

My deepest thanks also to Felix Leon Pfanschilling for many years of thought-provoking and enlightening discourse. The projects we worked on together were by far the most enjoyable and insightful.

I am deeply grateful to my family for their love, understanding, and ongoing support throughout my time at the university.

Finally, I am forever grateful to my Wife, Enya-Marie Clay, for encouraging and believing in me. Your steadfast support through this project means more to me than I can put into words.

Abstract

In this thesis, the use of polyoxometalates (POMs) in fuel cells and redox flow batteries (RFBs) is explored. Regarding their use in fuel cells, the primary topic is the development of a method for characterising the kinetic parameters of homogeneous biomass oxidation by POMs using electrochemical techniques. The method involves allowing biomass oxidation to proceed for a fixed period of time followed by applying an anodic current to the solution which results in oxidation of the POM back to its initial state. Phosphomolybdate (PMo_{12}) and glucose are used as example species and the kinetic parameters (rate constants, Arrhenius factor, activation energy) are determined using this technique. It is also shown that as the glucose becomes oxidised the reaction rate slows appreciably to the point where it effectively stalls, leaving a mixture of partially oxidised glucose and POMs which is difficult to separate.

Consequently, the immobilisation of POMs directly onto an electrode surface was investigated. The aim was to develop a heterogeneous catalyst so that the separation of POMs and biomass was less problematic. It was shown that $TBA_3PMo_{12}O_{40}$ could be deposited on a carbon felt electrode by soaking the electrode in an acetonitrile solution containing a small quantity of the POM followed by evaporating the solution. Analysis of the cyclic voltammograms showed that, at room temperature, the POM was indeed confined to the electrode surface and remained there over a long period of time and over repeated electrochemical oxidation and reduction. The mass of POM deposited on the electrode surface was also estimated using voltammetry.

Methods for increasing the accessible capacity of polyoxometalate redox flow batteries are also investigated using 3-electrode bulk electrolysis cells and 2-electrode flow batteries. The methods for increasing accessible capacity mainly involved altering the supporting electrolyte properties. The use of phosphomolybdic acid as a redox flow battery electrolyte is also explored. It is shown that PMo_{12} electrolytes have a high capacity retention and coulombic efficiency when used as a redox flow battery anolyte. A flow battery utilising 1 mM solution of PMo_{12} as the anolyte underwent 142 charge/discharge cycles without capacity loss. On testing a solution with a higher concentration of PMo_{12}, the capacity diminished more rapidly and the accessible capacity was reduced but the results are still relatively promising.

The use of silicotungstic acid (SiW_{12}) as a redox flow battery anolyte is also investigated, building on the work reported previously by Stimming group. [1, 2] It is shown here that the accessible capacity can be increased by a factor of 6 by adjusting the pH of the electrolyte. Cyclic voltammetry and bulk electrolysis experiments of SiW_{12} indicate that the POM can be reduced and oxidised by at least 12 electrons per molecule reversibly. Many of the redox

waves associated with aqueous solutions of SiW_{12} are in the -1.2–0.5 V vs SHE range, which allowed aqueous RFBs with a potential difference of $\geq$ up to 1.5 V to be demonstrated.

The use of polyamide based nanofiltration membranes as redox flow battery separators is briefly explored. The rationale for this was that the pores in the nanofiltration membrane are small enough to allow charge carriers such as (H^+, Li^+, Na^+ etc. through, but not POMs, which are substantially larger. The results showed that POMs which exist in equilibrium with smaller ions (specifically $[H_xPV_{14}O_{42}]^{9-x}$ (PV_{14}) are not compatible with this type of membrane because the smaller species are able to cross over. Furthermore, upon exposure to aqueous solutions the polyamide membrane appeared to rot after a period of weeks.

A calculator for redox flow batteries is presented which takes electrochemical parameters of the electrolytes, electrodes, and membranes, as well as the costs of critical components and returns the capital cost of a system with a breakdown of each component cost for any given power, energy, and efficiency combination. The capital cost of various different systems including iron-chrome, all vanadium, various POM batteries, and the AQDS-HBr batteries are compared and contrasted.

A theory of the thermodynamic properties of species with multiple redox couples is presented and verified. The well known Nernst equation allows the reduction potential of a single redox couple/reaction to be calculated. The theory described in chapter 3 builds on the Nernst equation to arrive at a series of equations which can describe an electrochemical system with any number of redox couples, meaning that the reduction potential of species such as POMs (which have many possible oxidation states) can be calculated precisely. Moreover, if the reduction potential and the standard reduction potentials are known, then the concentration of species in each oxidation state can also be precisely calculated. The method presented in chapter 3 removes a lot of the guess work in typical Tafel analysis.

The theoretical predictions of this model are verified experimentally. Using this theory in conjunction with rotating disk electrode experiments we show that it is possible to calculate the rate constants, transfer coefficients, and mass transport limiting current of the redox reactions of silicotungstic acid on a glassy carbon electrode.

Finally, an electrochemical model which describes the behaviour of POM redox flow batteries is presented and briefly verified against literature data. The model makes use of the equations presented in chapter 3 of this thesis, a Butler-Volmer description of the overpotential according to the kinetic and mass transport characteristics of the electrolyte, as well as diffusion, migration, and convection of species within the electrodes and through the membrane.

It is capable of generating a variety of data including a prediction of the voltage vs capac-

ity, concentration of various species with respect to their position in the electrode, expected power output, and amount of crossover of various species.

The primary contributions of this thesis are the development of a variety of electrochemical techniques and theory which can be used to investigate and explain the properties of polyoxomletalates in energy applications. In summary, this thesis builds upon the work previously carried out by Stimming group on polyoxometalate redox flow batteries, as well as contributing towards the improvement of biomass fuel cells, and the understanding of fundamental electrochemical principles that apply to polyoxometalates and various other electrochemically active species.

Introduction

Further research into renewable forms of energy conversion, as well as cost effective and efficient forms of energy storage are a necessity in order to minimise the impact of global climate change. Polyoxometalates (POMs) are a remarkable class of compounds which exhibit many properties that are desirable in energy applications. This thesis explores the potential of Polyoxometalates in energy applications, focusing on their role in biomass fuel cells and redox flow batteries.

The project's initial research area, which is covered in chapter 1 "Polyoxometalate mediated Biomass fuel cells" addresses a critical gap in previous research, that little effort has been conducted on the rate of biomass oxidation in POM mediated biomass fuel cells, and how effectively the polyoxometalates in solution catalyse the reaction. That research aim is achieved by the development of an electrochemical method that can be used to determine kinetic parameters of the biomass oxidation reaction. The procedure can be carried out with very basic equipment that should be present in most electrochemistry laboratories.

During this initial project it became clear that the rate of biomass oxidation slowed significantly as the reaction progressed. This was problematic because it resulted in a mixture of partially oxidised biomass and POMs which was difficult to separate. Consequently, heterogeneous catalysis, in which the POM was immobilised on an electrode surface was investigated. Despite successfully immobilising the POM on an electrode surface using a relatively simple technique this avenue of research was abandoned due to the instability of the deposited POM modified surface at high temperatures, which was necessary for the reaction to occur at an appreciable rate.

For a variety of reasons the focus of this project changed towards the development of redox flow batteries (RFBs), which was more in line with both the expertise and available resources of the group. Switching the focus of this project was enabled because there is a high degree of operational similarity between biomass fuel cells and flow batteries. In fact, during the fuel cell project it became apparent that phosphomolybdic acid would likely make for an ideal redox flow battery electrolyte.

In Chapter 2: "Polyoxometalate redox flow batteries", phosphomolybdic acid is successfully used as an RFB catholyte. This is important because to this authors knowledge, it is the first time a molybdenum based polyoxometalate has been used as an active material in a redox flow battery. Molybdenum based POMs share many similarities with tungsten based POMs (which are typically used in RFBs), but, as discussed in chapter 2, molybdenum is considerably cheaper and more abundant than tungsten.

In addition to this, it was shown that the accessible capacity of POMs is highly dependent on the solution conditions, in particular the pH. A major finding was that the accessible capacity of silicotungstic acid could be increased by a factor of 6 just by altering the pH of the solution.

Due to factors outside of the author's control, such as the Covid-19 pandemic limiting laboratory access, a further change in research area became practicable. A small side project presented in this thesis is a capital cost calculator, which allows researchers to determine approximately the cost of their system compared to other systems which are reported in the literature, or ones which have achieved commercialisation. This tool could be used to explore the viability of the proposed chemistry, and help secure investment for a project. However, during the development of this calculator, it became apparent that there was no established system for describing the equilibrium potential of species with multiple redox couples. The Nernst equation is suitable for describing a system with two possible oxidation states, but falls short of describing a system with three or more.

This issue was not dealt with by the capital cost calculator presented in chapter 2, but as a result of not being able to make use of a laboratory, the focus of this project shifted to the development of a theory which could accurately describe the reduction potential of polyoxometalates (and other species with more than two possible oxidation states). The results of this project are presented in chapter 3 "Thermodynamics of species with multiple redox centres".

Once Covid-19 restrictions were partially lifted, the authors of chapter 3 (Jack Mitchinson and Felix Pfanschilling) were able to make use of restricted laboratory access to verify their findings. The experimental results agree remarkably well with our predictions, and it is shown that the theory could be used in conjunction with data gathered on a rotating disk electrode to glean insights into the thermodynamic, kinetic, and mass transport behaviour of POM containing solutions.

In chapter 4 "A redox flow battery electrochemical model", an electrochemical model which describes in detail the operation of redox flow batteries is presented. The aim of developing this model is to build substantially on the cost calculator outlined in Chapter 2, and incorporate the theory presented in chapter 3. The model is quite extensive, and is largely agnostic to the flow battery chemistry. The goal of developing this model was to be able to build substantially on the aforementioned calculator, so that it was possible to predict capital cost much more accurately, and also to estimate the return on investment over the lifetime of the redox flow battery based on real-life scenarios (such as using the RFB in conjunction with a solar array or wind farm). However, due to time constraints and limited access to labora-

tory facilities, it was not possible to fully achieve the intended objectives, and experimental verification was not possible.

This research project presents significant findings in the areas of POM mediated biomass fuel cells, POM redox flow batteries, and general electrochemical theory that can be applied to a wide array of systems. It also contributes to calculating cost feasibility of redox flow batteries through the development of a cost calculator and electrochemical model presented in Chapter 2 and 4. The development of a theory to accurately describe the equilibrium potential of polyoxometalates (and other species with more than two possible oxidation states) in Chapter 3 is a particularly significant contribution to the field of electrochemistry.

Polyoxometalate properties and applications

Polyoxometalates are a class of metal oxides that are composed of several metal oxoanions linked together by shared oxygen atoms to form discreet clusters. The structures that can be adopted by POMs are incredibly expansive and diverse and tend to exhibit a great deal of symmetry.

Structure of POMs

There are two main classifications of POMs. Isopolyoxometalates have only one kind of metal included in the metal oxide framework, while heteropolyoxometalates are characterised by the presence of a heteroatom or group which is usually situated at the centre of the molecule and is surrounded by metal oxide framework. Typically, the building blocks of POMs adopt an octohedral (MO_6) geometry. Some examples of this are the decavanadate anion $[V_{10}O_{28}]^{6-}$ (Isopolyoxometalate), and the phosphomolybdate anion ($[PMo_{12}O_{40}]^{3-}$) (heteropolyoxometalate) which adopts a Keggin structure as depicted in figure 1. The geometry of POM building blocks can also be mixed. The trans-bicapped Keggin $[H_5PV_{14}O_{42}]^{5-}$ features two trigonal bipyramid VO^{3+} units which cap the Keggin structure on opposing sides.[3, 4] By adjusting the conditions of POM-containing solutions such as the pH and temperature, it is possible to transform the structure of POMs in various ways. Notably, several octohedral building blocks can be removed from certain POMs in a controlled fashion to create lacunary POMs. Additional metal oxyanions can then be added to a solution containing lacunary POMs to synthesise mixed-metal POMs.[5, 6] Lacunary POMs and mixed-metal POMs exhibit chemical properties which are different to the original POM, and are of significant interest to catalysis researchers.

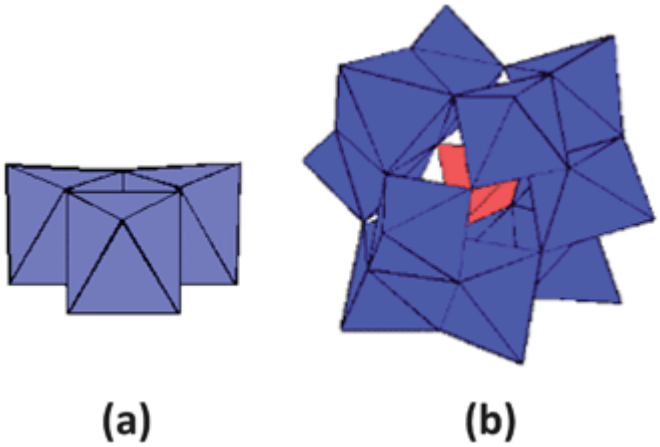

Figure 1: (a) Combination of three octahedra to form a trimetallic group M_3O_{13}. (b) Structure of the Keggin type POM. Reproduced with permission from [7].

Synthesis of POMs

The structural and elemental diversity of POMs that have been discovered to date is vast. The majority of elements can be incorporated into the structure of POMs, and there are many examples of POMs bonded to organic materials.[8] Typically however, the ions in POMs consist of groups V and VI metals. Many POMs can be produced in a "one-pot synthesis" by mixing the constituent building blocks and acidifying the solution. As the solution pH decreases, a series of condensation reactions leads to the self assembly of progressively larger clusters. If no heteroatom is present, an isopolyoxometalate will be produced. Conversely, if a suitable heteroatom is present, then a heteropolyoxometalate will be produced. Depending on the manner in which the POMs are prepared (temperature, pH, concentration, solvent etc. all play a role), a wide variety of POMs can be synthesised.

The synthesis of POMs typically occurs as a result of acid-catalysed condensation reactions that lead to the linkage of the individual oxo anions into a discrete cluster. As an example:

$12\,WO_4^{2-} + PO_4^{3-} + 24\,H^+ \longrightarrow [PW_{12}O_{40}]^{3-} + 12\,H_2O$.[9]

Applications of POMs

POMs are used in a variety of fields. In medicine, they have been shown to exhibit properties that combat tumours, infections, and the symptoms of Alzheimers disease. [10–13]. POMs and POM modified materials can also make for excellent catalysts. Their properties can be fine tuned by altering their chemical structure and composition, POMs can be highly stable

towards degradation from thermal and oxidative effects, and can also be self healing. Their structural properties give rise to unique redox behaviour and very high Brønsted acidity, which allows them to catalyse a wide range of reduction and oxidation reactions.

POMs have been shown to catalyse many different reactions including chemical fixation of CO_2, water electrolysis, dye and chemical warfare agent degradation, and biomass oxidation. [10, 14–17]

In the field of energy storage, POMs are being explored as active materials in the electrodes of intercalation batteries due to their stability with respect to repeated oxidation and reduction reactions, thermal stability, and their large number of redox active sites. [18, 19]

In the field of energy conversion, several examples of POMs as electron transfer mediators and biomass oxidation catalysts have emerged. The POM mediated biomass fuel cell, discussed in chapter 1, makes use of both the favourable catalytic properties of POMs, as well as their stability towards repeated oxidation and reduction. POM mediated biomass fuel cells have been successfully demonstrated using a variety of feed stocks, from powdered grasses to sewage, potentially allowing them to act as an energy converter whilst simultaneously treating waste that has a biological origin.

POMs have also been utilised in redox flow batteries due also to their large number of active redox sites, and also due to their high solubility in aqueous solutions containing small hard cations (such as Li^+ or H^+), as well as their fast electron transfer kinetics.[2, 20] A detailed description of redox flow batteries and the use of POMs in these devices is discussed in the introduction to chapter 2.

Chapter 1

Polyoxometalate mediated Biomass fuel cells

1.1 Introduction

The utilisation of biomass as a cost-effective, renewable, low-carbon source of energy can play a significant role in paving the road to a sustainable net-zero energy economy on a global scale. The "2016 Billion-Ton Report" was conducted to answer the question of whether there are enough biomass resources to alleviate dependence on fossil fuels. The report found that in the US alone, between 991-1147 million tons of dry biomass could be produced per year by 2030 for the purposes of energy generation whilst continuing to meet the demand for biomass in all other sectors (food, feed and fibre) at the cost of around 60 USD/ton. [21]

The question of whether extensive swathes of land should be used for the production of biomass exclusively for fuel use, as opposed to some alternative use such as food production or as habitats for endemic species/natural carbon sinks is a contentious issue and is the subject of ongoing political and societal debate.

In this short review, the use of biomass for energy production is discussed, and arguments are presented that show the production of liquid biofuels, including biodiesel and bioethanol, does not significantly contribute towards reducing carbon dioxide emissions. The argument is also made that the combustion of biodiesel/ethanol leads to the degradation of human health due to tail-pipe emissions. A literature review on the use of biomass in liquid fuel cells is then presented. The remainder of this chapter then describes the efforts toward the development of investigative techniques for developing liquid biomass fuel cells.

The comparison of biofuel to the novel biomass fuel cell concept, which is to be discussed,

is intended to serve as an example that the utilisation of biomass as an energy source through direct electrochemical means is a potentially viable solution to on-demand power generation. That being said, the technology is still very much in its infancy and needs considerable research before any commercial application is realised.

1.1.1 Biomass containing fuels

If all of the available land allocated to agriculture in the US were dedicated to producing biofuel, then the total estimated yield (340 billion litres) would make up for a substantial fraction of all US fuel consumption per year (530 billion litres). Of course, this is not at all practical because agricultural land is required for growth crops allocated to food production, and crops suitable for biofuel production require specific soil and climate conditions that are not universal. [21] The production of biodiesel from biomass is a time-consuming process that is expensive in terms of land, water, and energy usage.[22–24] The research presented by Pimentel and Patzek is of particular interest here, as it shows that the energy input/output ratio for producing biodiesel from a typical feedstock (sunflower seeds) is 1:0.76 once manufacturing processes, transport, additional material usage etc are all accounted for.[24] Biodiesel produced from sunflower seeds likely produces more carbon dioxide than a similar quantity of diesel derived from crude oil. One could make the argument that manufacturing processes could be powered by renewable energy generators such as solar and wind power; however, the installed capacity of green energy generators rarely (if ever) meets the total demand of the grid.[25] So it seems counter-productive to divert that energy towards biodiesel production, when there are more efficient uses of the available power.

Furthermore, the transesterification process, an essential step in biodiesel production, requires the use of glycerides and methanol. Glycerides are purified from crops with high oil content, and methanol is typically produced from synthetic gas (carbon monoxide and hydrogen). Synthetic gas is typically produced from methane (or natural gas), and there are many ways of producing methane from biomass and biomass-derived products. For instance, the pyrolysis of crude glycerol from biodiesel production results in the formation of hydrogen, carbon monoxide, carbon dioxide, and methane gas,[26, 27] i.e. syngas - which is used to produce methanol $2\,H_2 + CO \longrightarrow CH_4OH$. However, the primary and cheapest source of methane at present is shale gas and tight sands. At the time of writing, Yang et al. reported that the price of glycerol was 0.05 USD/lb (110 USD/tonne).[28] More recently, in April 2020, the cost of refined glycerine rose sharply to 900 USD/tonne[29]. Hence, whether or not pyrolysis of crude glycerol is used to produce methane would largely depend on mar-

ket factors, including external supply/demand for glycerol by large consumers, including the food, pharmaceutical, and personal care product industry. For a process that already requires heavy government subsidisation to be economically viable, it seems more likely that the syngas will be sourced from coal or natural gas, given its lower cost.[30] To a large extent, the production of biofuels is largely dependent on the extraction and utilisation of fossil fuels.

Moreover, the continued use of biodiesel in combustion engines for transportation - particularly in high-density urban environments will still lead to the production of harmful pollutants, including carbon monoxide and various hydrocarbons due to inefficient combustion, as well as nitrogen oxides from exposure of nitrogen to a high temperature/pressure environment. All of which contribute to increases in ambient air pollution. According to the world Health Organisation (WHO), this leads to 4.2 million deaths per year.[31] According to the same report by the WHO, 91 % of humans live in areas with excessive ambient air pollution levels. Long-term exposure to pollutants leads to irritation of numerous organs and increased risk of various diseases and health conditions such as asthma, reduced lung capacity, cancer, and reproductive issues.

Pimentel and Patzek also point out that the energy efficiency of photosynthesis is 0.25-1%, whilst modern solar panels are 12-20% efficient. Whilst the capital cost of a solar plant is certainly higher than, for instance, a corn field, the solar plant requires much less land to produce an equivalent amount of usable energy. The solar plant can be built almost anywhere, including spaces unsuitable for agriculture. After production, solar panels do not require water, and the infrastructure for transporting the energy generated by solar is much simpler and cheaper to build and maintain.

There are enormous quantities of waste biomass generated by food production which cannot be used as feedstock. Generally speaking, this biomass cannot be used to produce biodiesel or bioethanol due to low oil content. One use for this material (beyond composting) is energy generation for heating homes and cooking food. In some parts of the world, this is already widely practised - for instance, in Thailand, charcoal briquettes are produced from coconut shells that would otherwise go to waste.[32] WasteAid, a charity which aims to improve waste management systems, points out that this procedure is practised in low and middle-income countries such as India, Zambia, and Thailand - where the charcoal is usually mixed with wood vinegar to be used as a natural fertiliser.[32–37]

Charcoal production accounts for a tiny portion of "waste" biomass utilisation, and an enormous quantity of biomass is not utilised or sent to landfill. Methods for utilising the stored chemical energy in this waste biomass in an efficient way warrant attention by the research community, as there is potentially scope for waste biomass to be utilised as an oth-

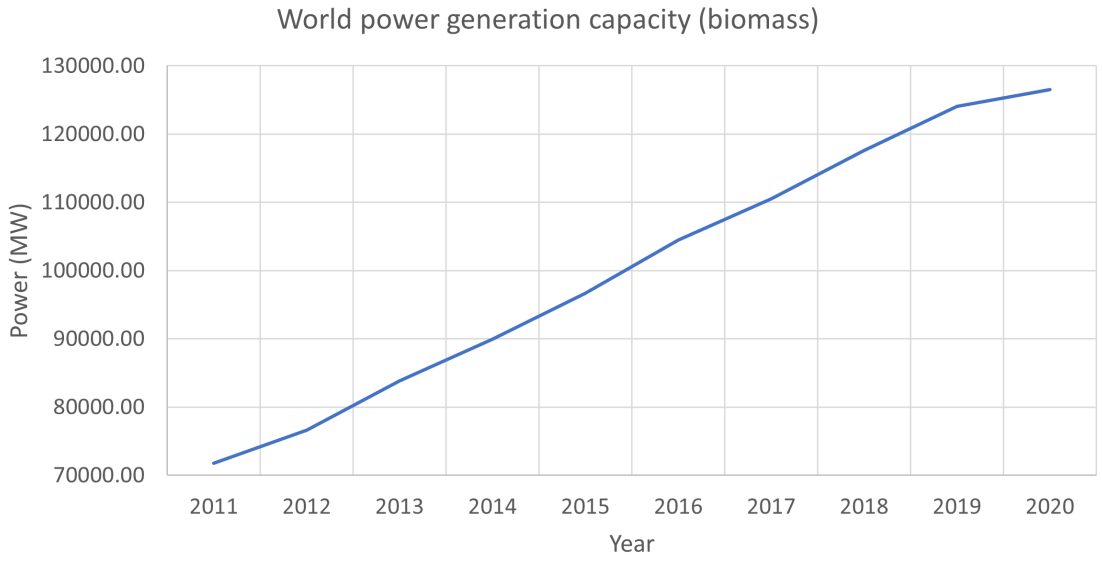

Figure 1.1: Global installed capacity of biomass based energy generation facilities. [41]

erwise underutilised source of energy in an environmentally friendly manner.

In developed and industrialised nations, a growing portion of energy needs is attributable to electricity generation. Especially now, at the start of the "green energy revolution, we see an ever-increasing demand for electricity.[38] There are many reasons for this, however, the primary driving factors are that energy generation from solar and wind are now cheaper than coal and other fossil fuel sources.[39] Additionally, the electrification of vehicles through the use of Li-ion batteries for personal transportation, and the electrolysis of water to produce hydrogen will see the energy needs of the world almost double by 2050. [40]

Whilst installed capacity and electricity generation from biomass have been growing steadily since the start of the millennium (142000 GWh in 2000 vs 522000 GWh in 2018), the fraction of electricity generated directly from biomass relative to all renewable sources has dropped from 0.81 to 0.22 in the same period.[41] (Figures 1.1 and 1.2)

In the early 2000s, electrical generation from wind rose significantly, the fraction of which increased from 0.18 in 2000 to 0.52 in 2011. Since then, it has remained roughly constant. This is not to say that the generation capacity from wind has not increased; In fact, the increase of wind and solar generation capability has been near exponential over the last two decades, whilst the increase in bioenergy capability has increased linearly. (Figure 1.3)

Caution must be exercised when analysing these figures, however, as 1 MW of wind, solar, and bioenergy installed capacity does not equate to an equivalent amount of produced energy over a given time period. Indeed, the main weakness of many renewable generation

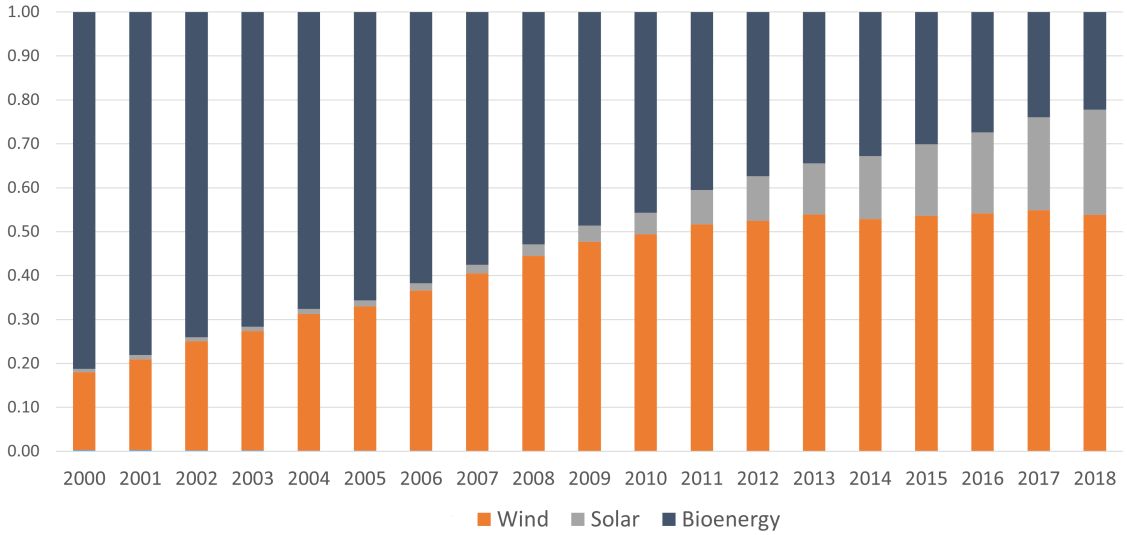

Figure 1.2: The fraction of marine (off-shore wind), wind (on-shore wind), solar, and bio-energy electrical energy generation as a fraction of the total electrical energy generated by renewable sources. [41]

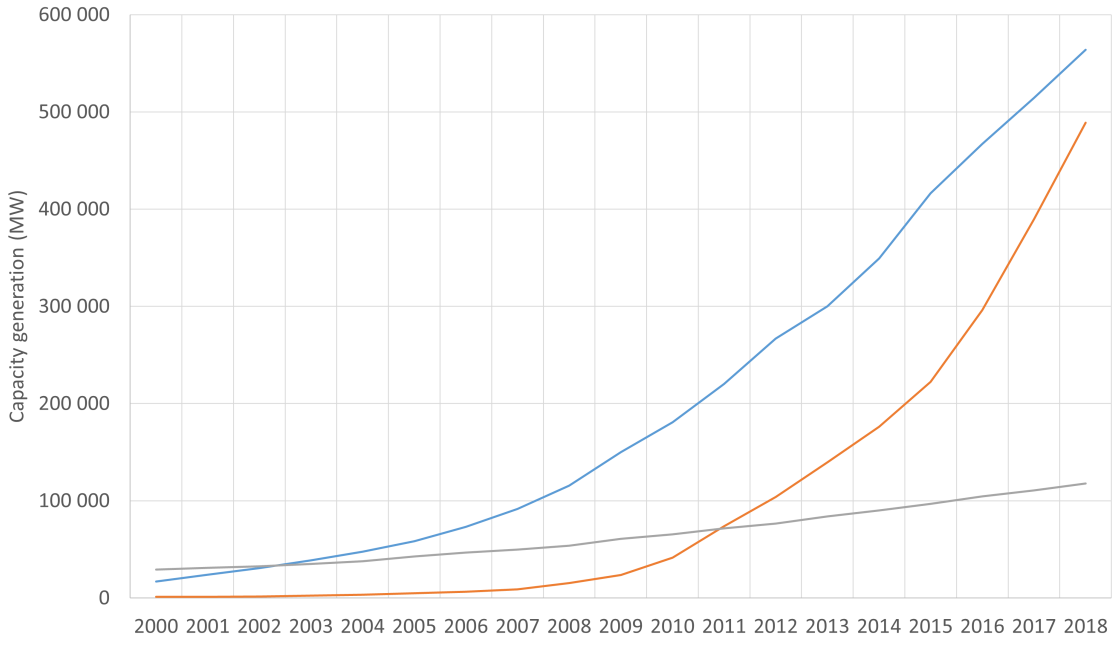

Figure 1.3: Installed capacity (MW) of wind, solar, and bio-electrical energy generation since year 2000. [41]. Wind: blue, solar: orange, biomass (grey).

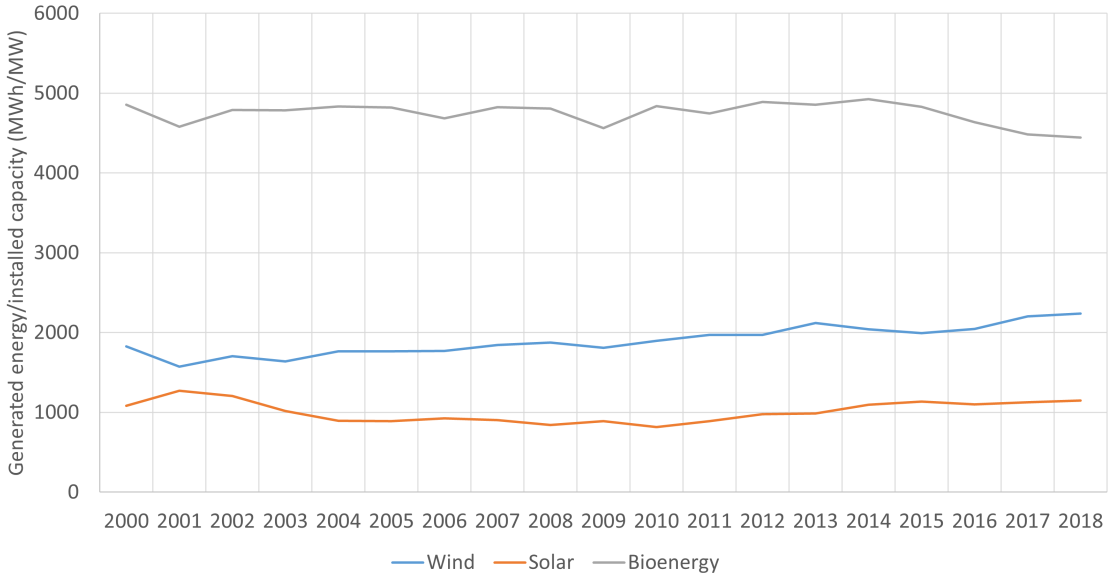

Figure 1.4: Ratio of energy generated (MWh) per unit of installed capacity (MW). [41]

sources is that they rely entirely on systems which exhibit a high degree of chaotic behaviour (wind speed and solar radiation). To some extent, bioenergy overcomes this problem because biomass (in this context) is an energy storage medium, not an energy source. In general, 1 MW of installed bioenergy leads to 4700 MWh of produced energy each year, whilst 1 MW of solar and wind currently produce 1200 MWh and 2200 MWh per year, respectively. (Figure 1.4)

This measure of capacity factor is a vital parameter, given the significant variation in actual energy produced. In terms of the total energy produced over a given period, 1 MW of bioenergy installed capacity is equivalent to 4 MW installed solar power. Interestingly, the ratio of produced energy to installed capacity for bioenergy has decreased slightly in different years whilst wind and solar have increased. In the latter case, this is due to the use of more efficient turbines and panels and is possibly indicative of a better understanding of weather patterns, which allows for better placement of solar/wind farms. The decreased ratio for bioenergy capacity is somewhat puzzling and is likely due to several factors. Since 'bioenergy' encompasses a vast array of different generation techniques, it is difficult to say where this relation originates.

The main advantage of biomass-derived energy over solar and wind is the ability to generate power/energy on demand. It is widely understood that energy storage is necessary for achieving a net-zero grid. One can easily see this by looking at the renewable energy generation and demand profiles of the United Kingdom's national grid.[25] On any given day,

the two do not match. It is also understood that the market for on-demand storage will not be satisfied with a single technology. A UK government white paper titled "Powering our Net Zero future" deals with this topic extensively.[42] Bioenergy is identified as one of the priority areas. The paper identifies biomass as a unique fuel source that can be used to produce electricity or be converted into hydrogen directly. Though, a more recent report, "UK Hydrogen Strategy," outlines a somewhat controversial strategy in which the vast majority of hydrogen produced in the UK will be done so through steam methane reformation.[43] Ill-informed policy and strategy aside, the potential for biomass as a significant contender for the on-demand energy market remains high, if currently unrealised to a large extent.

This review shows that there is a need to improve the efficiency of converting energy stored in biomass into electricity, and potentially biogas and hydrogen. Primarily, the efficiency is hindered because biomass requires a lot of pre-processing before being converted into a useful form. Other factors include the need for transportation of raw biomass, which has a relatively low energy density compared to the finished products (biodiesel, bioethanol), and fossil fuels. Of course, the refinement techniques could be improved, but any procedure which features multiple steps is subject to compound losses, and therefore, improving the overall efficiency is difficult.

Ultimately, we desire an affordable, practical, and scalable technology which can efficiently convert the energy contained in biomass directly into a valuable form of energy (heat/electricity) whilst producing as little waste as possible. As will be discussed, this is the motivation behind the research published by the groups of Deng, Liu, Xi, and Zhu.[17, 44–50]

1.1.2 Polyoxometalate mediated biomass fuel cells

Polyoxometalates (POMs) are a versatile group of oxygen containing ions (usually anions) which consist of multiple metal atoms bound together by oxygen atoms. The use of POMs as catalysts and in various other applications is well documented.[51–53] In addition to their ability to catalytically oxidise various organic molecules (including biomass), many POMs are highly soluble and stable in aqueous media. Consequently, they are of significant interest to researchers working on biomass fuel cells with homogenous catalysts.

In 2014, Liu et al. published results on a system in which biomass was oxidised by dissolved POMs at relatively high temperatures and/or under illumination. The POMs, now being reduced, are pumped to an anode in a liquid/gas fuel cell, where they are re-oxidised. Ultimately, electrons from the biomass were used to reduce oxygen in the cathode compartment, using POMs as a mediator. The biomass used in this experiment had very little prior processing - starch, lignin, cellulose, and even powdered grass and wood were all successfully utilised as a fuel.[16]

Despite being a seemingly promising concept, the direct biomass-to-electricity hybrid fuel cell has not yet generated much attention since it was published. Since then, less than 10 papers have been published on the topic, many of which came from Liu's group. The primary focus of these papers has been to investigate the different types of biomass POMs can catalytically oxidise and to maximise the power density of the fuel cell by altering parameters such as temperature, POM species, concentration etc.

At first glance, this lack of interest is somewhat confusing, given that it seemingly has the potential to fulfil the criteria set out at the end of section 1.1.1.

The working principle of the direct biomass-to-electricity hybrid fuel cell and its later variants is as follows:

- Biomass is added to a solution of acidified polyoxometalates (typically of the Keggin variety, and especially $PMo_{12}O_{40}{}^{3-}$ PMo_{12}). The solution is then heated or exposed to sunlight. The biomass and POM undergo a redox reaction in which the POM becomes reduced and protonated, and the biomass is oxidised.

- The POM solution is then pumped to the anodic half cell in a fuel cell, where it is oxidised back to itis fully oxidised and deprotonated. The reoxidation process is suspected to be proton-coupled, resulting in a proton crossing the separator, where it reacts with oxygen or another mediator, ultimately producing water.

- The POM solution is then pumped back to the reservoir where it can continually oxidise the biomass, ideally until complete oxidation to carbon dioxide occurs.
- The cathode compartment can feature any number of oxygen-reducing catalysts. Deng's original fuel cell featured a platinised carbon electrode which reduced a stream of oxygen to water. In a later work, they demonstrated an "all-POM" fuel cell, thus eliminating the need to use platinum.[17] Additionally, since the electron transfer mediators (POMs) were dissolved in solution, the energy/power characteristics of the fuel cell are decoupled - much like in a redox flow battery.

Using glucose as a fuel can simplify the overall reaction. In the reservoir, glucose transfers an electron and a proton to the POM, in this case, PMo_{12}:

$H_3PMo^{VI}{}_{12}O_{40} + \text{Glucose} \longrightarrow H_4PMo^{VI}{}_{11}Mo^{V}O_{40} + \text{Glucose}_{Ox}$

Where Glucose_{Ox} is an oxidised form of glucose. At the anode:

$H_4PMo^{VI}{}_{11}Mo^{V}O_{40} \longrightarrow H_3PMo^{VI}{}_{12}O_{40} + e^- + H^+$

Protons migrate across a cell membrane and react with O_2 or a mediator at the cathode:

$\frac{1}{2}\,O_2 + 2\,e^- + 2\,H^+ \longrightarrow H_2O$

There are many advantages to utilising biomass as a fuel source for POM fuel cells. With the exception of shredding or cutting down to size so that it fits in the reservoir, the biomass requires no pre-processing. If the biomass is initially insoluble, as is the case for grass, starch, cellulose etc., then the acidic solution catalyses the hydrolysis of the polymeric backbones to produce soluble oligomers. When this process occurs, the interfacial area of the biomass is increased, resulting in faster oxidation. It should also be noted that the solubilisation of biomass is not necessary for fuel cell operation since the POMs are soluble. They are able to oxidise the solid material (biomass) and then be pumped to the fuel cell.

The redox reaction between POMs and biomass will proceed spontaneously if the solution is exposed to light. This can be achieved on the lab scale by making the reservoir transparent and placing it near a simulated sunlight source or a window. Furthermore, the POM solution turns a deep blue and absorbs strongly in the 700-1000 nm range when reduced even to a small degree. When exposed to sunlight, Liu et al. found that a POM-biomass solution reached a temperature of 84^{o}C, which was 20^{o}C higher than a sample of deionised water under the same conditions.[16] A high temperature is desirable for this application to increase reaction rates.

At ambient pressure, the optimum conditions for biomass oxidation by POMs include exposure to sunlight and high temperature, ideally close to the boiling point of the solution, as this would lead to faster kinetics. Hypothetically, fuel cells could be relatively easily

adapted to use various waste heat sources. For instance, the fuel cell could be located near more traditional power stations and utilise the low-temperature waste heat produced when operating a turbine. If utilisation of waste heat is not an option, the fuel cell solution could easily be pumped through a modified thermal solar panel to achieve the necessary temperature for appreciable reaction rates. If the biomass is soluble, transparent panels could be used to directly expose the solution to light.

Furthermore, since the POMs themselves are dissolved in water, there is no need to remove the water content of biomass before adding it to the solution. Conversely, for the production of biochar and biodiesel, biomass gasification, and related techniques, the water content of biomass, which can vary enormously and be as high as $80-90\%$, must be removed through drying so that efficient and complete combustion can be achieved.[54] The relatively high heat of vaporisation of water significantly limits the efficiency of these techniques. Either the water is removed by active heating, which reduces the net-energy benefit of using biomass as a fuel source, or it must be passively dried by exposure to sunlight. Both are time-consuming and require large amounts of space. Depending on the available infrastructure, this process can also be manually intensive.

Of course, in either application, the water content must go somewhere, and water is also one of the byproducts of biomass oxidation. This water will progressively dilute the POM solution. However, since the solution temperature increases rapidly upon exposure to sunlight, it is reasonable to suggest that passive evaporation could be used to control the water content to a large extent and act as a source of cooling.

Deng et al. also showed that the biomass present in the solution would eventually undergo complete oxidation. Specifically,for samples of POM-biomass solution (where biomass is glucose, lignin, hemicellulose, and cellulose), after 200h of solar irradiation, the residual carbon in solution is $\leq 1\%$.

Since the POMs seem able to oxidise a variety of biomass types fully, a natural progression for this technology would be to utilise waste streams, e.g. agricultural and household biomass waste and even sewage. In 2017 Zhang et al. published results demonstrating the fuel cells' ability to produce electricity directly from sewage sludge.[55] To illustrate the practicality of the method, Zhang additionally showed that no pre-processing was necessary whatsoever to generate electricity from the sludge.

As discussed, biomass oxidation processes and subsequent electron transfer to an external circuit are decoupled. $PMo^{VI}{}_{11}Mo^{V}$ is stable in solutions for extended periods (provided oxygen content is low). If the reaction is allowed to proceed long enough, additional electrons can be transferred to POM. Liu et al. report that 2.13 electrons per POM are transferred to

the electrode after 'pre-charging' by heating to 95 ^{o}C for 6 hours. Using pre-charging methods similar to this, power densities of $\sim$ 10.8 mW cm^{-2} can be achieved using PMo_{12} as the catalyst when [PMo_{12}] = 0.25 M.[48]

The ability to precharge the fuel cell is advantageous because the energy stored in the reduced POM species is accessible instantaneously by connecting the fuel cell to an external load. One can envision this being quite useful in a setting where the fuel cell is intended to be used as a peaking power plant.

However, none of the aforementioned researchers has attempted to quantify the steady-state performance of the fuel cell. In practice, this can be somewhat difficult - specialist equipment is necessary to maintain a high temperature in a typical flow cell.

In practice, the complete oxidation of biomass to CO_2 takes a long time. Liu et al. reported that glucose, cellulose and other solutions were finally oxidised fully to CO_2 after 200 hours of constant light irradiation.[56] Additionally, it has been shown that the rate of reaction increases with the number of hydroxyl groups present on the biofuel. This results from hydrogen bonding interactions between the surface metal-oxygen bonds in the POM and hydroxyl groups in the biomass.[47] It seems likely that as the reaction progresses and the hydroxyl groups are oxidised to ketone/aldehyde groups, the intermolecular bonding interactions weaken and consequently lead to reduced reactivity.

If the reaction rate correlates strongly to the number of hydroxyl groups on the biomass, there will inevitably be a limit at which further oxidation of spent biomass is not productive. New biomass must then be introduced to the cell, but there is no reported method of separating the spent biomass solution from the homogenous catalysts (POM). The effects of large quantities of partly oxidised biomass on the system remain unexplored.

It is hypothesised that if the POM were irreversibly immobilised onto an electrode in some fashion that allows for the retention of catalytic activity, then this problem could be averted. Separating POMs from spent biomass would be as simple as draining the electrolyte.

An additional problem with the cells reported thus far is that cell performance is gauged by the power density at the electrode. However, the power densities are reported for cells which are pre-charged, but there is no information on how long the power density can be sustained. However, the measurement of the rate at which POMs can transfer electrons to the electrode is not representative of the ability of POMs to oxidise biomass.

It has been shown on numerous occasions that the electron transfer constant for POMs tends to be high, so it is unlikely that electron transfer at the electrode is the limiting step. [1, 57–62]

This work focuses mainly on PMo_{12}, which has been shown to act as an oxidation cata-

lyst for both partial and complete oxidation of various types of biomass (wheat grass powder, starch, glucose etc.) through thermochemical and photochemical pathways.[16, 45, 48, 56] In particular, this work is concerned with developing and utilising a method which allows for the elucidation of reaction kinetics of the POM-biomass redox reaction through the implementation of electrochemical techniques.

1.2 Experimental

1.2.1 Cyclic voltammetry

Cyclic voltammetry (CV) on solutions containing POMs was always carried out in a 3-electrode setup with a glassy carbon disk electrode measuring 3 mm in diameter (0.0706 cm^2). The counter electrode, a platinum wire for most solutions or a gold wire for chloride-containing solutions, was placed in the cell's main body unless a bulk electrolysis experiment was carried out on the solution. In this case the counter electrode was separated by a thick glass frit and submerged in a solution containing the supporting electrolyte of the main solution. Since the counter electrode wire was long and coiled, the active area of the counter electrode was substantially larger than the disk electrode. For acidic solutions not containing chloride ions, the counter electrode was a Basi mercury-mercurous sulphate electrode in 1 M H_2SO_4 (0.674 V vs SHE). A silver-silver chloride (Ag/AgCl) in 3 M NaCl reference electrode from BASi was used for chloride-containing solutions.

Before measurement, the solutions were flushed with nitrogen gas for at least two hours and kept under a nitrogen atmosphere during measurement. Voltammograms were recorded at numerous temperatures. Any other parameters (concentrations of species etc.) are specified where appropriate.

1.2.2 Reference electrode configuration

The potential of the MSE reference electrode was confirmed periodically by submerging two platinum wires and the MSE electrode into a 1 M H_2SO_4 solution and applying a cathodic current to one of the platinum wires (the working electrode) for 10 minutes until the solution and the chamber was saturated with hydrogen gas. Immediately after, the working electrode's potential was compared to the MSE working electrode. Invariably, the working electrode potential rises and quickly plateaus for 30 seconds or more before rising as the solution is no longer saturated with hydrogen gas. The average potential of the plateau is taken to be that of the reversible hydrogen electrode. This potential is then easily related to the SHE potential.

The potential of Ag/AgCl reference electrodes were verified by direct comparison to a Basi reference electrode that was only ever used for comparisons in 3 M NaCl solutions. This was done by submerging the reference electrodes into solution and comparing open circuit potentials over an extended period ($\sim$minutes).

Ag/AgCl electrodes were prepared in-house by submerging clean silver wire in a 3 M NaCl solution (working electrode) with a gold wire (counter electrode). An anodic current

was applied, causing the wire to turn black due to silver chloride formation. A high potential, typically 0.5 V vs SHE was applied to the electrode for several minutes, over which time the current diminished as a passivating layer of silver chloride formed. The working electrode's potential was then verified in the way described above.The potential of all electrodes prepared in this manner was within $\pm$ 2 mV of the reference potential.

1.2.3 Chronopotentiometric techniques

For the redox reaction:
$POM_{ox} + n\,e^- \longrightarrow POM_{re}$
the concentration of oxidised POM can be calculated using the Nernst equation (equation 1.1):

$$POM_{ox} = \frac{POM_{re}}{1 + e^{\frac{nF}{RT}(U_{eq} - U_{cell})}} \tag{1.1}$$

The open circuit potential (OCP) was measured for varying periods (e.g. 5, 10, 20, 40, 80 minutes). Directly after each measurement period, a large current (e.g. 50 mA) was applied at the bulk electrolysis working electrode to fully oxidise the POMs in solution (chronopotentiometry (CP)).

The working electrode potential at the end of each OCP step was record and the charge transferred during the reoxidation step was recorded. The working electrode potential can be used to estimate the oxidation state of the POM according to the Nernst equation. The total charge that passes through the working electrode during the CP step can also be used to calculate the oxidation state of the POM. Using these complimentary technique, the rate of biomass oxidation can easily be determined.

Further to this, experiments were conducted to determine the maximum sustainable current. An anodic current was applied to the cell for extended periods, and the potential was recorded. If the potential remains below 0.874 V (vs SHE) for an extended period, or if an extended plateau (potential vs time) is present, the current is considered stable. By starting with a high current and progressively decreasing it after the potential limit is reached, the maximum sustainable current can easily be determined.

The solution vessel is either partially submerged in an oil bath or placed in direct contact with a heating block on top of a temperature-controlled hot plate (Figures 1.5 and 1.6). The temperature of solutions is monitored by a thermostat encased in a glass vessel filled with water (an NMR tube proved to be a good fit), which is placed directly in the solution. The

Working electrode	Carbon felt (100 cm^2)
Counter electrode	Platinum wire
Reference electrode	MSE electrode (0.674 V vs SHE)
Supporting electrolyte	H_2SO_4 (1 M, 50 mL)
PMo_{12} concentration	10-50 mM
Glucose concentration	10-400 mM
Temperature	$50 - 95\ ^oC$
Atmosphere	N_2 (bubbled into solution)

Table 1.1: General cell details for the CP OCV procedure

thermostat communicates with the hotplate to ensure the solution temperature remains at the set value - within $\pm 1^oC$.

All electrodes were connected to gold wires to ensure good external electrical contact and avoid the risk of contamination from other metal species. In the case of the carbon felt electrode, the gold wire was inserted into the felt for several centimetres.

During all chronopotentiometric operations on homogenous solutions, the solution was continuously stirred. Nitrogen gas, humidified through a bubbler containing deionised water, was pumped directly into the solution chamber.

To avoid excessive electrolyte evaporation, the only opening to the cell was a reflux condenser, which was attached to a water chiller set to 10 ^{o}C. Typically, the experiment could be run for several days with only a few mL of water loss. When appropriate, deionised water from the clean nitrogen bubbler was added to the solution. This was done to avoid unnecessary O_2 ingress into the solution.

The applied anodic current is considered high because reduced POM can be re-oxidised in a short period relative to the OCV measurement time. Since the kinetics and thermodynamics are unknown at the beginning of the procedure, this requires some fine-tuning. Ideally, the time for the POM to be fully reoxidised is $< 1\%$ of the OCV procedure.

A cut-off voltage of +200 mV vs MSE (874 mV vs SHE) was used. This value was selected because a voltammogram of PMo_{12} shows that this potential is outside the potential region in which the POM is electrochemically active. It is also low enough that no significant oxygen evolution or biomass oxidation will occur due to electrolysis at the anode. The large size of the working electrode and the fast kinetics of POMs ensure a low overpotential.

When PMo_{12} is reduced, the solution colour changes to green and then to dark blue. After applying the anodic current, the solution colour consistently returned to yellow, indicating that the POM was fully oxidised.

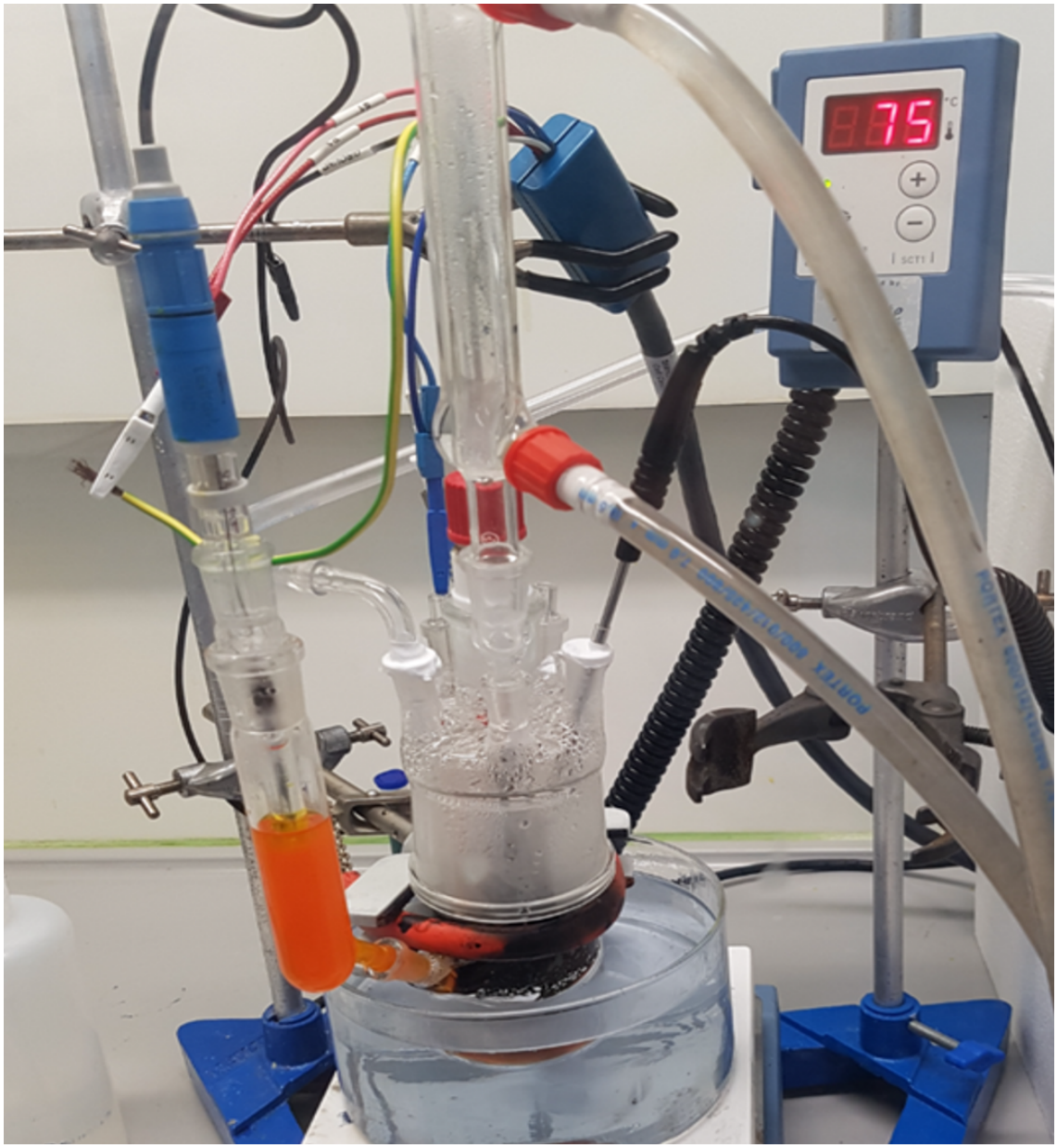

Figure 1.5: A picture of the setup used to investigate polyoxometalate and biomass solutions at elevated temperatures. In this particular instance, the reference electrode compartment is filled with the same solution as the main body to minimise the dilution of the main body solution. The orange colour arises from the presence of $H_4PVMo_{11}VO_{40}$ ($PVMo_{11}$). The $PVMo_{11}$ experimental results are not reported here but the experimental apparatus is the same.

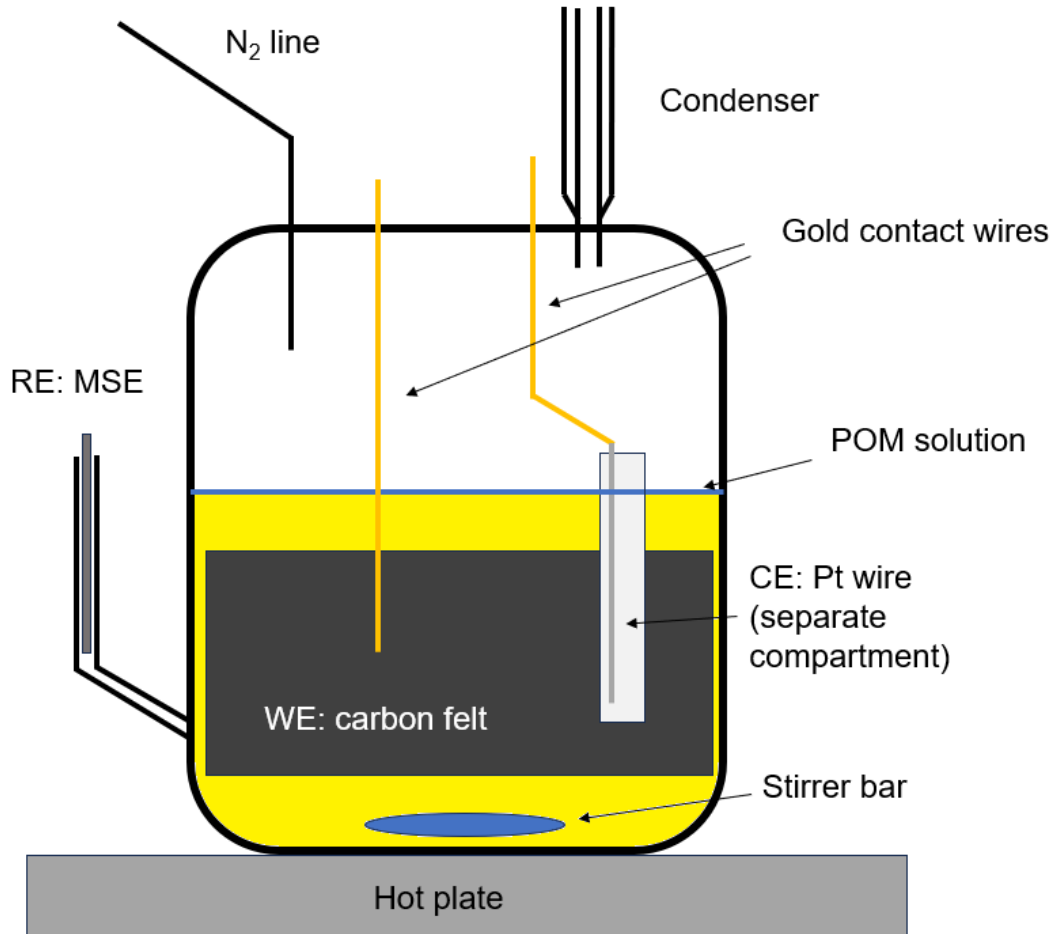

Figure 1.6: A schematic of the setup used to investigate polyoxometalate and biomass solutions at elevated temperatures. In early experiments, the cell was partially submerged in an oil bath, but there proved to be little difference in heating when in direct contact with a hot plate. The CE compartment was separated by a glass frit.

1.3 Results and discussion

1.3.1 Factors that influence the performance of POM-mediated biomass fuel cells

Thermodynamic Considerations

The most basic thermodynamic consideration is whether or not there is a driving force for the reaction to proceed. In the case of glucose oxidation, there is a significant driving force in the sense that the enthalpy of the reactants (H_r) is much higher than the enthalpy of the products (H_p). The increase in entropy (S) under standard conditions is also very high. Both conditions lead to a large and negative Gibbs free energy. Mathematically this is expressed as:

$$\Delta G = \Delta H - T\Delta S \tag{1.2}$$

A negative Gibbs free energy essentially applies to all biomass, at least when dry, so we can safely say this condition is satisfied.

In order for a POM-biomass fuel cell to generate power, several additional thermodynamic characteristics must be satisfied:

- the POM (mediator) at the anode (i.e. the half cell in which biomass oxidation occurs) must be able to oxidise biomass. For that to occur, the reduction potential of the POM (when oxidised) must be more positive than that of at least a chemically oxidisable group in the biomass molecules present.

- the POM at the cathode (i.e. the oxygen reduction side) must be able to reduce oxygen dissolved in the cathodic solution. In order for that to occur, the reduction potential of the POM when reduced must be lower than that of the oxygen reduction potential.

- the reduced form of the anodic POM must have a lower reduction potential than the oxidised form of the cathodic POM.

These thermodynamic conditions are visually depicted in Figure 1.7. The horizontal bar represents the potential scale. The long double-headed arrow on the top represents the actual fuel cell open circuit potential difference (at 0 overpotential). The two double-headed arrows at the bottom represent thermodynamic losses from oxidation and reduction of the biomass

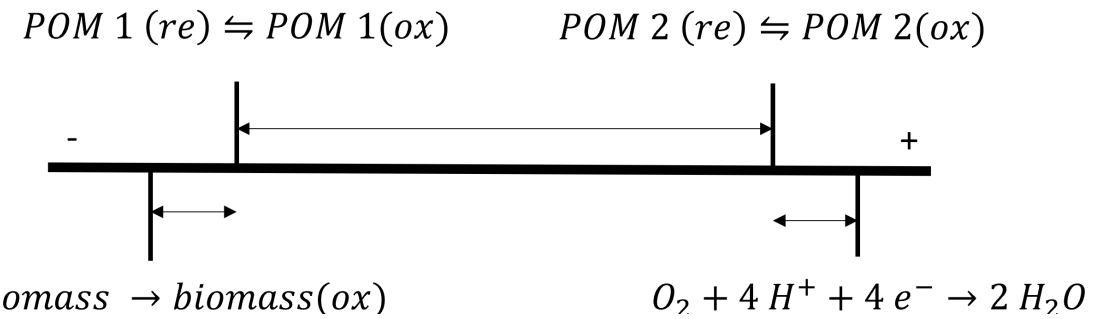

Figure 1.7: Representation of the fuel cell thermodynamic open circuit potential and the thermodynamic losses due to chemical oxidation of biomass and reduction of oxygen.

and oxygen, respectively. The length of all arrows (i.e. the potential difference) is subject to change as the reaction progresses.

The aim is to maximise the fuel cell potential difference whilst minimising chemical reduction/oxidation losses. As can be seen in figure 1.8, PMo_{12} exhibits a large number of redox waves over the potential region of interest, and is consequently well suited to the role of electron-transfer mediator in biomass fuel cells.

The reduction potential of different kinds of biomass varies considerably. Biomolecules come in many different forms (primarily lipids, proteins, carbohydrates, and nucleic acids) which vary considerably from one another. Each of these groups of biomolecules (e.g. carbohydrates) are made up of chemicals with a wide variety of functional groups and strucutres. The complexity of biomolecules, and their tendancy to undergo redox reactions in a non-reversible manner makes the study of their redox potentials difficult. This effect is compounded when one considers that as biochemicals become increasingly oxidised, they do not necessarily proceed uniformly, and the reduction potential will change as a mixture of species is produced.

Using glucose as an example, if the first step involves the oxidation of a hydroxyl group, then there are five possible reactions, all of which lead to the formation of unique products (Figure 1.9. Electrochemical characterisation of the biomass solutions and oxidised derivatives is beyond the scope of this work. However, we can take glucose oxidation to gluconic acid, which has a standard reduction potential of $V = 0.05$ V vs SHE as a rough guide for identifying suitable anodic POMs. Using this guide, one would expect that POMs with a redox potential(s) higher than 0.05 V can be used to oxidise biomass, whilst those with redox potentials lower than 0.05 V cannot.

A comparison of $PMo_{12}O_{40}{}^{3-}$ (PMo_{12}) and $SiW_{12}O_{40}{}^{4-}$ (SiW_{12}, two POMs with very similar structure (standard Keggin) demonstrates this principle rather well. From the CVs, we

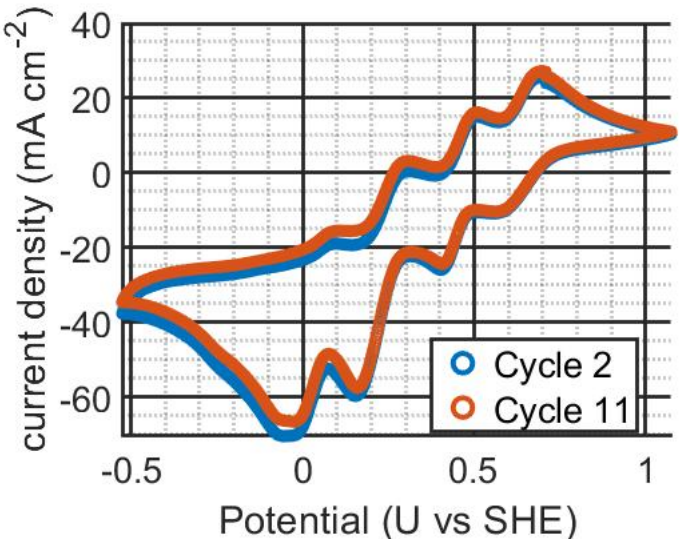

Figure 1.8: Voltammograms of PMo_{12} (300 mM) without supporting electrolyte, recorded on a glassy carbon electrode. Cycles 2 and 11 only. WE: glassy carbon disc (0.07 cm^2), CE: platinum wire, RE: mercury-mercurous sulphate electrode (0.674 V vs SHE), electrolyte: PMo_{12} 300 mM in water. Scan rate: 100 mV s^{-1}, Initial WE potential: 0.708 V vs SHE, initial sweep direction: positive, vertex WE potentials: 1.072 V vs SHE and -0.525 V vs SHE.

see that PMo_{12} has several redox reactions which occur well above 0.05 V , so a significant thermodynamic driving force for biomass oxidation is expected. SiW_{12} on the other hand, has redox reactions centred around 0.0 V vs SHE, and -0.26 V vs SHE. In the latter case, there is a small driving force when SiW_{12} is fully oxidised. For an elementary electron transfer, in which the activities of the oxidised and reduced species are the same, the Nernst equation predicts a 59 mV change in reduction potential for every order of magnitude change in the reaction quotient.

The fully oxidised form ($SiW_{12}{}^{VI}O_{40}{}^{4-}$ is denoted as $SiW_{12}(0)$, and the form reduced by one electron ($SiW_{11}{}^{VI}W^{V}\,O_{40}{}^{4-}$)as $SiW_{12}(-1)$. First used by Strickland, this convention will be adopted throughout the text. Whilst somewhat unconventional in the fields of inorganic chemistry and electrochemistry, it is necessary because POMs can be reduced by several electrons - as much as 32 in the case of $H_2W_{12}O_{40}{}^{4-}$.[8] This leads to a situation where the conventional system of assigning oxidation states to individual ions looks cumbersome and is difficult to read.[63, 64] In addition, there is sufficient evidence from NMR studies of vanadium-based POMs and computational studies to show that when POMs are reduced, the electrons are delocalised over all or part of the molecule.[65, 66] Naturally, the extent of delocalisation depends on the specific POM in question, the oxidation state, the isomeric

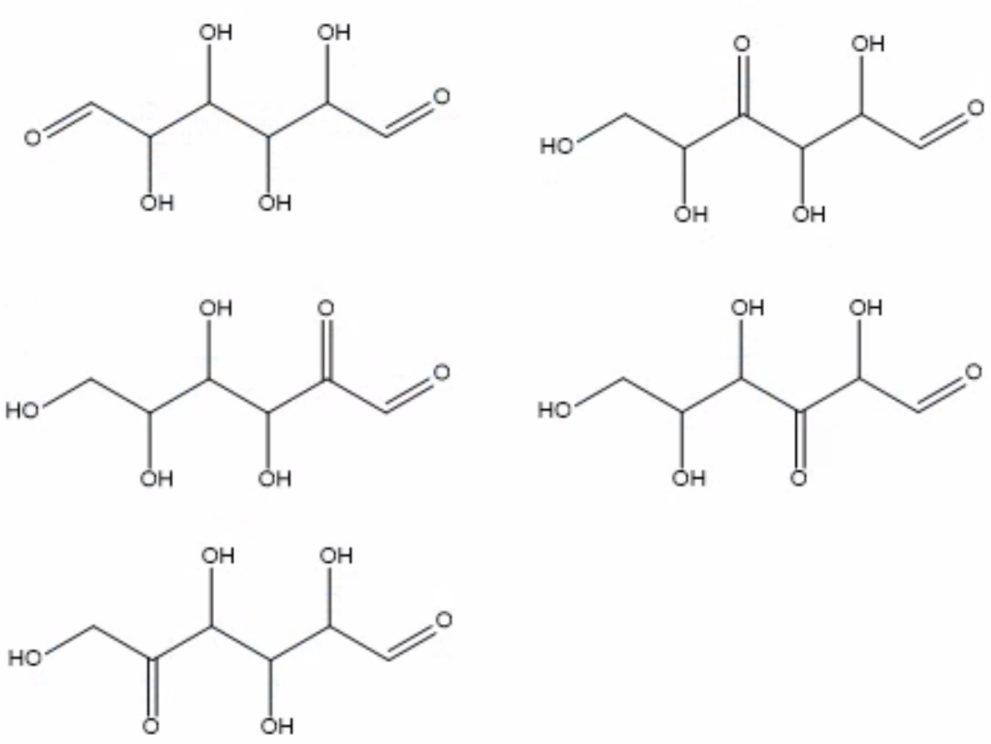

Figure 1.9: Possible oxidation products of glucose resulting from the oxidation of one of the five hydroxyl groups.

Potential vs SHE (V)	Compound	Oxidation states	n	supporting electrolyte	reference
-0.35	α-$PW_{12}O_{40}$	-2 $\longrightarrow$ -3	1	1 M $HClO_4$	[51]
-0.34	α-$PW_{12}O_{40}$	-1 $\longrightarrow$ -2	1	1 M $HClO_4$	[51]
-0.18	α-$SiW_{12}O_{40}$	-1 $\longrightarrow$ -2	1	1 M HCl	[51]
0.02	α-$SiW_{12}O_{40}$	0 $\longrightarrow$ -1	1	1 M HCl	[51]
0.02	α-$PMo_{12}O_{40}$	-3 $\longrightarrow$ -4	1	Water, pH 0.3	Figure 1.8
0.13	α-$SiMo_{12}O_{40}$	-4 $\longrightarrow$ -6	2	0.5 M HCl	[67]
0.22	α-$PW_{12}O_{40}$	0 $\longrightarrow$ -1	1	1 M $HClO_4$	[51]
0.23	α-$PMo_{12}O_{40}$	-3 $\longrightarrow$ -4	1	Water, pH 0.3	Figure 1.8
0.37	α-$SiMo_{12}O_{40}$	-2 $\longrightarrow$ -4	2	0.5 M HCl	[67]
0.43	α-$SiMo_{12}O_{40}$	-2 $\longrightarrow$ -4	2	0.5 M HCl in equal parts EtOH:H_2O	[67]
0.46	α-$PMo_{12}O_{40}$	-2 $\longrightarrow$ -1	1	Water, pH 0.3	Figure 1.8
0.49	α-$SiMo_{12}O_{40}$	0 $\longrightarrow$ -2	2	0.5 M HCl	[67]
0.54	α-$SiMo_{12}O_{40}$	0 $\longrightarrow$ -2	2	0.5 M HCl in equal parts EtOH:H_2O	[67]
0.56	β-$SiMo_{12}O_{40}$	-2 $\longrightarrow$ -4	2	0.5 M HCl in equal parts EtOH:H_2O	[67]
0.63	α-$PMo_{12}O_{40}$	0 $\longrightarrow$ -1	1	Water, pH 0.3	Figure 1.8
0.66	β-$SiMo_{12}O_{40}$	0 $\longrightarrow$ 0	2	0.5 M HCl in equal parts EtOH:H_2O	[67]

Table 1.2: List of redox couples of various POMs, their redox potentials, relevant oxidation states, and supporting electrolytes.

configuration and so on. It would also appear that as the POMs undergo electrochemical reactions, changes in physical properties, such as rotation of discrete M_3O_{13} clusters (where M is an arbitrary metal), which leads to the formation of new isomers. In short, the electrochemical and physical characteristics of POMs are extremely complex and, due to the nature of the elements involved, quite difficult to investigate. The specifics of where an electron will end up in the molecule and its impact on the overall structure (if any) is largely uninvestigated. Hence, to assign oxidation states to individual metal atoms in the POM would be misleading.

With that said, if the quotient $SiW_{12}(-1)/\,SiW_{12}(0) \leq$ x at 100 C then the reduction of glucose to gluconic acid will not occur. Conversely, if PMo_{12} is used instead, the reaction can proceed much further. Other considerations must be made of course, but experimentation using the CP OCV that will be discussed later show that oxidation by SiW_{12} occurs at $< 1\%$ of the rate of oxidation by PMo_{12}.

One of the main advantages of using POMs in this context is that so many species and redox reactions are available to explore. Table 1.2 shows that with a handful of POMs, the documented redox reaction standard potentials span an appreciable range

Theoretically, the range of POMs available for this application is essentially limitless.

Pope points out that almost all elements in the periodic table have been incorporated into the structure of POMs.[8] The elemental composition, size, structure, isomeric configuration, and so on all impact the properties of POMs. A review of the vast literature on POMs could reveal ideal candidates for both the anodic and cathodic processes in the biomass fuel cell. Unfortunately, a large majority of the POMs synthesised and characterised to date have not been tested under the conditions in which we would ideally operate a fuel cell.

The electrochemical characteristics of the more complex POMs (lacunary, substituted, very large POMs etc) remain unknown. The labs in which the majority of these POMs were produced seem to focus primarily on synthesis and obtaining the crystal structure of the newfound species. Furthermore, investigations into the properties of more "exotic" POMs show that many POMs are either unstable or only quasi-stable in aqueous solutions, especially when exposed to higher temperatures.

Similarly, the research conducted herein is limited by the available time and resources. The equipment that is necessary to synthesise, purify, and characterise POM species was largely unavailable. Furthermore, the lack of electrochemical characterisation of the simpler polyoxometalates under typical fuel cell conditions warrants immediate attention. Therefore, this work focuses primarily on PMo_{12}, which has previously been shown to oxidise biomass and act as an electron transport mediator to the anode.

kinetic considerations

The second set of considerations stems from the chemicals' kinetic properties. The thermodynamic driving force for oxidation of dry biomass is high (as discussed at the beginning of section 1.3.1); however, many abundant forms of biomass are (fortunately) inert towards oxidation under typical ambient conditions. These types of biomass (sugar/starch/lignin/cellulose etc.) are ideal for fuel cell use. This is because the available energy under ambient conditions is too low to allow the reaction to proceed. In general, terms, when two reactants (such as biomass and oxygen) interact with each other to form a product, they must proceed through some intermediary configuration known as the transition state prior to the formation of the products. The free energy of the transition state is always higher than the free energy of the initial and final state, or else the reactions would proceed rapidly until the lowest possible free energy state is attained.

S_{n2} nucleophilic substitution reactions illustrate this concept quite well. The reactants and products have lower energy than the transition state. As the nucleophile approaches the tetrahedral carbon compound, the bond angles of the adjacent groups (A, B, C) become

warped such that they are in a single plane, and their angles towards each other approach 120^{o}C. In the transition state, both the nucleophile and the group being ejected are opposite to each other and have a partial bond to the central carbon atom. This trigonal bipyramidal structure is higher in energy than the reactant and the product for several reasons.

Firstly, there is no way in which the s and p orbitals on the carbon atom can hybridise to form a stable structure with five groups attached. Secondly, the addition of a group with a full or partial negative charge (i.e. the nucleophile) leads to a build-up of a "partial" positive charge ($\delta+$) on the central carbon atom. Coulombic repulsion leads to the destabilisation of all bonds with the carbon atom. Thirdly, due to the orientation of the approach of the nucleophile, a substantial negative charge (i.e. electrons) is present in the antibonding orbital of the group to be ejected. [68]

The complexity of large polymeric chains and even simple monomers such as glucose make specific discussions about the reaction mechanisms in a biomass fuel cell challenging (hence the illustrative example). If we consider the case of biomass oxidation by either POMs or directly by oxygen, the mechanisms of the reaction are many and not fully understood. In order to have a detailed discussion about the precise mechanisms, the following needs to be considered:

- The various sites at which oxidation could occur
- The chemical properties of the oxidant
- The possible conformations of the monomer/oligomer/polymer
- The degree of existing oxidation
- The influence of supporting electrolytes and other species present in solution
- The transition state geometry and associated properties
- The mechanism by which the reaction progresses

What can be said with certainty, however, is that the energy required for the reaction to proceed through the transition state to a product at an appreciable rate is not available under ambient conditions or even at an elevated temperature of $<$ 100 ^{o}C in the absence of some form of catalyst. For a fuel cell to function, the electrons from the biomass should travel through an external circuit prior to oxygen reduction. This can be achieved by directly contacting the biomass to an electrode with a large anodic overpotential. However, that

would not result in an efficient fuel cell unless a suitable oxidation catalyst is present. In addition, the alternative chemical pathway must feature a lower activation energy for biomass oxidation (i.e. catalysis).

Under light irradiation and/or heating, PMo_{12} and a handful of other POMs will act as catalysts for biomass oxidation. Generally, a solution containing POMs and biomass is heated or irradiated with sunlight (or a facsimile thereof).[16] Over time, the POMs oxidise the biomass and become chemically reduced. The reduced POMs are then electrochemically reoxidised to their initial state at the anode of a fuel cell, allowing for further biomass oxidation to proceed.

The POM-Biomass fuel cell has four distinct processes that can affect the reaction rate. They are:

- The chemical oxidation of biomass
- The transfer of electrons from POMs to the anode (electrochemical reoxidation)
- The chemical reduction of oxygen
- The transfer of electrons to the transfer mediator at the cathode (electrochemical reduction)

The final process in the above list is mitigated in the case where oxygen is directly reduced at the cathode.

To date, the focus has been almost exclusively on the processes which occur directly at the electrode surface. To my knowledge, every paper on this subject quantifies the performance of the fuel cell based on the power or current density achieved at the cell. In all of these cases, the metric is based on a setup where the oxidation of biomass has been allowed to proceed for hours or days beforehand. In other words, the cells are precharged, and the power/current density reported is based on the cell response to a short current pulse, as opposed to prolonged operation.

This trend is very problematic as it indicates a lack of understanding of the properties of flow cells and the factors that govern their electrochemical characteristics. At this point, it is sufficient to say that the power/current density achievable is based on factors such as flow rate, the oxidation state of species, temperature, electrode/flow path geometry, properties of the electrodes, and properties of the separator. Any of these factors can be optimised (e.g. increasing flow rate) to increase power and current density in a flow cell setup. However, this metric likely has nothing to do with the rate-limiting steps of the system, which are the oxidation of biomass and the reduction of oxygen.

There is a small amount of work on the kinetic properties of biomass oxidation by POMs. In their 2014 paper, Liu et al.[16] proposed a mechanism for the oxidation of starch by PMo_{12} under light irradiation. The proposed mechanism is adapted from observations made by Yamase et al.[69].

The proposed mechanism includes the formation of an intermolecular charge transfer complex between an oxygen atom on a MoO_6 unit, and a hydroxyl group on the starch molecule. Then, through a series of intermolecular charge transfers, the oxygen becomes protonated to form a hydroxyl group on the MoO_6 unit, the metal centre of which is reduced from a $+6$ to $+5$ oxidation state. Due to the complexity of the proposed mechanism, a full description is not provided here.

The evidence provided to support the mechanism is limited to the infrared spectra of the proposed complex compared to native starch. The authors compare the position of peaks allocated to $Mo-O$ bonds in PMo_{12} from the literature to samples which they report are complexed, POM-biomass intermediaries. The wavenumber of the peaks present in the fingerprint region varies by less than 10 cm^{-1}. They then compare the spectra of native starch to a spectrum of the proposed complex and claim that a shift in the hydroxyl peak and an increase in the intensity of the $C=O$ peak indicates the presence of the proposed complex.

The body of evidence presented in this paper is insufficient to confirm the presence of an intermediate complex between starch and the POM, let alone elucidate a detailed mechanism. In isolation, there are too many unknowns to draw a conclusion from IR data. Slight differences in the peaks attributed to the POM in a complex compared to a spectrum found in the literature can be attributed to various effects, including differences in instrumentation, the presence of moisture in a sample, and even small temperature variations. The increase in the intensity of the $C=O$ stretching band can potentially be attributed to the presence of partially oxidised starch. Since we also do not know the manner in which the proposed complex was isolated, how dry it is (or whether it is even in solution or present as a solid), the shift in the $O-H$ peak may be attributed to the presence of water, or any number of chemical changes in the oxidised starch.

The evidence presented in numerous papers to date is that PMo_{12} does indeed oxidise various kinds of biomass and organic molecules, but it is still unclear exactly how this occurs. One issue with the proposed mechanism is that if the POM forms a charge-transfer complex with insoluble organic material, this would immobilise the POM and hinder electron transfer to the anode.

Furthermore, the oxidative catalysis of organic molecules by POMs has been explored in depth, and under aerobic conditions, this is well understood.[69–71]. However, in this

particular application chemical reoxidation of the POM (which acts as oxidation catalyst and electrons transfer mediator to the electrode) would be considered a parasitic reaction that reduces fuel utilisation and results in a less efficient fuel cell. This in turn poses an even larger issue, which is that complete oxidation of hydrocarbons to carbon dioxide in a fuel cell requires a source of chemical oxygen to be present in the anode compartment. However, this is absent for many of the mechanisms proposed by the POM-biomass fuel cell research community.[16, 17, 46, 72] Xu et al. propose a reaction in which water acts as the source of oxygen ($C_6H_{12}O_6 + 6\,H_2O + 24\,Fe^{3+} \longrightarrow 6\,CO_2 + 24\,H^+ + 24\,Fe^{2+}$, (note that $FeCl_3$ was used as an oxidant in addition to POMs).[50] Neumann and Sarma also studied the catalytic effects of POMs on biomass under anaerobic conditions, and proposed that the POM under investigation $H_5PV_2MO_{10}O_{40}$ may act as a water gas shift catalyst in mineral acid (H_2SO_4).[73] However, the conditions in their experiment differ significantly to those in the biomass fuel cell experiments to date.

Further, very little work has been conducted toward determining basic kinetic parameters, such as the activation energy, rate constants, rate order, and so on. The primary contribution of the work in this chapter is the elucidation of these parameters and the design of an experimental procedure which allows this process to be repeated for alternative POM species in a relatively short amount of time.

Mass transport considerations

There are two aspects pertaining to mass transport which must be considered. Firstly, the reaction of POMs and biomass requires that both chemicals come into close contact. Secondly, the POMs or POM-biomass complex must come into close contact with the electrode interface for charge transfer to occur.

The first consideration is primarily of concern when the biomass is in the solid state, and/or especially when it is hydrophobic. When biomass is in the solid state, it should be shredded or powdered prior to introduction to the fuel cell/reservoir to maximise the contact with the electrolyte. In previous studies, it has been observed that starch and other compounds will become soluble and hydrophilic as the reaction progresses.

In this work, the difficulty was overcome by using glucose, which is highly soluble. The effect of the concentration of glucose on the rate of catalysis was explored using the CP OCV procedure described in section 1.2.3.

The issue of transport of POMs or POM-biomass complexes to the electrode surface is largely overcome by using carbon-felt electrodes, since it offers an extremely high surface

area and excellent chemical and temperature tolerance. [74] In addition to being reasonably conductive and modifiable through heat and chemical treatments. Characterisation of the electrodes beyond their general properties is not necessary here. The primary focus is on the characterisation and general improvement of the rate-limiting factors - which, as discussed, are biomass oxidation and oxygen reduction.

1.3.2 Determination of the kinetic parameters of POM-catalysed glucose oxidation in aqueous solution

As discussed in section 1.3.1, very little work has been conducted towards elucidating the reaction kinetics of the oxidation of biomass by polyoxometalates. In this section, electrochemical techniques, including the CP OCP procedure described in section 1.2.3, are used to quantify the reaction rates of biomass oxidation at various temperatures and concentrations. Using this information, the Arrhenius parameters are calculated.

It will then be shown that the rate constant and Arrhenius parameters can be used to predict the maximum sustainable current for the half cell. Furthermore, experiments are carried out which show that the performance of the fuel cell directly correlates to the oxidation degree of the biomass present in the solution.

POM-catalysed Biomass oxidation rate investigation

The CP OCP procedure outlined in section 1.2.3 was carried out on solutions with various concentrations of PMo_{12} and glucose at different temperatures. The data presented here features solutions with a large excess of glucose (4-20 times greater than the POM concentration). Since the glucose concentration is much greater than that of POM, and because each glucose molecule contains many possible reaction sites, several loops of the CP OCP procedure can be carried out on the same solution without a significant change in the experimental conditions.

The data presented in Figure 1.10 was recorded from a cell with [PMo_{12}] = 10 mM, [Glucose] = 200 mM, at $T = 80^oC$ over the course of about 48 hours. During this time, the charge transferred after each OCP measurement initially increased for about 3-4 loops (one loop takes roughly 3.5 hours). The charge transferred after each OCP measurement remained consistent. Liu et al. also observed this effect when using starch instead of glucose. They suggested that the increase in reaction rate may be due to the production of smaller oligomers which are more easily oxidised. [16] Whilst that may be the case for polymeric biomass; it seems unlikely that this is the case for glucose. During the 48-hour experiment, an average of 0.74

electrons per glucose molecule (711 C) was transferred to PMo_{12}, meaning the dissociation of glucose into multiple derivatives is unlikely.

The initial inrease in rate with respect to time was not investigated further, and the effect could potentially arise for several reasons. For instance, it was previously discussed that when PMo_{12} is added to an acidic solution, the POM may dissociate into its constituent parts, which allows the molybdate and phosphate ions to accept protons and shift the pH to a higher value. This occurs (hypothetically) until the pH is sufficiently high for the POM to remain stable in the solution. However, as glucose is oxidised, the aldehyde/ester and hydroxyl groups on glucose are converted to carboxylate groups, which have a relatively high pKa value and act as proton acceptors. This could 'free up' the molybdate and phosphate ions allowing the reformation of additional POM species, thereby leading to a higher concentration and a faster rate of oxidation.

The charge transfer from each CP process was calculated and recorded in Figure 1.11. The charge transferred provides an insight into the concentration of reduced POM species in solution ($PMo_{12}(-1)$) at different periods in time. Plotting $ln[PMo_{12}(0)]$ vs time (Figure 1.12) reveals a linear trend, indicating that the reaction kinetics can be characterised as first order, or at least pseudo-first order (as there is a large excess of glucose).

As mentioned previously, the degree of POM reduction alters the electrochemical potential of the solution, and this can be estimated from the open circuit potential at the working electrode (Figure 1.12). Additionally, the reduction degree can be calculated from the charge transferred during the CP step. The change in reduction degree over time can be recorded using these two complementary techniques. Then, the reaction order can be determined, and the rate constant calculated.

A plot of $\ln(PMo_{12}(0))$ as calculated by each method vs time shows that the reaction is first order with respect to $[PMo_{12}(0)]$, the calculated rate constants (k), are also in good agreement (Figure 1.13). The CP method predicts $k = 1.37 * 10^{-4}\ s^{-1}$ and the OCP method predicts $k = 1.62 * 10^{-4} s^{-1}$ over the results attained in loops 4-14.

Since [Glucose]$\gg$ $[PMo_{12}(0)]$, the rate equation can be approximated as $rate = k[PMo_{12}(0)]$. Both k and $[PMo_{12}(0)]$ are known, so the maximum attainable rate can be predicted by using equation 1.3:

$$I = rate_{cell} N_A e t \tag{1.3}$$

Where $rate_{cell}$ is the rate constant multiplied by the initial $PMo_{12}(0)$ amount, N_A is the Avogadro constant, e is the elementary charge, and t is time. For a cell containing a solution

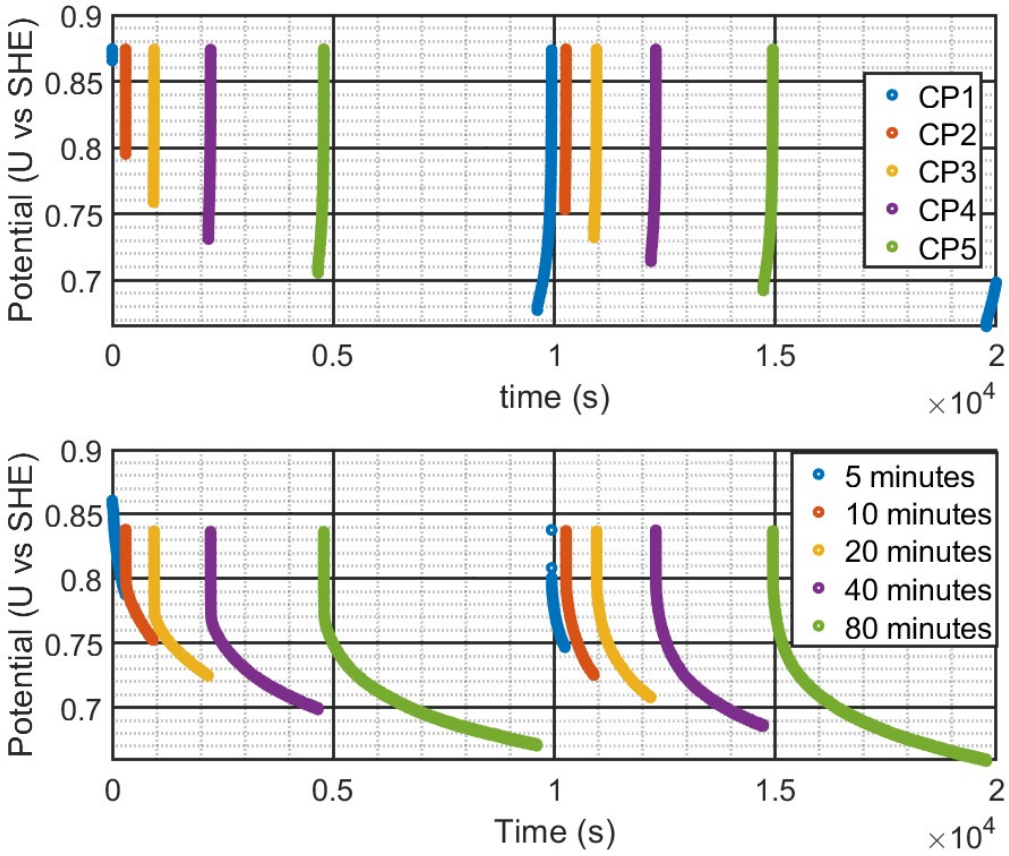

Figure 1.10: Top: potential vs time of the working electrode during CP periods during a typical CP OCP procedure. Bottom: potential vs time of the working electrode during OCP periods for the CP OCP procedure. WE: untreated carbon felt (100 cm^2), CE: platinum wire in 1 M H_2SO_4, RE: MSE (0.674 V vs SHE), electrolyte: PMo_{12} 10 mM, glucose 200 mM, H_2SO_4 1 M volume: 50 mL, CP step cut off potential: 0.874 V vs SHE, CP step current: 50 mA, temperature: 80^{o}C.

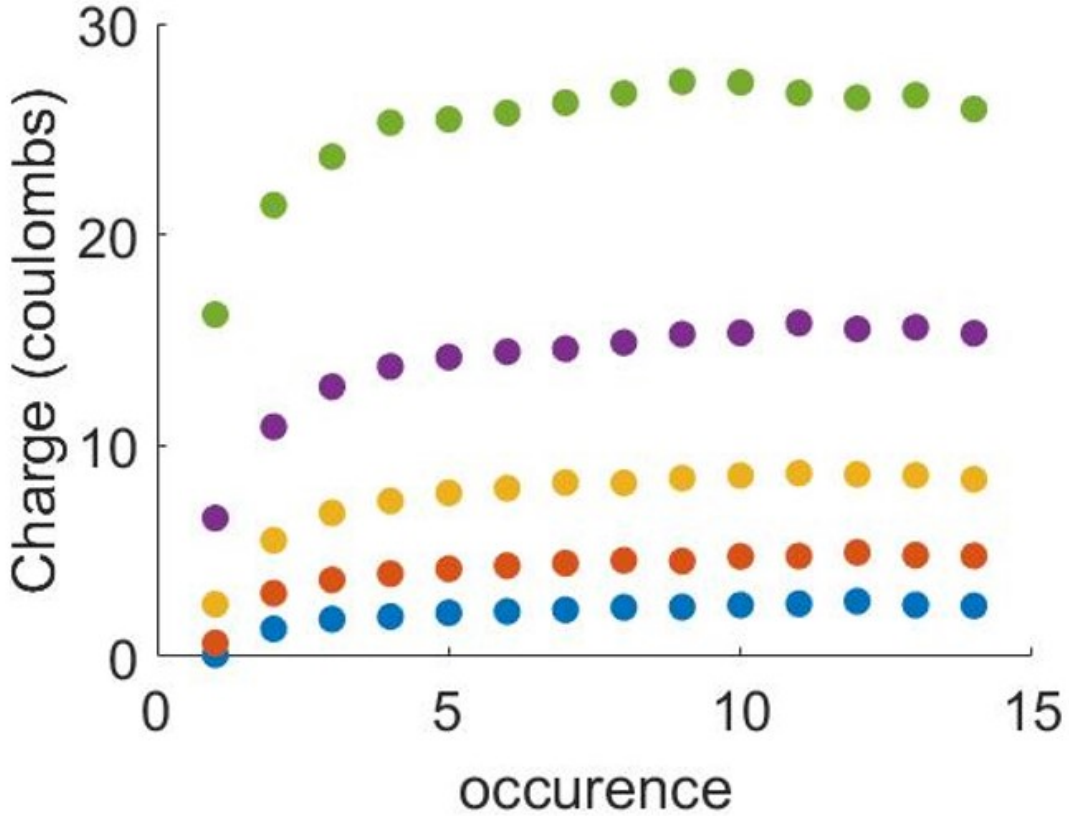

Figure 1.11: Charge transferred (C) during the CP procedures in the CP OCP experiment for a PMo_{12} 10 mM, glucose 200 mM solution at 80 ^{o}C. WE: untreated carbon felt (100 cm^2), CE: platinum wire in 1 M H_2SO_4, RE: MSE (0.674 V vs SHE), electrolyte: PMo_{12} 10 mM, glucose 200 mM, H_2SO_4 1 M volume: 50 mL, CP step cut off potential: 0.874 V vs SHE, CP step current: 50 mA, temperature: 80^{o}C.

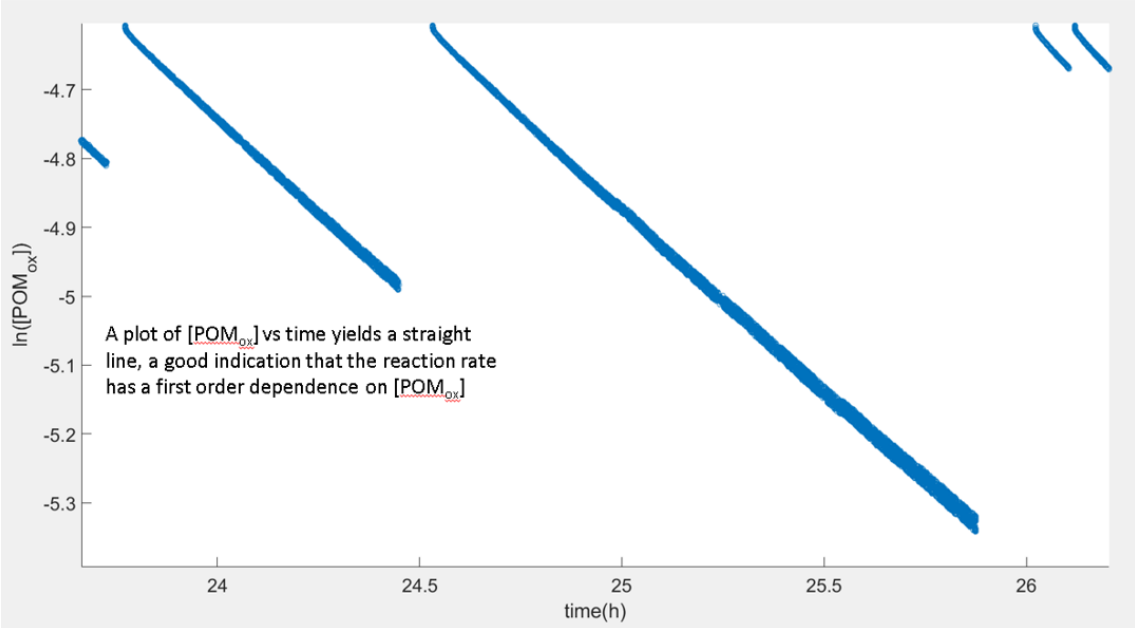

Figure 1.12: $ln([PMo_{12}(0)])$ vs time (h) for [PMo_{12}] = 10 mM, [Glucose] = 200 mM at $T = 80^oC$ shwoing a linear relationship which is indicative of a first order, or pseudo first order reaction. WE: untreated carbon felt (100 cm^2), CE: platinum wire in 1 M H_2SO_4, RE: MSE (0.674 V vs SHE), electrolyte: PMo_{12} 10 mM, glucose 200 mM, H_2SO_4 1 M volume: 50 mL, CP step cut off potential: 0.874 V vs SHE, CP step current: 50 mA, temperature: 80^oC.

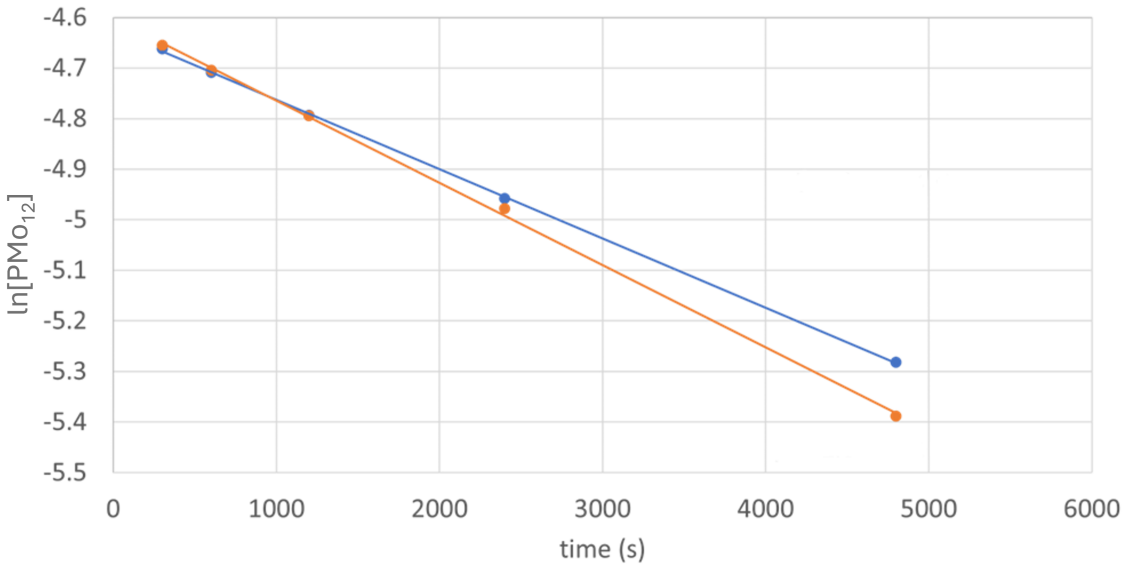

Figure 1.13: $ln([PMo_{12}(0)])$ vs time (h) for [PMo_{12}] = 10 mM, [Glucose] = 200 mM at $T = 80^oC$. The trend lines are a comparison between the CP OCP (blue, $y = 1.37*10^{-4}x - 4.63$) and open circuit potential measurement (orange, $y = 1.62 * 10^{-4}x - 4.60$) methods, which are in good agreement. WE: untreated carbon felt (100 cm^2), CE: platinum wire in 1 M H_2SO_4, RE: MSE (0.674 V vs SHE), electrolyte: PMo_{12} 10 mM, glucose 200 mM, H_2SO_4 1 M, volume: 50 mL, CP step cut off potential: 0.874 V vs SHE, CP step current: 50 mA, temperature: 80^oC.

of $PMo_{12}(0)$ (10 mM, 50 mL) at 80^{o}C the maximum attainable rate is predicted to be 7.22 mA, assuming $k = 1.50 * 10^{-4}s^{-1}$. The predicted rate is an upper limit as $PMo_{12}(-1)$ must be present in the solution for the electron transfer process to proceed. The maximum attainable current is also limited by the cut-off potential. If the reduced POM concentration decreases, the charge transfer resistance increases, resulting in a larger overpotential.

In a follow-up experiment, it was found that a current of +5 mA could be applied to the cell continuously for at least 10 hours, which is close to the value predicted by the rate constant. Under similar conditions, it was also shown that a constant current of 20 mA could be drawn from a cell with [$PMo_{12}(0)$] =50 mM. Since there is evidence to suggest that the reaction rate increases with time (Figure 1.11) it may be possible to achieve currents closer to the predicted limit by simply allowing the experiment to run for longer.

It was also shown that if the temperature was raised to 95^{o}C a $\sim 4-5$ fold increase in maximum sustainable current is observed. The observed increase in reaction rate with respect to temperature warranted further investigation. The OCP CP procedure was repeated for similar cells [$PMo_{12}(0)$] =10 mM, [Glucose] =200 mM at $T = 50,\ 60,\ 70,\ and\ 95$ ^{o}C in order to determine the parent activation energy of the oxidation process.

At 50^{o}C, the oxidation process is so slow that even after two hours of heating, no appreciable current can be drawn from the cell. For this reason, the OCP was recorded for 14 hours, and the resulting [$PMo_{12}(0)$] concentration was calculated from the OCP method only. The experiment conducted at 95^{o}C was unsuccessful due to evaporation from a broken seal. However, in a related experiment, a current of 19 mA was drawn from the cell for 10 hours, allowing k to be estimated: $k_{95} = 3.94 * 10^{-4}$ s^{-1}. The value is in good agreement with those results presented in figures 1.14 and 1.15.

A plot of $ln(k) vs \frac{1}{T}$ for the five different data sets for various temperatures yields a straight line with $slope = -E_a/R$ (figures 1.14 and 1.15). The parent activation energy can then easily be calculated: $E_a = 11598R = 96.4$ kJ mol^{-1}. The pre-exponential factor can then be calculated from the Arrhenius equation (1.4):

$$A = \frac{k}{e^{-\frac{E_a}{RT}}} = 1.91 * 10^{10} s^{-1} \tag{1.4}$$

The Arrhenius parameters and activation energy for this reaction are likely parent values which include activation energies for all possible reactions of the POM with glucose. The use of ^{1}H and ^{31}P NMR to elucidate the products of the reaction at given points throughout the reaction was attempted. However, several difficulties were encountered. The electrochemical cell could not be sealed due to design limitations and safety concerns over the build-up of

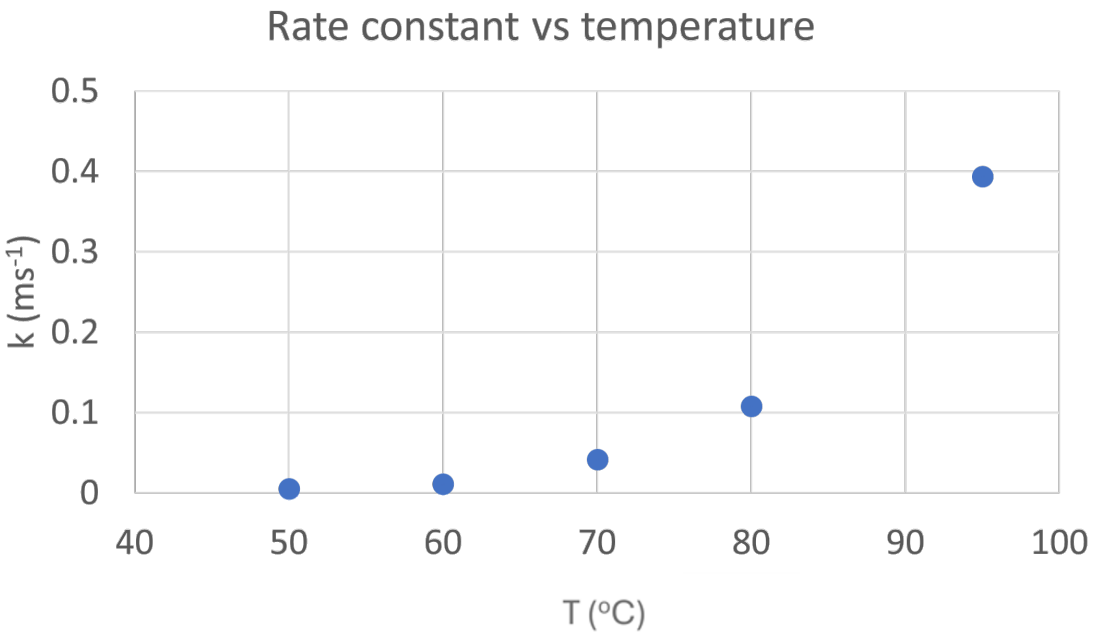

Figure 1.14: Calculated rate constants vs temperature for a solution containing [PMo_{12}] (10 mM), [Glucose] = 200 mM.

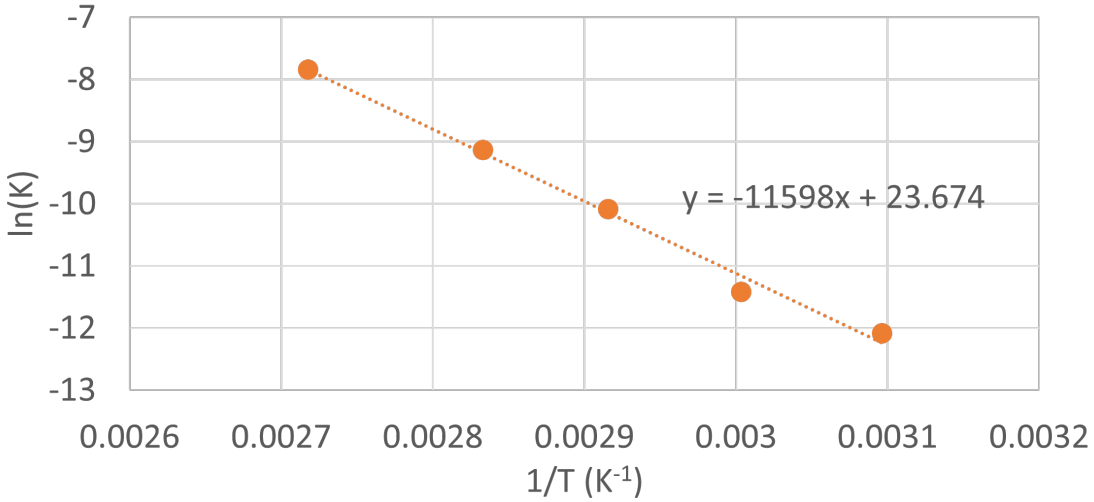

Figure 1.15: $ln(k)$ vs $1/T$ plot of the data presented in Figure 1.14

evolved gases at elevated temperatures meaning a large quantity of D_2O would have had to be used in the cell directly. The incoming stream of nitrogen would also have had to be humidified with deuterated solvent, meaning several hundred millilitres of D_2O would be used per experiment.

The oxidation of glucose could have been carried out without the electrochemical cell simply by heating a small vial of POM and glucose in a deuterated solvent. However, even if the resultant products could be identified from this experiment, the kinetic isotope effect would render the results largely invalid. The kinetic isotope effect refers to the change in reaction rate observed when nuclei in participating molecules are switched for one of their isotopes (e.g. H for D). The extent of this effect is not known and could potentially be significant. As a side note, in future work, it may be possible to elucidate the reaction mechanisms by utilising the kinetic isotope effect by strategically substituting H for D at different locations on the glucose molecule.

Another issue is the lack of sensitivity of C-13 NMR. It is not useful for determining concentrations in solution, and relatively high concentrations are needed for detection to occur in the first instance. Since there are already six distinct peaks for carbon, and more for hydrogen, identifying new products through this technique without first separating the compounds would be difficult. Ultimately, no useful information was gained through NMR during this investigation.

Even though reaction rates for individual processes were not characterised, we can still begin to evaluate the performance of POMs as biomass oxidation catalysts in terms of their ability to oxidise biomass, as opposed to their ability to undergo electrochemical oxidation. The advantage of this technique is that it will allow a systematic comparison of catalyst candidates which uses less material due to the use of a half cell, and it directly measures the rate-limiting step, at least in the case where the oxidation is slower than electron transfer.

Moreover, this technique utilises a 3-electrode setup, so the potential at which the reaction occurs can easily be determined - a critical parameter which plays a role in determining the max potential difference across the cell and, ultimately, how much energy it can provide. The three-electrode setup also allows for the complimentary charge transfer and OCP methods for oxidation state determination to be used.

The experimental method described does have some limitations. Data acquisition at high temperatures (especially near the boiling point of the solution) can be difficult. Evaporation and bubble formation at high temperatures at the CE/RE interface can lead to erroneous measurements. At low temperatures, the reaction proceeds so slowly that the CP OCP method cannot be utilised in a timely manner due to insufficient charge transfer in the CP

step. Moreover, the specific products cannot be identified without using complementary techniques.

Despite these limitations, the method allows one to characterise the kinetic properties of the POM-mediated biomass fuel cell in a largely agnostic way to the POM or biomass species present in the solution. By using this method, it is possible to predict the maximum sustainable current density (and likely the power density in a full cell) of the fuel cell based on the rate-determining step.

Maximum sustainable reaction rate of PMo_{12} catalysed glucose oxidation in aqueous solution

Now that the rate constant has been established, it should be possible to predict the maximum possible rate of oxidation and, therefore, the energy output of a given fuel cell over a prolonged period. The experimental setup for this is identical to the cell described in section 1.2.3 and Table 1.1. The basic procedure involves applying an anodic current until a cut-off potential is reached (0.874 V vs SHE). Once the cut-off potential is reached, open circuit conditions are applied for a short period (5 minutes) and then a slightly lower anodic current is applied. If the current is sustainable, the cut-off potential will not be reached during the measurement period.

For a cell with properties described in Table 1.3, the theoretical maximum sustainable current can be calculated using the rate constant derived in section 1.3.2 at 80^{o}C ($k = 1.1 * 10^{-4} s^{-1}$), the maximum sustainable current should be $5.13 mA$. In reality, the maximum theoretical current cannot be sustained for a prolonged period. This is because the maximum rate is achieved when the POM is in its fully oxidised state (i.e. the reactant is present in its greatest amount). However, when this is the case, no electrochemical reaction can occur between the POM and the electrode, so the potential will rise rapidly until OER occurs. Therefore, the maximum current is expected to be in the region of 5 mA or lower.

Figure 1.16 demonstrates that the expected outcome is true. At 10 mA, 8 mA, and 7 mA, the maximum electrode potential is reached fairly quickly, and there is a clear trend of an increase in potential with respect to time. The increase in potential with respect to time is a clear indication that the rate of biomass oxidation is lower than the rate of POM oxidation at the working electrode. As a consequence of this, the oxidation state of POMs in solution increases until the working electrode potential limit of 0.874 V vs SHE is reached.

At 6 mA, there are anomalous jumps in the potential. This is likely due to bubble formation at the reference electrode junction limiting the conductivity to the working electrode. The jumps are therefore considered erroneous.

Working electrode	Carbon felt (geometric area 100 cm^2)
Counter electrode	Platinum wire
Reference electrode	Mercury-mercurous sulphate electrode (0.674 V vs SHE)
Electrolyte	H_2SO_4 (1 M, 50 mL)
PMo_{12} concentration	10 mM
Glucose concentration	200 mM
Volume of electrolyte	50 mL
Temperature	80^{o}C
Atmosphere	N_2 (bubbled into solution)

Table 1.3: Cell details for the maximum sustainable reaction rate experiment. (10 mM POM concentration)

When the current is 5 mA, these jumps still occur but are much smaller. The main result is that the potential remained more or less constant throughout the roughly 40,000 seconds (11 hours) over which a 5 mA anodic current was applied. In fact, the procedure of applying 5 mA only ended because the cut-off condition for time elapsed was satisfied in the controlling software.

At 4 mA, a slow decrease in potential occurs. This is likely due to the net reduction of the POM in solution due to the rate of biomass oxidation exceeding the rate of electron transfer at the working electrode. This has two significant effects on the system. Firstly, according to the Nernst equation, the reduction potential is lower for systems in a lower oxidation state. Secondly, the increase in reduced species results in greater mass transport to the electrode interface, leading to a reduced overpotential. Though it is beyond the scope of this research project, finding the right balance between the application of current, the widening of the potential difference across the cell through the presence of excess reduced species, and the mass transport characteristics of the cell is critical for ensuring the operation of an energy-efficient fuel cell.

To verify this result, another cell with higher concentrations of glucose and POM was assembled. The properties of which are described in Table 1.4

In retrospect, it would have been more rigorous to use the same glucose concentration for both of these experiments. At the time, I felt that it would be beneficial to have more glucose in the solution to maintain the concentration of unreacted species for as long as possible. In both of these experiments, however, glucose is indeed present in significant excess, and it is only claimed that the resulting rate is first order **or** pseudo-first order.

With that said, it is expected that with a 5-fold increase in POM, a 5-fold increase in reaction rate, and therefore maximum sustainable current (i.e. 25 mA) should be attainable.

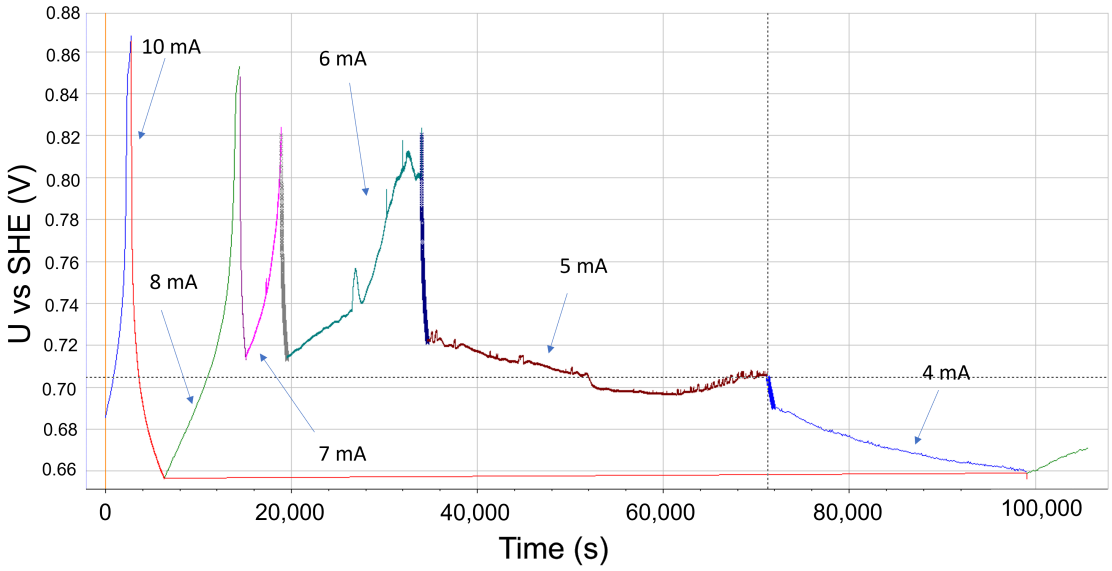

Figure 1.16: Plot of potential vs time for various current values at a carbon felt working electrode in a cell described in Table 1.3. The coloured lines which are not labelled represent periods in which cell is under the open circuit condition. WE: untreated carbon felt (100 cm^2), CE: platinum wire in 1 M H_2SO_4, RE: MSE (0.674 V vs SHE), electrolyte: PMo_{12} 10 mM, glucose 200 mM, H_2SO_4 1 M, volume: 50 mL, CP step cut off potential: 0.874 V vs SHE, CP step current: 4-10 mA, temperature: 80^{o}C.

Working electrode	Carbon felt (geometric area 100 cm^2)
Counter electrode	Platinum wire
Reference electrode	Mercury-mercurous sulphate electrode (0.674 V vs SHE)
Electrolyte	H_2SO_4 (1 M, 50 mL)
PMo_{12} concentration	50 mM
Glucose concentration	400 mM
Volume of electrolyte	50 mL
Temperature	80^{o}C, 95^{o}C, and 100^{o}C,
Atmosphere	N_2 (bubbled into solution)

Table 1.4: Cell details for the maximum sustainable reaction rate experiment. (50 mM POM concentration)

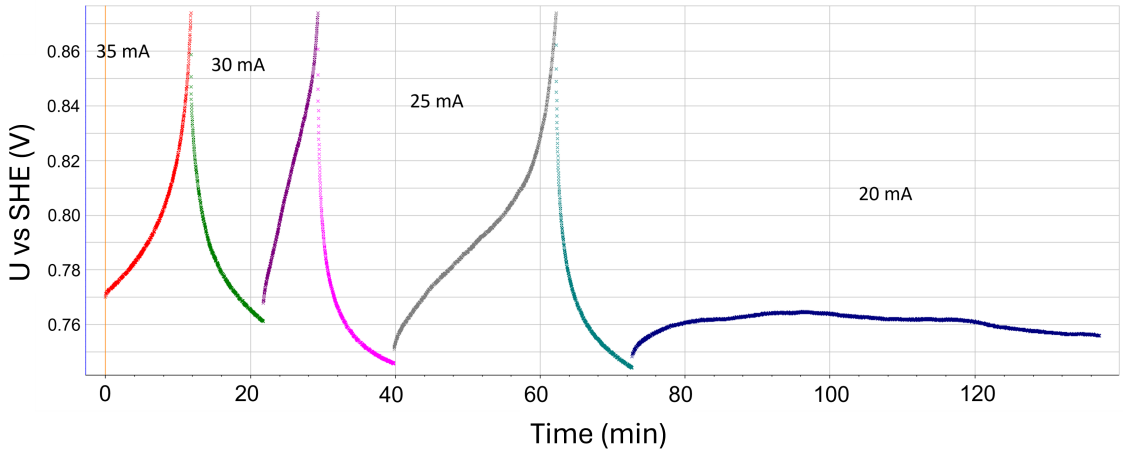

Figure 1.17: Plot of potential vs time for various values of current at a carbon felt working electrode in a cell described in Table 1.4. The coloured lines which are not labelled represent periods in which cell is under the open circuit condition. WE: untreated carbon felt (100 cm^2), CE: platinum wire in 1 M H_2SO_4, RE: MSE (0.674 V vs SHE), electrolyte: PMo_{12} 50 mM, glucose 400 mM, H_2SO_4 1 M, volume: 50 mL, CP step cut off potential: 0.874 V vs SHE, CP step current: 20-35 mA, temperature: 80^{o}C.

Figure 1.17 shows that at least a 4 fold increase in current is sustainable, which is broadly in line with expected results.

The discrepancy between the expected and observed current remains unexplained. However, it is likely due to the increased concentration of POM and/or glucose leading to a change in how the two chemicals interact in solution (e.g. solvation shell disruption). A five-fold increase in concentration from 10 mM to 50 mM does not sound significant until one considers the size of POMs. Put another way, the concentration of molybdenum in the solution has increased from 120 mM to 600 mM.

As illustrated by Figure 1.15, there is an approximate 4 fold increase in the rate constant with an increase in temperature from 80 ^{o}C to 95 ^{o}C. Therefore, a four-fold increase in the maximum sustainable current is expected. Based on the Arrhenius parameters that were calculated previously, it is possible to predict the rate constant, and subsequent reaction rate for any given concentration and temperature:

$$k_{95} = (1.91 * 10)^{10} e^{-\frac{96400}{R*368}} = 3.96 * 10^{-4} \mathrm{s}^{-1} \tag{1.5}$$

$$k_{100} = (1.91 * 10)^{10} e^{-\frac{96400}{R*373}} = 6.04 * 10^{-4} \mathrm{s}^{-1} \tag{1.6}$$

x (K)	$ln(k)$	k	predicted rate ratio	observed rate ratio
353	-9.181	$1.03 * 10^{-4}$ s^{-1}	1	1
368	-7.842	$3.93 * 10^{-4}$ s^{-1}	3.8	4
373	-7.420	$5.99 * 10^{-4}$ s^{-1}	5.8	5.5

Table 1.5: Comparison of the relative rates of reaction as predicted by the Arrhenius equation and observed results.

Using the rate constants for 95 ^{o}C and 100 ^{o}C, the respective maximum sustainable current is expected to be in the region of 95 mA, and 146 mA respectively. These values are somewhat higher than observed (80 mA and 110 mA, respectively). However, as a result of the high temperatures, bubbles formed continuously on the internal surface of the cell, including the reference electrode junction. This unfortunate occurrence meant that the cell had to be continuously monitored so that no blockages occurred. The maximum sustainable current was only maintained for several minutes, as opposed to several hours, as in other experiments.

Furthermore, the relation established in Figure 1.15 was used to determine the expected rate constants for the various temperatures. From the calculated rate constants, the predicted **relative** rate was calculated and compared to the observed relative rate. The predicted and observed relative rates (Table 1.5) match each other very closely. The error only arises in the actual magnitude of the rate, indicating that the concentration may be slightly lower than reported.

So far, all experiments have been carried out on a fuel (i.e. glucose) that is unoxidised or largely unoxidised. This was achieved by having a large excess of glucose in solution relative to POM, so that the characteristics of the POM could be studied in isolation to effects from the fuel. The next logical step is to study the effects of the glucose oxidation state on the reaction rate.

Investigation of the rate PMo_{12} catalysed oxidation when glucose is partially oxidised

As previously discussed, it is difficult to investigate the properties of glucose and its derivatives in solution for various reasons. In the electrochemical cell prepared for these experiments, it is much easier to infer information about the fuel from the results of electrochemical procedures, even though the electrochemically active species is the POM. Through coulomb counting, it is possible to estimate the degree to which glucose has been oxidised.

In an electrochemical cell with the properties described in Table 1.3, the maximum sustainable current experiment was carried out over the course of several days. This time, the

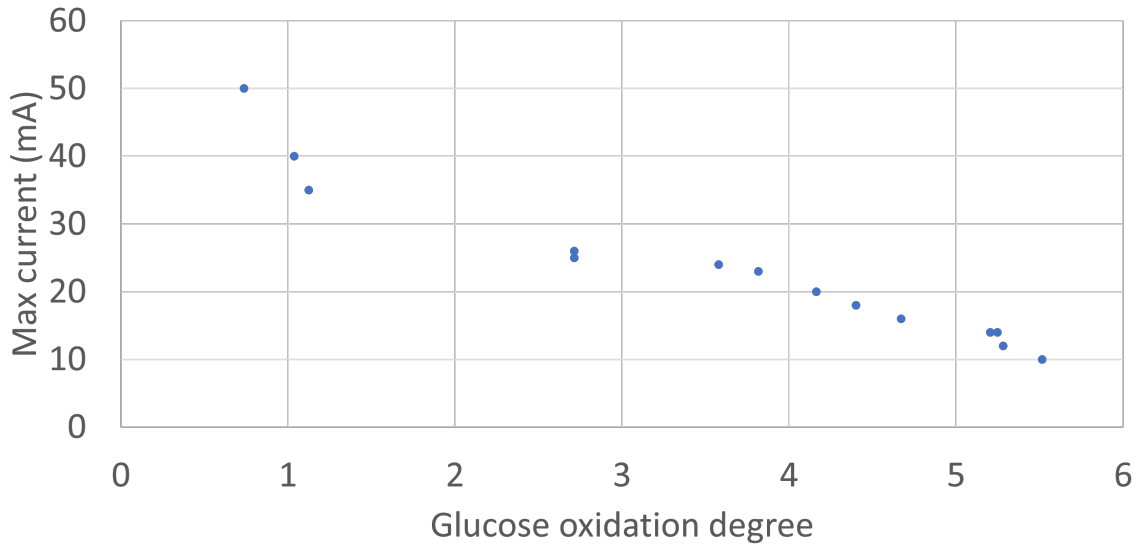

Figure 1.18: A plot of maximum sustainable current (i.e. the highest current which can be maintained while the potential of the working electrode remains $\leq$0.874 V vs SHE) vs the glucose oxidation degree for a cell with properties described in Table 1.4. WE: untreated carbon felt (100 cm^2), CE: platinum wire in 1 M H_2SO_4, RE: MSE (0.674 V vs SHE), electrolyte: PMo_{12} 50 mM, glucose 400 mM, H_2SO_4 1 M, volume: 50 mL, CP step cut off potential: 0.874 V vs SHE, CP step current: 20-35 mA, temperature: 80^{o}C

maximum sustainable current with respect to the glucose oxidation degree was recorded and plotted in Figure 1.18. In this instance, the glucose oxidation degree is defined as the number of electrons transferred to a glucose molecule in solution. This value is inferred by the charge passed through the working electrode. At the end of the experiment, 5.5 electrons per glucose molecule were transferred, and 110 electrons were transferred per PMo_{12} molecule.

A definitive negative linear correlation exists between max sustainable current and oxidation degree. A similar observation was made by a systematic study of POM oxidation on polyols by Wu et al.[47] They identify that the reaction rate is primarily related to the amount of -OH groups present on the biomass and identify higher polyhydric alcohols as the optimal fuel source for this kind of fuel cell. Whilst that is certainly true for maximising reaction rate when the fuel is relatively fresh, the research conducted here shows that as the -OH groups are depleted, the reaction rate drops dramatically. In other words, the reaction effectively stalls when the solution consists of partially oxidised biomass.

This result is entirely unsurprising. The oxidation of glucose by POM can only occur under the conditions set out in Table 1.3 because the oxidation of primary and secondary

alcohols to aldehydes and ketones, respectively, does not require dissolved oxygen in solution. Once the alcohol groups are depleted, further oxidation is difficult or impossible because there is no free oxygen in the solution. Additionally, the oxidation of ketones is considered very difficult because it requires the adjacent carbon-carbon bonds to be broken.

It is worth noting that Xu et al. demonstrated that biomass could be fully converted to carbon dioxide and water with a similar fuel cell set-up.[50] However, no mention is made of the purge gas in their experimental section, and no information on the oxidation state of glucose is available beyond 210 minutes (over a 21-day experiment). However, it can be seen that even in the first 210 minutes, the oxidation rate slows dramatically, which may explain why it took much longer for complete oxidation.

The inverse relation between the reaction rate of biomass oxidation and oxidation state of the biomass seems to be the biggest hurdle in developing POM-mediated biomass fuel cells so far. Incomplete oxidation by itself is not so much of an issue because, in theory, the mixture of partly oxidised biomass could be transferred to some other kind of reactor. Zhao et al. propose a POM fuel cell as a method of processing lignin (220 million tonnes of which is produced per year by the paper industry and is currently burned) into soluble biomass, which can then be used to produce sugars and other valuable chemicals. [48] The main problem arises when one tries to separate the mixtures. The POMs investigated in this study and partially oxidised glucose have high solubility in an aqueous solution. The fuel cell presented by Zhao et al. showed that the effect of oxidising lignin was to make it more soluble. It is worth noting that the biomass used to produce sugars after reaction with the POM was actually the residual **solids** from the experiment. So, the problem of separating the soluble biomass and the POM remains.

There are some potential solutions to this problem that are worth exploring. For instance, it is well known that the solubility of POMs depends heavily on the countercation.[8] Broadly speaking, the solubility of group 5 and 6 POMs (V, Mo, W) decrease when they are able to form a salt with a large counter cation. [75] One notable example is that of $SiW_{12}O_{40}{}^{3-}$, which has a solubility of about 0.6-0.8 M when the counter ion is hydrogen or sodium, but this decreases to a few mM when the counter ion is potassium. Another example is that of most Keggin POMs with tetrabutylammonium (TBA). Introducing TBA to an aqueous solution containing Keggin POMs (amongst others) will result in complete precipitation of the TBA-POM salt.

The resulting salt must be chemically processed in both cases to return it to a soluble form meaning that the fuel cell could only be operated in a batch mode, which would be incredibly inefficient. The more realistic option is to immobilise the POM on a high surface

area electrode so biomass oxidation can occur directly at the electrode surface. This idea was explored and the findings are detailed in the following section.

Investigation of PMo_{12} immobilised on a carbon felt electrode surface

A yellowish, cloudy precipitate forms that quickly settles if not stirred upon the addition of tetrabutylammonium (TBA) ions to a solution containing PMo_{12}. When dried, the TBA-POM salts tend to form hydrophobic flakes, which are soluble in organic solvents such as acetonitrile and acetone. The flakes are easily crushed in a pestle and mortar to form a fine powder that can be further dried. When the powder is added to acetonitrile or acetone, the solution takes on a deep, dark, yellow colour.

Small square (1 cm^2) pieces of carbon felt were boiled in an acetonitrile solution containing TBA_3PMo_{12} (0.8 mM) and then removed from the solution and left to dry overnight. The idea is that when the POM is in solution, it can penetrate the carbon felt very well and soak the entire surface area. Upon drying, the POM-TBA salt will precipitate and deposit on the surface of the electrode. When the felt is hydrated with water, or a water-based electrolyte, the POM-TBA salt (being insoluble in water) should remain on the surface of the felt. Then, through direct contact with the electrode and the solution, the POM should act as a surface coating that allows direct heterogeneous oxidation of biomass.

The volume of the felt is approximately 0.4 cm^3, and the porosity is expected to be in the region of 94% (according to the manufacturer data sheet). Assuming the entire void space is filled with electrolyte, the maximum possible amount of POM available for surface deposition is 300 nmol. However, due to low viscosity, when the felt was removed from solution, a significant portion of liquid dropped back into the beaker. Therefore, it seems unlikely that the entire void space was filled, meaning the amount of POM available for deposition is probably much lower than 300 nmol.

Cyclic voltammograms of the felt electrodes in aqueous solution were recorded to verify that the POM remained intact and electrochemically active. Figure 1.19 shows voltammograms for four different carbon felt samples that were treated in the manner described above.

For felts treated with the POM-containing solution, two characteristic peaks around 400 mV and 540 mV vs SHE are present. The felts were labelled CFTBA(1-5). Felts CFTBA1, CFTBA3, and CFTBA5 have approximately similar voltammograms, whilst felt 2 has a considerably larger peak current and underlying baseline current. It is unclear why this is the case.

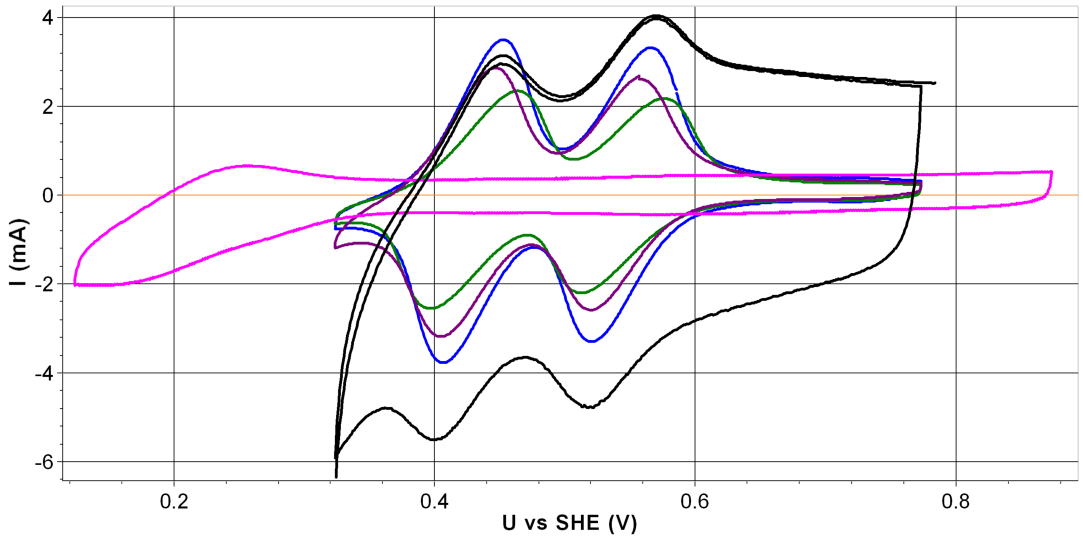

Figure 1.19: Initial cyclic voltammograms of carbon felt electrodes treated with TBA_3PMo_{12} (0.8 mM) solution. WE: carbon felt treated with TBA_3PMo_{12} 1 cm^2, CE: platinum wire, RE: mercury-mercurous sulphate electrode (0.674 V vs SHE), electrolyte: H_2SO_4 (1 M). Scan rate: 100 mV s^{-1}, Initial WE potential: 0.55-0.60 V vs SHE, initial sweep direction: positive, vertex WE potentials: 0.77 V vs SHE and 0.32 V vs SHE. CFTBA1: blue, CFTBA2: black, CFTBA3: green, CFTBA4: purple, blank CF: pink.

The sweeps in the positive direction depicted in Figure 1.19 show that at potentials higher than the peak current at 0.55 V vs SHE the current drops to a level comparable to the blank electrode and the response remains consistently flat between 0.65 and 0.77 V. This is a good indication that the redox reactants (POMs) have been depleted, and that the current can be fully attributed to the capacitance of the working electrode. Essentially this means there is a finite number of reactants in the vicinity of the working electrode, and consequently that the POM is very likely deposited on the electrode surface.

Figure 1.20 shows cyclic voltammograms of CFTBA1 at various scan speeds (10, 25, and 100 mV s^{-1}, and Figure 1.21 shows the maximum current of the four redox waves present in each voltammogram pltoted against scan speed. The linear relationship between peak current and scan speed for each redox wave is evidence that the reaction is not mass transport limited, and is further evidence for the POM being confined to the electrode surface. [76]

It is possible to calculate the charge attributable to the redox active species on the electrode surface through the integration of the current vs potential ($\delta I/\delta U$) and subtracting the charge which is attributable to the double layer capacitance of the carbon felt. Figure 1.22 depicts the voltammogram of CFTBA1 overlaid with a plot of charge vs potential. The latter

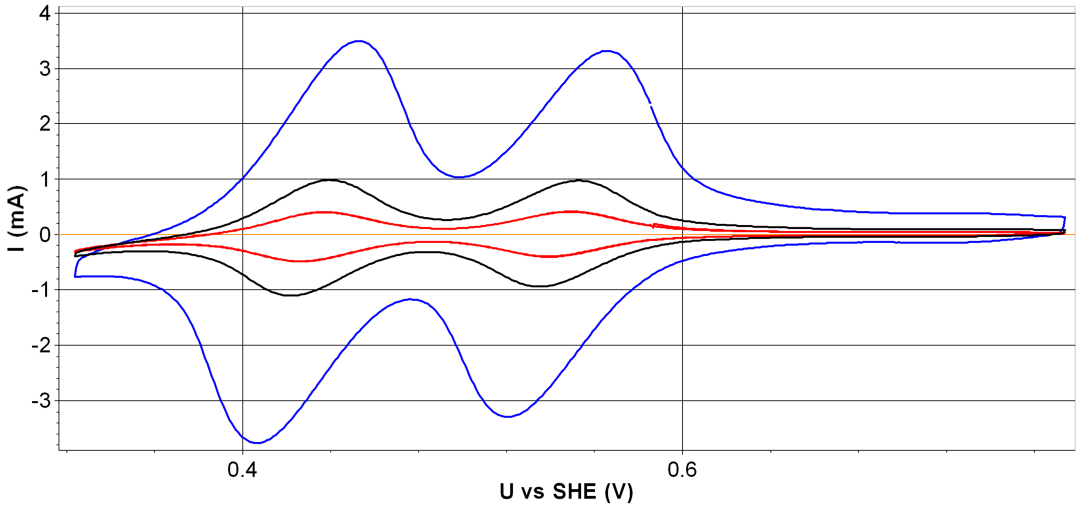

Figure 1.20: Cyclic voltammograms of CFTBA1 at various scan speeds. WE: carbon felt treated with TBA_3PMo_{12} 1 cm^2, CE: platinum wire, RE: mercury-mercurous sulphate electrode (0.674 V vs SHE), electrolyte: H_2SO_4 (1 M). Scan rate: 10 (red), 25 (black), and 100 (blue) mV s^{-1}, Initial WE potential: 0.58 V vs SHE, initial sweep direction: positive, vertex WE potentials: 0.77 V vs SHE and 0.32 V vs SHE.

value can be easily attained by multiplying the double-layer charging current (which is attained from the flat section of the voltammogram ($\geq$650 mV)) by the time to sweep between one voltage and another.

Using the second oxidation and reduction peaks of CFTBA1 as an example, the Faradaic charge was calculated on cyclic voltammograms with varied scan speed (10, 25 and 100 mV s^{-1}). The results in Table 1.6 are in relatively good agreement. By diving the average of the values listed in the table by Faraday's constant the amount of redox active PMo_{12} on the carbon felt surface is calculated to be approximately 20 nmol. The calculated amount of deposited POM is an order of magnitude or so lower than the theoretical maximum amount of POM available in the solution (assuming full saturation). However, as previously discussed, it seems unlikely that full saturation was achieved, and some material would also be deposited on the bottom of the felt's container. Under these circumstances, the amount of deposited POM is in line with expectations.

Next, the five felts were exposed to different environments to determine their stability with respect to conditions found in the biomass fuel cell. CFTBA1 was stored in lab-temperature deionised water. CFTBA2 was stored in water at 70 °C. CFTBA3 was stored in 1 M H_2SO_4 aqueous solution at 70 °C. CFTBA4 was stored in room temperature 1 M H_2SO_4 aqueous solution. The felts were stored in the respective environments overnight.

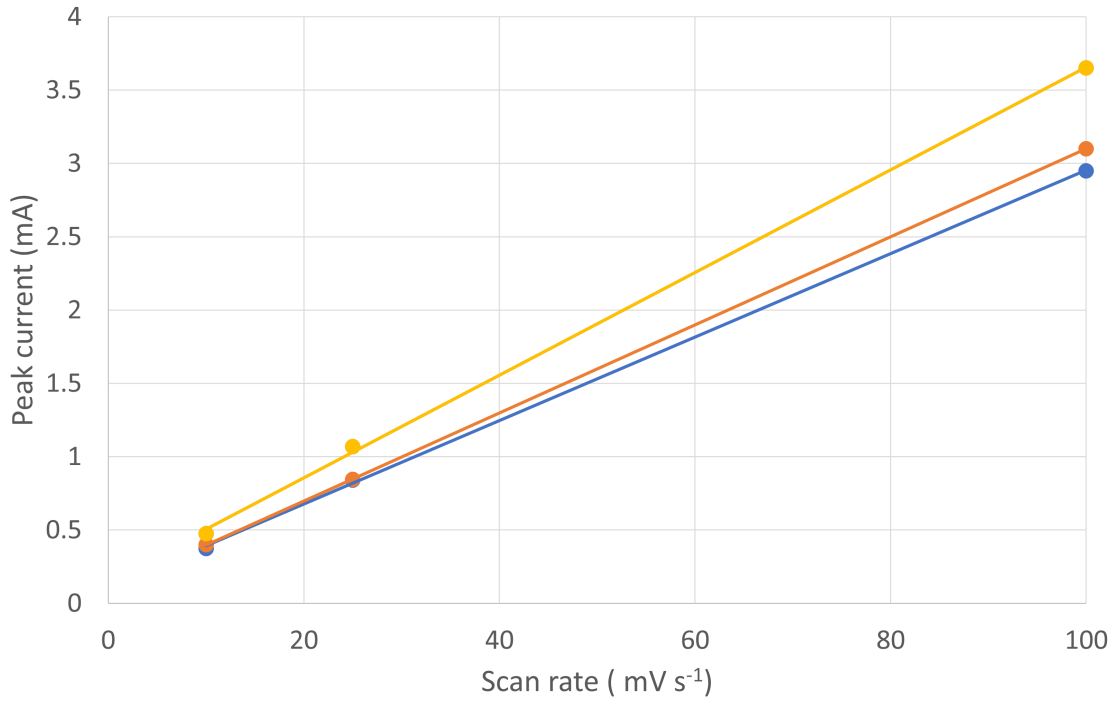

Figure 1.21: Peak current (absolute value) of each of the four redox waves present in Figure 1.20 versus scan speeds. WE: carbon felt treated with TBA_3PMo_{12} 1 cm^2 (CFTBA1), CE: platinum wire, RE: mercury-mercurous sulphate electrode (0.674 V vs SHE), electrolyte: H_2SO_4 (1 M). Scan rate: 10, 25, and 100 mV s^{-1}, Initial WE potential: 0.58 V vs SHE, initial sweep direction: positive, vertex WE potentials: 0.77 V vs SHE and 0.32 V vs SHE. $PMo_{12}(-1) \longrightarrow PMo_{12}(0)$: grey, $PMo_{12}(-2) \longrightarrow PMo_{12}(-1)$: orange, $PMo_{12}(0) \longrightarrow PMo_{12}(-1)$: right, $PMo_{12}(-1) \longrightarrow PMo_{12}(-2)$: yellow. Note that the grey and blue traces overlap significantly.

Scan speed (mV s^{-1})	Faradaic charge anodic wave (mC)	Faradaic charge cathodic wave (mC)
100	1.87	1.71
50	1.95	1.72
25	1.99	1.77

Table 1.6: Faradaic charge attributable to PMo_{12} deposited on a carbon felt working electrode (CFTBA1) calculated at varying scan speeds. WE: carbon felt treated with TBA_3PMo_{12} 1 cm^2 (CFTBA1), CE: platinum wire, RE: mercury-mercurous sulphate electrode (0.674 V vs SHE), electrolyte: H_2SO_4 (1 M). Scan rate: 10 (red), 25 (black), and 100 (blue) mV s^{-1}, Initial WE potential: 0.1-0.15 V vs SHE, initial sweep direction: positive, vertex WE potentials: 0.100 V vs SHE and -0.350 V vs SHE. Pre-treatment CVs: blue, post-treatment CVs (red).

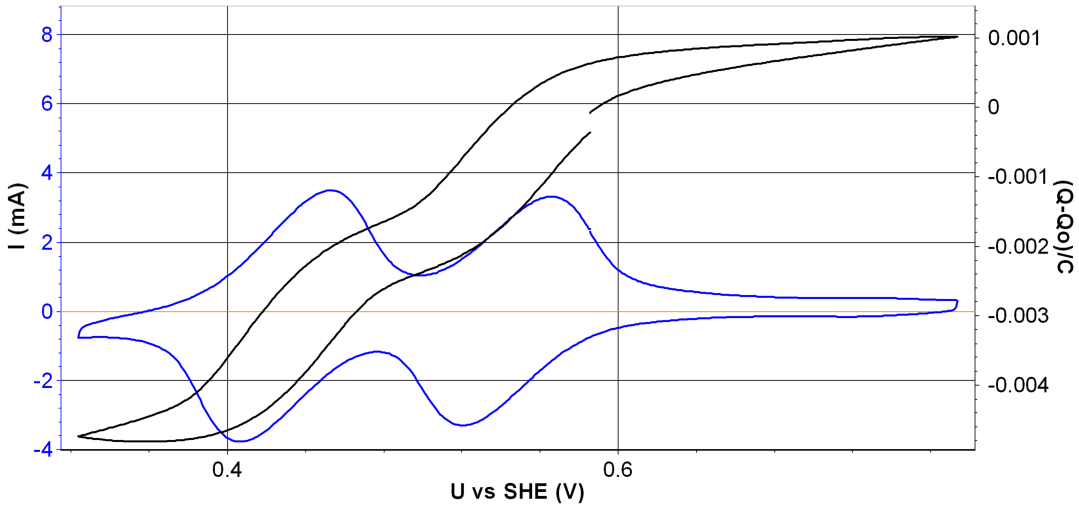

Figure 1.22: Cyclic voltammogram of CFTBA1 at 100 mV s^{-1} and overlaid plot of charge vs potential. WE: carbon felt treated with TBA_3PMo_{12} 1 cm^2, CE: platinum wire, RE: mercury-mercurous sulphate electrode (0.674 V vs SHE), electrolyte: H_2SO_4 (1 M). Scan rate: 100 mV s^{-1}, Initial WE potential: 0.58 V vs SHE, initial sweep direction: positive, vertex WE potentials: 0.77 V vs SHE and 0.32 V vs SHE. Voltammogram (blue), charge vs potential (black)

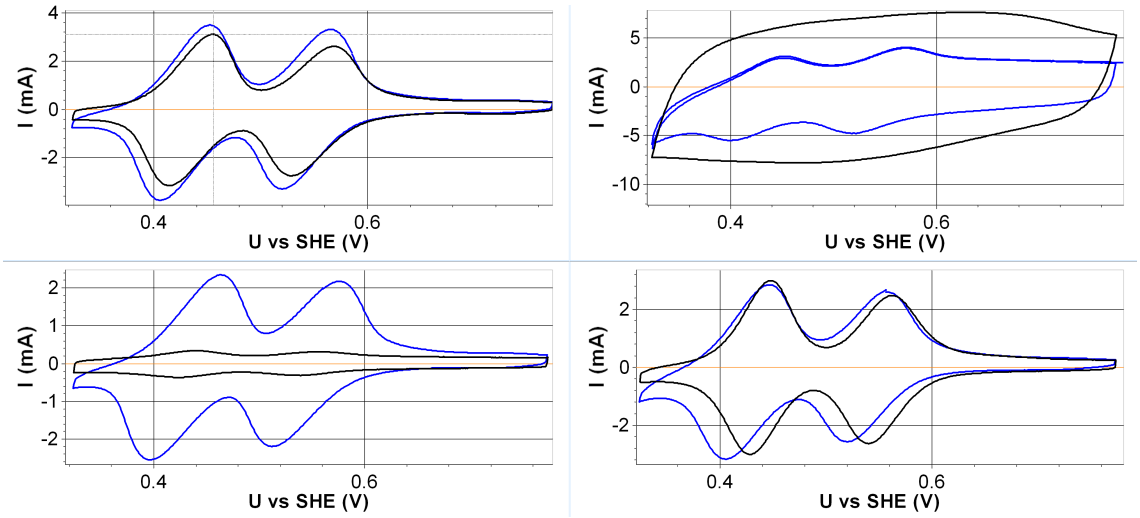

Figure 1.23: Cyclic voltammograms of carbon felt electrodes (CFTBA1-4) treated with TBA_3PMo_{12} (0.8 mM) solution after being stored overnight in their respective environments. WE: carbon felt treated with TBA_3PMo_{12} 1 cm^2, CE: platinum wire, RE: mercury-mercurous sulphate electrode (0.674 V vs SHE), electrolyte: H_2SO_4 (1 M). Scan rate: 100 mV s^{-1}, initial sweep direction: positive, vertex WE potentials: 0.77 V vs SHE and 0.32 V vs SHE. Pre-treatment CVs: blue, post-treatment CVs (black). Top left: CFTBA1, top right: CFTBA2, bottom left: CFTBA3, bottom right: CFTBA4. Open circuit potentials pre and post treatment: CFTBA1: 0.60 V & 0.43 V vs SHE, CFTBA2: 0.76 V & 0.49 V vs SHE, CFTBA3: 0.57 V & 0.68 V vs SHE, CFTBA4: 0.57 V & 0.71 V vs SHE.

From Figure 1.23 it can be seen that exposure to a high-temperature environment leads to reduced electrochemical activity of the felt electrode. The presence of sulfuric acid does not lead to a reduction in availability of POM on the electrode surface, however the open circuit potential of the two electrodes stored in sulfuric acid increase by 120-140 mV. Conversely, open circuit potential of the samples which were stored in water decreased, indicating that the POM is in a reduced state. The reason for this is unclear because the TBA_3PMo_{12} was in the fully oxidised state when prepared, and the open circuit potential of the electrodes post-treatment would indicate that that this remains the case after the POM has been deposited on the carbon felt surface.

Clearly, in order for PMo_{12} to become reduced, it must have oxidised either the electrode surface, or the TBA cations (no other species which can be oxidised are present). It should be relatively straightforward to establish whether the POM oxidises the electrode surface by measuring the capacitance over time directly after POM deposition. As carbon felt becomes oxidised, the surface becomes hydrophilic and the electrochemical surface area increases, consequently the capacitance increases. This could be achieved using standard electrochemical techniques such as electrochemical impedance spectroscopy, or voltammetry.

In this study, not enough samples were generated for a comparative study, and the voltammograms were not recorded for some time after deposition of the POM. Further studies into TBA_3PMo_{12} deposition on electrode surfaces may benefit from investigating the cause of PMo_{12} reduction.

CFTBA5 was heated to 150 ^{o}C in an oven for 3 hours to confirm that exposure to high temperature leads to a reduction in electrochemical activity. Figure 1.24 shows the cyclic voltammograms before and after treatment. The purpose of this experiment is to isolate the effect of an electrolyte or liquid on the POM. For felt samples 1-4, it is possible that the POM is dissolved in the electrolyte and is no longer in contact with it. However, this is not possible in a dry environment, so the POM must still be located on the electrode surface.

With that in mind, it is interesting to note that the peak separation increases significantly after treatment, but the charge transferred over a single cycle remains roughly the same. This suggests that the POM is still confined to the electrode surface, but the peak to peak separation of each redox wave is significantly larger ($\sim$ 100 mV), indicating a decrease in the rate of electron transfer. No further investigation was carried out, but one possible explanation is that heating the POM to 150 ^oC leads to melting and subsequent agglomeration of the POM into larger surface structures. It is expected that the conductivity of these surface structures is somewhat lower than the carbon felt, which would hinder electron transfer.

Due to the absence of suitable equipment to investigate the physical processes at the elec-

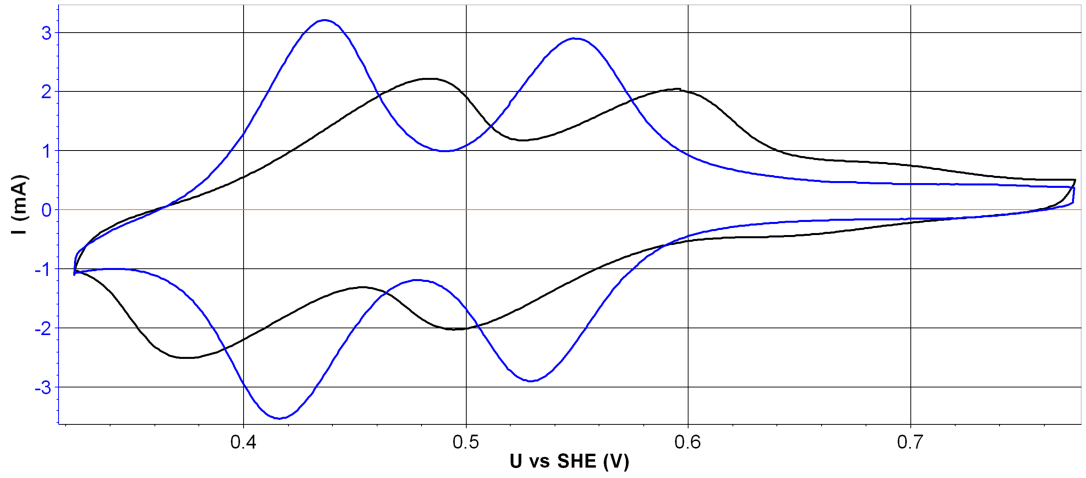

Figure 1.24: Cyclic voltammograms of carbon felt electrodes treated with TBA_3PMo_{12} (0.8 mM) solution before and after being heated to 150°C for 3 hours. WE: carbon felt treated with TBA_3PMo_{12} 1 cm^2, CE: platinum wire, RE: mercury-mercurous sulphate electrode (0.674 V vs SHE), electrolyte: H_2SO_4 (1 M). Scan rate: 100 mV s^{-1}, initial sweep direction: positive, vertex WE potentials: 0.77 V vs SHE and 0.32 V vs SHE. Pre-treatment CVs: blue, post-treatment CVs (black). Open circuit potentials pre and post treatment: 0.53 V & 0.61 V vs SHE.

trode surface, no further investigation was conducted on heterogeneous catalysis. However, the POMs appear stable at low temperatures, even after extended cycling (Figure 1.25).

1.3.3 Conclusion

The suitability of PMo_{12} as a biomass fuel cell catalyst/electron mediator in homogeneous solution has been assessed. An experimental procedure for determining the kinetic parameters in a semi-automated way has been developed and tested. The method utilises charge counting and oxidation state correlation with open circuit potential as independent but complementary metrics to monitor the progress of the reaction.

It was shown that when glucose is fully oxidised, PMo_{12} is a relatively good biomass oxidation catalyst. However, as the fuel becomes oxidised, the effectiveness of the POM as a catalyst decreases, which leads to the production of partly oxidised biomass and POM solutions which would be inseparable in a practical application. At this point, the reduced effectiveness of the POM to oxidise biomass is a significant obstacle that must be overcome.

A systematic study of the effectiveness of POMs as oxidation catalysts on simple organic molecules with various functional groups (such as methanol, ethanol, ethanal, propanone etc.) could be a helpful step toward identifying the mechanism of the reaction and the kinetic

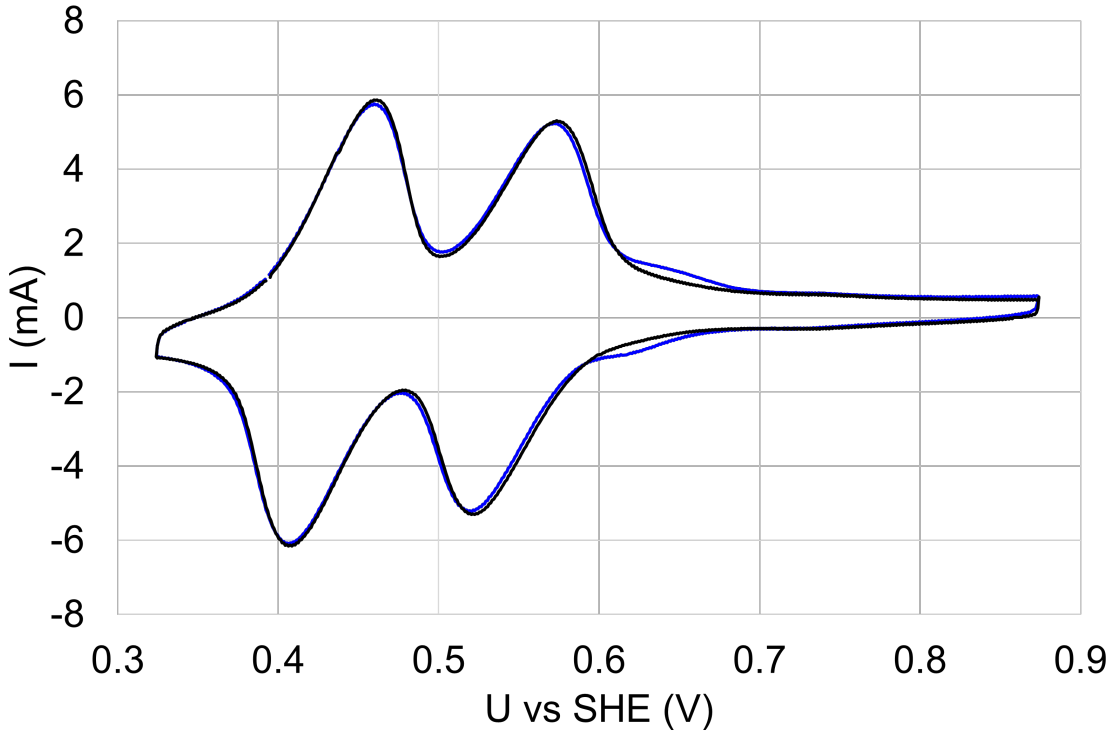

Figure 1.25: Cyclic voltammograms of carbon felt electrodes treated with TBA_3PMo_{12} (0.8 mM) solution (no further treatment). Cycles 1 and 800 are shown here. WE: carbon felt treated with TBA_3PMo_{12} 1 cm^2, CE: platinum wire, RE: mercury-mercurous sulphate electrode (0.674 V vs SHE), electrolyte: H_2SO_4 (1 M). Scan rate: 100 mV s^{-1}, Initial WE potential: 0.77 V vs SHE, initial sweep direction: positive, vertex WE potentials: 0.77 V vs SHE and 0.32 V vs SHE. Pre-treatment CVs: blue, post-treatment CVs (red).

parameters.

Chapter 2

Polyoxometalate redox flow batteries

2.1 Introduction

Storage of easily accessible energy on a large scale is a necessary step towards decarbonisation and stabilisation of the electrical grid, which will progressively utilise more wind and solar energy technologies as a primary power source. Energy storage is necessary because the utilisation of these power sources is dependent on weather effects and so is inherently intermittent, meaning supply and demand are not consistent.

One means of storing easily accessible energy on a large scale is the implementation of electrochemical applications such as batteries. There are many different kinds of electrochemical batteries, which store and release energy through various chemical mechanisms. The advantages and disadvantages of using a specific battery depend heavily on the application.

For example, intercalation batteries, especially those which utilise lithium ions, are exceptionally well suited for mobile applications such as smartphones, laptops, and personal automobiles. Their high volumetric and gravimetric energy and power density mean that they can be integrated into mobile applications without using too much space or adding too much weight.

Conversely, redox flow batteries (RFBs) are unsuited to mobile applications because their gravimetric and volumetric energy density is typically 10-100 times lower than that of intercalation batteries. However, volumetric and gravimetric energy densities are not particularly important for large-scale grid storage. In fact, batteries with large energy densities tend to come with safety concerns, which, given the size of storage installations necessary for grid decarbonisation, would lead to substantial risk.

This chapter deals with polyoxometalate redox flow batteries and covers various topics. A capital cost calculator was developed that can be applied to general flow battery chemistries. This model is described, and the results are discussed. The primary findings in this chapter involve the investigation of different POMs and electrolyte conditions and how these can lead to the development of properties desired in a flow battery.

Before that, it is worth briefly summarising what a redox flow battery is, why it is suited to large-capacity stationary storage applications, and the main challenges for RFBs in general.

2.1.1 Redox flow battery fundamental concepts

Figure 2.1 shows a basic concept of a redox flow battery. In the centre, there is a cell or stack (multiple cells stacked together) in series or parallel. Each cell is comprised of two half-cells, each containing an electrode, which is separated by a semi-permeable membrane. On either side of the cell, separate electrolytes (generally called anolyte and catholyte) are stored in tanks. The anolyte and catholyte contain electrochemically active species that can undergo reversible redox reactions. The reduction potential of the electrolytes gives rise to a potential difference across the cell. The two species are transported to the cell stack via tubing and pumps. Once inside the cell, the electrolytes directly contact the electrodes. The semi-permeable membrane allows current to flow between the two, typically in the form of specific cations and anions like hydronium and sulphate.

Consequently, a connection to an external power supply or load will cause a net current to flow in the cell stack. On charging, the anolyte will become reduced, and the catholyte will become oxidised. The anolyte will be oxidised on discharge, and the catholyte will be reduced.

The relatively simple nature of a redox flow battery has allowed researchers to investigate many different electrochemically active chemicals, supporting electrolytes, solvents, and so on. In essence, all that is needed for a redox flow battery to act as an electrochemical storage device is two chemical species that can reversibly undergo redox reactions at different reduction potentials. There are many examples of RFBs that utilise metal ions, such as the iron-chromium flow battery developed significantly by NASA in the 1980s.[77] In addition, organic molecules such as anthraquinones can be used in flow batteries. Some notable examples are as follows:

- A nonaqueous all-fullerene flow battery.[20]
- A zinc-bromine flow battery, in which the zinc plates onto the electrode surface upon

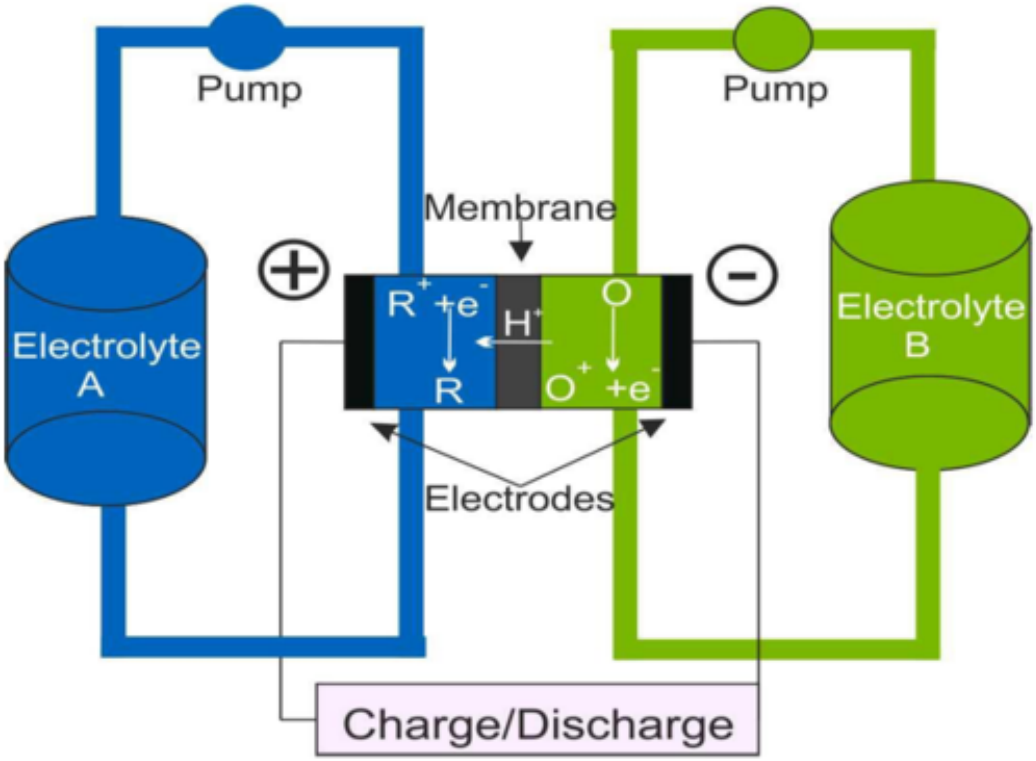

Figure 2.1: Simplistic diagram of a redox flow battery cell.

reduction.[78]

- The all-vanadium flow battery, in which the anolyte and catholyte contain the same constituents and can be remixed to restore the cell's capacity. [79]
- A hydrogen-manganese flow battery, where the two electrolytes are in different (gas and liquid) phases. [80]

Besides the flexibility of RFBs with respect to chemistry, their main advantage derives from decoupling device power and energy. For example, suppose an application necessitates a large amount of energy but low overall output power. In that case, this can easily be achieved by installing larger tanks to store more electrolyte.

Other kinds of batteries, such as those that rely on intercalation, are not as flexible in this regard. The electrodes need to be thicker to increase the energy density of an intercalation cell (assuming chemistry is fixed). However, thicker electrodes lead to an increased path length for the ions (typically Li), leading to a higher overpotential and reducing the cell's efficiency. This leads to more significant heat generation and general degradation mechanisms associated with high voltage. Hence, large amounts of intercalation cells must be used for applications requiring a large amount of energy, meaning the power specification could be much higher than needed. This quickly becomes uneconomical relative to a flow battery.

In addition, flow batteries are comparatively easy to recycle. The most valuable component that can be salvaged is the electrolyte (or the active species it contains), which can easily be recovered by evaporating the solvent.

Comparatively, intercalation batteries are built into modules and packs, generally held together by glues that cannot easily dissolve. Therefore, it takes much manual effort to pry the modules into single cells. Alternatively, the entire modules are shredded and sent to a recycling facility where pyrolysis is used to remove the graphite, glue, separator material etc., and the metals are then recovered.

Flow batteries also provide access to a much more comprehensive range of possible chemistries, including abundant, readily available, and cost-effective elements such as iron and chromium. Many RFBs also utilise relatively simple organic molecules that can be derived from natural feedstocks, paving the way for a very low-carbon form of energy storage.

Furthermore, the low energy density gives rise to a very safe battery. In the case where the solvent is water, there is no risk of thermal runaway, venting of toxic or flammable gases, fire, or explosions. There is a trade-off, of course, as many of the electrolytes used in RFBs contain species that are dangerous to humans and the environment. For instance, a spill of solutions

containing vanadium and chromium would have damaging effects to the surroundings and care would need to be taken to ensure local waterways are not contaminated.

From an economic perspective, many flow batteries are (in theory) very cheap to build, make use of very abundant elements, and do not require enormous capital-intensive facilities to produce. To demonstrate this point, a capital cost calculator that is based on the underlying electrochemical properties of flow batteries was developed, and is discussed in section 2.4

2.1.2 Factors that affect the performance of redox flow batteries

Redox flow batteries come with their own particular set of challenges that need to be overcome before wide-scale implementation can be achieved.

Capacity loss mechanisms

For example, the all-vanadium flow battery (VRFB) is probably the most well-understood and widely adopted RFB. The largest VRFB to date can store 800 MWh of electricity when fully charged and has a maximum discharge power of 200 MW.[81]

The VRFB has been popularised primarily because it overcomes one of the most pressing challenges flow batteries face: the crossover of active species through the membrane. In general, membrane crossover leads to irreversible capacity loss because there is no practical way of separating anolyte and catholyte when mixed.

There are three main factors which contribute towards crossover in a flow battery. The first of which is the large diffusion gradient across the membrane due to a highly concentrated solution of a species on one side and, ideally, none on the other. The second driving force occurs when the electrodes are polarised, and the ions in the solution migrate through the electric field. Thirdly, the flowfield characteristics of individual cells in larger stacks must be considered because minor deviations in electrolyte properties, such as viscosity or electrode morphology, for example, will lead to differential pressure across the cell, which will also lead to electrolyte crossover.

Therefore, to understand and overcome the problem of electrolyte crossover, the prospective researcher must simultaneously account for diffusion, active migration due to the electric field, and convection across the membrane due to pressure differences. In addition, these elements must be considered for a fluid that is actively being pumped through a complex three-dimensional structure.

Individually, these issues can be overcome in various ways. Diffusion can be mitigated

by reducing the membrane's pore size; however, this generally leads to reduced conductivity and a larger potential drop when a current is applied. Migration through the electrical field can be somewhat overcome by using membranes which preferentially allow the transport of cations or anions respectively in conjunction with active species that are anionic or cationic, respectively.

The VRFB essentially sidesteps these issues by having a virtually identical electrolyte on either side of the cell. The only thing that differs is the oxidation state of vanadium in solution. This arrangement is only feasible because vanadium is one of the few species to have at least four stable oxidation states (V(II), V(III), V(IV) and V(V)) that are highly soluble in aqueous solutions.

Of course, vanadium ions still cross the membrane in both directions, leading to self-discharge. However, the electrolytes can periodically be mixed to rebalance the vanadium concentration on either side. Then, the initial capacity can be restored.

A similar approach can sometimes be taken when the active species in either half-cell is different. For instance, researchers at NASA realised that mixing equal amounts of iron and chromium in a single electrolyte used on both sides allowed them to use thinner and more conductive membranes. This was done at the expense of energy density (the maximum concentration of active species had to be reduced), and crossover of species due to the membrane being more permeable. For some species, this would be a rather expensive solution, but iron and chromium are very cheap and widely available.

Consideration must also be given to solvent crossover. Different chemical environments on either side of the membrane can give rise to osmotic pressure, which can dilute one side and concentrate the other. This potentiallys leads to performance losses due to insufficient active species in a half cell at any given time for a target current density or power output. In some cases, species concentration may increase enough to lead to precipitation. This issue is particularly important to flow batteries where the pH on either side differs significantly.

There are also various ways in which the electrolyte can degrade, or change in such a way that the capacity is not accessible. For instance, if the active species can also undergo irreversible chemical reactions when exposed to a given potential, the nature of the electrolyte changes, and that capacity is no longer available. This is of particular concern for flow batteries which make use of complex organic species. Fortunately, chemical changes are easily detected in organic RFBs when in situ NMR can be utilised.

When high temperatures occur, the vanadium redox flow battery suffers from irreversible precipitation of V^{V}. At about $55 - 60\ ^{o}C$ V^{v} forms vanadium pentoxide, which dissolves so slowly in aqueous solution it is considered insoluble. Therefore, active cooling is necessary

for larger installations to dissipate excess heat.[82]

As will be discussed later, $PV_{14}O_{42}$ (which has been used in POM RFBs) forms a green precipitate under certain conditions, especially when it is reduced to a high degree.

Competing electrochemical reactions, such as hydrogen evolution on the anolyte side, can also occur. This leads to a mismatch in the state of charge between the anolyte and catholyte, ultimately rendering the capacity of the anolyte inaccessible. Furthermore, if HER occurs in a battery which allows for electrolyte remixing, the average oxidation state of the electrolytes will increase on remixing, such that the capacity cannot be fully recovered without further intervention.[83] Capacity recovery can be achieved by using chemical oxidants; however, this may alter other electrolyte properties if, for example, the side products remain in solution. Another option is to put a cell supplied with hydrogen on one side in parallel to the main stack. The hydrogen can be oxidised and, in doing so, electrochemically reduce the active species to the appropriate extent. Both options affect the overall energy efficiency and add to the list of components that must be maintained (e.g. regular refuelling of an oxidant).

Electrolyte properties

There are numerous electrolyte properties which ultimately have an impact on the operation of an RFB. For instance, an obvious finding is that increasing the active species concentration generally increases capacity. Another is that increasing the supporting electrolyte concentration generally leads to increased electrolyte conductivity. However, more complex effects can result from altering electrolyte properties. For instance, Holland-Cunz et al. found that substituting sulfuric acid for phosphoric acid as a supporting electrolyte in a VRFB resulted in a 67-fold increase in the standard rate constant (k^0).[65] The faster electron transfer lead to the development of a cell that operated at lower overpotentials relative to a cell with sulfuric acid as the supporting electrolyte.

The energy density of RFB electrolytes is quite low relative to other battery types, but this is fairly unimportant when the application is stationary storage. An appreciable active species concentration can be achieved due to the ability to store electrolytes in tanks of arbitrary size. However, it is still worthwhile to try and maximise the energy density of the electrolyte as this will result in a lower cost for storage media, higher power density due to active material availability, and lower stack cost due to higher power density. For a given pair of electrochemically active species, there are various ways to increase the energy density of the electrolyte.

The most obvious is to increase the concentration of the active species. Typically, com-

mercialised technologies have a solubility in the range of 1-2 M. There are various challenges associated with increasing concentration. For instance, a more concentrated solution is typically more viscous and will result in a greater pressure loss when pumped through a cell. This will also result in reduced electrolyte conductivity due to increased viscosity. Also, as the concentration increases, the species in the solution can deviate significantly from ideal behaviour, which can have unwanted side effects.[84] A viscous solution also allows for less diffusion to take place, so the transport of material to the electrode interface becomes an issue. Care must also be taken that the active species is soluble in both the oxidised and reduced states for extended periods at higher concentrations.

One other approach, which applies to species which undergo proton-coupled electron transfer, is altering the pH to increase or decrease the reduction potential so that the potential difference across the cell can be maximised. Altering the pH of a solution can also contribute significantly to the stability of dissolved species. For example, ferricyanide, which is often used as a well-behaved active species at the positive half-cell, will react with strong acids to release cyanide gas.[85] Not only does this lead to irreversible capacity loss, but it is also hazardous to lab users.

The effect of varying pH in a solution containing POMs can remarkably impact the solution's properties. In his seminal literature review, Pope gives an excellent account of the research regarding highly reduced states of heteropoly molybdates and tungstates.[8] The tungstates, in particular, can reportedly be reduced to a much lower oxidation state than what was accessed in the PW12/PV14 battery reported previously by Stimming group.[1] Of particular interest is α-$[(H_2)W_{12}O_{40}]^{5-}$ (a compound which has the Keggin structure with two hydrogen atoms delocalised in the centre) which can be reduced by up to 32 electrons. Similar trends are observed for the other polytungstates. SiW_{12}, for instance, can be reversibly reduced by up to 20 electrons.

Depending on the standard potentials, and the reduction potential range of a given active species, it may be desirable to increase or decrease the pH accordingly. For example, for a species with an electrochemical reaction that has a standard potential 0 V vs SHE that is not proton-coupled, a higher pH is desirable as this will offset the hydrogen evolution reaction and minimise the parasitic current on a given cycle. Since the reduction potential shifts in the negative direction as the active species is reduced, a higher pH would allow for a lower oxidation state to be attained without the risk of hydrogen evolution. This in turn contributes to the increased capacity of the battery.

Conversely, increasing the pH can destabilise many metal and metal oxide species in aqueous solutions. As will be shown later in this chapter, fully oxidised PMo_{12} will readily

dissociate into molybdate and phosphate species at higher pH but will reform when the pH is returned to a low value.

An increase in pH can also lead to reduced solution conductivity. This is especially a problem for cation exchange membranes, which preferentially allow the transport of cations through the membrane. Nafion, which is the most popular cation exchange membrane in use, is designed for its ability to conduct protons well. Other cations do pass through it freely but free protons are exceptional in their ability as charge carriers due to hopping mechanisms.

Current density and energy efficiency

For various reasons, a relatively high current density is desirable for flow batteries. There are different ways that this can be measured. However, it is typical in RFB research to measure metrics relating to power output, such as power density (W cm^2) and current density (mA cm^2), with respect to the geometric electrode area.

Primarily, the driving factor for this is the need for reduced flow battery stack costs. Studies of the capital cost of redox flow batteries typically show that the cost of RFB stacks is one of the main contributing factors to overall capital cost. This is especially true when expensive membrane materials like Nafion are utilised. So, a higher power density with respect to electrode area results in a decrease in overall stack size, cost, and complexity.

However, there are a variety of challenges that need to be overcome for this to occur. Firstly, many active species (such as vanadium) exhibit slow reaction kinetics when undergoing oxidation or reduction at an electrode surface. The rate constant for the VO^{2+}/VO_2^+ reaction is typically in the region of 10^{-7} cm s^{-1}, which is rather low. A low rate constant results in a low exchange current at the electrode surface; hence, a lower perturbation for a given overpotential occurs. Effectively this means that higher charging voltages are needed, and lower discharging voltages occur, so the efficiency of the battery suffers.

The inefficiency of the battery can lead to all sorts of issues depending on the chemistry involved. For example, if the battery is very large, then the heat generated through cycling can build up over time and result in the electrolyte becoming hot. Because of the inverse relationship between volume and surface area, the problem worsens as the battery becomes larger. In the case of the VRFB, this is especially troublesome. At about $50 - 55\ ^oC$, V(V) irreversibly precipitates out of solution and forms vanadium oxide species. Not only does this lead to irreversible capacity fade, but it can also clog up the stack and result in a larger pressure loss, resulting in further inefficiencies. The stack/cell can become completely clogged and leak in extreme cases. An example of how precipitation in a flow cell can lead to blockages can be

Figure 2.2: The result of precipitation of PV_{14} due to over-reduction. In a later section, the stability of PV_{14} in the reduced state will be discussed in more detail.

seen in Figure 2.2, in which a polyoxometalate has precipitated due to excessive reduction.

One other challenge is the amount of reactive material in the cell/stack at any given time. As the reaction proceeds, the electrolyte becomes oxidised/reduced, reducing the cell's available material. Less active material in the half cell results in lower concentrations of active material at the electrode interface, so a larger overpotential is needed to achieve a target reaction rate. Also, as the reactants become oxidised/reduced, the reduction potential in the cell/stack changes, and it deviates from the average reduction potential in the tanks.

Generally, these problems are overcome by utilising porous three-dimensional electrodes such as carbon felt. Carbon felt is ideal for overcoming these issues because it has a large electrochemically active surface area, and its three-dimensional nature means that large void spaces are available inside of the electrode. So at any given time more active material is available. The caveat is that a thicker electrode will lead to a longer path for a charge carrier to travel through the solution before it crosses the membrane. In other words, thicker electrodes

provide more surface area for the reaction to occur, effectively reducing the overpotential for a target current density. However, they also lead to increased solution resistance by increasing the mean free path of charge carriers to the other half cell; consequently, as the electrode becomes thicker, the effectiveness of increased surface area becomes less significant. Since the resistance to current flow is lowest at the surface in contact with the membrane (assuming homogenous concentration), the amount of current that flows diminishes with respect to distance from the membrane. Generally, carbon felt electrodes for flow batteries are about 3-5 mm thick and are slightly compressed to ensure good contact with the current collector.[86]

Although no research was found on the subject, it seems likely that the difference in the solution reduction potential as it leaves the stack, and that of the solution in the tanks leads to energy losses (in the form of heat generation) when the two are remixed. As an extreme example, if we say the catholyte in a VRFB is initially fully reduced (V^{2+}), and 5% of the total volume of A is passed through a half cell and fully oxidised to V^{3+}, the reduction potential of the solution in the half cell is several hundred milivolts higher than that of the bulk solution in the tank. In this example, not only do the losses from kinetic and mass transport effects have to be considered, but also the thermodynamic losses associated with reducing the electrolyte well beyond the average oxidation state in the tank, thereby reducing the maximum possible potential difference of the cell. Furthermore, on re-entering the tank, the average oxidation state will equilibrate to $V^{2.05}$ and heat will be generated due to mixing two solutions with a chemical potential difference.

Two solutions exist to address this issue. Firstly, the amount of active material passing through the cell per unit of time can be increased by operating the pump at a faster rate. Consequently increasing convection parallel to the membrane surface and minimising the difference in oxidation state between the stack and the tank. However, increasing pumping speed leads to a number of issues, such as increased pressure drop across the stack. The primary effect of this is to reduce the overall energy efficiency of the battery (something which is often disregarded during single-cell and short-stack testing). Additionally, carbon felt can become compressed at high flow rates, leading to increased pressure loss and even reduced or different flow patterns through various areas of the electrode. If the pressure drop is very high, this can lead to leaks and accelerated fatigue of the components in the pump.

Secondly, the current density can be decreased so that the oxidation state of active species (and therefore the reduction potential) in the stack and tank do not deviate too much. This does result in a more considerable capital cost though, as a larger stack means larger electrodes, housing, membrane etc., are needed. A balance must be struck between the various parameters associated with electrolyte flow. Some researchers have addressed the various as-

pects mentioned above. However, a detailed treatment was not found and likely requires complex CFD simulations that are only useful for specific stack and cell geometries.

2.1.3 Polyoxometalate redox flow battery fundamental concepts

Polyoxometalates have a variety of properties which are desirable when employed as active species in a redox flow battery. The main potential benefit of POM RFBs is that their large size generally gives rise to much faster electron transfer kinetics than analogous single metal centre species. Their large size also significantly hinders transport through commonly utilised cation exchange membranes such as Nafion to the point where it is negligible over several thousand charge/discharge cycles.

POM RFBs should not lose capacity due to crossover, can have a much higher power density than species with slower kinetics, and should be able to make use of smaller stacks which make use of less material and are cheaper.

Furthermore, as can clearly be seen in Figure 1.8 in chapter 1 POMs are able to undergo multiple redox reactions at various different potentials. For a given concentration, the capacity of POMs is much higher than a single metal ion species. Furthermore, the standard potential of the reactions associated with electron transfer generally decreases rapidly as the POM is reduced. As will be shown later, this allows for aqueous cells with wide potential windows.

It is important to note that although POMs have multiple redox couples, the total capacity in terms of coulombs per mole of a single metal ion (e.g. V^V) might be much lower. As an example, if a solution containing 100 mM of $PV_{14})_{42}$ is used as a catholyte and can be reduced by 7 F mol^{-1} (i.e. one mole of PV_{14} can be reduced by 7 moles of electrons), this means that it has a (charge) capacity 7 times greater than a 100 mM solution of V^V. However, the amount of vanadium needed to make the POM is 14 times greater, so the capacity per mole/kg of vanadium used is half as much.

Therefore, the argument in favour of the POM RFB relies heavily on the ability of POMs to be reduced by a significant number of electrons reversibly. Alternatively, the POMs must have a wider potential window than the single metal ions, or the constituent elements must be so cheap that the cost of using additional material is outweighed by the other benefits that POMs have when utilised in RFBs, (e.g. higher power density, negligible membrane crossover, fast kinetics etc.).

It is possible to reduce some polyoxometalates to a very large degree. Hervé showed that it was possible to reduce the metatungstate ion $([(H_2)W_{12}O_{40}]^{6-}$ by up to 32 electrons from

the fully oxidised state on a dropping mercury electrode.[87] If we use an analogous example to the previous paragraph, this would result in a capacity increase per kg of metal used by a factor of 2.67 before the significant decrease in standard potential is even considered.

Whether a POM RFB can compete with existing technologies is currently unclear, but it is worth investigating.

The first POM RFB was presented in 2013 by Pratt et al.[88] The battery utilised a substituted Keggin type POM ($[SiV_3W_9O_{40}]^{7-}$) as active species on both negative and positive half cells. Aqueous and nonaqueous varieties of the cell were produced and tested in the 2013 paper. The rationale behind using a substituted POM (one in which there are at least two metal elements present) is that there is typically a large difference in standard reduction potentials between the two types of metal. In the aqueous case, the first reduction ($V^{V} \longrightarrow V^{IV}$) occurs at around 1.6 V vs SHE, and the first reduction of tungsten ($W^{VI} \longrightarrow W^{V}$) occurs around 0.4 V vs SHE.

The use of symmetric electrolytes means that active species crossover can be tolerated. This significantly simplifies the setup of the flow battery and, in theory, allows one to use a much thinner, more permeable membrane with a higher ionic conductivity.

The downside is that much of the available capacity in the POMs is not being utilised. In the catholyte, all of the tungsten remains unused, and in the anolyte, all of the vanadium is unused throughout the operation of the cell. This is not an issue if the metals are inexpensive, but this is unfortunately not the case for vanadium and tungsten.[89, 90]

The cell had a relatively low capacity that faded to approximately 85 % of its initial value over the course of 100 cycles. The current density is also quite low (2 mA cm^2), but this is primarily due to the low concentration of POM (20 mM).

As a closing statement, the authors claim that the amount of supporting acid needed for operation is much lower than for a typical vanadium flow battery. Though this is true, the relevance of this statement is negligible due to the enormous difference in active species concentration (20 mM vs $\sim$ 1.6 M).

In 2018, the first asymmetric POM RFB, which utilised $[SiW_{12}O_{40}]^{4-}$ and $[PV_{14}O_{42}]^{9-}$ polyanions as the active species, was presented by Friedl et al.[1] This followed a series of articles from Stimming Group and partners which analysed the electrochemical and chemical properties of POMs and polyoxoanions in a variety of applications and conditions.[58, 60, 91–93]

The development of an asymmetric POM RFB allowed some of the issues that faced the various symmetric cells to be overcome.[88, 94–96] The primary obstacle is that substituted POMs are much more challenging to prepare than unsubstituted ones. They also tend to be

less stable in aqueous solutions. As previously discussed, their capacity is also limited due to the underutilisation of metal centres.

As part of the aforementioned study, the electron transfer constants for SiW_{12}/SiW_{12}^{-} and $SiW_{12}^{-}/SiW_{12}^{2-}$ on glassy carbon was shown to be 3-4 orders of magnitude higher than that of the V^{2+}/V^{3+} reaction. k^0 was not reported for PV_{14}, probably because there are 5-6 overlapping redox reactions in the potential range that is of interest, so it is difficult to attribute a rate constant to any given redox couple. However, it was shown that the redox reactions were electrochemically reversible through plotting the peak current density from a cyclic voltammogram against the square root of scan rate revealing a linear relationship.[97]

The charge-discharge curve clearly shows two plateaus on charging and discharging the battery. The capacity that can be attributed to each corresponds well with the expected capacity for a 2-electron reduction/oxidation of the electrolytes.

Notably, it is shown that hydrazine can be used as a chemical reducing agent to restore or increase the capacity. On addition of hydrazine to the PV_{14} reservoir, the capacity increases past its initial value. The addition of hydrazine is accompanied by a change in solution colour from dark brown to green and an increase in pH indicating that the POM has been reduced.

In-situ V^{51} NMR was also used to show that PV_{14} can be reduced and oxidised electrochemically with no effect on the structure of the molecule. The disappearance of vanadium peaks in the NMR spectrum also indicates that the charge is delocalised across the entire molecule. This is a possible explanation for why the kinetics are fast. Later work showed that upscaling the cell from 25 cm^2 to 1400 cm^2 could be achieved without adverse effects. [2] In fact, the normalised resistance towards charge transfer and diffusion decreased by a factor of 10 and 2 respectively. This is likely due to the processing technique of the felt being different and the flow path in the larger cell favouring increased mass transport but highlights the importance of these parameters on flow cell operation.

The coulombic efficiency of the larger cell was much higher (96% vs 99 %), probably due to lower oxygen ingress in the larger cell/reservoir relative to the volume of electrolyte. However, the capacity per mole was lower, averaging about 1.4 electrons per molecule at full capacity.

One issue of note is the high ohmic resistance of the cell, which is attributed to low solution conductivity. The relatively high pH ($\geq$2) that is required for PV_{14} to be stable means that other cations must be used to facilitate charge transfer. In this case, a mixture of Na^+ and Li^+ is used, which both have a lower conductivity than hydrogen ions. K^+ is more conductive, but there is an inverse relationship between cation size and POM solubility - the maximum concentration of many Keggin POMs when K^+ is added to solution reduced to a

few mM.

Another strategy would be to use an anion exchange membrane or a size exclusion membrane. However, this may cause issues because POMs are anionic, so their transport would be somewhat facilitated through the membrane, provided the pore size is not too small.

In 2019 Feng et al. reported on a battery which used phosphotungstic acid ($H_3PW_{12}O_{40}$) and hydrogen iodide as active solutions in the anolyte and catholyte compartments respectively.[62] The cell is interesting because it is a rare example of a semi-symmetrical in which the hydrogen iodide is also present in the anolyte to alleviate the osmotic pressure between the two solutions. This approach means that the effect of iodide crossover is minimised since it occurs in both half cells to a large extent. One of the cells assembled by Feng achieves an energy efficiency of 80.1% and coulombic efficiency of 99.6%. This is broadly comparable to what one would expect for an all-vanadium RFB and is a good demonstration that POMs could be a serious competitor in the flow battery landscape.

Significant chemical and electrochemical challenges remain, however. For instance, expensive materials such as tungsten and vanadium significantly add to these systems' capital costs. This is especially true considering the underutilisation of redox couples.

The work presented in this chapter focuses heavily on exploring methods for increasing the accessible capacity of POMs and finding more cost-effective electrolytes than tungsten-based POMs. A calculator is also presented, allowing users to input basic chemical and electrochemical parameters and generate a rough approximation of capital cost. This can serve as an early indication as to whether a given RFB chemistry can be competitive.

2.2 Experimental procedures

2.2.1 3+ electrode cell general procedures

The general procedures for cyclic voltammetry on homogenous POM-containing solutions (and control solutions such as the supporting electrolyte) were all carried out in a similar fashion. A glass electrochemical cell with either 50 or 100 mL volume was thoroughly rinsed with deionised water (18.2 MΩ cm at the source) at least five times. All disk working electrodes (glassy carbon from BASi) were polished using an aluminium oxide slurry on a polishing pad in a figure-of-eight pattern for two minutes. The roughness/specific active surface area was generally not calculated unless otherwise stated. After polishing, the working electrode and all other electrodes were rinsed with deionised water to remove impurities.

The supporting electrolytes (sodium chloride, lithium chloride, phosphoric acid, sulfu-

ric acid etc.) were prepared by dissolving them directly in deionised water. PMo_{12} and SiW_{12} were available in solid form with hydrogen as the cation from Merck. The appropriate amounts were weighed and added to the solution containing supporting electrolytes. If the pH was adjusted, this was achieved by adding small amounts of 1 M NaOH, LiOH, or HCl aqueous solution.

PV_{14} is not commercially available and was prepared in house in an analogous fashion to that reported in previous papers by our group and others.[1, 3, 98, 99] The presence of PV_{14} was confirmed by ^{51}V NMR (chemical shift of peaks: 532, 584, and 598 ppm). [3]

After the addition of supporting electrolytes and POMs, the volume was adjusted to the appropriate amount in a volumetric flask and then added to the electrochemical cell. The solutions were then bubbled with nitrogen gas that had been bubbled through deionised water. This was done to minimise the evaporation of solution in long-term experiments. The solutions were bubbled for at least one hour (12 hours if a felt electrode was present) before electrochemical experiments were carried out.

Throughout the course of the experiment, the electrochemical cell was sealed as much as possible. A constant stream of nitrogen gas was pumped above the solution surface so there was no visible disturbance. This was done to generate a positive pressure inside the cell and exclude as much oxygen as possible.

Electrolysis cells were prepared similarly, except the counter electrode was located behind a glass frit, and the counter electrode compartment was open to the atmosphere. This was done to minimise the mixing of evolved gases (e.g. oxygen, hydrogen, chlorine) with the environment of the main solution. Magnetic stirrer bars were used to mix the solution and ensure efficient transport to the working electrode.

For some experiments, the temperature and pH were monitored throughout using a temperature probe that was encased in glass and inserted into the main solution, and a glass pH probe that was frequently calibrated using solutions of known pH. For solutions which were maintained at above ambient temperature, this was achieved by using a hot plate which automatically heated the solution until the thermometer encased in glass reached a target temperature.

2.2.2 Synthesis of PV_{14}

A typical procedure presented here is for PV_{14} with a Li^+ counter ion. $LiVO_3$ (63.55 g, 600 mmol) is added to distilled water (250 mL) and heated until boiling to afford a pale yellow solution which is slightly cloudy. After boiling for one hour, the solution is cooled to room

temperature, and phosphoric acid (85%, 17.29 g, 150 mM) is added to afford a P:V ratio of 1/4. The addition of phosphoric acid leads to the formation of a dark red/brown solution colour. The pH of the solution is adjusted to 2.0 by adding small amounts of concentrated hydrochloric acid. The solution is then stirred for at least 12 hours, after which the pH drifts upwards to 3-4. More concentrated HCl is added to decrease the pH to a final value of 2.3. After several hours a small sample is taken, and the presence of PV_{14} is confirmed by characteristic peaks by ^{51}V NMR. [3] This constitutes a typical procedure for synthesising stock solution for redox flow battery studies. The stock solutions were stored at room temperature in the lab and diluted to the appropriate concentration with either 1 M LiCl or 1 M NaCl solutions where appropriate. The concentration of PV_{14} solution was deduced from the amount of vanadium added to the solution. The stock solution was typically prepared with a high concentration ($\geq$200 mM). In order to prepare a solution with a given target concentration, an appropriate amount of PV_{14} stock solution was added to a solution containing supporting electrolyte with a pH of 2.3. On addition of PV_{14}, the pH would generally rise slightly, so hydrochloric acid was added to reduce the pH to 2.3. The pH continues to drift for about 12-24 hours after dilution. The solution was always monitored for 24 hours after dilution - and HCl was added as needed.

The $[H_xPV_{14}O_{42}]^{-9-x}$ anion (PV_{14}) was synthesised in the following way: $NaVO_3$ (73.98 g (96% purity) was dissolved in approximately 250 mL of deionised water and boiled to afford a brown solution. The solution was boiled for one hour. After this, the solution was transferred to an ice-cold water bath to decrease the temperature rapidly, and H_3PO_4 (10.4 mL, 85% w/w) was added to afford a dark brown solution. The solution was then stirred for 12 hours. After stirring, the solution pH had risen to 5.24. A significant quantity of dark brown precipitate was present in the solution. HCl (37% w/w) was used to titrate the solution. After the addition of 9 mL of HCL solution, the pH drops to 4, the precipitate began to dissolve into the solution, and the pH takes longer to stabilise. After 16.5 mL of HCl solution was added, the precipitate had fully dissolved, and the pH was 2.18. 17.6 mL of HCl solution was added in total, and the solution was left to stir for 3 hours, after which the pH had risen to 3.01. A further 2.5 mL of HCl solution was added to decrease the pH to 2.25. The solution was left to stir overnight. The next day, the pH had risen to 2.8, and a further 2.1 mL of HCl solution was added to decrease the pH to 2.25. The addition of water increased the volume to 250 mL. After standing for several days, the pH had increased again to 3.3, and a dark brown precipitate was present. 5.4 mL of HCl solution was added, and the pH decreased to 2.31. A large amount of precipitate was still present, so the solution was filtered. The precipitate was dissolved in water and added to the main solution. The pH stabilised at 2.32. The solu-

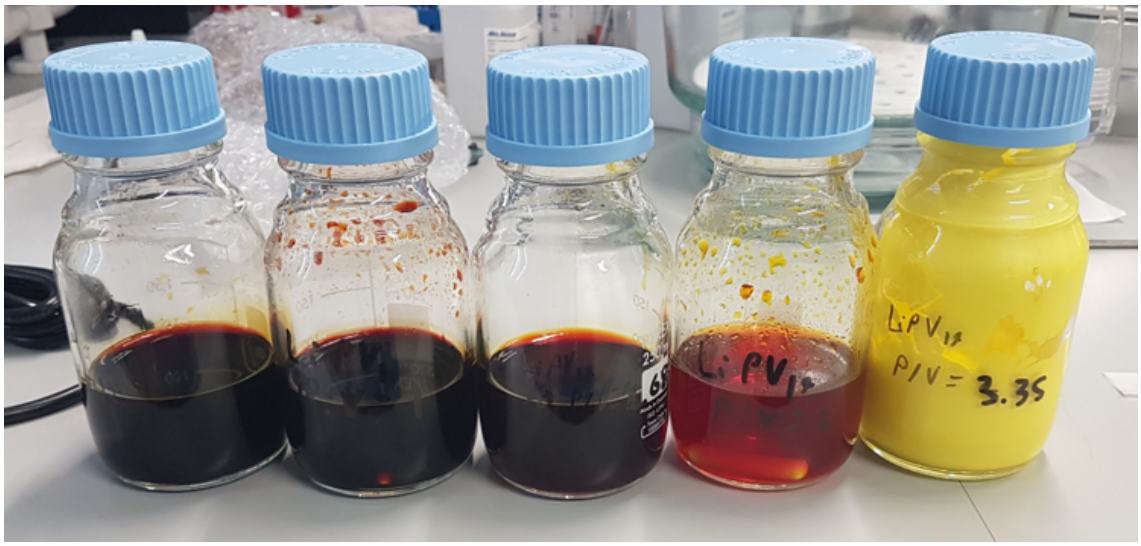

Figure 2.3: PV_{14} solutions with varied pH and P:V ratio. From left to right, P:V ratio: 0.5, 1, 1.68, 2, 3.38, and pH: 5, 2.07, 1.48, 1.16, and 0.96.

tion was refiltered, and a small amount of brick red precipitate was left over which would not dissolve on further addition of water. The precipitate was dried and weighed 0.6790 g. Presumably, the precipitate was an impurity. The main solution volume was increased to 500 mL to afford a final vanadium concentration of 1.103 M and a pH of 2.31. No precipitate was present. V^{51} NMR confirmed that PV_{14} was the only detectable vanadium species present in the solution (chemical shift of peaks: 532, 584, and 598 ppm).

In addition to the synthetic procedures above, a slightly modified version was used to produce solutions with varied P:V ratio. This was done as part of an investigation into the effects of varied phosphate concentration, reduction degree, and temperature on POM stability. After the addition of phosphoric acid and prior to adjusting the pH to a final value of 2.3, the pH values for the five solutions (P:V ratio: 0.5, 1, 1.68, 2, 3.38) were 5, 2.07, 1.48, 1.16, and 0.96 respectively. Solutions with a P:V ratio of 1.5-1.68 have the characteristic colour of PV_{14}. The solution with a P:V ratio of 2 was much lighter in colour. The sample with a P:V ratio of 3.38 was bright yellow and was highly viscous and sticky. An image of the samples prior to adjusting the pH can be seen in Figure 2.3. The pH of solutions was adjusted to 2.3 using HCl or LiOH as necessary, and all samples took on the expected appearance of a PV_{14} solution (i.e. dark red/brown liquid) with no precipitate. The volume of each solution was increased to 150 mL, affording a final PV_{14} concentration of 28 mM (confirmed by V^{51} NMR).

12 10 mL samples of each solution were placed into sample vials. Each set of 12 samples

Stability of PV14 after 14h in respective temperature

			Oxidation state	0			-2			-4			-6		
	P:V	c (mM)	Temperature (°C)	25	45	70	25	45	70	25	45	70	25	45	70
LiPV14	0.5	2.8		Y	Y	Y	Y	Y	Y	Y	Y	N	Y	Y	N
LiPV14	1	2.8		Y	Y	Y	N	N	N	Y	N	N	Y	N	N
LiPV14	1.68	2.8		Y	Y	Y	N	N	N	N	N	N	N	N	N
LiPV14	2	2.8		Y	Y	Y	N	N	N	N	N	N	N	N	N
LiPV14	3.38	2.8		Y	Y	Y	N	N	N	N	N	N	N	N	N
LiPV14	0.25	85		Y	Y	Y	Y	Y	N	Y	N	N	N	N	N
LiPV14	0.25	178		Y	Y	Y	Y	N	N	N	N	N	N	N	N
NaPV14	0.25	80		Y	Y	Y	Y	N	N	N	N	N	N	N	N

Stability of PV14 after 4 days in respective temperature

			Oxidation state	0			-2			-4			-6		
	P:V	c (mM)	Temperature (°C)	25	45	70	25	45	70	25	45	70	25	45	70
LiPV14	0.5	2.8		Y	Y	Y	Y	Y	Y	Y	Y	Y	Y	Y	NA
LiPV14	1	2.8		Y	Y	Y	Y	N	Y	Y	N	N	Y	N	N
LiPV14	1.68	2.8		Y	Y	Y	N	N	N	N	N	N	N	N	N
LiPV14	2	2.8		Y	Y	Y	N	N	N	N	N	N	N	N	N
LiPV14	3.38	2.8		Y	Y	Y	N	N	N	N	N	N	N	N	N
LiPV14	0.25	85		Y	Y	N	Y	Y	N	N	N	N	N	N	N
LiPV14	0.25	178		Y	Y	N	N	Y	N	N	N	N	N	N	N
NaPV14	0.25	80		Y	Y	N	N	N	N	N	N	N	N	N	N

Figure 2.4: PV_{14} solutions with varied cation, temperature, P:V ratio, temperature, and oxidation state. The colour-coded cells indicate whether precipitate was present under the given set of conditions. Green 'Y' indicates no solution is present. Yellow 'Y' indicates either very little precipitate is present or it is unclear. Red 'N' indicates a significant amount of precipitate is present.

was split into four sub-sets with various amounts of hydrazine solution added to reduce the species to a varied extent. The samples were then stored at different temperatures (25, 45, and 70 C). Table 2.4 details the oxidation state, P:V ratio, the concentration of species, and temperature, and indicates whether precipitate was present 14h and 4 days after hydrazine addition. Solutions of $LiPV_{14}$ (P:V 0.25, c = 85 mM and 178 mM), as well as $NaPV_{14}$ (P:V 0.25, c = 80 mM) were also tested as part of this study.

2.2.3 In-situ UV titration of PMo_{12}

The stability of PMo_{12} with respect to pH was investigated using UV spectroscopy. In order to do this, solutions containing 0.022 mM and 3 mM of PMo_{12} were prepared with 1 M LiCl as the supporting electrolyte as described above. The pH was adjusted by adding 1 M LiOH

in small amounts whilst stirring. The solution was stirred for several minutes between each addition of hydroxide-containing solution. Simultaneously, the solution was pumped to a flow-through UV sampling cell with quartz windows and a path length of 10 mm. UV spectra were recorded after each addition of hydroxide. When the pH reached 10, concentrated hydrochloric acid was added to reduce the pH to 2.00. The solution was stirred for several minutes, and further UV spectra were recorded.

2.2.4 Flow battery studies

Solutions were prepared in a similar manner as described in section 2.2.1. Flow batteries (5x5 cells from C-Tech Innovation) were used in all flow battery studies. Carbon felt (GFD 4.6 mm thickness, from SGL Carbon) and membrane material (Nafion 212 unless otherwise stated) were cut to the appropriate size using cutting templates. Unless otherwise stated, the carbon felt electrodes were treated by heating to 500 ^{o}C for three hours in air. This was done to produce oxidised functional groups on the electrode surface and ensure good wettability. Nafion was soaked for at least several hours or overnight in a solution containing the supporting electrolyte of the solutions to be studied, typically 1 M NaCl or LiCl with a pH of around 2.3. The cell housing and components were rinsed thoroughly with deionised water several times by pumping, and dried thoroughly prior to experiments by flowing dry nitrogen gas through the cell. This procedure is useful for two reasons. Firstly, it significantly reduces the probability of any contaminants in the cell. Secondly, if a leak is present, cleaning is much easier, and no valuable electrolyte materials are wasted.

The C-Tech cell is constructed so that the void space (where the electrode is located) is the same size, irrespective of how tightly the cell is sealed. Therefore, the cell bolts were typically hand tightened as much as possible, followed by a one quarter turn with a wrench. The torque was not recorded.

The anolyte and catholyte solutions were placed in reservoirs, which were glass bottles with plastic lids. The lids had holes drilled into them, the size of which corresponded to the outer diameter of the tubing connected to the cell and a capillary tube. A capillary tube was inserted directly into the solution, and a stream of hydrated nitrogen was bubbled into it throughout the experiments. The entire setup was placed inside a transparent box with ports for the potentiostat cables, nitrogen lines, and power cables. The solution was circulated and flushed with nitrogen overnight prior to the commencement of experiments. The transparent box was reasonably well sealed and helped to prevent oxygen from diffusing into the reservoirs and through the tubing.

A Biologic BCS was used as the cycler where two electrode experiments were conducted. For three electrode experiments, a Biologic SP300 was used.

Various reference electrodes were used depending on the solution and the experiment being conducted. The most commonly used were Ag/AgCl in 3.0 M KCl, and the Mercury-Mercurous sulphate (MSE) electrode in saturated K_2SO_4 or 0.5 M H_2SO_4 solution.

After experiments were completed, the flow batteries were cleaned by circulating 1 M solutions of sulfuric acid in batches. This was necessary because it was found that PV_{14} leaves small amounts of precipitate in the neoprene tubing, which is not soluble in water. The cells were then rinsed with deionised water several times for at least one hour and subsequently dried at 70^oC in air.

2.3 Results and discussion

2.3.1 PMo_{12} as a redox flow battery anolyte

As a result of the work conducted in chapter 1, it was quite clear that PMo_{12} can undergo many repeated oxidation and reduction reactions without being irreversibly chemically altered. The POM is also stable over a wide temperature, at least $20 - 100\ ^o$C.

As discussed, there is also a significant drive to minimise the use of expensive metals for flow batteries. The price of tungsten and molybdenum has changed considerably over the last decade. However, during this time the price of tungsten has always been higher than that of molybdenum. Moreover, the cost of molybdenum has trended downward during that time frame.[90, 100] The 2018 costs of molybdenum and tungsten are compared in Table 2.1. Since molybdenum also has a much lower molecular weight than tungsten, the price per mole is about four times lower.

With the cost reduction and demonstrated the ability of PMo_{12} to undergo multiple redox reactions without noticeable degradation, a series of experiments were carried out to determine the suitability of the POM as an active species in an RFB.

Metal	Price ($ tonne^{-1})	M_w (g mol^{-1})	Amount (mol tonne^{-1})	price $ mol^{-1}	world reserves (tonnes)	Reduction potential
W	30,000	184	5430	5.55	2,500,000	lower
Mo	16,000	96	10,500	1.52	19,000,000	higher

Table 2.1: Comparison of costs for tungsten and molybdenum

WE	glassy carbon disk
CE	carbon felt
RE	SCE in 1M KCl (264 mV vs SHE)
Solution	1 M LiCl, 0.03 mM PMo_{12}
pH	2.51
scan speed	100 mV s^{-1}

Table 2.2: Cyclic voltammetry cell details for the voltammograms displayed in Figure 2.5

WE	glassy carbon disk
CE	carbon felt
RE	SCE in 1M KCl (264 mV vs SHE)
Solution	1 M LiCl, 0.6 mM PMo_{12}
pH	2.24
scan speed	10-250 mV s^{-1}

Table 2.3: Cyclic voltammetry cell details for the voltammograms displayed in Figure 2.6

Evaluation of chemical and electrochemical characteristics

The intention was to demonstrate PMo_{12} as anolyte with PV_{14} as the catholyte. Therefore, cyclic voltammograms of PMo_{12} were recorded in 1M LiCl aqueous solution. The rationale here is that PV_{14} is not stable if sulfuric acid is present in solution - it very rapidly decomposes into vanadium ions such as $VOSO_4$. Moreover, voltammetry of 1 M sulfuric acid and 1 M LiCl shows that the onset of hydrogen evolution in lithium chloride solution occurs at a much lower potential, which is beneficial as it allows PMo_{12} to be reduced to a greater extent before onset of significant hydrogen evolution occurs. The experimental conditions are detailed in Table 2.2.

A cyclic voltammogram can be seen in Figure 2.5. Many reduction and oxidation peaks are present over a range of about 1.5 V, beginning at 400 mV vs SHE and ending with suspected hydrogen evolution at about -1.2 V. The results indicate that PMo_{12} is stable and electrochemically active in an aqueous lithium chloride containing solution.

Next, a new solution with a higher concentration of PMo_{12} was prepared (Table 2.3) , and cyclic voltammograms with varied scan speeds were recorded. The maximum current of five easily identifiable peaks (I_p) were recorded and plotted against the square root of the scan speed (figures 2.6 and 2.7). The linear relationship between the peak current and square root of scan speed suggests that the redox activity is electrochemically reversible and that the POMs are freely diffusing in solution.[97]

However, this is not the only criteria for electrochemical reversibility. In order for an

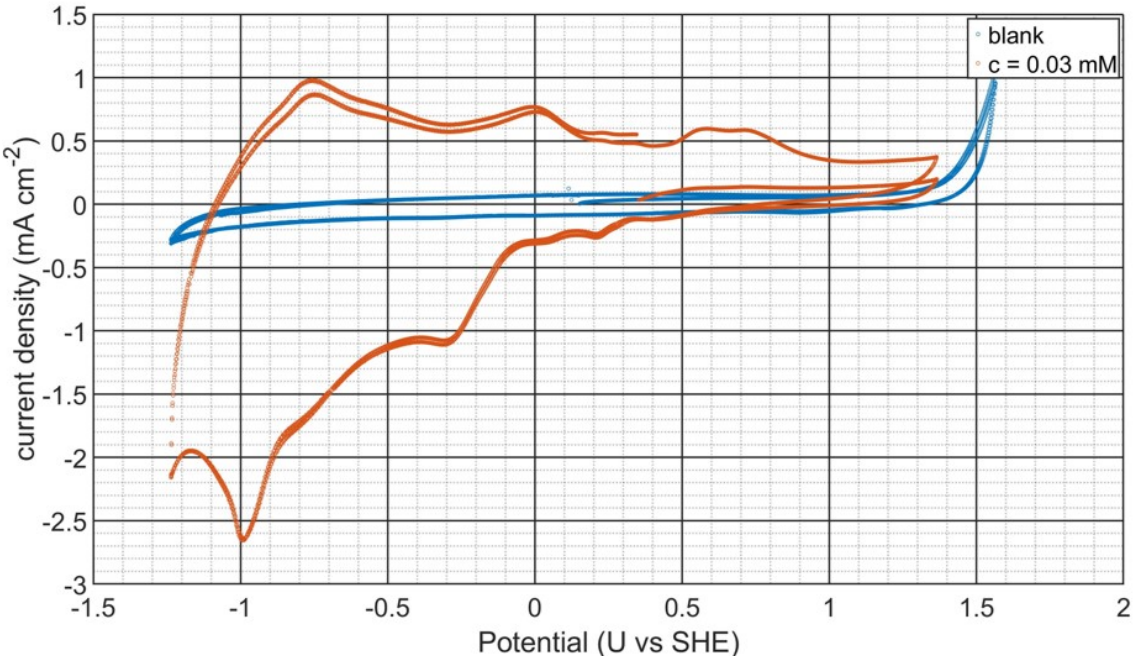

Figure 2.5: Cyclic voltammogram of PMo_{12} in 1 M LiCl and (blank) 1 M LiCl. WE: glassy carbon disk (7.07 mm^2), CE: carbon felt, RE: SCE in 1 M KCL (0.264 V vs SHE), electrolyte: PMo_{12} 0 & 0.03 mM, LiCl (1 M), pH 2.51. Scan rate: 100 mV s^{-1}, Initial WE potential: 0.35 V vs SHE, initial sweep direction: positive, vertex WE potentials: 1.6 V vs SHE and -1.25 V vs SHE.

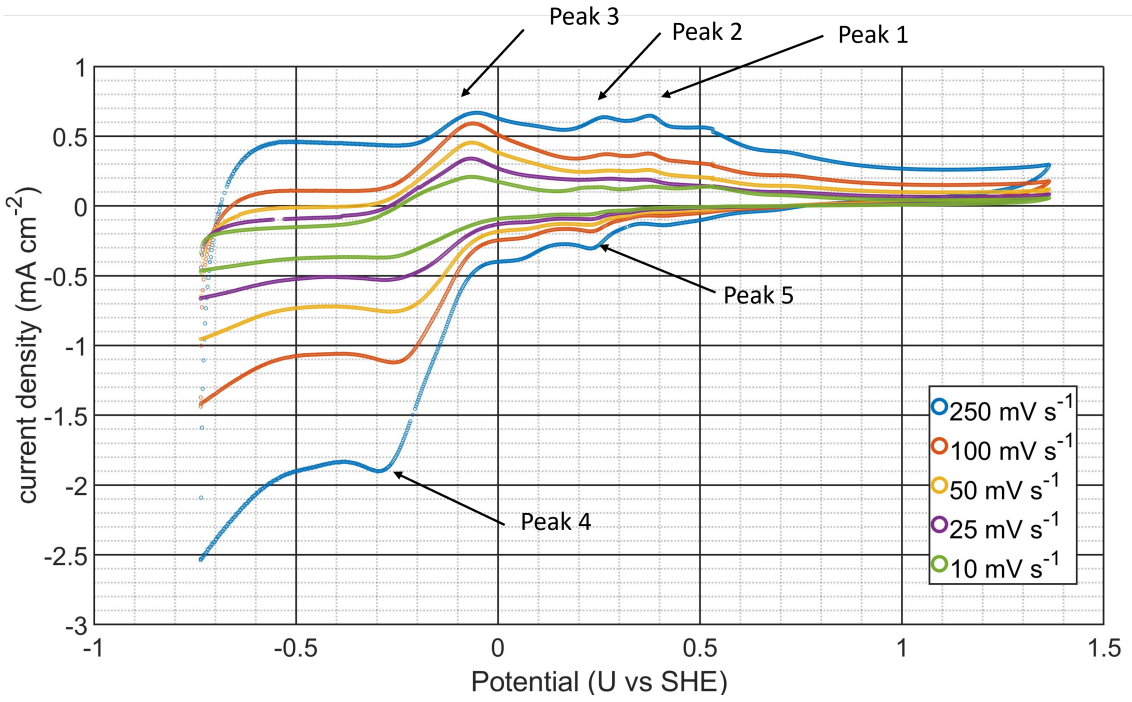

Figure 2.6: Cyclic voltammogram of PMo_{12} in 1 M LiCl at various scan speeds. WE: glassy carbon disk (7.07 mm^2), CE: carbon felt, RE: SCE in 1 M KCL (0.264 V vs SHE), electrolyte: PMo_{12} 0.6 mM, LiCl (1 M), pH: 2,24. Scan rate: 10-250 mV s^{-1}, Initial WE potential: 0.35 V vs SHE, initial sweep direction: positive, vertex WE potentials: 1.38 V vs SHE and -0.75 V vs SHE.

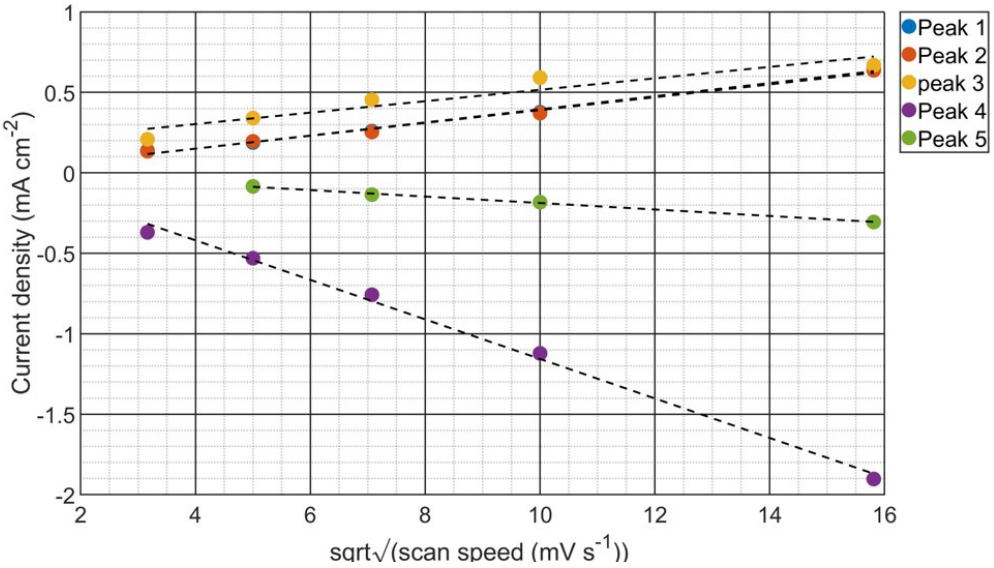

Figure 2.7: Plot of the peak current density vs square root of scan speed for five separate peaks labelled in Figure 2.6

electrochemical reaction to be considered reversible (or nernstian), the kinetics must be fast enough that thermodynamic equilibrium is achieved essentially instantaneously. So, for a system in which the potential of an electrode is being swept linearly, the potential at which the peak current occurs (U_p) is determined by the rate of mass transport of the redox species to the electrode surface, and is independent of the sweep rate. Of the peaks identified in figure 2.7, peaks 1 and 5 satisfy this criteria, but peaks 2, 3, and 4 do not. In the case of peak 4, the difference in peak position (comparing 25 mV s^{-1} to 250 mV s^{-1}) is approximately 25 mV. The shift in U_p on both the anodic and cathodic waves centred at approximately -150 mV vs SHE, as well as the significant difference in the magnitude of the current response is indicative of a quasi-reversible process. In a quasireversible system, the forward and reverse reactions exhibit significantly different kinetic and/or mass transport characteristics.

For instance, if a redox active species undergoes isomerisation or other transformation as a result of electrochemical reduction, the resultant species characteristics (especially the diffusion coefficient and standard rate constant) will provoke an unsymmetrical electrochemical response (as is the case with peaks 3 and 4).

A further criteria for a nernstian system is that the peak to peak separation is given by 2.22 $^{RT}/_{nF}$ (57 mV at 25 ^{o}C for a one-electron reaction).[97] For the PMo_{12} cyclic voltammograms depicted in figure 2.7 many of the cathodic waves do not have easily identifiable anodic counterparts, making an analysis of peak separations impossible for most of the waves that are present. Peak 2 and peak 5 could correspond to to the same reaction, and in this case the peak separation of $\sim$ 30 mV could indicate that this is a 2-electron process. However, if the POM does indeed isomerise (or otherwise change structurally) as a result of electrochemical reduction then this may be coincidental.

In future work, voltammograms of PMo_{12} should be conducted with various different potential limits so that individual redox waves can be studied in isolation. From the data that are available it would appear that the PMo_{12} redox system is non-nernstian despite the linear relationship between peak current and the square root of scan speed.

The stability of PMo_{12} with respect to pH was also investigated. The experimental setup is described in section 2.2.3, and the titration curves are displayed in Figure 2.9. The UV spectrum between 200-450 nanometres was also recorded(Figure 2.8), and the highest wavelength at which maximum absorbance was reached is plotted vs OH equivalents added. This was necessitated because the extinction coefficient for PMo_{12} 12 is incredibly high, so even when the concentration is very low (0.22 mM), the UV spectra cannot be fully resolved. Of course, resolving the peaks at lower concentrations of PMo_{12} may be possible or at reduced path length. However, the stability of $PMo_{12} \leq 0.022$ mM concentrations is insignificant to the

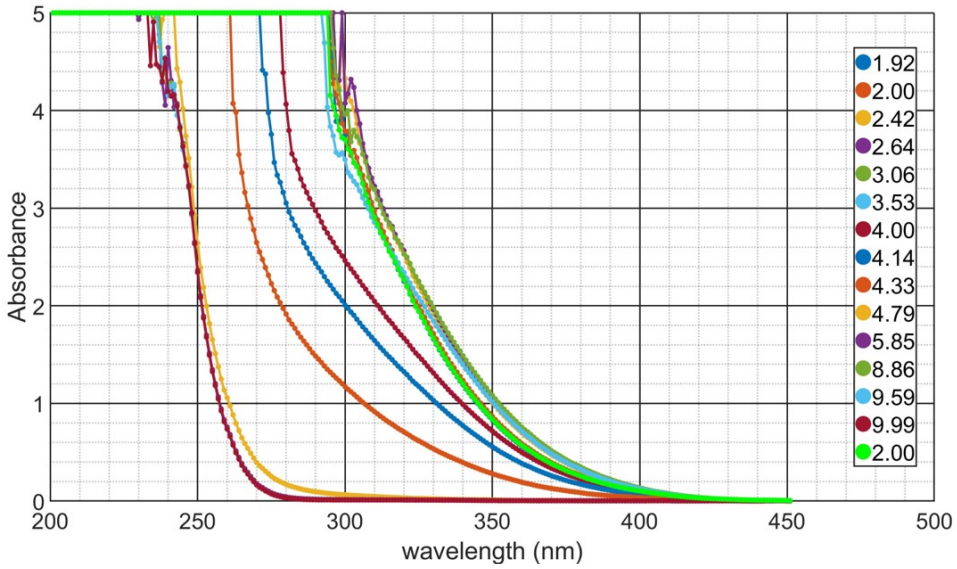

Figure 2.8: UV-Visible light transmission spectra for a 3 mM PMo_{12} solution at varied pH. The values in the legend indicate the pH, and are sequential with respect to the time of measurement.

intended application. Furthermore, at concentrations this low, the redox peaks associated with PMo_{12} cannot be distinguished from background noise.

As shown in Figure 2.9 the pH rises linearly with the addition of hydroxide until pH $\approx$ 2.1. After which, the gradient increases gradually until a point of inflexion (equivalence point) at pH $\approx$ 3.5. Given that over this range three OH^- equivalents are added, it would appear that the pKa for the first three protonations are roughly equal (pKa $\approx$ 1.95). After PMo_{12} is fully protonated (i.e. $H_3PMo_{12}O_{40}$), any further addition of hydroxide leads to a decrease in the lowest wavelength at which maximum absorbance is reached.

Figure 2.8 shows the UV spectra for the 3 mM solution at various pH values. When the pH rises, the spectra shifts to the left. However, beyond pH $\approx$ 8, there is no further change to the spectra. Since the concentration of species is too high to see the peak, it is not possible to say with much certainty, but it is quite likely that the POM has fully dissociated into molybdate and phosphate ions. The reason for this is twofold - first, the UV spectra are consistent with the spectra of molybdate in the 240-450 nm range (the onset of a peak).[101] Secondly, the synthesis of PMo_{12} is achieved through the addition of a strong acid to a solution containing molybdate and phosphate ions.[102] As can be seen in Figure 2.8, when the pH is reduced to 2 by the addition of concentrated HCl, the onset of the peak in the UV spectra shifts to a longer wavelength ($\sim$ 400 nm) and is nearly identical to the initial readings, indicating that

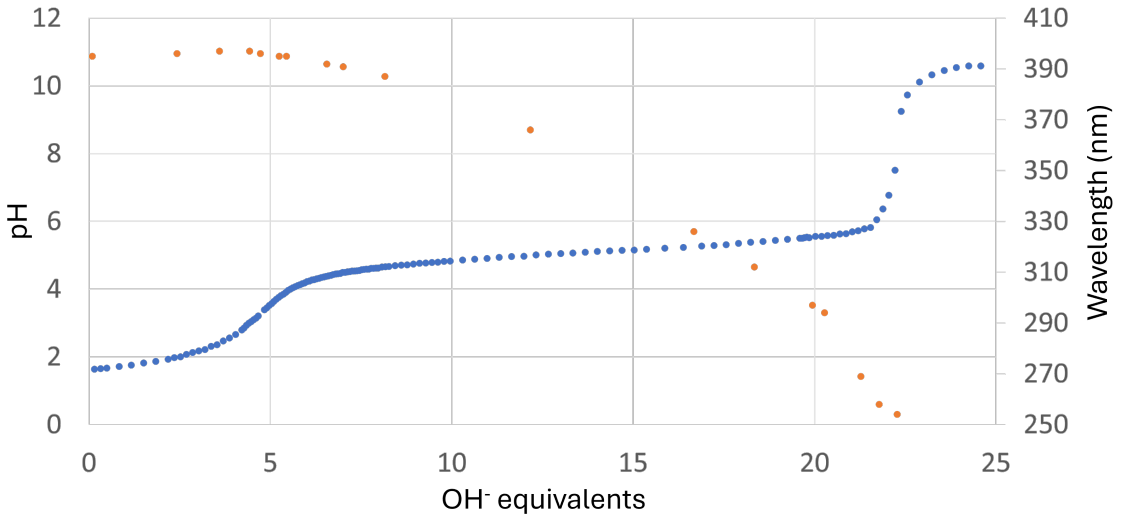

Figure 2.9: The titration curve for a solution of 3 mM PMo_{12} in 1 M LiCl (blue dots), and the lowest wavelength at which maximum absorbance was reached. pH: blue dots, wavelength: orange dots.

WE	glassy carbon disk
CE	carbon felt
RE	SCE in 1M KCl (264 mV vs SHE)
Solution	1 M LiCl, 1 mM PMo_{12}
pH	2.24
scan speed	10-250 mV s^{-1}

Table 2.4: Cyclic voltammetry experimental setup

PMo_{12} has reformed.

Since the peak cannot be observed, it is clear that UV spectrophotometry will be of limited usefulness for the investigation of PMo_{12}. However, it can be ascertained that PMo_{12} is stable up to about pH 4.5. Given that the intended catholyte solution has a pH range of 1-3, [2] this range is acceptable.

Next, the stability of PMo_{12} with respect to repeated electrochemical oxidation and reduction at low and high temperatures was investigated. A three-electrode electrochemical cell with properties described in Table 2.4 was assembled.

70 cyclic voltammograms with a scan rate of 100 mV s^{-1} with a potential range of -0.75 V to 1.35 V vs SHE) were recorded continuously on the glassy carbon working electrode. The results can be seen in Figure 2.10. Only seven of the cycles are shown for clarity, but it can be seen that there is a large degree of consistency across all cycles.

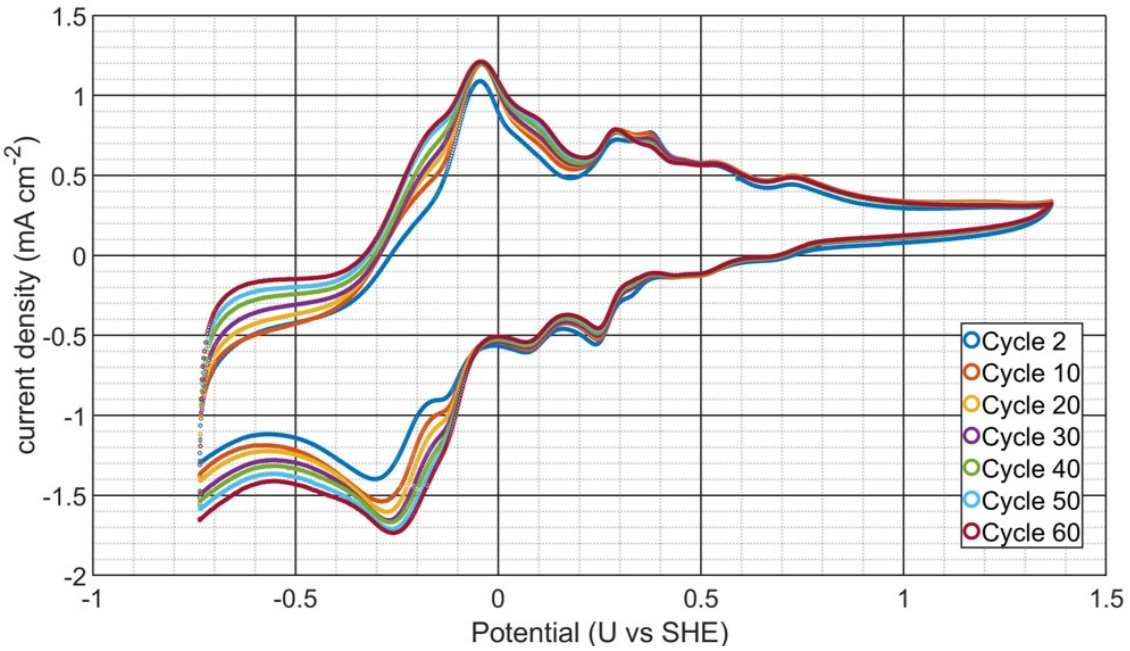

Figure 2.10: Cyclic voltammograms for a solution PMo_{12} as described in Table 2.4. 70 cycles were recorded in total, but only 7 are shown for clarity. WE: glassy carbon disk (7.07 mm^2), CE: carbon felt, RE: SCE in 1 M KCL (0.264 V vs SHE), electrolyte: PMo_{12} 1 mM, LiCl (1 M), pH: 2,24. Scan rate: 100 mV s^{-1}, Initial WE potential: 0.35 V vs SHE, initial sweep direction: positive, vertex WE potentials: 1.38 V vs SHE and -0.75 V vs SHE.

There are some slight differences across the displayed cycles. For instance, the second cycle generally has a lower current density for a given potential relative to the others. However, as is common with extended voltammetry experiments on Keggin POMs, if there is a net reduction of the species in the vicinity of the working electrode a thin blue/green stream of material forms which pools at the bottom of the vessel indicating that the reduced form is denser than the oxidised form. The effect on the voltammogram is that over time, an uncontrolled convection current forms, which moves reduced material away from the electrode, and brings oxidised material. Therefore, an increase in peak current density occurs as a result of increased convection.

One other feature of note is that the two anodic peaks at approximately 290 mV and 380 mV vs SHE appear to increase and decrease respectively in proportionate amounts. A similar effect was observed on reduction of silicomolybdates by Strickland. [63, 64] Strickland attributed this phenomenon to the isomerisation of $SiMo_{12}$, and it seems reasonable that this could also be the case here.

The properties of PMo_{12} at higher concentrations are also of interest, and will be discussed in the next section. For this reason, a PMo_{12} (10 mL, 300 mM) solution was prepared, which is close to the concentration limit of approximately 330 mM. With the addition of POM, the solution turned bright yellow and became viscous. In this case, no supporting electrolyte . This is because the POM dissociates ($H_3PMo_{12}O_{40} \rightleftharpoons 3\,H^+ + PMo_{12}O_{40}{}^{3-}$) to form a highly acidic solution, so should have high conductivity. The pH was then 0.33, corresponding to a hydrogen ion concentration of 0.47 M. The solution was placed in an electrochemical cell described in Table 2.5, and cyclic voltammograms over a potential range of -0.52 to 1.07 V were recorded. Figure 2.11 displays a voltammogram of this solution, which exhibits somewhat different characteristics to the voltammograms displayed in Figure 2.10. Some of these differences; such as the shift in the position of high potential anodic and cathodic peaks, were expected. Factors that influence these values include the complexation of the species in solution (or lack thereof), shifts in acid-base equilibria, solvation shell structure, and other chemical effects, which can be described by a shift in the activity of the POM at a much higher concentration. In a 300 mM solution (assuming the density is 1 g cm^{-3}), the POM accounts for 55% of the mass, so changes in the chemical medium compared to a solution of 1-10 mM are bound to be of significance.

Additionally, there is a junction potential between the working and reference electrode. This effect arises due to differences in concentration and mobility of ions on either side of a boundary such as a glass frit or salt bridge. Ions will diffuse across the boundary from the area with a higher concentration to the area of low concentration. The diffusion of species

leads to a build up of charge, which then hinders migration of ions with a similar charge and accelerates the migration of ions with the opposite charge until the net current across the boundary is zero. The junction potential is established very quickly, and is typically stable across a long period of time.

This effect can be largely minimised by using the same concentration and type of electrolyte in both the main solution and reference electrode compartment. For example, if the electrolyte is 1 M HCl in both compartments, there is no net diffusion of species in either direction, so no junction potential arises. In cases where this is not possible, utilising an electrolyte with comparatively high concentration in which the mobility of the cation and anion are very similar such as KCl is desirable. The high concentration ensures that the majority of charge transport across the boundary is facilitated by KCl, and although a junction potential still arises due to the crossover of these species, their polarity is opposite so the net junction potential is minimal.[76]

In some of the experiments detailed in this work, an Ag/AgCl electrode with 1 M NaCl was used. Sodium and chloride ions have significantly different mobility in aqueous solution, so a junction potential will have been present. However, the use of this electrolyte is necessitated (especially in long experiments) because the presence of potassium ions (the typical cation used in conjunction with Ag/AgCl electrodes) could lead to the precipitation of the POMs. The decision of using 1 M NaCl was made because this is the same species and concentration of the supporting electrolyte of the main solution. So, although a junction potential is present, it should be consistent throughout the experiment (assuming the crossover of POMs is negligible).

As the POM was fully oxidised, the net charge transfer was overwhelmingly cathodic. Shortly after performing a cathodic sweep, a stream of green material can be seen sinking from the electrode to the bottom of the vessel. As there was no way to prevent uncontrolled convection to the electrode surface, voltammograms of various scan speed cannot be used to determine electrochemical reversibility as was done in Figure 2.7. However, the peak separations for the redox events centred around 0.75, 0.55, and 0.38 V are very large - 0.125, 0.101, and 0.146 V, respectively, which would suggest a significant degree of electrochemical irreversibility. [97] However, this is at odds with the large current density at the working electrode.

Below ∼0.5 V vs SHE, there is a clear divergence in electrochemical behaviour. Most notably, the large anodic peak centred around -50 mV vs SHE is not present at high concentrations. In fact, several more peaks are present at lower concentrations over the same potential range. The profile at high concentration does not change with repeated cycling,

WE	glassy carbon disk 0.0707 cm^2
CE	Au wire
RE	MSE in 1 m H_2SO_4 (0.674 V vs SHE)
Solution	300 mM PMo_{12}
pH	0.33
scan speed	100 mV s^{-1}

Table 2.5: Cyclic voltammetry experimental setup

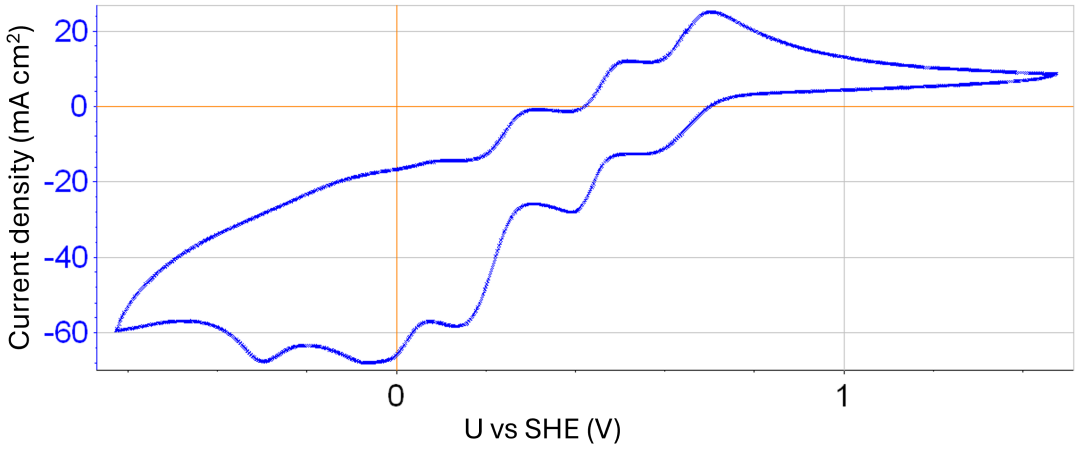

Figure 2.11: Cyclic voltammograms for a solution PMo_{12} as described in Table 2.4. WE: glassy carbon disk (7.07 mm^2), CE: Au wire, RE: MSE in 1 m H_2SO_4 (0.674 V vs SHE), electrolyte: PMo_{12} 300 mM, pH: 0.33. Scan rate: 100 mV s^{-1}, Initial WE potential: 0.35 V vs SHE, initial sweep direction: positive, vertex WE potentials: 1.5 V vs SHE and -0.65 V vs SHE.

whereas at low concentration, there are differences in the anodic peaks at 300 mV vs SHE as previously described.

A further solution of PMo_{12} was prepared and placed in a bulk electrolysis cell with properties described in Table 2.6. Cyclic voltammograms were recorded at various oxidation states using WE2. WE1 was used to electrolyse the solution. Figure 2.12 shows four voltammograms for three different oxidation states. The legend displays the previous oxidation state on the left and the oxidation state at the time of measurement on the right. As PMo_{12} is reduced, the cyclic voltammogram changes significantly - the position of many of the peaks except those at 500 and 700 mV vs SHE can no longer be distinguished, and new peaks appear. The current density also decreases significantly. This suggests that the chemical properties of PMo_{12} change significantly upon reduction. However, on reoxidation to the

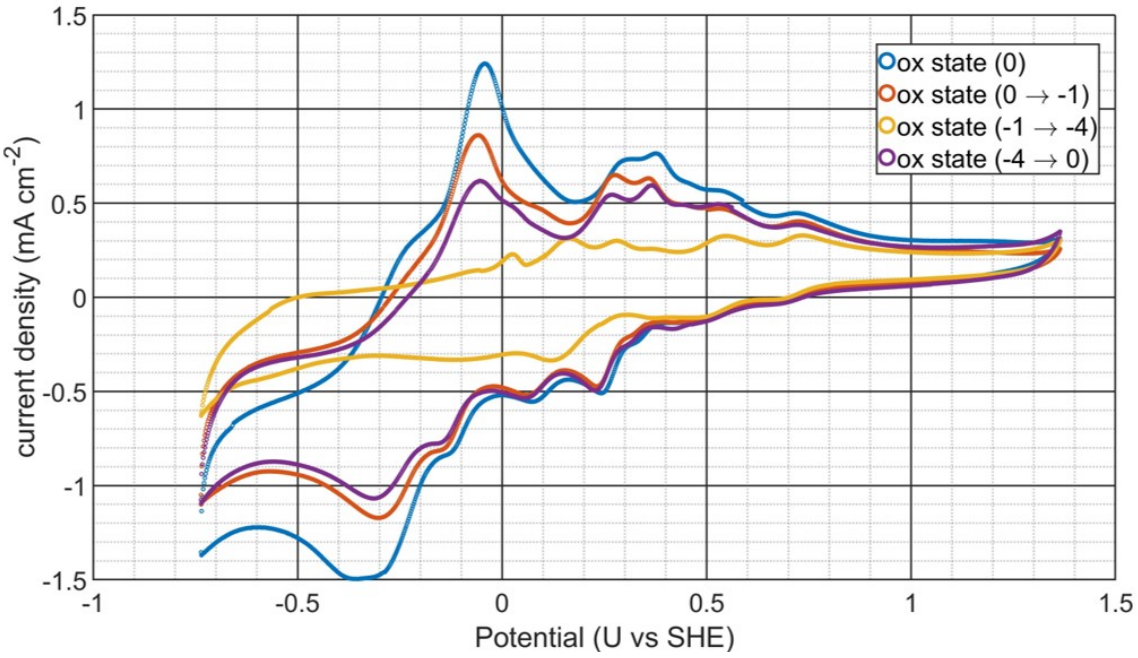

Figure 2.12: Cyclic voltammograms of the solution described in Table 2.6. The legend indicates the oxidation state prior to the electrolysis step on the left of the arrow. The number on the right of the arrow indicates the oxidation state of the POM when the voltammogram was recorded. WE1: carbon felt, WE2: glassy carbon disk (7.07 mm^2) CE: carbon felt, RE: SCE in 1M KCl (264 mV vs SHE) , electrolyte: PMo_{12} 1 mM and 1 M LiCl, pH: 2.24. Scan rate: 100 mV s^{-1}, initial sweep direction: positive, vertex WE potentials: 1.35 V vs SHE and -0.73 V vs SHE.

initial state the shape of the voltammogram is restored indicating that the chemical change is reversible.

One possible explanation for the reduction in current density is that; since current density is proportional to concentration, the POM has dissociated and does not fully reassemble on oxidation. However, the decrease in current density is not consistent across the whole voltammogram and is more noticeable at voltages below 0 V vs SHE. This is unusual behaviour and no reasonable explanation has been identified.

100 cycles of bulk electrolysis by $\sim$4 $F\,\mathrm{mol}^{-1}$ were carried out over the course of one day in order to determine whether the apparent chemical change of PMo_{12} when reduced had an impact on the reversibility of the electrochemical reaction. The coulombic efficiency for each cycle was in excess of 99%, however; and the charge transferred across each cycle was consistent throughout the experiment.

Even at elevated temperatures, the coulombic efficiency on electrochemical reduction

WE1	Carbon felt
WE2	Glassy carbon disk
CE	carbon felt
RE	SCE in 1M KCl (264 mV vs SHE)
Solution	1 M LiCl, 1 mM PMo_{12}
pH	2.24
scan speed	100 mV s^{-1}

Table 2.6: Bulk electrolysis and voltammetry experimental setup

and oxidation by 4 F mol^{-1} is very high, as can be seen in Figure 2.13. Further evidence for a chemical change can be seen in Figure 2.14 - on reduction, there are two evenly spaced plateaus which possibly correspond to separate two-electron redox couples, i.e.

$PMo_{12}(0) + 2\,e^- \longrightarrow PMo_{12}(-2)$

$PMo_{12}(-2) + 2\,e^- \longrightarrow PMo_{12}(-4)$

On oxidation, there are initially two smaller plateaus, followed by a large one (the plateau widths correspond to 1, 1, and 2 F mol^{-1} oxidations respectively), which could indicate the following reactions are taking place:

$PMo_{12}(-4) \longrightarrow PMo_{12}(-3) + e^-$

$PMo_{12}(-3) \longrightarrow PMo_{12}(-2) + e^-$

$PMo_{12}(-2) \longrightarrow PMo_{12}(0) + 2\,e^-$

Although the evidence would suggest isomerisation during reduction and oxidation, the high coulombic efficiency is an encouraging result. It indicates a high degree of reversibility for repeated oxidation/reduction, even at 80 ^oC.

Identifying redox flow battery electrolytes that can function at higher temperatures is desirable as this will reduce the need for thermal management in large installations. For example, if the volumetric energy density of a redox flow battery is 20 $Wh\,L^{-1}$, a 1 MWh installation would require 50,000 litres of anolyte and catholyte solution. Since the roundtrip efficiency of flow batteries is typically quite low (about 70-80%), about 200-300 kWh of heat energy will be produced on a full cycle. For lab-scale experiments, heat dissipation is achieved quickly with the surroundings because the surface area of the battery and reservoirs is quite large with respect to the volume. However, this ratio is much lower for larger installations, so thermal management systems need to be implemented if the electrolyte or battery components are temperature-sensitive. This is particularly problematic for the vanadium redox

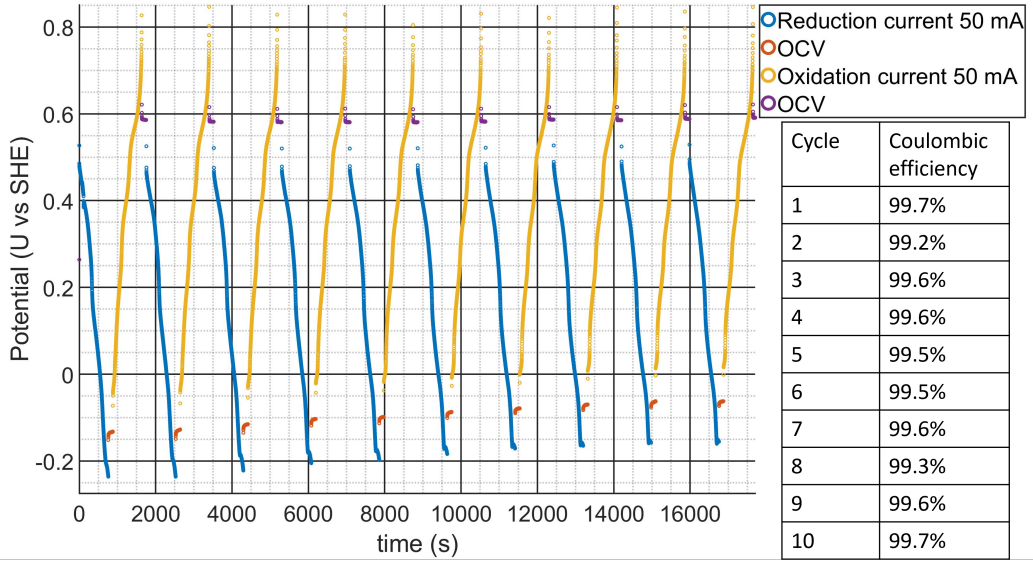

Cycle	Coulombic efficiency
1	99.7%
2	99.2%
3	99.6%
4	99.6%
5	99.5%
6	99.5%
7	99.6%
8	99.3%
9	99.6%
10	99.7%

Figure 2.13: Bulk electrolysis reduction and oxidation cycles on a solution containing PMo_{12} as described in Table 2.6. T = 80°C. WE1: carbon felt, WE2: glassy carbon disk (7.07 mm^2) CE: carbon felt, RE: SCE in 1M KCl (264 mV vs SHE) , electrolyte: PMo_{12} 1 mM and 1 M LiCl, pH: 2.24. WE potential cut off on oxidation: 0.83 V vs SHE.

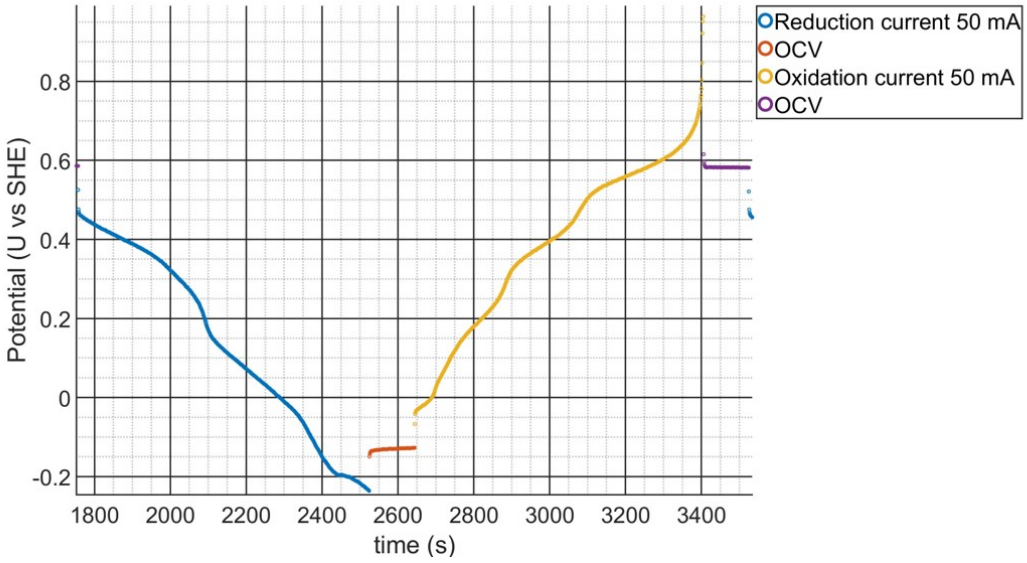

Figure 2.14: The same data presented in Figure 2.13, expanded so that the plateaus can easily be distinguished.

Anode	Carbon felt (25 cm^2)
Cathode	Carbon felt (25 cm^2)
Anolyte	1 M LiCl, 1 mM PMo_{12}, 60 mL
Catholyte	1 M LiCl, 1 mM PV_{14}, 100 mL
Separator	Nafion 117

Table 2.7: Redox flow battery properties.

flow battery - without additives, V^V will irreversibly precipitate at temperatures above 40 ^oC.[82]

Moreover, if a battery can be operated at a higher temperature, then it is expected that the efficiency will improve. according to the Arrhenius equation $k^0 \propto e^{-1/T}$, and according to the Einstein-Smoluchowski equation, $D \propto T$ (where D is the diffusion coefficient).[76] Therefore, as long as the active species is chemically unaffected, the overpotential due to kinetic and mass transport factors should be lower at a higher temperature. Operating at higher temperatures also allows the waste heat to be utilised more effectively.

In summary, the POM can be reversibly reduced and oxidised many times with no effect on the stored capacity or coulombic efficiency, despite an apparent chemical change when reduced. The pH stability window is broadly in-line with that of PV_{14}, the POM is stable over a wide range of concentrations, and the concentration limit is reasonably high. Analysis of the voltammograms at varied scan speeds shows that the POM is freely diffusing in solution.

Determination of the capacity and capacity retention of a PMo_{12}/PV_{14} redox flow battery

As was shown in the previous section, an investigation into the chemical and electrochemical properties of PMo_{12} indicate a high degree of suitability for use in an RFB.

A flow battery with the properties detailed in Table 2.7 was assembled according to the procedure described in section 2.2.4. Prior to addition of the catholyte solution to the flow battery, it was reduced electrochemically in a bulk electrolysis cell by 4 F mol^{-1} so that the average oxidation state was $PV_{14}(-4)$.

The primary objective of this investigation was to determine the stability of PMo_{12} as an anolyte over many cycles. Therefore, a constant current, constant voltage (CC-CV) procedure was used during cycling. The battery is initially charged with a +50 mA current until a target potential difference is reached (initially 0.5 V). At this point, the potential difference is held at 0.5 V until the current dropped to below +1 mA. For a 60 mL solution of 1 mM PMo_{12}, a capacity of 1.6 mAh corresponds to 1 F mol^{-1}.

Figure 2.15 shows the first 10 cycles, during which the capacity increases from 3.25 mAh

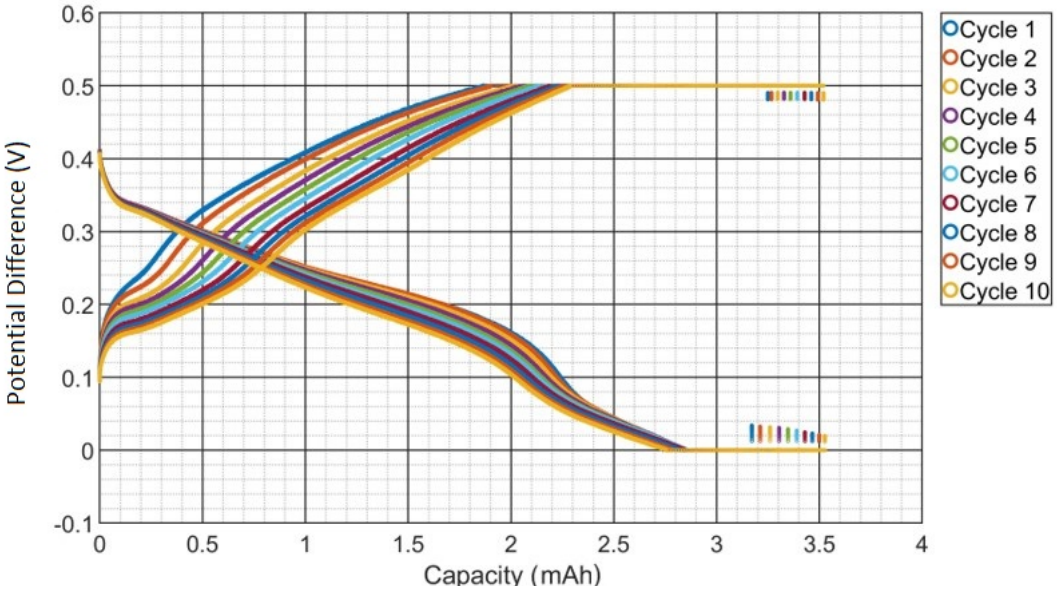

Figure 2.15: Potential vs capacity plot for 10 cycles of the flow battery described in Table 2.7. Constant charge-convstant voltage (CC-CV) procedure used, CC current: 50 mA, cut off voltages at 0 V and 0.5 V, CV hold at 0 V and 0.5 V until the current decreased to 5 mA. After 82 cycles the upper cut-off potential was increased to 0.75 V.

to 3.54 mAh, which corresponds to a capacity of 2.2 F mol^{-1}. The battery was operated for 142 cycles (Figure 2.16). Initially, the coulombic efficiency and capacity rose for the first 16 cycles to 3.6 mAh and then decreased slightly before stabilising at $\approx$ 3.4 mAh (2.1 F mol^{-1}). Throughout this period, the coulombic efficiency averaged 99.5% indicating a high stability level. After 82 cycles, the cut-off voltage was increased to 0.75 V. The capacity rose significantly to 5.5-6 mAh over the remaining 60 cycles, and the coulombic efficiency remained above 99%, increasing with respect to cycle number. The maximum recorded capacity was 6.1 mAh (3.8 F mol^{-1}).

After cycling, voltammograms of the fully oxidised PMo_{12} solution used in the redox flow battery exhibited a similar profile to that of the voltammograms shown in Figure 2.12, further demonstrating that the POM is chemically stable after repeated electrochemical oxidation and reduction.

The capacity retention over 140 cycles, and the doubling in capacity as a result of increasing the voltage by 0.25 V, and the similarity in voltammograms before and after cycling are encouraging results. However, accounting for both electrolytes' volume and assuming an average discharge potential of 0.5 V, the volumetric energy density is very low, at approximately 0.02 Wh L^{-1}.

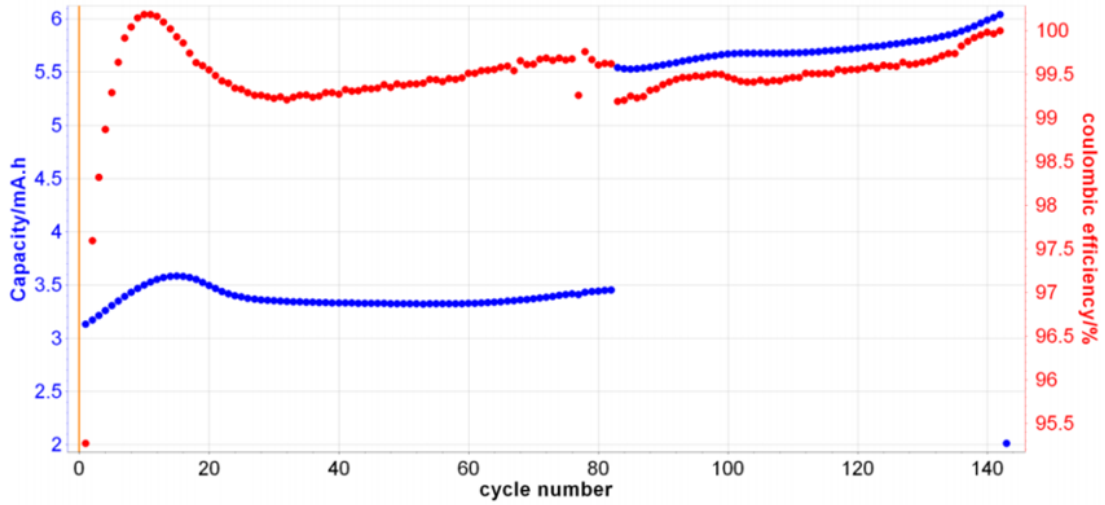

Figure 2.16: Discharge capacity, and coulombic efficiency vs cycle number for 140 cycles. Constant charge-convstant voltage (CC-CV) procedure used, CC current: 50 mA, cut off voltages at 0 V and 0.5 V (first 82 cycles), CV hold at 0 V and 0.5 V (first 82 cycles) until the current decreased to 5 mA. After 82 cycles the upper cut-off potential was increased to 0.75 V.

Anode	Carbon felt (25 cm^2)
Cathode	Carbon felt (25 cm^2)
Anolyte	1 M LiCl, 80 mM PMo_{12}, 70 mL
Catholyte	1 M LiCl, 80 mM PV_{14}, 70 mL
Separator	Nafion 117

Table 2.8: Redox flow battery properties.

A new flow battery was assembled with the properties described in Table 2.7. The intention was to test whether the findings from the flow battery described in Table 2.8 translated to a battery with a much higher concentration. In this case, however, a constant current (CC) only charge/discharge procedure was applied to be comparable with a typical redox flow battery study and increase the cycling speed.

In this case, the PV_{14} was reduced by the addition of hydrazine solution (253 μL, 35% w/w water) by $\sim$2 F mol^{-1}. The applied current was $\pm$ 200 mA (8 mA cm^{-2}, which is comparable to RFBs with a concentration of 80 mM previously reported by our group. A 1 F mol^{-1} reduction/oxidation corresponds to 540 C (150 mAh). Figure 2.17 shows the charge and discharge capacity vs cycle number for the cell for the first 61 cycles. The initial cut-off potential was 0.5 V for one cycle. The capacity was much lower than anticipated (274 C (76 mAh, 0.5 F mol^{-1}), and it was initially thought that this was due to the reduction degree

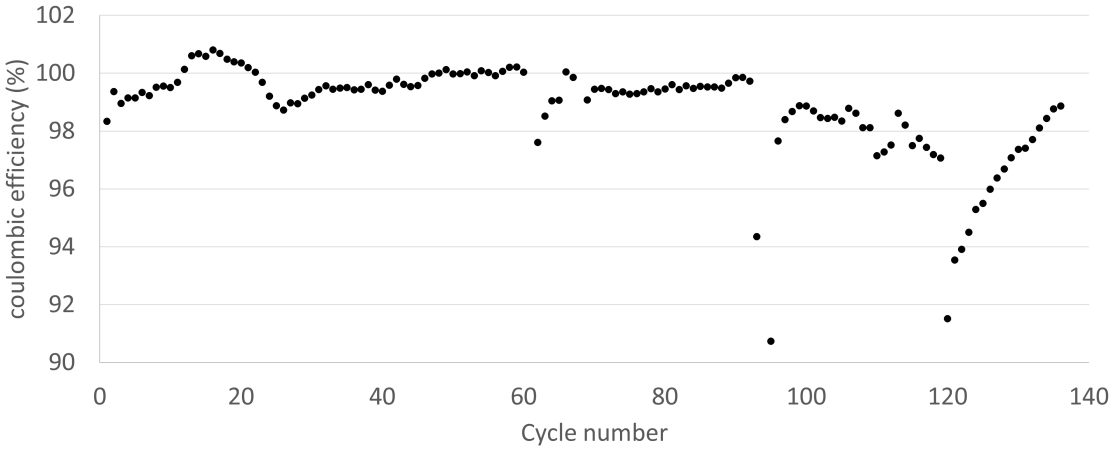

Figure 2.17: Coulombic efficiency for all 140 cycles of the RFB described in Table 2.8.

of PV_{14} being quite low. This means the catholyte solution has a higher starting potential than the previous experiment, so the cut-off voltage is reached sooner. Therefore, the cut-off voltage was increased to 0.75 V to compensate. However, this only lead to an increase in capacity of 47 C, so the cut-off voltage was increased further to 1 V. For one cycle, this seemed relatively promising, as the capacity rose to 460 C (127 mAh). However, it sharply fell over the next ten cycles to approximately 270 C (75 mAh) for 15 cycles and decreased further to 201 C (56 mAh) (figure 2.17).

Figure 2.19 shows the charge and discharge capacity and the coulombic efficiency with respect to cycle number for the first 61 cycles. On cycle 61, water purged with nitrogen gas was added to the electrolyte tanks to restore the volume to its original value. On visual inspection of the electrolytes, it was noticed that even in the fully discharged state, the colour of the catholyte solution was dark brown/red, which indicates that PV_{14} is fully oxidised. Therefore, the drop in capacity is attributed to oxygen ingress into either one or both of the electrolyte tanks.

The cycling procedure was paused, and the issue of reduced capacity was resolved by the addition of 390 μL of hydrazine 35% w/w (enough to reduce the PV_{14} solution by $\approx$ 4 F mol^{-1}) to the catholyte. After a few hours, the colour of the solution turned dark green, indicating that PV_{14} was in a reduced state. Cycling resumed with the same cut-off criteria and current density as previously, and an increase in capacity to 873 C (243 mAh, $\approx$ 1.62 F mol^{-1}) was observed. Over seven cycles, the capacity remained constant, and the coulombic efficiency ranged between 97.6-100.0% over this period.

In order to increase the data collection rate, the voltage cut-off limit was increased to 1.5

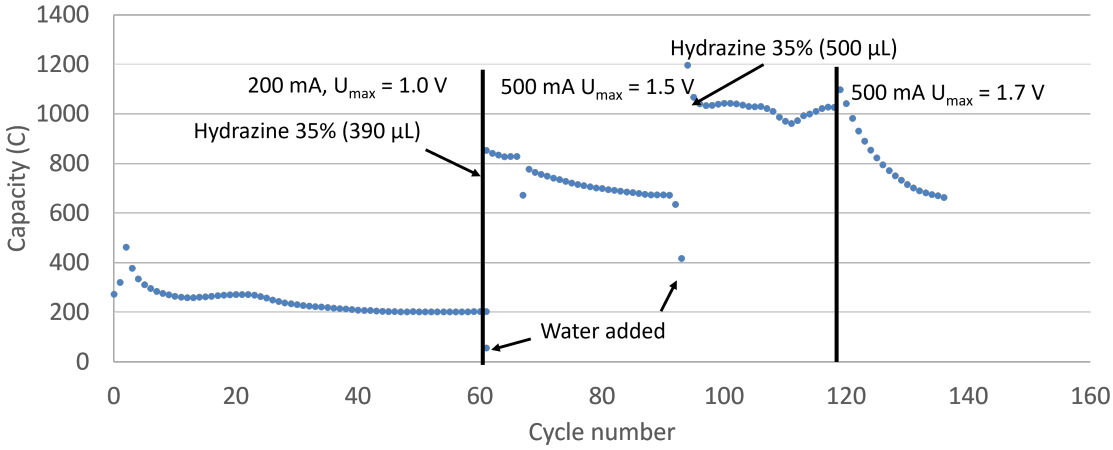

Figure 2.18: Capacity vs cycle number for the RFB described in Table 2.8.

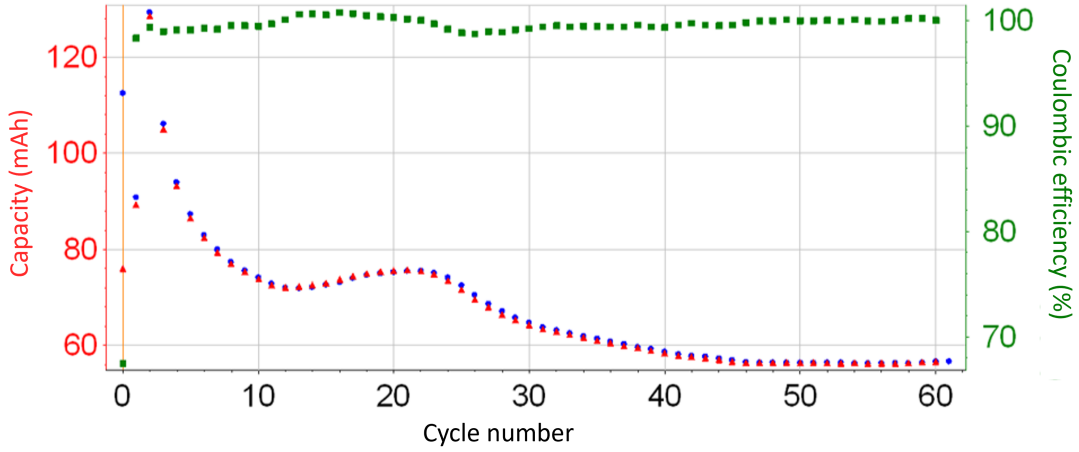

Figure 2.19: Charge capacity, discharge capacity, and coulombic efficiency for the first 61 cycles of the RFB described in Table 2.8.

V, and the current was increased to 500 mA, decreasing the average cycle time from 3.5h to 50 minutes (cycles 61-92). Initially, there was a slight decrease in capacity, but it stabilised at approximately 670(186 mAh) - which was still relatively low. More hydrazine was added on cycle 94, and the capacity increased to approximately 1040 C (288 mAh, $\approx$ 1.92 F mol^{-1}) (cycles 94-118). Then, the voltage cut-off was increased to 1.7 V, and the capacity sharply faded to 663 C, and it can be seen in Figure 2.17 that the coulombic efficiency decreased significantly. At this point, the cycling procedure was discontinued.

In summary, the effect of increasing the concentration of active species was a decrease in accessible capacity per mole from (3.8 F mol^{-1}) to ($\approx$ 1.92 F mol^{-1}). The reason for this is unclear, but given the increase in capacity on the addition of hydrazine to the PV_{14} solution,

POM	max reduction degree
$[(H_2)W_{12}O_{40}]^{5-}$	32
$[(Si)W_{12}O_{40}]^{5-}$	20
$[(B)W_{12}O_{40}]^{5-}$	25
$[(P)W_{12}O_{40}]^{5-}$	6

Table 2.9: Various tungsten-containing Keggin POMs and the number of electrons by which they can be reduced according to Pope.[8]

it may be due to oxygen ingress that rapidly oxidised the active species. Further investigations might benefit from the initial electrochemical reduction of PV_{14} solution, although this takes a very long time at higher concentrations depending on the electrolysis cell used. In principle, PMo_{12} is a good candidate for use in a flow battery. However, it remains unclear whether the chemical reversibility with respect to repeated oxidation/reduction reactions and capacity retention translates to solutions of higher concentration.

2.3.2 SiW_{12} as a redox flow battery anolyte

SiW_{12} has been demonstrated by our group as a redox flow battery anolyte; however, the maximum demonstrated molar capacity is approximately 2 F mol^{-1}. [1, 2]. According to Pope, the maximum reduction degree for various Keggin polytungstate species should allow for a much higher capacity. Table 2.9 displays data for various heteropolytungstates replicated from Pope's seminal book "Heteropoly and Isoply Oxometalates". [8] The book itself was written four decades ago, and the journal articles that the tabulated data refers to are sometimes much older. Many of the references are, therefore, difficult to access. It was ascertained from an article written by Gilbert Herve that tungstate POMs which are reduced to a high degree are not stable in acidic media. Additionally, the ability to access reduce tungstate POMs to very low oxidation states was only confirmed using linear sweep polarography on a dropping mercury electrode. No literature was found (or could be interpreted) about the reduction of Keggin polytungstates in bulk or whether they are stable with respect to repeated oxidation and reduction.

In an attempt to replicate the findings of Herve, a series of solutions with varied pH were prepared, and cyclic voltammograms were recorded. The cell details are listed in Table 2.10, and a selection the voltammograms can be seen in Figure 2.20. It was found that at pH ≤ 2 three peaks associated with SiW_{12} on the cathodic sweep could be resolved that correspond to:

$SiW_{12}(0) + e^- \rightleftharpoons SiW_{12}(-1)$

WE	Glassy carbon disk
WE2	Carbon felt
CE	Pt wire in 1M Na_2SO_4
RE1	Ag/AgCl 1 M NaCl (220 mV vs SHE)
RE2	MSE 1 M H_2SO_4 (624 mV vs SHE)
Solution	1 M NaCl, 5 mM SiW_{12}
pH	1.7-7.0
scan speed	100 mV s^{-1}

Table 2.10: Cyclic voltammetry experimental setup.

$SiW_{12}(-1) + e^- \rightleftharpoons SiW_{12}(-2)$
$SiW_{12}(-2) + 2\,e^- \rightleftharpoons SiW_{12}(-4)$

At pH $>$ 2, the two-electron reduction splits into two one-electrode reductions that occur at lower potential:
$SiW_{12}(-2) + e^- \rightleftharpoons SiW_{12}(-3)$
$SiW_{12}(-3) + e^- \rightleftharpoons SiW_{12}(-4)$
Moreover, the standard reduction potentials do not vary with pH, indicating that they are not proton-coupled. In a previous study by Friedl et al. it was shown that the two-electron redox reaction (SiW_{12}(-2) $\rightleftharpoons$ SiW_{12}(-4)) does not split into two separate redox reactions up to a pH of 6 when the supporting electrolyte is 1 M H_2SO_4. Furthermore, it was shown that "potentials in the vicinity of the third redox wave the POMs irreversibly modify the electrode which leads to its decomposition and catalysis of the hydrogen evolution reaction (HER)."

The voltammograms in Figure 2.20 and 2.21 show that when the supporting electrolyte is 1 M NaCl, the electrochemical behaviour of the solution is quite different (Table 2.11). Firstly, at a pH $\leq$ 2, the standard potential of the SiW_{12}(-2) $\rightleftharpoons$ SiW_{12}(-4) is shifted significantly to a lower potential. Secondly, the peak-to-peak separation is greater, indicating that the redox reaction is slower (i.e. less electrochemically reversible). Thirdly, the first and second standard reduction potentials have slightly different values, and the separation between the anodic and cathodic peaks is slightly larger.

In Figure 2.20 it can also be seen that at pH 6, the intensity of the peaks diminishes relative to those at lower pH, indicating that SiW_{12} is unstable at higher pH. This is analogous to the behaviour of PMo_{12} described in section 2.3.1 (Figure 2.9 in which the POM dissociates into single valent metal oxide species, acting as a buffer as the pH increases.

Moreover, it can be seen in Figure 2.21 that in a 1 M NaCl solution, hydrogen evolution does not overlap the SiW_{12}(-2) $\rightleftharpoons$ SiW_{12}(-4) reaction, and the presence of anodic peaks on

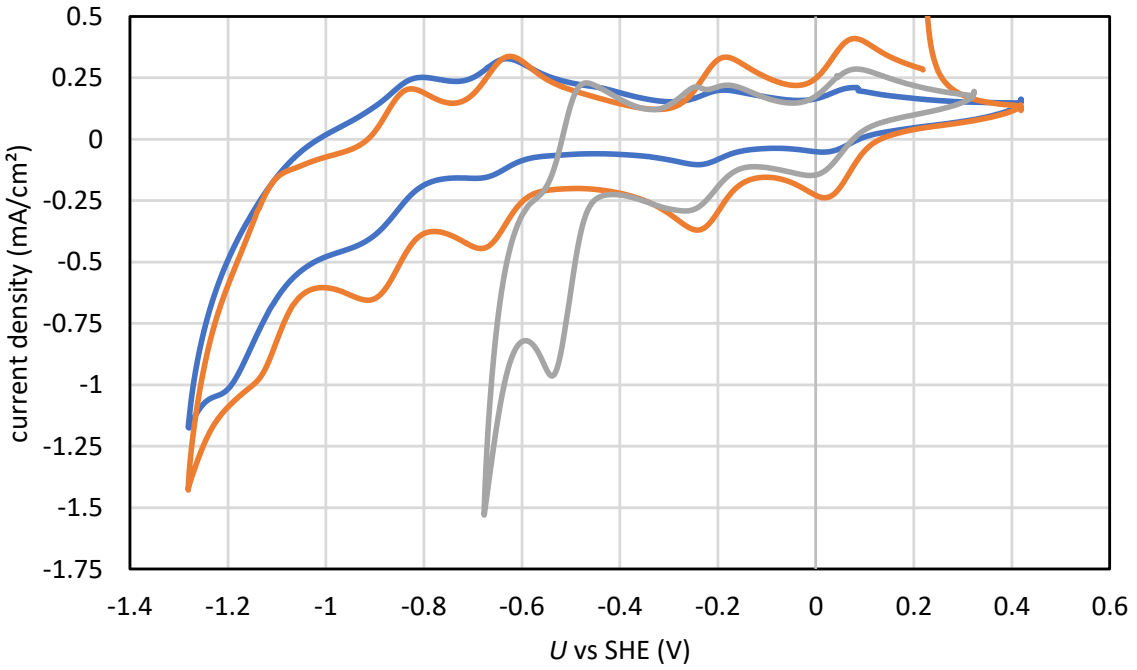

Figure 2.20: Cyclic voltammetry of SiW_{12} 1 mM in 1 M NaCl at pH 1.7 (grey), 5.7 (orange), and 6.0 (blue). WE: glassy carbon disk, CE: Pt wire, RE: Ag/AgCl in 1 M NaCl (+220 mV vs SHE), electrolyte: SiW_{12} 5 mM and 1 M NaCl, **pH: 1.7-7.0. Scan rate: 100 mV s^{-1}, initial sweep direction: positive, vertex WE potentials: 0.42 V vs SHE and -0.7 & -1.3 V vs SHE.

Redox reaction	pH	SE	n	U^o v SHE (V)	ΔU
$SiW_{12}(0) \rightleftharpoons SiW_{12}(-1)$	1-6	1 M H_2SO_4	1	0.01	57
$SiW_{12}(-1) \rightleftharpoons SiW_{12}(-2)$	1-6	1 M H_2SO_4	1	-0.21	56
$SiW_{12}(-2) \rightleftharpoons SiW_{12}(-4)$	1-6	1 M H_2SO_4	2	-0.37	29
$SiW_{12}(0) \rightleftharpoons SiW_{12}(-1)$	<2	1 M NaCl	1	0.02	76
$SiW_{12}(-1) \rightleftharpoons SiW_{12}(-2)$	<2	1 M NaCl	1	-0.23	67
$SiW_{12}(-2) \rightleftharpoons SiW_{12}(-4)$	<2	1 M NaCl	2	-0.52	50
$SiW_{12}(0) \rightleftharpoons SiW_{12}(-1)$	>2	1 M NaCl	1	0.03	67
$SiW_{12}(-1) \rightleftharpoons SiW_{12}(-2)$	>2	1 M NaCl	1	-0.23	50
$SiW_{12}(-2) \rightleftharpoons SiW_{12}(-3)$	>2	1 M NaCl	1	-0.65	69
$SiW_{12}(-3) \rightleftharpoons SiW_{12}(-4)$	>2	1 M NaCl	1	-0.87	80
$SiW_{12}(-4) \rightleftharpoons SiW_{12}(-6)$	>2	1 M NaCl	2	-1.13	163

Table 2.11: Redox reactions of SiW_{12} in various supporting electrolytes (SE) at varied pH, their standard reduction potentials, and the number of electrons transferred.

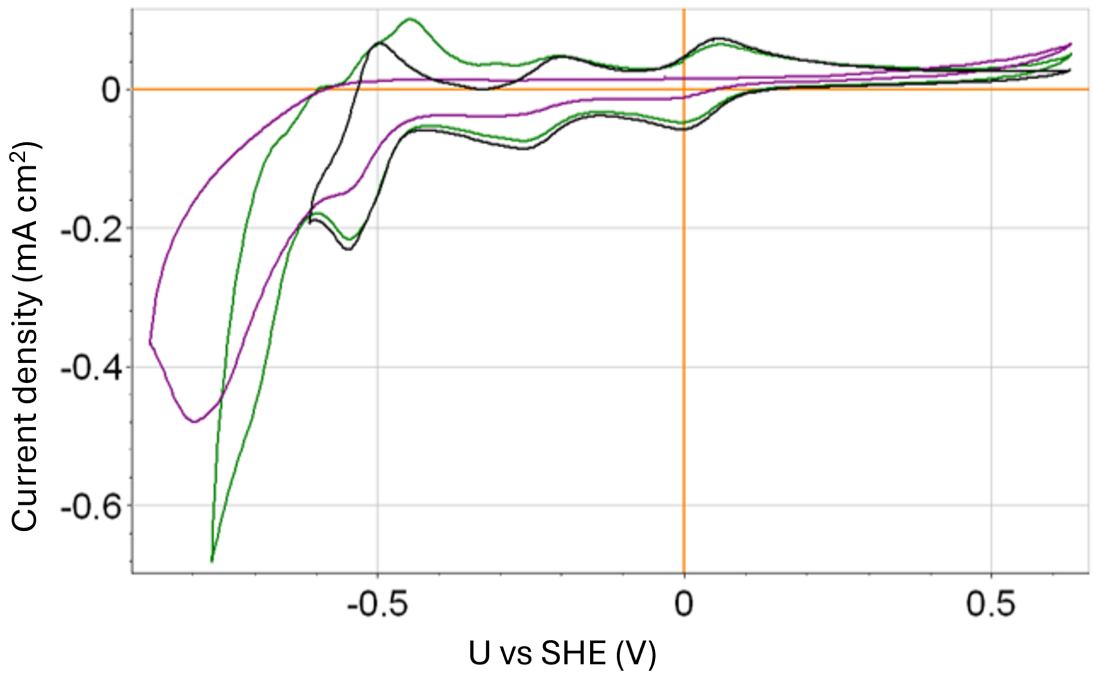

Figure 2.21: Voltammograms of SiW_{12} in 1 M NaCl at pH 1.7. The lower potential limit is varied. WE: glassy carbon disk, CE: Pt wire, RE: Ag/AgCl in 1 M NaCl (+220 mV vs SHE), electrolyte: SiW_{12} 5 mM and 1 M NaCl, Scan rate: 100 mV s^{-1}, initial sweep direction: positive, vertex WE potentials: 0.6 V vs SHE and -0.65 to -0.95 V vs SHE.

the return sweep indicates that production of SiW_{12}(-4) does not lead to the POM dissociation. Extending the potential range reveals a large reduction peak at -0.8 V vs SHE. If this peak is partially resolved by sweeping to -0.75 V, the corresponding anodic peak shifts positively by +50 mV and increases in intensity. If the peak is fully resolved, then the anodic peaks are no longer present, indicating that the POM is no longer being oxidised, and has likely dissociated.

A SiW_{12} solution of lower concentration (1 mM) was prepared for extended bulk electrolysis experiments, Table 2.12 shows the cell details. The initial pH was adjusted to 5.2 with sodium hydroxide solution, and cyclic voltammograms were recorded. The solution was electrochemically reduced by 15.9 mAh (5.9 F mol^{-1}) and fully reoxidised (2 cycles). Both cycles have 100.0% coulombic efficiency, and the voltammograms after cycling were unchanged. Figure 2.22 shows the capacity vs potential plots for the second cycle. Vertical lines spaced 2.68 mAh apart correspond to a (1 F mol^{-1}) reduction/oxidation. On reduction, it can be seen that the first four plateaus correspond to 1, a one-electron reduction, and the fifth and final plateau corresponds to a 2-electron reduction. This is in line with expectations derived

WE	Glassy carbon disk
WE2	Carbon felt
CE	Pt wire in 1M Na_2SO_4
RE1	Ag/AgCl 1 M NaCl (220 mV vs SHE)
RE2	MSE 1 M H_2SO_4 (624 mV vs SHE)
Solution	1 M NaCl, 1 mM SiW_{12}
pH	5.2-7.21
scan speed	$10 - 100$ mV s^{-1}

Table 2.12: Cyclic voltammetry and bulk electrolysis experimental parameters

from the peak separations detailed in Table 2.11. However, the plateau width is not exactly 2.68 mAh (or 5.36 mAh for the final plateau) in each case, so it is suspected that the chemical nature of the POM may change somewhat on reduction. The evidence for this is more apparent on reoxidation of the species, as the anodic plateau widths correspond to 1, 2, 1, 1, and 1 electron oxidation, respectively. Figure 2.23 shows a potential vs oxidation state plot using the same data as Figure 2.22, and shows the two are not fully symmetrical. If the reduction is fully electrochemically and chemically reversible with no significant change in the structure of POM, then the plots in Figure 2.23 are expected to be symmetrical, with a ΔU present due to the overpotential. Voltammograms before and after cycling indicate that whatever change has occurred is reversed on reoxidation.

The voltammograms displayed in Figure 2.24 are of the reduced species SiW_{12}(-2.1). There is little difference relative to the fully oxidised species shown in 2.20.

Next, the solution was reduced by 2 F mol^{-1}, and it was noticed that the pH increased from 5.2 to 6.2, which is beyond the window of stability for fully oxidised SiW_{12}. It should be noted that the change in pH probably came about due to an increase in the pKa of the reduced species. So, although the electrochemical reduction is not proton-coupled, the resulting species has increased electron density (due to the addition of 2 electrons), so it is likely more basic than the oxidised species. Cyclic voltammograms of SiW_{12}(-2) were recorded at pH 6.21, 7.0, and 7.21; and compared to the fully oxidised species (pH 5.21) in Figure 2.26. The differences between all voltammograms is minor. It was expected that the intensity of peaks would diminish at higher pH (as is the case with the fully oxidised species), but it appears that the reduced form of SiW_{12} is stable at pH$\geq$6, while the oxidised form is not. This is significant because the hydrogen evolution reaction is offset to lower potentials at higher pH. So a higher pH should allow for an increase in accessible oxidation states of SiW_{12} (i.e. larger accessible capacity). However, in this scenario, care must be taken to not fully to oxidise the species while the pH is $\geq$6, or the POM will dissociate. In practice, this could be achieved

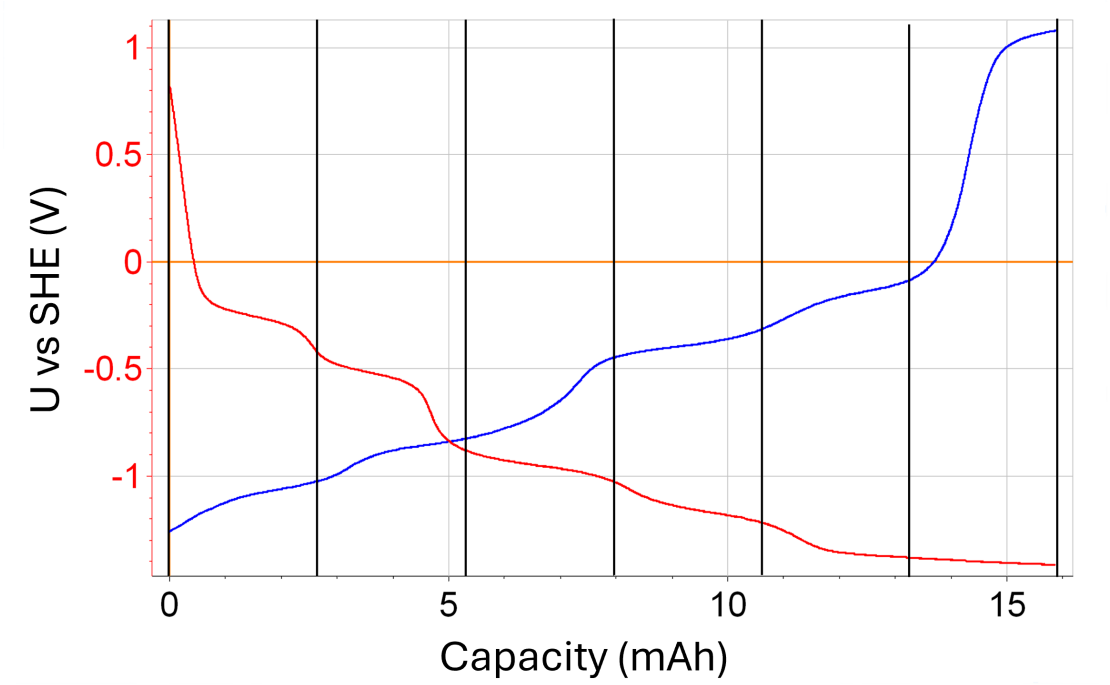

Figure 2.22: The potential vs capacity plot of a charge/discharge cycle for the electrolysis cell described in Table 2.12.

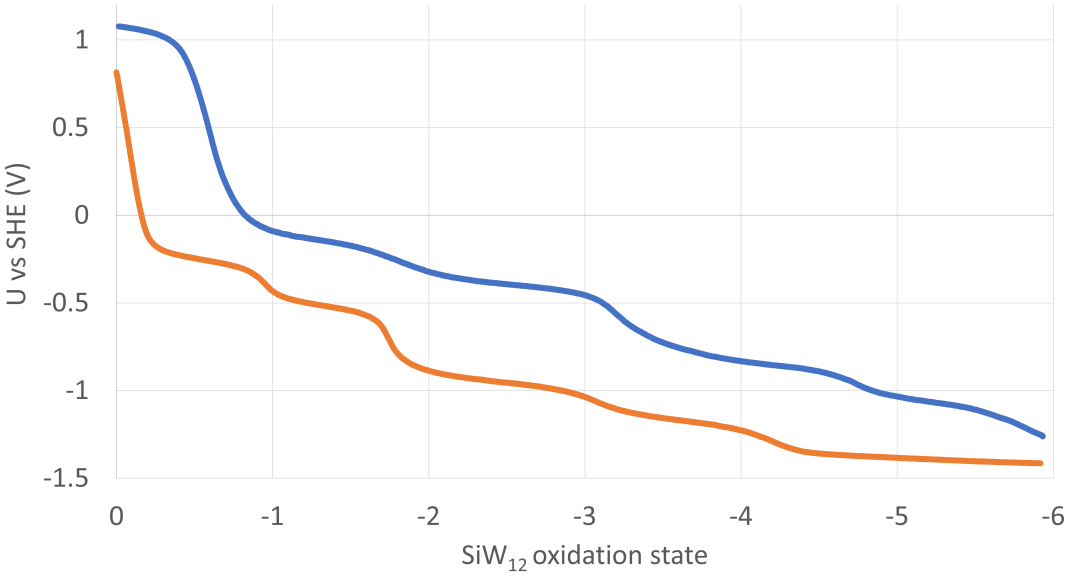

Figure 2.23: A potential vs oxidation state plot for the same cycle displayed in Figure 2.22. This kind of plot highlights the asymmetry of the oxidation and reduction chemical pathways.

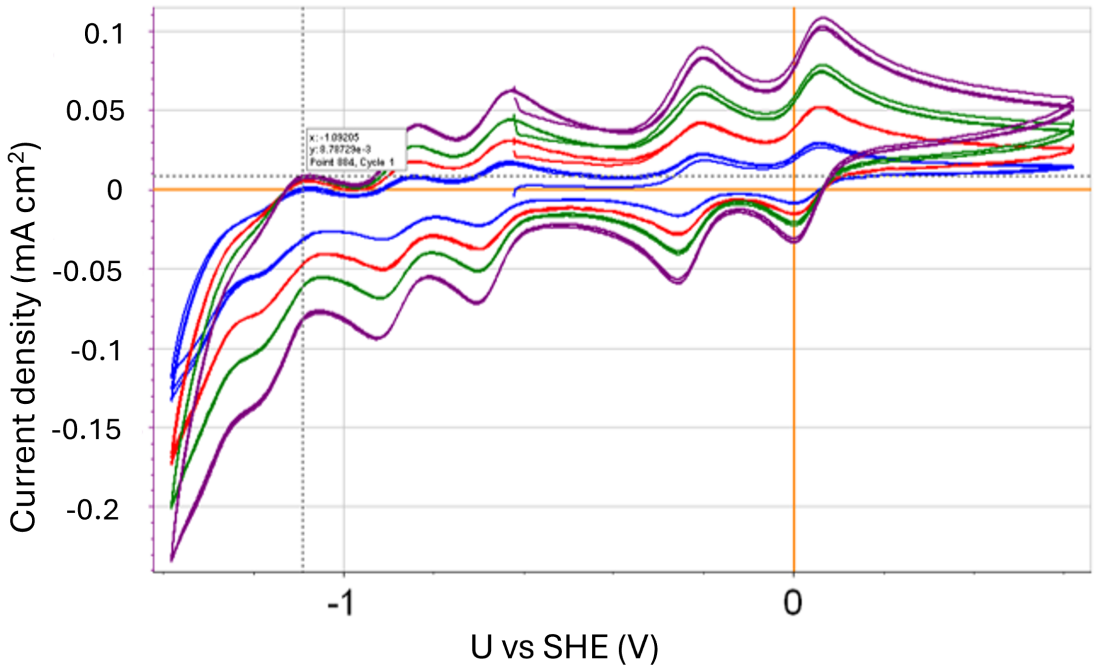

Figure 2.24: Cyclic voltammetry of SiW_{12} (5 mM) in NaCl (1 M) at various scan speeds. WE: glassy carbon disk, CE: Pt wire in 1 M Na_2SO_4, RE: Ag/AgCl in 1 M NaCl (+220 mV vs SHE), electrolyte: SiW_{12} 1 mM and 1 M NaCl, initial sweep direction: positive, vertex WE potentials: 0.6 V vs SHE and -1.4 V vs SHE. Scan rate: 10 (blue), 25 (red), 50 (green) and 100 (purple) mV s^{-1}

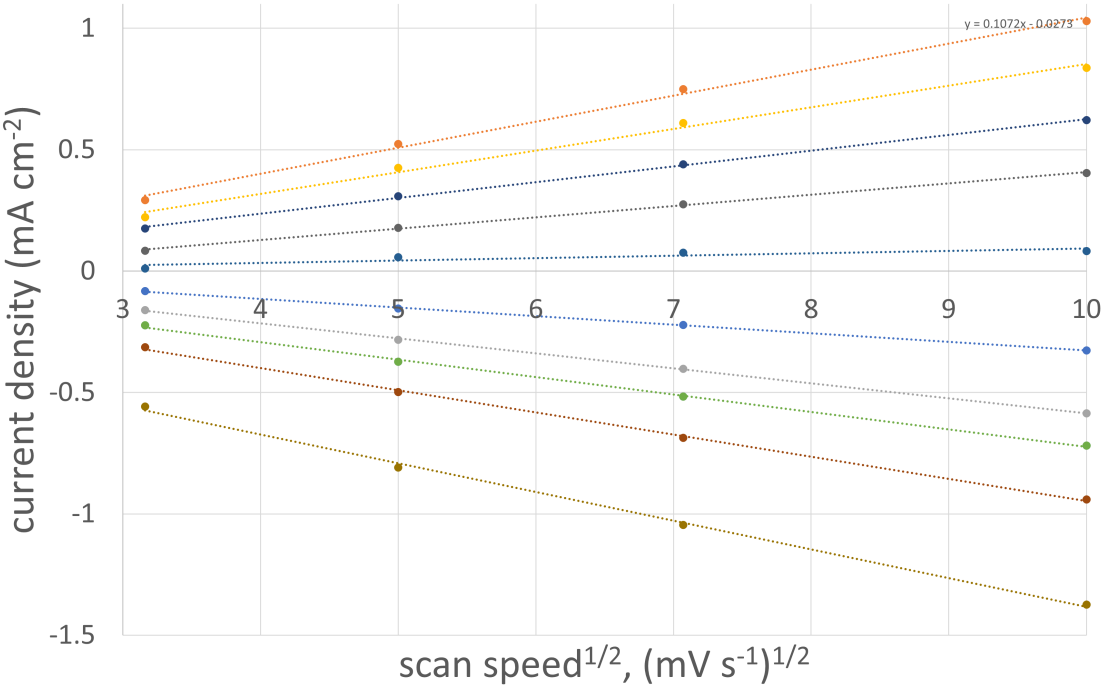

Figure 2.25: Cyclic voltammograms of a 1 mM solution of SiW_{12}, as described in Table 2.12. Red, green, and blue traces are at oxidation state -2, at pH of 7.0, 6.2 and 7.21, respectively. The purple trace is at oxidation state 0 and pH 5.2.

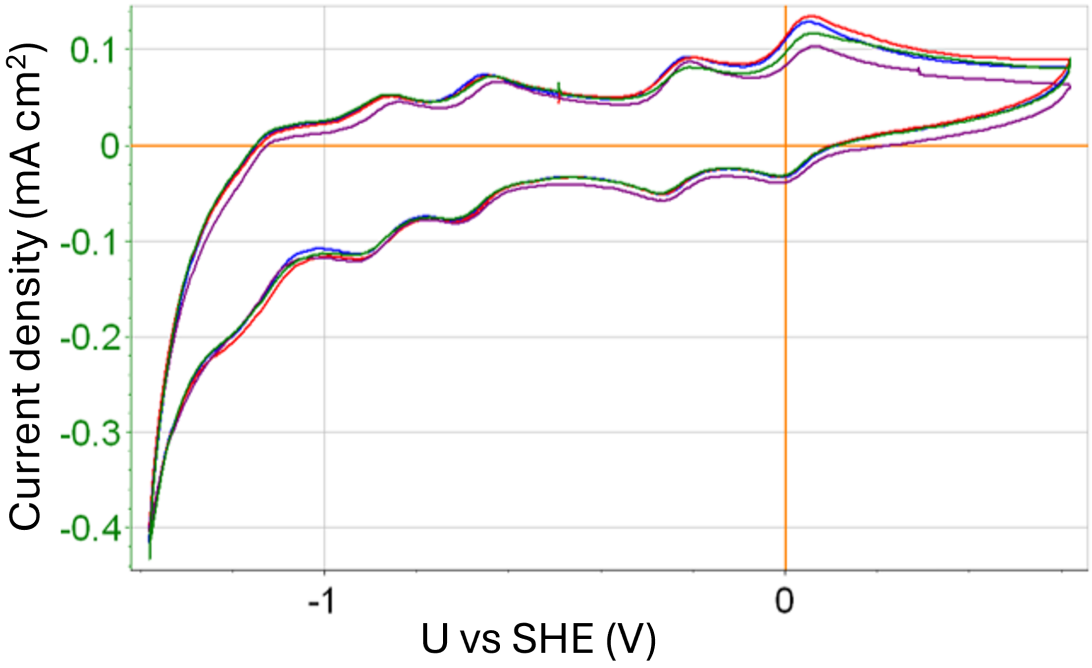

Figure 2.26: Cyclic voltammograms of SiW_{12} in various oxidation states and values of pH. Blue: SiW_{12}(-2), pH 7.21. Red: SiW_{12}(-2), pH 7.00. Green: SiW_{12}(-2), pH 6.2. Purple: SiW_{12}(0), pH 5.20. WE: glassy carbon disk, CE: Pt wire in 1 M Na_2SO_4, RE: Ag/AgCl in 1 M NaCl (+220 mV vs SHE), electrolyte: SiW_{12} 1 mM and 1 M NaCl, initial sweep direction: positive, Scan rate: 100 mV s^{-1}, vertex potentials: 0.6 V and -1.38 V vs SHE.

by reducing to SiW_{12}(-2) and adding NaOH until the pH rises to ∼7, and monitoring the OCP throughout cycling to ensure it does not rise above ∼-3000 mV vs SHE.

With a starting pH of 7.21 and an oxidation state of -2, the solution was reduced by 26.4 mAh (9.85 F mol^{-1}) to an oxidation state of approximately -12, and then reoxidised. This procedure was repeated 14 times. Figure 2.27 shows the potential vs capacity plots for the 15 cycles. Figure 2.28 shows the same data in a potential vs oxidation state plot with the data from Figure 2.23 overlayed. The applied current was decreased in the latter experiment to avoid hydrogen evolution, so the difference in potential for similar oxidation states is expected. The asymmetry between the anodic and cathodic reactions is even more pronounced when the POM is highly reduced. After the first electrochemical reduction step, voltammograms were recorded on SiW_{12}(-12). On reoxidation to SiW_{12}(-2), further voltammograms were recorded. The results are shown in Figure 2.29. The position of peaks on the anodic change slightly when the oxidation state is -12. This may be due to a concentration effect, however, as the largest anodic peak shift pon consecutive cycling. The peaks on the cathodic

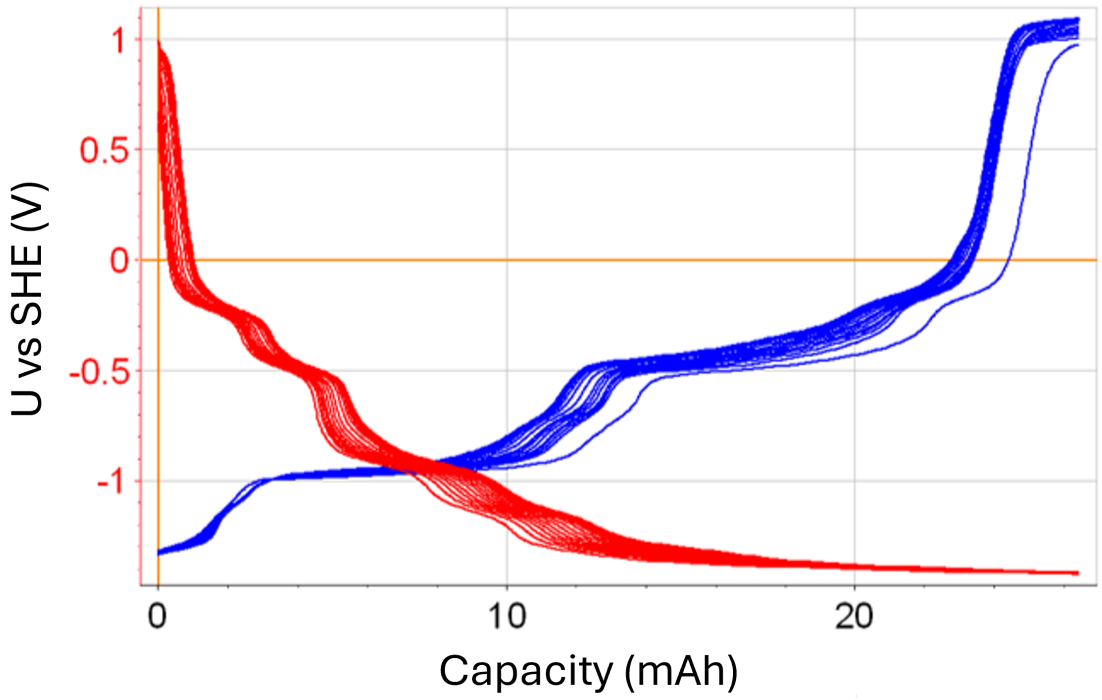

Figure 2.27: Potential vs capacity plot for SiW_{12} bulk electrolysis experiment.

sweep are also less pronounced, but again, this is expected given the low oxidation state. There is also an anodic plateau at approximately -400 mV vs SHE when the oxidation state is -12. On reoxidation, the voltammograms return to their original shape.

Determination of the capacity and capacity retention of SiW_{12} as a redox flow battery anolyte

Various redox flow batteries were assembled and tested with the aim of increasing the accessible capacity of SiW_{12} when used as an anolyte. Previous work by Friedl et al. showed that SiW_{12} could undergo a reduction of 2 F mol $^{-1}$ reversibly for hundreds of cycles when the initial pH is 2 or lower. [1, 2]. In the previous section, it was shown that at higher pH values, SiW_{12} could be reduced further, up to at least 12 F mol $^{-1}$, but this leads to significant changes in the pH (up to pH 10-11 in some instances). It was established that SiW_{12} could undergo electrochemical oxidation and reduction reversibly with a high coulombic efficiency despite the evidence that SiW_{12} undergoes a reversible chemical change when reduced (much like PMo_{12}). However, it is unclear whether the significant change in pH will have unintended side effects on the operation of a redox flow battery.

For instance, a significant differential in pH could lead to considerable osmotic pressure, leading to water transfer across the membrane, causing one side to become diluted and the

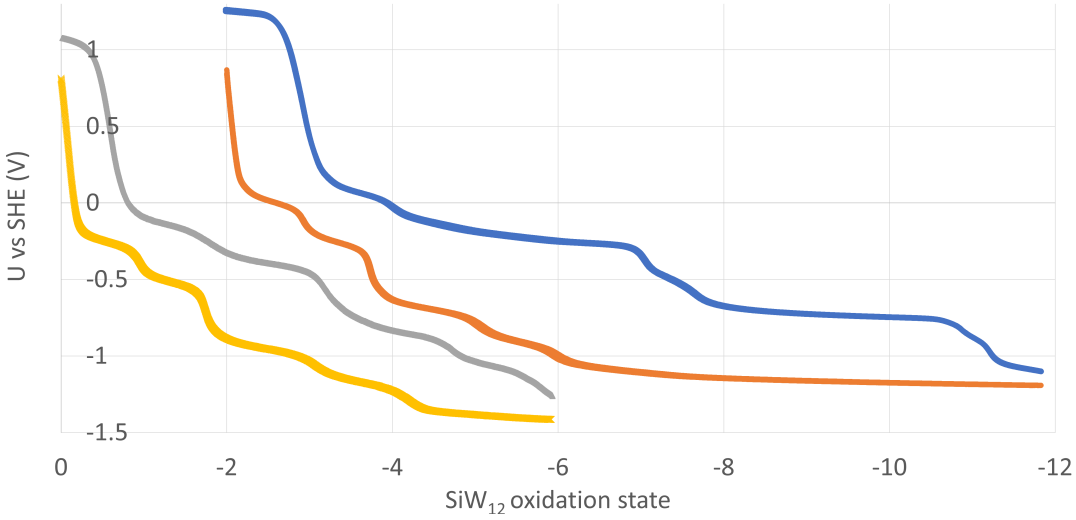

Figure 2.28: Potential vs oxidation state plot for SiW_{12} bulk electrolysis experiment. Blue: Oxidation from -12 to -2. Orange: reduction from -2 to -12. Grey: oxidation from -6 to 0. Yellow: reduction from 0 to -6.

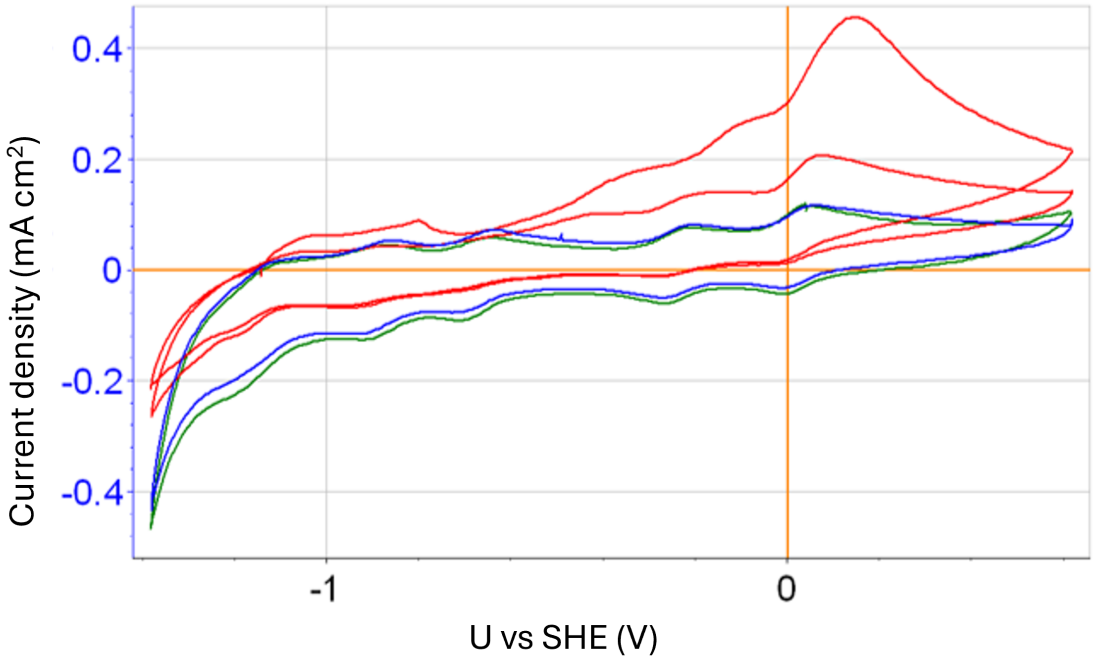

Figure 2.29: Voltammograms of SiW_{12} initially at an oxidation state of -2 (blue), then at an oxidation state of -12 (red, 2 consecutive cycles), then again at oxidation state -2 after reoxidation (green). WE: glassy carbon disk, CE: Pt wire in 1 M Na_2SO_4, RE: Ag/AgCl in 1 M NaCl (+220 mV vs SHE), electrolyte: SiW_{12} 1 mM and 1 M NaCl, initial sweep direction: positive, Scan rate: 100 mV s^{-1}, vertex potentials: 0.6 V and -1.38 V vs SHE.

Anode	Carbon felt (25 cm^2)
Cathode	Carbon felt (25 cm^2)
Anolyte	1 M LiCl, 10 mM SiW_{12}, 70 mL, pH 4.25
Catholyte	1 M LiCl, 35 mM H_3PO_4, 10 mM PV_{14}, 70 mL, pH 2.35
Separator	NFS (Synder Filtration)

Table 2.13: Redox flow battery properties.

other to be highly concentrated. Water crossover could lead to the precipitation of active species if the solution becomes too concentrated. Also, an imbalance in concentration could lead to higher overpotentials, as material availability at the electrode surface in one half-cell will be diminished. A large difference in pH across the membrane could also lead to the crossover of hydrogen ions due to diffusion. Selling et al. demonstrated that the stability of PV_{14} is highly sensitive to the pH of the solution.[3] PV_{14} is in thermodynamic equilibrium with other vanadate species such as $[V_{10}O_{28}]^{6-}$.

The first redox flow cell to be tested is described in Table 2.13. Prior to the addition of the catholyte solution to the RFB, it was chemically reduced by hydrazine (95μL, 35% w/w, 6 F mol^{-1}).

The suitability of nanofiltration membranes as separators in the POM-containing flow battery was also studied during this investigation. It has been hypothesised that, due to the large size of POMs, size exclusion membranes could be used as an effective separator material whilst allowing good conductivity of charge carriers such as Na^+ or Li^+ through the membrane. The polyamide-based "NFS" membrane produced by Synder filtration was designed to remove sulphate from seawater before waterflood injection into oil reservoirs.[103] This is achieved by controlling the membrane's pore size so that species with a molecular weight higher than 100-250 Da cannot pass through. The membrane reduces the amount of lactose and magnesium sulphate in a water stream by 99.5%. Therefore, it was expected that the crossover of POMs would be much lower. Furthermore, the membrane only removes 50% of NaCl in a water stream, so it is expected that the conductivity of the supporting electrolyte in an RFB would be high. Synder has also tested the membrane over a wide range of pH values (2-10.5) and temperature (ambient-50^{o}C).

After assembling the battery and circulating the electrolytes for several hours, impedance spectroscopy across the cell showed that the ohmic resistance was $\sim 0.4\ \Omega$, corresponding to an area resistance of 10 $\Omega\ cm^2$. This is broadly in line with the ohmic resistance observed in other POM batteries. [1, 2]

Over several days, the battery cycled at a current density of 4 mA cm^{-2} and produced

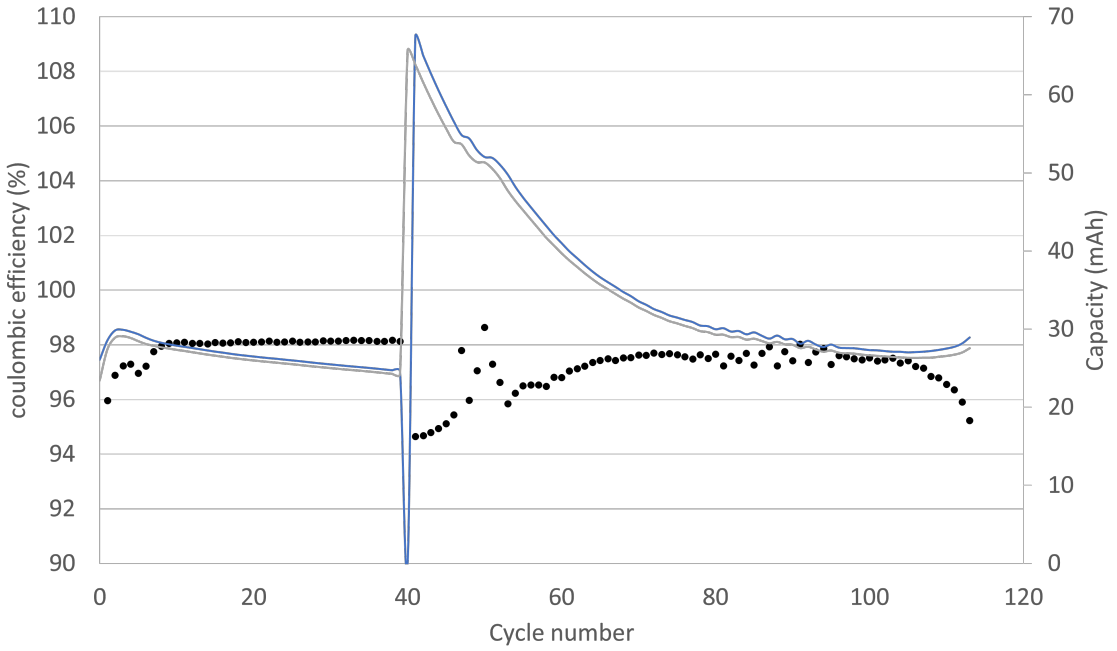

Figure 2.30: Plots of the coulombic efficiency (black circles), as well as charge and discharge capacity (blue and grey lines, respectively) vs cycle number.

reasonably promising results. Potential difference cut offs were U_{min} = 0.1, and U_{max} = 1.0 V for the first 41 cycles. The capacity on the first cycle was 26 mAh, which rose to 30 mAh by cycle 3. The accessible capacity then steadily decreased until cycle 40. For the first 9 cycles, the coulombic efficiency varied between 96-98% and then remained at 98.1% for the remaining 40 cycles (Figure 2.30).

Before cycle 41, another impedance spectrum was recorded, and the ohmic resistance had risen to 0.51 Ω (12.75 Ω cm^2), which could be due to membrane fouling.

The current density was increased to 10 mA cm^{-2}, and U_{max} was increased to 2 V. Additionally, the voltage was held at 2 V until the current density dropped to 0.4 mA cm^{-2}. This was done in an attempt to maximise the accessible capacity of SiW_{12}. As shown in Figure 2.30, this worked to an extent. The accessed capacity rose to 65.6 mAh (3.5 F mol^{-1}), 75% higher than previously reported. However, as can also be seen, the capacity faded rapidly over the following cycles, eventually stabilising at around 30 mAh (1.6 F mol^{-1}). Some of this capacity loss can be attributed to a leak on the anolyte side that was only detected once the battery was disassembled.

The battery was fully charged so that PV_{14} was in the fully oxidised state, and SiW_{12} was in a reduced state. The pH of the anolyte and catholyte were 8.64 and 2.18, respectively,

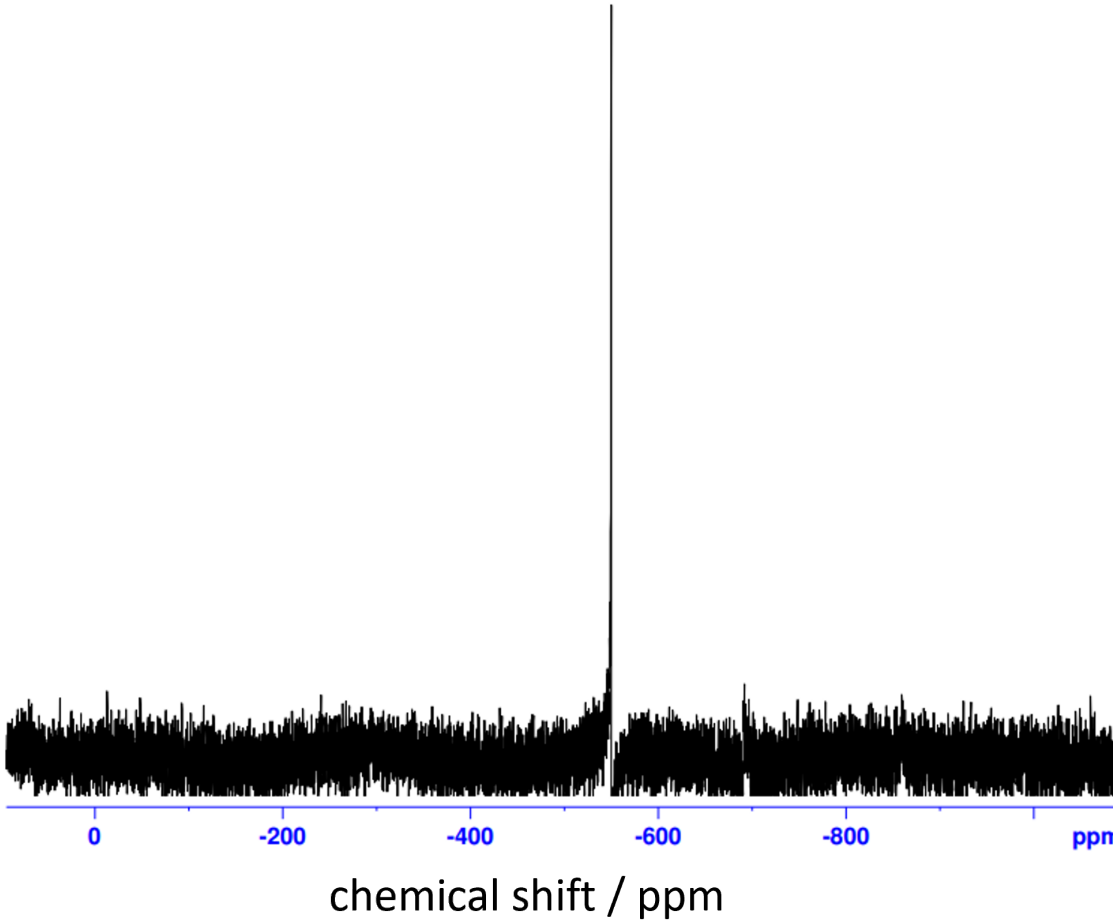

Figure 2.31: Post-mortem ^{51}V NMR spectrum of the catholyte solution indicating the presence of $[VO_2(H_2O)_4]^+$.

which is within the expected parameters. Hydrogen peroxide was added to the anolyte to fully oxidise it, which should have changed the deep blue colour of the solution to transparent. However, the solution colour changed to red and remained so after 24 hours of exposure to air. This is a visual indication that peroxo vanadium (V) complexes are present in the solution. [104]

A portion of the anolyte solution was transferred to a 3-electrode cell with a glassy carbon disk electrode(WE), a gold wire (CE), and an Ag/AgCl reference electrode. The presence of SiW_{12} was confirmed, but there was an additional anodic peak at 0.717 V vs SHE and a cathodic peak at 0.620 V vs SHE. These are attributed to the presence of vanadium in the solution, indicating that there is significant crossover through the membrane. A V^{51} NMR spectra of the catholyte as shown in Figure 2.31 supports this conclusion.

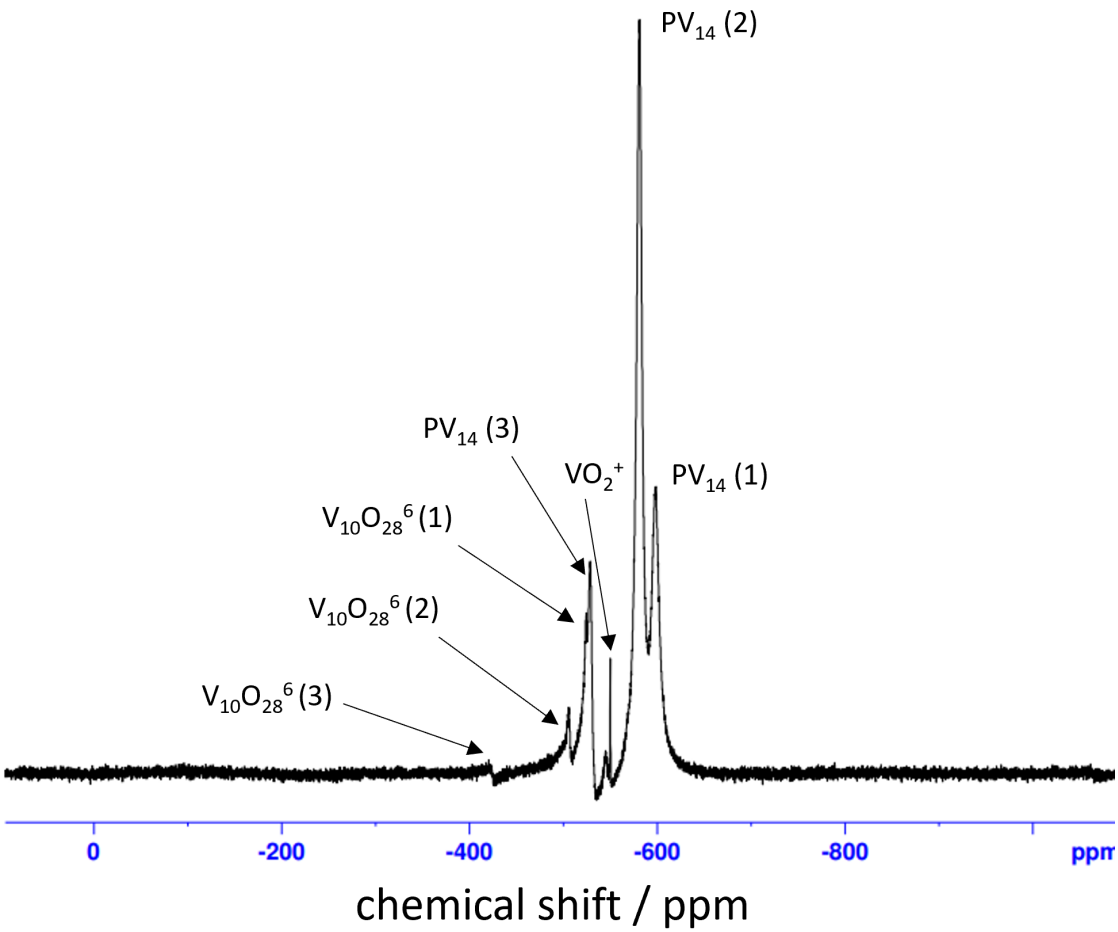

Figure 2.32: Post-mortem ^{51}V NMR spectrum of the anolyte solution indicating that some PV_{14} has dissociated into decavanadate and vanadium ions and VO_2^+.

A ^{51}V NMR spectrum of the anolyte shows that PV_{14} is still present in solution, but the equilibrium has shifted so that $V_{10}O_{28}^{6-}$ and single vanadium ions are also present. The reason this occurred is unclear, as the pH is 2.2, so PV_{14} should be the only detectable vanadium species present. One possible explanation is that phosphate ions can cross through the membrane, leading to a shift in equilibrium.

Plots of the voltage vs capacity for selected cycles are shown in Figure 2.33. On cycle 62, the battery began to behave anomalously. Towards the end of the discharge procedure (C = 35 mAh), the voltage decreased rapidly. It then increased for a short period by approximately 100 mV before decreasing again until it ultimately fell to 0 V. This phenomenon occurred on each cycle after cycle 62, but the capacity value at which it occurred decreased, while the voltage at which it occurred increased. By cycle 102, the capacity at which this occurred had

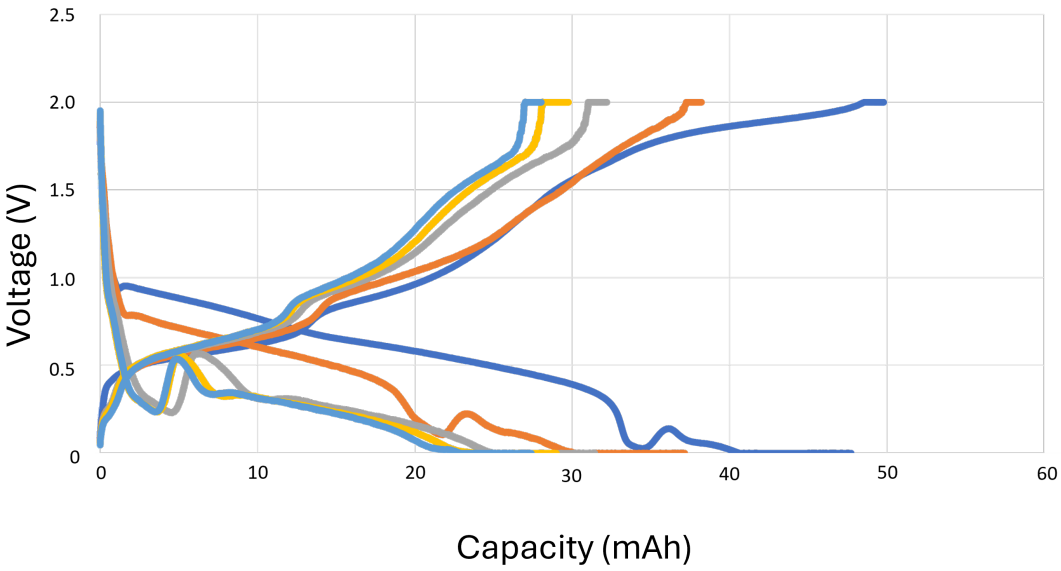

Figure 2.33: Voltage vs capacity plots for selected cycles of the battery described in Table 2.13.Cycle 62 (dark blue), 72 (orange), 82 (grey), 92 (yellow), and 102 (light blue)

decreased to about 5 mAh, and the rise in voltage was 300 mV.

No explanation for this strange behaviour was identified, but several possible explanations exist. It could potentially indicate that as the anolyte is oxidised, its potential decreases, or as the catholyte is reduced, its potential increases. However, this seems impossible without significant changes to the chemical properties of the solution. The shift in the equilibrium of the catholyte solution, which leads to the dissociation of PV_{14} into vanadium ions (and other species) may be the root cause. As was shown by Friedl et al., the reduction potential of PV_{14} is much lower than that of V^{IV}/V^{V}.[1] So, it could be the case that reduction of PV_{14} causes the POM to dissociate into vanadium ions (primarily V^{V}), causing the potential of the solution to increase. Even though the discharge voltage increases, this effect (if it is indeed the cause) is undesirable because vanadium ions could easily cross the size exchange membrane and, indeed, a Nafion membrane. [105]

Another redox flow cell was assembled with the properties listed in Table 2.14. The idea is that if the phosphoric acid concentrations were equivalent on either side of the membrane, there would be no net crossover of phosphate ions due to diffusion. Therefore, the conditions for PV_{14} stability should be satisfied. Both catholyte solutions were chemically reduced by hydrazine (95μL, 35% w/w, enough to reduce the PV_{14} by 6 F mol^{-1}) prior to addition to the battery. The battery was charged with a current density of 8 mA cm^{-2} and voltage cut-offs at 0 V and 1.8 V. The solution colour gradually turned purple, indicating that vanadium was still

Anode	Carbon felt (25 cm^2)
Cathode	Carbon felt (25 cm^2)
Anolyte	1 M LiCl, 35 mM H_3PO_4, 10 mM SiW_{12}, 70 mL, pH 3.98
Catholyte	1 M LiCl, 35 mM H_3PO_4, 10 mM PV_{14}, 70 mL, pH 2.35
Separator	NFS (Synder Filtration) and Nafion 117

Table 2.14: The properties of two redox flow batteries are equivalent except for the separator. i.e. one was assembled with an NFS membrane, and the other was assembled with Nafion 117.

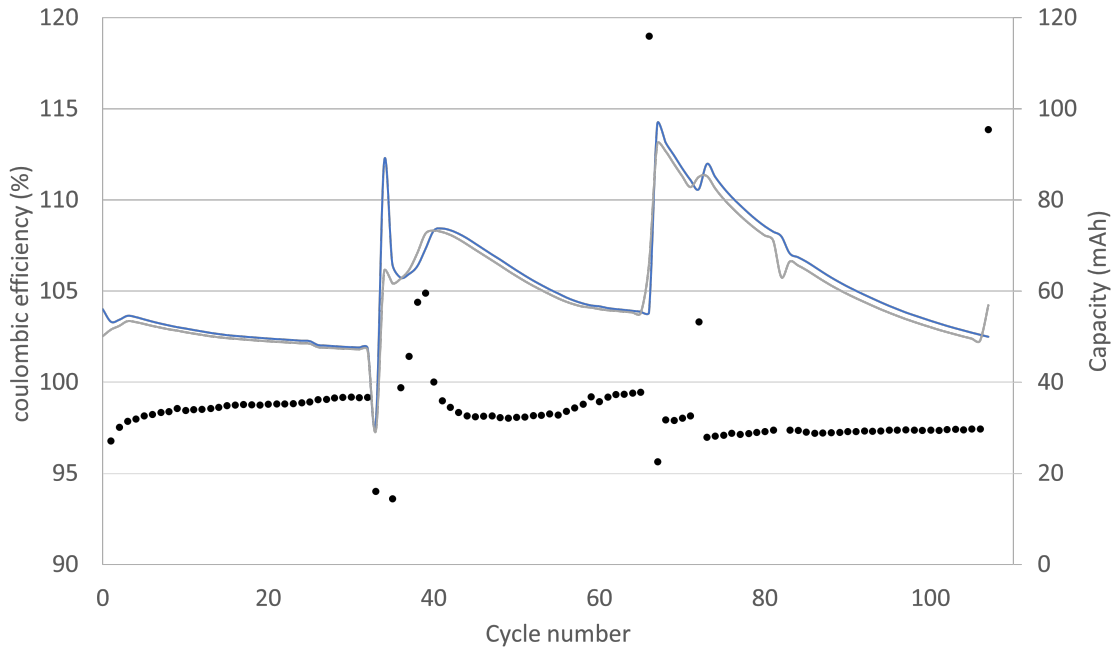

Figure 2.34: Coulombic efficiency, and charge/discharge capacity vs cycle number for the battery described in Table 2.14.

crossing the membrane. Either PV_{14} or the small number of vanadium ions present in the solution were crossing the membrane. The battery was stopped, disassembled and cleaned. Evidently, the NFS membrane is not well suited as a separator, at least in conjunction with PV_{14}.

The flow cell with a Nafion 117 membrane was assembled shortly after (two days after the addition of hydrazine to the PV_{14}) and cycled with a similar current density and cut-off voltages.

A total of 107 cycles were recorded. A plot of coulombic efficiency and charge and discharge capacity is shown in Figure 2.34. A voltage vs capacity plot of a typical cycle (cycle 17) is shown in Figure 2.35.

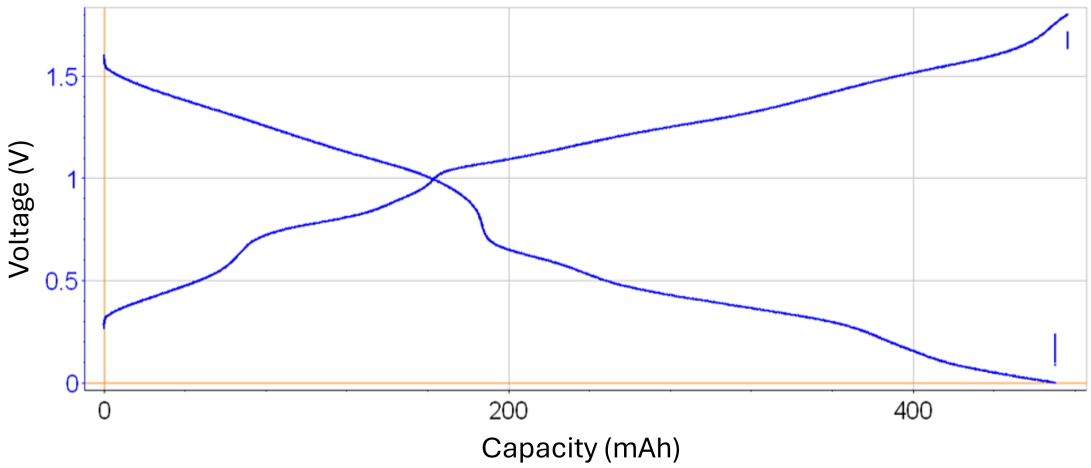

Figure 2.35: A voltage vs capacity plot of a typical cycle (cycle 17) of the flow battery described in Table 2.14. The current density was 8 mA cm^{-2}, and the cut-off voltages were 1.7 V on charge and 0 V on discharge.

The initial discharge capacity was 180 C (50 mAh, 2.66 F mol^{-1}) and gradually dropped to 169 C (47 mAh, 2.5 F mol^{-1}) by cycle 32. When fully charged, the PV_{14} solution was red/brown, indicating it was fully oxidised. The capacity is lower than expected, probably because, after two days of being stored, oxygen ingress led to oxidation of the solution. Prior to cycle 33, additional hydrazine (48μL, 35% w/w, enough to reduce the PV_{14} by 3 F mol^{-1}) was added to the solution and allowed to rest for 2 hours. On cycle 33, the capacity was much lower than expected, but the inlet tube for the catholyte was not in solution so no electrolyte was pumped to the stack. On cycle 34, the position of the inlet tube was corrected, and the discharge capacity rose to 230 C (64 mAh, 3.4 F mol^{-1}) and steadily climbed to a maximum of 263 C (73 mAh, 3.89 F mol^{-1}) on cycle 40, before decreasing to 198 C (55 mAh, 2.93 F mol^{-1}) on cycle 66. At this point, the anolyte (SiW_{12}) solution was not being fully oxidised as evidenced by the dark blue solution colour.

To compensate for this, an additional 20 mL of 10 mM PV_{14} solution was added to the catholyte tank. However, this had very little effect on the capacity. So, a further 48μL of hydrazine solution was added to the catholyte prior to cycle 67. This caused the discharge capacity to rise to 347 C (96 mAh, 5.14 F mol^{-1}). Over the subsequent 40 cycles, the discharge capacity decreased to 176 C (49 mAh, 2.6 F mol^{-1}). At some point after cycle 66, the anolyte solution began to leak, and a dark blue solution puddled at the bottom of the cell. The relatively fast decrease in capacity is attributed to this leak. However, it is possible that oxygen ingress also caused oxidation of the anolyte and catholyte throughout the cycling

procedure.

The above experiments demonstrated that increasing the pH of the anolyte SiW_{12} solution allows for at least a 150% increase in accessible capacity per mole. However, the rate at which capacity faded was an issue, especially when the size exclusion membrane was used. In that case, the capacity fade was caused by the crossover of vanadium ions or PV_{14} into the anolyte chamber and was, therefore, irreversible. By using a cation exchange membrane (Nafion 117), this problem was alleviated, and although the capacity did fade quickly, it could be reversibly recovered by the addition of hydrazine. It is suspected that the leading cause was a leak of the anolyte, but the decrease in capacity in earlier cycles is likely due to oxygen ingress. Further work on this system could benefit from using nitrogen of a higher purity as the purge gas and better sealing of the system.

As there was no evidence of crossover of SiW_{12} into the catholyte half cell, it was suspected that this type of membrane could still be used in a POM containing RFB. However, an ideal POM candidate for the catholyte half-cell could not be found, so ferrocyanide was used as the catholyte. In many respects, ferrocyanide is an ideal candidate for a redox flow battery electrolyte. Its stability towards repeated electrochemical oxidation and reduction are very high. The standard rate constant for electron transfer is high ($k^0 \approx 10^{-2}\ cm\ s^{-1}$on glassy carbon). It is stable in a range of chemical environments, has a high solubility limit ($\sim$1.46 M), and is thermally stable to 140^{o}C. Ferrocyanide is also extremely cheap, composed entirely of highly abundant elements, and is already produced on an industrial scale. Moreover, ferrocyanide has a fairly high molecular weight (212 g mol^{-1}) which may hinder transport through a size exclusion membrane. The major downside is that the standard reduction potential for the [Fe(CN)$_6^{2-}$]/[Fe(CN)$_6^{3-}$] is practically in the centre of the electrochemical stability window for water. Therefore, it is not particularly suited to being an anolyte or a catholyte. The potential difference that can be achieved when it is used in a battery is bound to be fairly low. The properties of this electrolyte are not investigated here because they have been studied extensively elsewhere. [76, 85, 106–113]

A new RFB cell was assembled with the properties listed in Table 2.15. Typically, ferrocyanide is present as the potassium salt. However, as previously discussed, this limits the solubility of POMs to about 10 mM. So, the concentration of SiW_{12} was set to 10 mM. To the ferrocyanide solution, a supporting electrolyte of NaCl (1 M) was used, which should limit the amount of potassium crossover through the membrane. Because the maximum accessible capacity of ferrocyanide is 1 F mol^{-1} (i.e. it only has one redox couple), the volume of the solution needs to be much higher than the POM solution. Because the effect of highly reducing SiW_{12} is still not fully understood, the flow cell was tested in a fume cupboard in case

Anode	Carbon felt (25 cm^2)
Cathode	Carbon felt (25 cm^2)
Anolyte	1 M NaCl, 10 mM SiW_{12}, 60 mL, pH 4.25
Catholyte	1 M NaCl, 10 mM [$K_4Fe(CN)_6^{2.5-}$], 1000 mL
Separator	NFS (Synder Filtration)

Table 2.15: Redox flow battery properties.

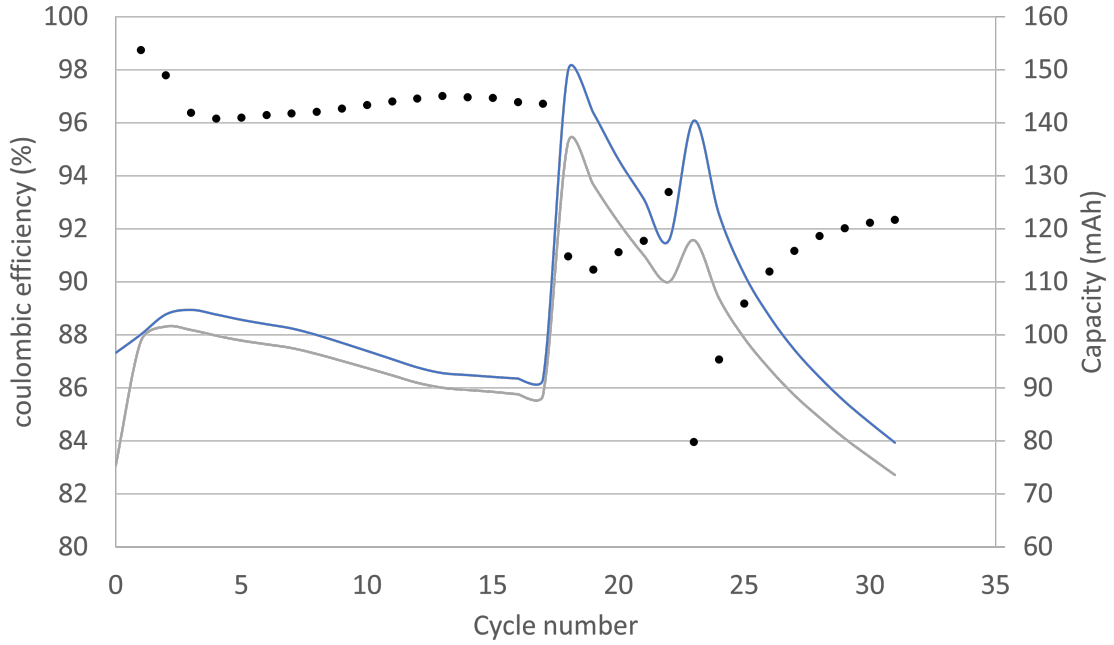

Figure 2.36: Coulombic efficiency, and charge/discharge capacity vs cycle number for the battery described in Table 2.15.

an unexpected change in pH led to HCN evolution. The charge and discharge capacity and coulombic efficiency vs cycle number plot are displayed in Figure 2.36.

After assembly, the RFB was cycled at a constant current density of 8 mA cm^{-2} with voltage limits at 1.7 and 0 V for 17 cycles. The discharge capacity of the first cycle was 75 mAh, which increased to a maximum of 101 mAh by cycle 2. From there, a gradual decrease in capacity to 88 mAh occurred. The coulombic efficiency over the first 18 cycles was reasonably high, levelling out by cycle 3 at 96-97%.

Figure 2.37 shows a typical voltage vs capacity plot for a cycle. On charging, the first plateau has a width of 7.4 mAh because the SiW_{12} is not fully oxidised. The following three plateaus have widths that are approximately 15 mAh. Even though the voltage is a two-electrode measurement, the presence of plateaus can be entirely attributed to the electro-

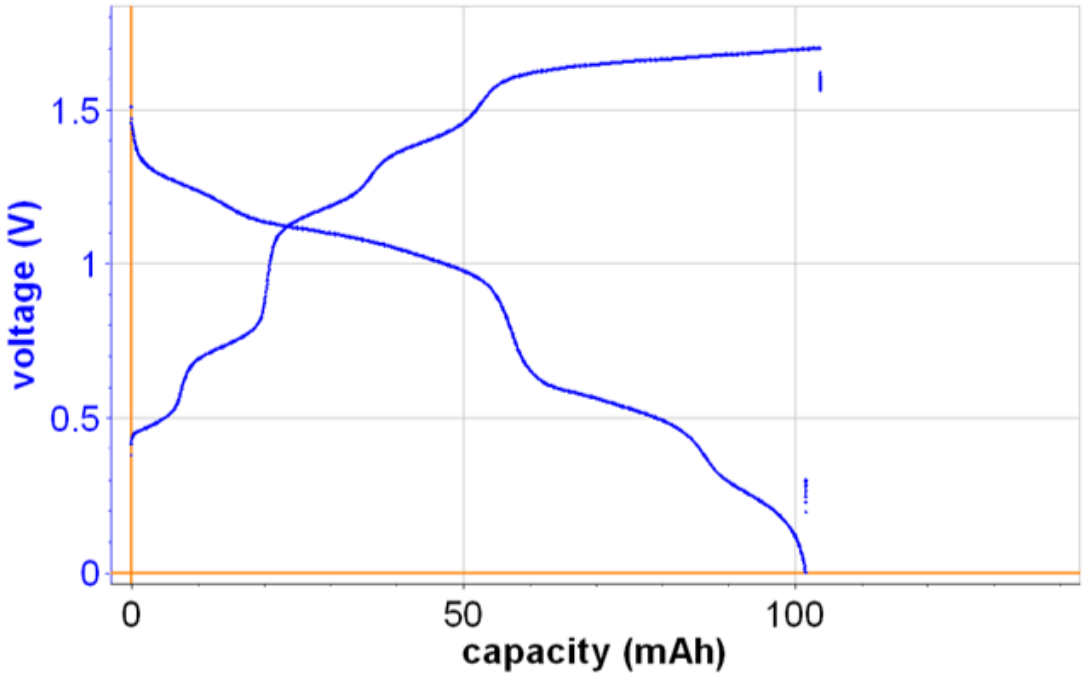

Figure 2.37: A voltage vs capacity plot for cycle 2 of the flow battery described in Table 2.15.

chemical behaviour of SiW_{12}. The catholyte solution is present in large excess. Since the behaviour of the ferricyanide/ferrocyanide system is described well by the Nernst equation, a large change in SOC would not result in the formation of additional plateaus or even a significant change in reduction potential. For example, if the SOC of the solution changed from 0.1 to 0.9 would result in a reduction potential increase of 113 mV:

$$\frac{RT}{nF} ln \left(\frac{0.9}{0.1} \div \frac{0.1}{0.9} \right) = 0.113 \text{ V} \tag{2.1}$$

A plateau width of 15.8 mAh corresponds well with a 1 F mol-1 reduction of SiW_{12}, so we can safely say that the first four plateaus are attributable to 1-electron reductions. The largest and final plateau has a width of 51 mAh (3.22 F mol-1), but does not represent the full extent of the plateau because the cut-off voltage was reached. At the end of cycle 2, the oxidation state of the anolyte is approximately SiW_{12}(-7). On discharge, the first plateau corresponds to (at least) a 1 electron oxidation, and the second plateau (15-56 mAh) may actually be two superimposed plateaus, as the gradient ($\frac{dV}{dQ}$) decreases slightly at 1.05 V. A similar phenomenon is observed on the third plateau (56-86 mAh) at 0.55 V. The effect is very subtle, but is clearly visible in the $\frac{dV}{dt}$ plot displayed in Figure 2.38.

On the charge cycle (first half), there is a clear plateau in the $\frac{dV}{dt}$ vs time plot at the begin-

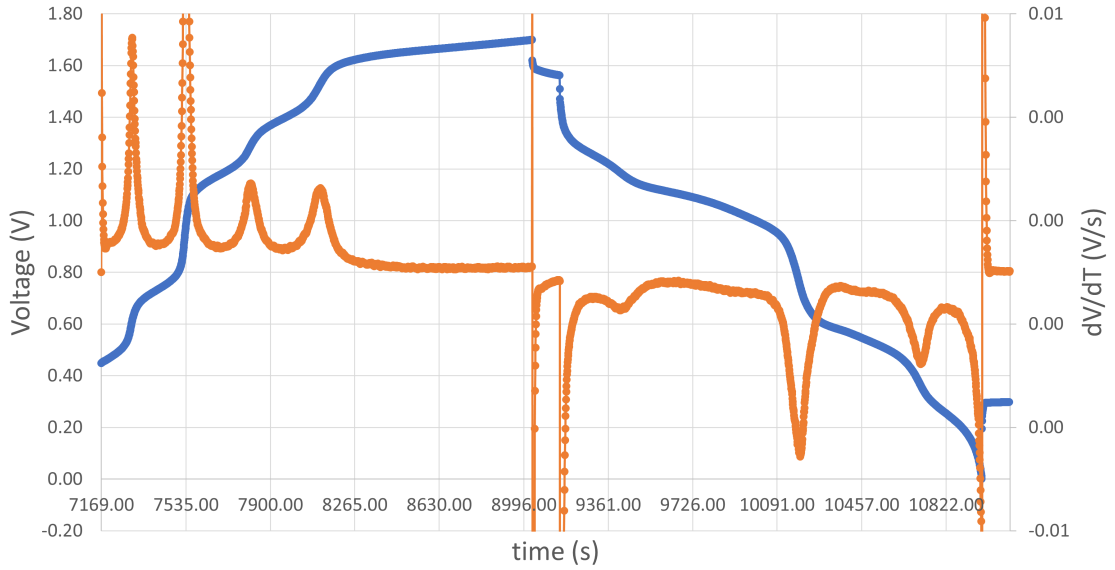

Figure 2.38: A voltage vs time (since the beginning of the experiment) plot of the second cycle (left axis), and a plot of $\frac{dV}{dt}$ vs time on the right axis. dV/dT was calculated based on a moving average of V over 10 seconds.

ning and end of each plateau. On discharge (second half), this is also true where the plateaus are obvious. However, as discussed, there is a clear change in gradient in the centre of the second and third plateaus. Therefore, it is proposed that the reoxidation reaction proceeds like so: $SiW_{12}(-7) \longrightarrow SiW_{12}(-6) \longrightarrow SiW_{12}(-4) \longrightarrow SiW_{12}(-3) \longrightarrow SiW_{12}(-2) \longrightarrow SiW_{12}(-1)$. Therefore, that the POM is acting as expected according to the findings displayed in Figure 2.28.

As can also be seen in Figure 2.28, there is a large plateau at -1200 mV vs SHE (at least 6 F mol^{-1}), where the reduction potential does not increase significantly. Therefore, on cycle 18, the upper voltage limit was increased to 1.8 V, and the charge capacity rose to 150 mAh, but the discharge capacity was significantly lower at 136 mAh. Taking into account that the anolyte oxidation state was approximately SiW_{12}(-0.5), and assuming no side reactions occurred at the beginning of the charging procedure, the oxidation state at the end of the procedure was approximately SiW_{12}(-10). However, the marked decrease in coulombic efficiency and the accompanying increase in capacity decay on subsequent cycles would suggest that the oxidation state is more likely $\sim SiW_{12}$(-9).

The maximum recorded discharge capacity is a 4.5-fold increase than reported previously for SiW_{12}.[2] Despite this, the capacity fades very quickly. In the previous section, it was shown that the coulombic efficiency in a 3-electrode bulk electrolysis cell was close to 100%.

However, in the RFB this value is much lower. One possible explanation for this is hydrogen evolution at the anode. The standard reduction potential of the ferricyanide/ferrocyanide couple is +0.3704 V vs SHE. Meaning that at the upper voltage cut-off of 1.8 V, the reduction potential of the anolyte is in the region of -1.4 V vs SHE. Even though the pH of the solution is likely relatively high at this point, it seems quite likely that there would be a significant driving force for hydrogen evolution at this potential.

On cycle 23, the current density was reduced to 4 mA cm^{-2}, causing the charge capacity to rise by 23 mAh, but the discharge capacity only rises by about 4 mAh. The capacity decay per cycle continued at approximately the same rate as before. Although the cycles now take twice as long to charge to the same capacity, indicating that the capacity loss is not due to calendar ageing of some kind, which would indicate that significant species crossover is not occurring. Because the upper cut-off voltage remained the same, the cell potential difference was higher for a more extended period. If hydrogen evolution does occur at high potentials, this will lead to a mismatch in the state of charge of the electrolytes. HER would manifest as a decrease in coulombic efficiency, as observed for cycle 23 and subsequent cycles.

After 31 cycles, the cell was disassembled. The membrane had become discoloured and had warped. The discolouration was worse around the edges of the cell (where there was no contact with the electrolyte). The separator also smelled distinctly of rotten meat. Usually, the smell comes from the decomposition of proteins into volatile amine species. Since the membrane is a polyamide, a similar process likely occurred throughout cycling. Despite somewhat promising initial results as a separator for the SiW_{12}/Ferrocyanide battery, the issues of crossover of species and the decomposition of the membrane while cycling meant investigations into this material as a separator were discontinued. However, it was at least demonstrated that a size exclusion membrane could be used successfully in a flow POM-based flow battery when the species are not in equilibrium with more minor (single metal) species. Further investigations into polyamide-based size-exclusion membranes could benefit from the addition of an anti-bacterial agent and assembly in a sterile environment. Alternatively, size-exclusion membranes composed of other polymers which are not susceptible to decomposition (such as ceramics) could also yield promising results.

The next and final RFB in this series with properties listed in Table 2.16 was assembled. This RFB is identical to that reported by Friedl et al. except that the starting pH of the anolyte was higher (originally 1.7, in this work, 3.98). The purpose of this experiment was to identify whether the increased concentration (80 mM vs 10 mM) would affect the electrochemical behaviour of the anolyte when reduced to oxidation states lower than SiW_{12}(-2).

The cell was cycled at 8 mA cm^{-2}, with cut-off voltages of 1.8 V and 0 V. On cycle 4,

Anode	Carbon felt (25 cm^2)
Cathode	Carbon felt (25 cm^2)
Anolyte	1 M LiCl, 35 mM H_3PO_4, 80 mM SiW_{12}, 60 mL, pH 3.98
Catholyte	1 M LiCl, 35 mM H_3PO_4, 80 mM PV_{14}, 60 mL, pH 2.35
Separator	Nafion 117

Table 2.16: The properties of two redox flow batteries which are equivalent except for the separator. i.e. one was assembled with an NFS membrane, and the other was assembled with Nafion 117.

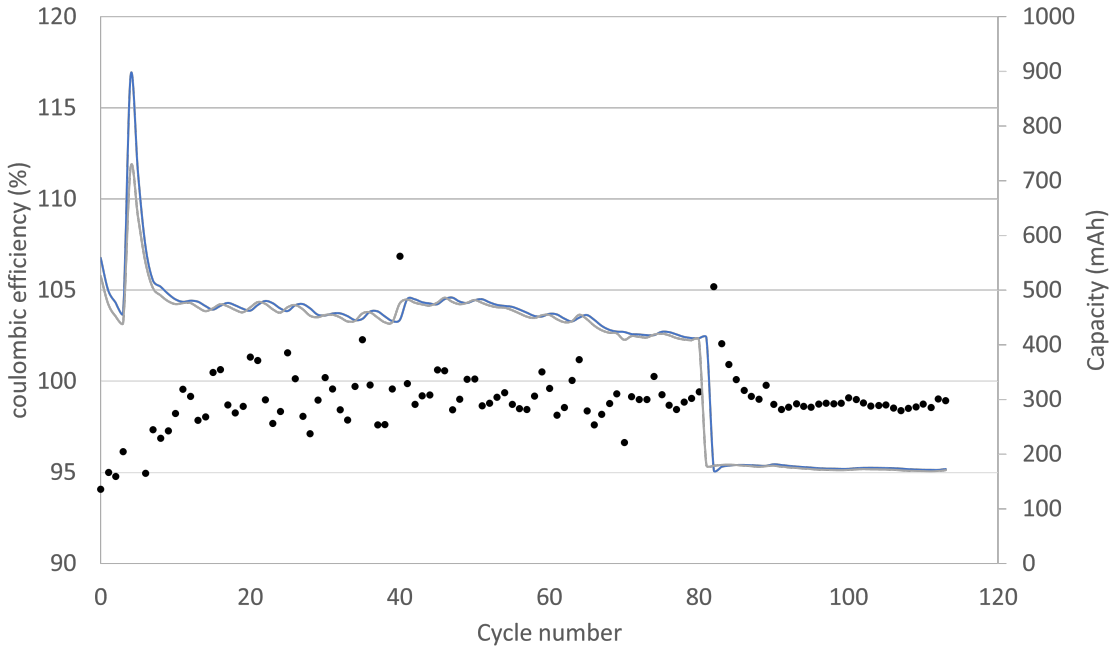

Figure 2.39: Coulombic efficiency, and capacity vs cycle number.

the discharge capacity was 1891 C, which corresponds to 4.67 F mol^{-1}. The capacity sharply decreased until cycle 10 and stabilised at $\sim$ 1700 C (470 mAh, 3.67 F mol^{-1}) until cycle 80. The capacity and coulombic efficiency vs cycle number plot is shown in Figure 2.39. A typical voltage vs capacity plot is shown in Figure 2.40.

The initial sharp decrease in capacity could not be explained; however, after cycle 10, the capacity decay was minimal, and the coulombic efficiency was comparable to that of cells described earlier in this series. Figure 2.40 shows that on charge, there are four plateaus present which roughly correspond to a 1 F mol^{-1} reduction of SiW_{12}. However, the final two are superimposed, making them difficult to identify. On discharge, there are also four plateaus present, the second of which is too short to account for a 1 F mol^{-1} oxidation of SiW_{12} or reduction of PV_{14}. However, the reduction potential of the catholyte solution is expected

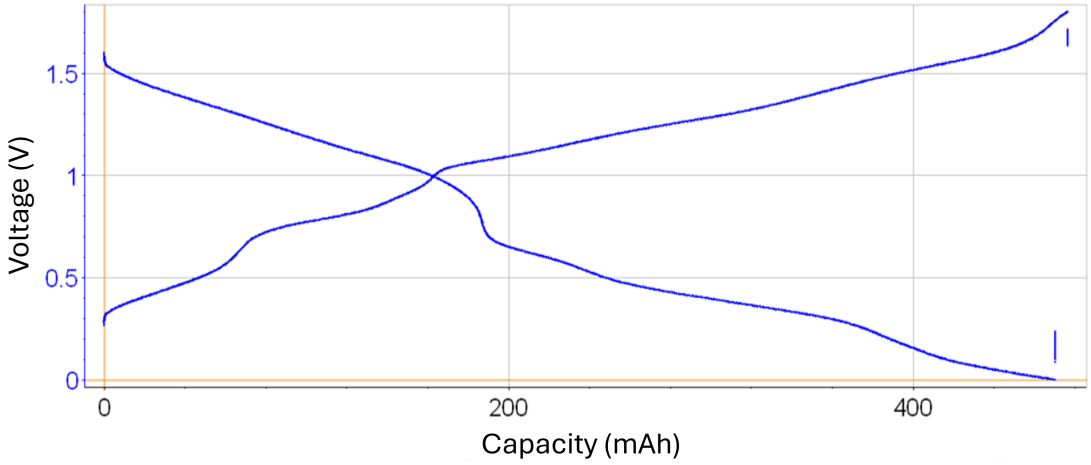

Figure 2.40: A typical voltage vs capacity plot for the cell described in table 2.16.

to change significantly in this setup and exhibit plateaus of its own. Hence, this is not entirely unexpected, and is likely caused by the superimposition of plateaus of the two different POM species. On cycle 82 the voltage cut-off was decreased to 1.4 V, and the accessible capacity dropped to 615 C (171 mAh, 1.3 F mol^{-1}), which is in line with expectations from the literature.

2.3.3 Stability of PV_{14} in aqueous solutions with respect to variations in counter cation, concentration, P:V ratio, temperature, and oxidation state over a four day period

During the investigation of redox flow batteries with PV_{14} as the catholyte, precipitation would occur and lead to the blockage of the flow battery, and an accompanying reduction in capacity (as previously shown in Figure 2.2). As discuseed at length by Selling et al., the vanadophosphate system is highly complex, and the stability of PV_{14} with respect to other species is dependent on many variables such as pH, P:V ratio, and temperature.[3] However, for use in a redox flow battery, the stability of PV_{14} with respect to these variables when the catholyte is in a reduced state is also of interest. In this section, an attempt is made to determine the effects of counter cation, temperature, P:V ratio, and reduction degree on the stability of PV_{14}.

The driving force for conducting this experiment was the precipitation of PV_{14} which ultimately led to failure of various different flow batteries. The cells in question are not reported here in detail because very little useful electrochemical data was produced. However,

Stability of PV14 after 14h in respective temperature

			Oxidation state	0			-2			-4			-6		
	P:V	c (mM)	Temperature (°C)	25	45	70	25	45	70	25	45	70	25	45	70
LiPV14	0.5	2.8		Y	Y	Y	Y	Y	Y	Y	Y	N	Y	Y	N
LiPV14	1	2.8		Y	Y	Y	N	N	N	Y	N	N	Y	N	N
LiPV14	1.68	2.8		Y	Y	Y	N	N	N	N	N	N	N	N	N
LiPV14	2	2.8		Y	Y	Y	N	N	N	N	N	N	N	N	N
LiPV14	3.38	2.8		Y	Y	Y	N	N	N	N	N	N	N	N	N
LiPV14	0.25	85		Y	Y	Y	Y	Y	N	Y	N	N	N	N	N
LiPV14	0.25	178		Y	Y	Y	Y	N	N	N	N	N	N	N	N
NaPV14	0.25	80		Y	Y	Y	Y	N	N	N	N	N	N	N	N

Stability of PV14 after 4 days in respective temperature

			Oxidation state	0			-2			-4			-6		
	P:V	c (mM)	Temperature (°C)	25	45	70	25	45	70	25	45	70	25	45	70
LiPV14	0.5	2.8		Y	Y	Y	Y	Y	Y	Y	Y	Y	Y	Y	NA
LiPV14	1	2.8		Y	Y	Y	Y	N	Y	Y	N	N	Y	N	N
LiPV14	1.68	2.8		Y	Y	Y	N	N	N	N	N	N	N	N	N
LiPV14	2	2.8		Y	Y	Y	N	N	N	N	N	N	N	N	N
LiPV14	3.38	2.8		Y	Y	Y	N	N	N	N	N	N	N	N	N
LiPV14	0.25	85		Y	Y	N	Y	Y	N	N	N	N	N	N	N
LiPV14	0.25	178		Y	Y	N	N	Y	N	N	N	N	N	N	N
NaPV14	0.25	80		Y	Y	N	N	N	N	N	N	N	N	N	N

Figure 2.41: PV_{14} solutions with varied cation, temperature, P:V ratio, temperature, and oxidation state. The colour-coded cells indicate whether precipitate was present under the given set of conditions. Green 'Y' indicates no solution is present. Yellow 'Y' indicates either very little precipitate is present or it is unclear. Red 'N' indicates a significant amount of precipitate is present.

PV_{14} would precipitate quite often and lead to the scenario depicted in Figure 2.2. This wasted valuable material and lead to a difficult and lengthy cleanup process. Therefore, the criteria for stability in this case is whether or not precipitate forms under a given set of conditions.

Figure 2.41, (which is first depicted in the experimental section of this chapter, and is replicated below) shows that the fully oxidised form of PV_{14} is stable under most of the conditions tested, but does precipitate when the POM is at high temperature and high concentration. This is in line with the findings of Selling et al.[3]

When the POM is reduced to any extent, precipitate forms in almost all of the conditions tested. This is true even of the 80 and 85 mM samples that were typically used in redox flow battery experiments. This is problematic because the reason for precipitation was not found, and only occurs some of the time i.e. the effect has not been reliably replicated so far. Powder

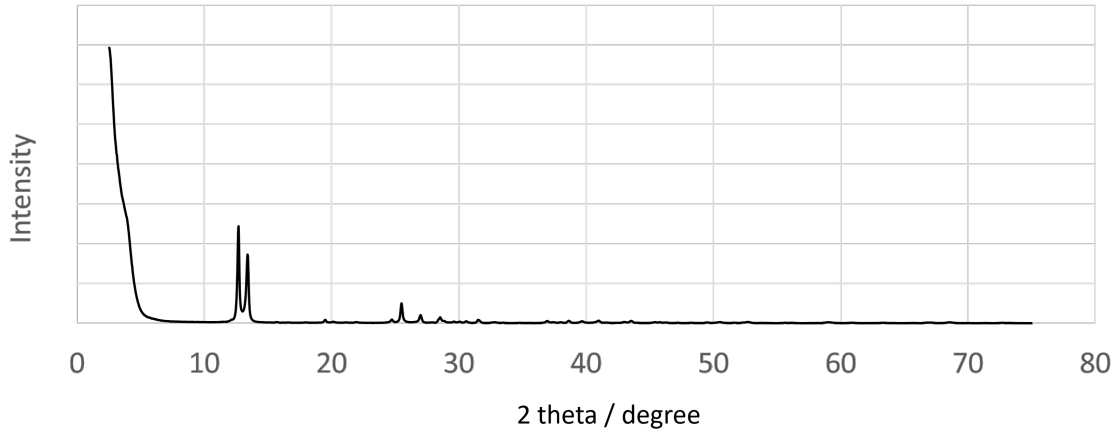

Figure 2.42: XRD patterns for the uncharacterised precipitate that appears on reduction of PV_{14}.

XRD and IR spectra were recorded on the green precipitate, as shown in Figure 2.42 and 2.43. Neither of the recorded spectra are similar to those reported in the literature, so it can be concluded at least that the green precipitate is no longer PV_{14}.[114, 115] The best guess as to why the precipitate forms, is due to some issue with the batches of lithium and sodium vanadate species provided to us, since the issue was not reported in the original investigation into PV_{14} as a RFB catholyte.

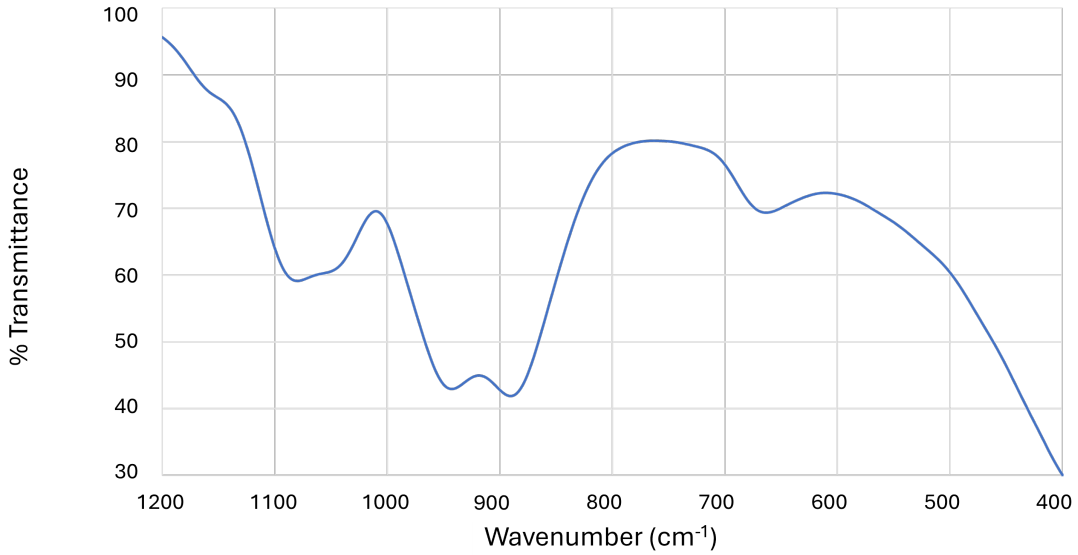

Figure 2.43: IR spectrum for the uncharacterised precipitate that appears on reduction of PV_{14}.

2.4 A capital cost calculator for redox flow batteries

The rationale behind building a universal calculator for RFB capital cost estimation was to ascertain whether it makes good sense from an economic perspective to upscale a specific RFB technology beyond single-cell studies.

Investigating active species, which are expensive, but otherwise have desirable characteristics, is essential for developing a sound understanding of a group of compounds like POMs. This is clearly evident when one considers that almost all POM batteries demonstrated to date feature tungsten-containing POMs. This is not because the research community believes these active species could be used in batteries in an economically competitive way, but because POMs which contain a lot of tungsten are particularly accessible in a number of ways. They are widely available from chemical manufacturers, are generally easy to synthesise and are generally more chemically stable than other species.

The electrochemistry of tungsten-containing Keggin POMs is also very easy to study, as they tend to be stable over a wide potential range, and undergo electrochemical oxidation and reduction at potentials which are well spaced out, and exhibit a large degree of electrochemical reversibility.

The systems which have been studied to date are therefore intended to investigate whether POMs; as a group of chemical compounds, are suitable for use in redox flow batteries in terms

of their chemical and electrochemical properties.

It is widely understood that new and less expensive POMs must be synthesised and characterised for the field to progress. For instance, POMs, which are primarily made from iron, manganese, and aluminium oxides, are of significant interest, as these materials are incredibly cheap and readily available in vast quantities.[94, 116, 117]

It makes logical sense that POMs composed of other elements have similar properties to those already studied because the most commonly used POMs contain (for example) tungsten, vanadium, molybdenum, and manganese all exhibit relatively similar properties. This is because it is the structure of POMs, as well as the nature of any particular metal, which gives rise to the electrochemical properties.

We can therefore infer an approximate capital cost of POM batteries composed of different elements based on the properties of those which are already characterised.

Obviously, the validity of any claims hinges on whether or not POMs composed primarily of cheap metals (e.g. iron) can be synthesised and stabilised. However, given the plethora of uses for POMs in other chemical industries, there is a significant and ongoing research effort to discover new species. Consequently, it seems likely that progress will occur in this direction.[91, 93, 94, 118–120]

2.4.1 Description of calculations

A program was developed in MATLAB which is able to calculate the initial costs of redox flow batteries based on physical and chemical parameters that the user defines via a graphical user interface. The primary equations utilised by the program use specified values of power, discharge time, and the number of cells, as well as the parameters mentioned above to calculate:

- Volumes and total cost of
  - Anolyte
  - Catholyte
  - Various supporting electrolytes
- Area and total cost of
  - Electrodes
  - Membrane

- Cost of other materials
- Total capital cost
- Unit capital cost

The default parameters in the GUI (Figure 2.44) are based on an 'All vanadium RFB' case. However, the user can change parameters as needed.

The paramaters for the model are listed in Table 2.17.

Calculation of Volume and total cost of electrolytes

The volume and cost of anolyte are calculated using the following equations:

$$V_a = \frac{E}{n_a c_a F \Delta U \eta (\Delta SOC)} \tag{2.2}$$

$$cost_{a\,total} = V_a c_a M_{r_a}\, cost_{unit\,a} \tag{2.3}$$

The costs of supporting electrolytes are calculated based on their molar ratio to the redox species (anolyte or catholyte as appropriate), their relative mass, and unit cost. The program can calculate the costs of up to three supporting electrolytes per redox species. Supporting electrolyte example equation (cost of anolyte support 1):

$$cost_{c\,total} = V_a c_a M_{r_a}\, cost_{unit\,c} \tag{2.4}$$

The calculation is repeated for the volume of catholyte:

$$V_c = \frac{E}{n_c c_c F \Delta U \eta (\Delta SOC)} \tag{2.5}$$

$$cost_{c\,total} = V_a c_a M_{r_a}\, cost_{unit\,c} \tag{2.6}$$

The cost of supporting electrolytes for the catholyte is calculated in a similar manner:

$$cost_{ES_{a1}} = c_{ESa1} * V_a * cost_{ESa1} * M_r \tag{2.7}$$

Calculation of area and cost of cell electrodes and membrane

The area of the anolyte half cells is calculated by:

V_a	volume of anolyte (m^3)
E	energy (J)
n_a	electrons transferred per mole of anolyte
c_a	concentration of anolyte (mol m^{-3})
F	Faradays constant (C mol^{-1})
ΔU	average discharge voltage (V)
η	efficiency of cell
ΔSOC	change in state of charge
$cost_a$	capital cost of anolyte ($)
M_{r_a}	molecular mass of anolyte (kg mol^{-1})
$cost_a$	unit cost of anolyte ($ kg^{-1})
n_a	electrons transferred per mole of catholyte
c_a	concentration of catholyte (mol m^{-3})
$cost_c$	capital cost of anolyte ($)
Mr_c	molecular mass of anolyte (kg mol^{-1})
$cost_c$	unit cost of anolyte ($ kg^{-1})
$cost_{ES_{a1}}$	capital cost of anolyte supporting electrolyte ($)
$c_{ES_{a1}}$	concentration of electrolyte (mol m^{-3})
V_a	volume of anolyte (m^3)
$cost_{ES_{a1}}$	unit cost of electrolyte (mol m^{-3})
M_r	molar mass (kg mol^{-1})
A_a	area of all anolyte half cells (m^2)
P	power (W)
ΔU	average discharge voltage (V)
k^0	electron transfer constant (m s^{-1})
η	efficiency of cell
F	Faraday constant (C mol^{-1})
c_a	concentration of anolyte (mol m^{-3})
θ	electrode roughness
n_a	electrons transferred per mole of anolyte
N_c	number of cells
A_{cell}	total area of the cell
C_{cost_E}	total cost of electrode ($)
$Cost_f$	unit cost of felt ($ m^{-2})
$Cost_m$	unit cost of mesh ($ m^{-2})
$Cost_M$	total cost of membrane ($)
$Cost_{mem}$	unit cost of membrane ($ m^{-2})

Table 2.17: Table of parameters and associated symbols

$$A_a \;=\; \frac{P}{\Delta U k^0 \eta F c \theta n N} \tag{2.8}$$

$$A_{cell} = A_a \;+\; A_c \tag{2.9}$$

Where A_c is simply a repetition of equation 2.8 for the anolyte half cell.

The voltage efficiency (ηV) is based on the relationship:

$$\eta_V \;=\; \frac{\Delta U \;-\; IR}{\Delta U \;+\; IR} \tag{2.10}$$

Which is valid only at low overpotential but is a good first approximation for the purposes of estimating capital cost.

The total resistance (R) is the cumulative value of the charge transfer resistance (R_{CT}), the membrane resistance (R_{mem}), and the contact resistance (R_{con}) of the electrodes:

$$R \;= R_{CT} \;+\; R_{mem} \;+\; R_{con} \tag{2.11}$$

The charge transfer resistance is also calculated based on the relationship at low overpotential:

$$R_{CT} = \frac{R_g T}{n^2 F^2 A k^0 c_0 \theta} \tag{2.12}$$

The membrane and contact resistance are calculated based on area-specific resistances found in the literature:

$$R_{mem} \;=\; \frac{R^0_{mem}}{A} \tag{2.13}$$

$$R_{con} \;=\; \frac{R^0_{con}}{A} \tag{2.14}$$

Rearranging equation 2.10 for R yields equation 2.15

$$R \;=\; \frac{\Delta U(1 \;-\; \eta V)}{I(1 \;+\; \eta V)} \tag{2.15}$$

Equation 2.15 can then be rearranged and expanded to calculate the total area required for a given discharge requirement (which is specified by the user).

$$A = \frac{\Delta U(1 - \eta V)}{I(1 + \eta V)} * \left(2\frac{R_g T}{n^2 F^2 k^0 c_0 \theta} + R^0_{mem} + 2R^0_{con}\right) \tag{2.16}$$

Equation 2.16 allows the user to control all parameters that influence the area of the stack.

The electrode properties of each cell are assumed to be equal. Since there are two half cells, the electrode area is 2A.

The total electrode cost is given by:

$$cost_E = 2A(cost_m + cost_f) \tag{2.17}$$

The cost of the membrane is analogously given by:

$$cost_M = A * cost_{mem} \tag{2.18}$$

The area for both the anolyte and catholyte half cells are calculated independently based on their respective chemical properties (n, c etc.). If one calculation yields a larger result than the other, then the larger value is taken to be the value of A since both electrodes must be the same size.

For the same reason, it is assumed that the user will input the lower of the two-electron transfer constants if the anolyte and catholyte species are chemically different.

Limitations of the capital cost calculator

At first glance, it is easy to identify several issues with the capital cost calculator.

Equations 2.2 and 2.5 can not accurately represent the volume needed to satisfy a particular E for active species which have two or more redox centres with different standard redox electrochemical potentials. In this scenario, the meaning of ΔSOC can also become ambiguous.

Equations 2.16 and 2.9 are also problematic for a number of reasons. The value of k^0 is only taken from one active species (always the lowest value). If the values of rate constants for each active species are sufficiently different, then the charge transfer resistance contribution can be overestimated. Moreover, θ is an arbitrary fudge factor intended to account for the large surface area of carbon felt and carbon mesh electrodes. It assumes that all areas of the electrode are utilised equally and that the electrochemical kinetics are equivalent across all surfaces, which is almost certainly not the case for a real system.

Equations 2.18 and 2.12 would indicate that there is a linear relationship between the resistance due to charge transfer, which is only accurate at low overpotentials. Moreover,

no consideration is given to the effects of mass transport and active species depletion at the electrode surface.

The behaviour of membranes is also oversimplified. Equation 2.13 would suggest that the resistance that arises from a separator is purely ohmic, but this is most certainly not the case.

Therefore, the capital cost calculator can only be used to indicate whether a given redox flow battery can be competitive. For instance, the target unit cost for energy storage devices is in the region of 100 USD kWh^{-1}, so if the calculator estimates a given RFB configuration unit capital cost to be 10,000 USD kWh^{-1}, then it is likely not worth pursuing.

The calculator can also be used to indicate whether or not a specific line of research is worthwhile. For instance, if 90% of the RFB resistance comes from charge transfer, then there is little point in looking for materials with lower contact resistance.

Moreover, the calculation for materials cost is quite basic and assumes a similar architecture for a range of active species, which is certainly not realistic. However, this is very difficult to quantify for individual systems due to the limited availability of examples in the literature.

Even with the above limitations, the calculator still gives good results that broadly agree with the comparative calculators available in the literature.[121–124]

2.4.2 Comparison of the calculated capital cost of various redox flow battery chemistries

A comparison of various redox flow battery chemistries was conducted using data from the literature. Details of the input parameters for the various batteries are listed in tables 2.18-2.22.

Comments on specifications and parameters of the iron-chromium redox flow battery

Most of the work conducted on Fe-Cr RFBs was done in the 1980s by NASA. Copies of the original reports have been published online. However, there appear to be several instances in which reports have not been uploaded, and there is no central point of access to works relating to their RFB studies. For this reason, and since the research is over 30 years old, certain specifications for the RFB have not been found.

NASA reports that using a cation exchange membrane results in an additional OCV loss of 50-70 mV due to significant mass transport across the membrane. Since the program does not account for mass transport effects, the discharge potential is set to 1.12 V to compensate. This can be justified because if η_v = 100% were to be achieved, the maximum voltage would

Specifications	
Power output	1 MW
Discharge time	12 h
Number of cells	10
Physical paramaters	
Average potential difference (ΔV)	1.12 [125]
System efficiency	0.9
Voltage efficiency	0.8
SOC_{max}	0.953 [125]
SOC_{min}	0.047 [125]
Electron transfer constant	$4.7 * 10^{-5}$ cm s^{-1}[60]
Electrode roughness	150
Membrane specific resistance	0.8 Ω cm^2[60]
Electrode contact resistance	0.5 Ω cm^2[60]
Chemical paramaters	
Anolyte concentration	1 M
Anolyte supporting concentration	2 M HCl
Catholyte concentration	1 M
Catholyte supporting concentration	2 M HCl
Electrons transferred from anolyte per molecule	1
Electrons transferred from catholyte per molecule	1
Molecular mass of anolyte	107.8 g mol^{-1}
Molecular mass of supporting anolyte species	36.46 g mol^{-1}
Molecular mass of catholyte	107.8 g mol^{-1}
Molecular mass of supporting catholyte species	36.46 g mol^{-1}
Unit costs	
Anolyte	1.55 USD kg^{-1}
Anolyte supporting species	0.6 USD kg^{-1}
Catholyte	1.55 USD kg^{-1}
Catholyte supporting species	0.6 USD kg^{-1}
Membrane	500 USD m^{-2}
Carbon felt	70 USD m^{-2}
Carbon mesh	48 USD m^{-2}

Table 2.18: Input parameters for calculating capital cost of the iron-chromium redox flow battery developed by NASA.[125]

Specifications	
Power output	1 MW
Discharge time	12 h
Number of cells	10
Physical paramaters	
Average potential difference (ΔV)	1.40
System efficiency	0.9
Voltage efficiency	0.8
SOC_{max}	0.8
SOC_{min}	0.1
Electron transfer constant	$1.7 * 10^{-6}$ cm $s^{-}1$
Electrode roughness	150
Membrane specific resistance	2.5 Ω cm^2
Electrode contact resistance	0.5 Ω cm^2
Chemical paramaters	
Anolyte concentration	1.6 M
Anolyte supporting concentration	5 M H_2SO_4
Catholyte concentration	1.6 M
Catholyte supporting concentration	5 M H_2SO_4
Electrons transferred from anolyte per molecule	1
Electrons transferred from catholyte per molecule	1
Molecular mass of anolyte	181.88 g mol^{-1}
Molecular mass of supporting anolyte species	98.08 g mol^{-1}
Molecular mass of catholyte	181.88 g mol^{-1}
Molecular mass of supporting catholyte species	98.08 g mol^{-1}
Unit costs	
Anolyte	21 USD kg^{-1}
Anolyte supporting species	0.25 USD kg^{-1}
Catholyte	21 USD kg^{-1}
Catholyte supporting species	0.25 USD kg^{-1}
Membrane	500 USD m^{-2}
Carbon felt	70 USD m^{-2}
Carbon mesh	48 USD m^{-2}

Table 2.19: Input parameters for calculating capital cost of the vanadium redox flow battery, described by various sources. [59, 60, 89, 126–129]

Specifications	
Power output	1 MW
Discharge time	12 h
Number of cells	10
Physical paramaters	
Average potential difference (ΔV)	0.853
System efficiency	0.9
Voltage efficiency	0.8
SOC_{max}	0.5
SOC_{min}	0.05
Electron transfer constant	$7.2 * 10^{-3}$ cm s^{-}1
Electrode roughness	150
Membrane specific resistance	2.5 Ω cm^2
Electrode contact resistance	0.5 Ω cm^2
Chemical paramaters	
Anolyte concentration	1 M
Anolyte supporting concentration	1 M H_2SO_4
Catholyte concentration	0.5 M
Catholyte supporting concentration	3 M HBr
Electrons transferred from anolyte per molecule	2
Electrons transferred from catholyte per molecule	2
Molecular mass of anolyte	208.21 g mol^{-1}
Molecular mass of supporting anolyte species	98.08 g mol^{-1}
Molecular mass of catholyte	159.8 g mol^{-1}
Molecular mass of supporting catholyte species	79.90 g mol^{-1}
Unit costs	
Anolyte	10.27 USD kg^{-1}
Anolyte supporting species	0.2 USD kg^{-1}
Catholyte	4.5 USD kg^{-1}
Catholyte supporting species	2.25 USD kg^{-1}
Membrane	500 USD m^{-2}
Carbon felt	70 USD m^{-2}
Carbon mesh	48 USD m^{-2}

Table 2.20: Input parameters for calculating capital cost of the AQDS-Br redox flow battery developed by Huskinson et al.[130]

Specifications	
Power output	1 MW
Discharge time	12 h
Number of cells	10
Physical paramaters	
Average potential difference (ΔV)	0.75
System efficiency	0.9
Voltage efficiency	0.8
SOC_{max}	0.95
SOC_{min}	0.05
Electron transfer constant	0.01 cm $s^{-}1$
Electrode roughness	150
Membrane specific resistance	1.4 Ω cm^2
Electrode contact resistance	1.4 Ω cm^2
Chemical paramaters	
Anolyte concentration	0.08 M
Anolyte supporting concentration	1 M NaCl
Catholyte concentration	0.08 M
Catholyte supporting concentration	1 M NaCl
Electrons transferred from anolyte per molecule	4
Electrons transferred from catholyte per molecule	4
Molecular mass of anolyte	1822 g mol^{-1}
Molecular mass of supporting anolyte species	58.44 g mol^{-1}
Molecular mass of catholyte	1416 g mol^{-1}
Molecular mass of supporting catholyte species	58.44 g mol^{-1}
Unit costs	
Anolyte	18.24 USD kg^{-1}
Anolyte supporting species	0 USD kg^{-1}
Catholyte	21.7 USD kg^{-1}
Catholyte supporting species	0 USD kg^{-1}
Membrane	500 USD m^{-2}
Carbon felt	70 USD m^{-2}
Carbon mesh	48 USD m^{-2}

Table 2.21: Predicted capital cost of the PMo_{12}/PV_{14} cell described in an earlier section.

Specifications	
Power output	1 MW
Discharge time	12 h
Number of cells	10
Physical paramaters	
Average potential difference (ΔV)	1.3
System efficiency	0.9
Voltage efficiency	0.8
SOC_{max}	0.95
SOC_{min}	0.05
Electron transfer constant	0.01 cm s^{-}1
Electrode roughness	150
Membrane specific resistance	1.4 Ω cm^2
Electrode contact resistance	1.4 Ω cm^2
Chemical paramaters	
Anolyte concentration	0.01 M
Anolyte supporting concentration	1 M NaCl
Catholyte concentration	0.01 M
Catholyte supporting concentration	1 M NaCl
Electrons transferred from anolyte per molecule	9
Electrons transferred from catholyte per molecule	1
Molecular mass of anolyte	2874 g mol^{-1}
Molecular mass of supporting anolyte species	58.44 g mol^{-1}
Molecular mass of catholyte	1416 g mol^{-1}
Molecular mass of supporting catholyte species	58.44 g mol^{-1}
Unit costs	
Anolyte	18.24 USD kg^{-1}
Anolyte supporting species	0 USD kg^{-1}
Catholyte	21.7 USD kg^{-1}
Catholyte supporting species	0 USD kg^{-1}
Membrane	500 USD m^{-2}
Carbon felt	70 USD m^{-2}
Carbon mesh	48 USD m^{-2}

Table 2.22: Predicted capital cost of the SiW_{12}/Ferrocyanide cell described in an earlier section.

still be significantly smaller than that predicted by the Nernst equation due to the crossover of ions.

The unit price of the cation exchange membranes was not cited in the literature, so the unit cost of membrane materials is assumed to be consistent with other redox flow batteries. This provides a fairer comparison and is in line with the cost of the most well-known cation exchange membrane, Nafion. Because of low membrane resistivity and high standard rate constant, the Fe-Cr RFB requires a relatively smaller stack area relative to the VRFB, so the contribution of the stack to the capital cost is less significant.

A cell with membrane resistivity of 0.8 Ω cm^2 could be operated normally between 4.7-95.3% SOC.[125] Specific details such as unit cost and composition of these membranes were not accessible online in most cases. However, the ML-21 membrane was reported to be a low-selectivity cation exchange membrane constructed from radiation-grafted polyethene.[131] The cost and method of preparation were not reported. The membrane resistivity of ML-21 is used in the following calculations, and the unit cost is assumed to be 500 USD m^{-2}.

The cell must be operated at a temperature of 65 ^{o}C to prevent the formation of chromium species which are redox inactive and therefore reduce the reaction rate at the chromium electrode.

Additionally, a bismuth catalyst is required to speed up electron transfer at the chromium electrode. The catalyst functions most effectively when the electrode is covered by at least 35 μg cm^{-2} bismuth metal – increasing the coverage beyond this amount has no appreciable effect on reaction kinetics.[125] Due to the periodic mixing of electrolytes for rebalancing, it is necessary to have a bismuth concentration that is at least sufficiently high enough to coat two electrodes. As the cost of bismuth is relatively low, this does not contribute significantly to capital cost.

Chromite ore (FeCr2O4) is the most abundant source of chromium, which also conveniently contains iron. Ferrochromium is manufactured from chromite ore and costs around 1.03 USD kg^{-1}. The relative mass of anolyte and catholyte redox species is calculated from the combined mass of iron and chromium, as this is representative of the raw material used (ferrochromium). Since the amount of chromium in ferrochromium (FeCr) can differ between 50-70%, it is assumed that Fe and Cr are present in roughly equal molar concentrations. Ferrochromium must be chlorinated to generate the soluble redox active species. A further 50% of the basic unit cost is added to represent these costs, giving an updated unit cost of 1.55 USD kg$^-$1

In addition to the parameters mentioned in Table 2.18, the capital cost of bismuth catalyst is taken into account and is calculated by:

$$Bismuth\ cost\ =\ \theta A * cost_{cat} \tag{2.19}$$

$cost_{cat}$: unit cost of catalyst USD kg^{-1} The cost of bismuth is quite low, according to the USGS mineral commodity summaries (2017), the price of bismuth was roughly 4.95 USD kg^{-1} in 2018. Consequently, the cost of bismuth accounts for $\leq$1% of the overall capital cost.[132]

Comments on specifications and parameters of the vanadium redox flow battery

Determining reasonable parameters for the Fe-Cr RFB was relatively straightforward. NASA made a concerted effort over many years to research and develop the prototype to build a pilot plant and subsequently use it for utility-scale energy storage. In fact, in the concluding remarks of NASA's final report, they state that "the redox system is now considered to be ready for scale up to a size adequate to evaluate its true potential for the commercial market for energy storage". In 1984 the technology was transferred to Standard Oil of Ohio (SOHIO) with the understanding that they would continue the development of the project. BP fully acquired SOHIO in 1987. Since then, the published literature on the Fe-Cr RFB has been sparse.

Conversely, the available literature on the vanadium RFB is vast and largely uncoordinated. The research from public institutions primarily focuses on single aspects of the RFB, such as determining the charge transfer kinetics at porous electrodes, quantifying the hydrogen evolution at the anode, and reporting on the performance of novel electrode materials. [74, 129, 133–139] The downside of this is that there seems to be little concerted effort towards development and no standardisation between research groups. It was impossible to find a single project that provided all of the input details needed for the model, so the values were taken from various sources.

Comments on specifications and parameters of the organic AQDS/HBr redox flow battery

9,10-anthraquinone-2,7-disulphonic acid (AQDS) is produced by a double electrophilic-aromatic-substitution reaction of anthraquinone – a naturally occurring and easily synthesised compound which is quite cheap ($3 - 5$ USD kg^{-1}). Assuming the synthetic route presented by Huskinson et al. is used, the central ring acts as a meta-director for the two outer rings.[68] Since there is a mirror plane which intersects all three aromatic rings, substitution is equally likely to occur on either meta position of each ring, this leads to a mixture of products as seen in Figure 2.45. These chemicals have similar chemical and physical properties and are

difficult to separate. The researchers recorded cyclic voltammograms on the mixture of compounds and found that they exhibited similar electrochemical activity to the purified AQDS. The percentage composition of the mixture is 37% AQDS (B), 60% 9,10-anthraquinone-2,6-disulphonic acid (C) and 3% 9,10-anthraquinone-2-sulphonic acid (A).

However, no charge/discharge cycling tests were conducted on the mixture of products so it is unclear whether the mixture is suitable for repeated cycling.

Considering that at best, 37% of anthraquinone is converted to AQDS, and neglecting the price of sulfonation (sulphuric acid costs around 0.2 USD kg^{-1}), the basic cost of producing AQDS is 10.27USD kg^{-1}. Note that, since the cost of sulphuric acid is negligible, the relative mass of the anolyte species is based on anthraquinone alone. The half-cell using 1 M AQDS + 1 M H2SO4 discharges over a voltage range of 0.7-0.3 V. However, the standard cell potential difference is 853 mV.

The researchers also report the cyclic voltammograms for a closely related species (DHAQDS) with a lower standard potential. The authors claim that the synthesis of hydroxyl-substituted anthraquinones is easily achieved and cheap, which is true. However, the synthesis of DHAQDS is more complex than that of AQDS, and the oxidation step will undoubtedly significantly impact cost due to the formation of several isomeric compounds. The reduced yield that arises from this multi-step synthetic route must be considered.

HBr is industrially produced by reacting hydrogen and bromine at high temperatures. The cell contains 3 M HBr, if 2 moles of HBr are produced for every mole of Br_2, and discounting the cost of hydrogen gas, and production costs, the basic cost of HBr is half that of Br_2 2.25 USD kg^{-1}.

Comments on specifications and parameters of the POM-based redox flow batteries

The parameters used to calculate the capital cost for POM RFBs are based mainly on this chapter's findings and previous papers on the SiW_{12}/PV_{14} system. For instance, in a 2019 paper, the normalised ohmic resistance of a large (1400^{-2} cell was found to be 2.8 Ω.[2] However, the ohmic resistance is a lumped value of the electrode contact resistance and the ohmic resistance due to the membrane. Therefore, for the purpose of capital cost calculations, the value is split evenly across contact and membrane resistivity.

The cost of PV_{14} is assumed to be 14 times the cost of the same quantity of vanadium electrolyte in the VRFB described in Table 2.19. The costs of SiW_{12} and PMo_{12} are calculated based on the cost of tungsten and molybdenum given in Table 2.1. Synthesising the POMs would undoubtedly add cost to this estimation. However, given that the synthetic procedures

for all materials involved are “one-pot”, the additional cost is expected to be small.

The cost of Ferricyanide is based on the current price from several vendors and is broadly in line with the price of the Fe-Cr electrolytes.[140–142]

The average potential difference of the PMo_{12}/PV_{14} battery is set to 0.75 V. For the SiW_{12}/Ferrocyanide battery, it is set to 1.3 V. These values should be treated with caution for multiple reasons. In the experiments listed above, no practical lower voltage limit was established. Also, since POMs have multiple redox couples utilised throughout cycling, the capital cost calculator described here cannot accurately indicate the energy stored in a POM-RFB. As it turns out, a description of species with multiple redox couples is somewhat complex. This topic is dealt with in chapter 3, but is beyond the scope of the capital cost calculator described here. With that in mind, it is felt that the calculator can still give a very rough estimation of the cost of the various system components.

Results of the capital cost calculation and discussion

A breakdown of the contribution of each system component (electrodes, membrane, anolyte, catholyte, materials, electrolyte support, and catalyst), as well as tabulated data on the unit capital cost, are displayed in Figure 2.46

Perhaps unsurprisingly, the Fe-Cr RFB is the cheapest by a significant margin, and the electrolytes make up a tiny portion of the overall system cost (6%). It seems likely that this kind of flow battery is well suited to high energy capacity, long duration storage. The meagre cost of electrolytes means that (for instance) a doubling in energy capacity would only lead to a 6-10% increase in the total cost and offer a significant reduction in unit capital cost.

The primary cost of the battery is associated with the membrane (41%). However, this is based on the price of a Nafion cation exchange membrane. Since the electrolytes used in this RFB are symmetrical, research into the use of size exclusion membranes could lead to a significant cost reduction, albeit at the expense of reversible electrolyte crossover and diminished energy efficiency.

The major cost associated with the VRFB is the anolyte and catholyte (76%). Similar to the Fe-Cr RFB, the VRFB could potentially reduce capital costs by using a size exclusion membrane. However, since the membrane only makes up a small portion (11%) of the overall cost, the potential savings are quite low. Instead, the VRFB might be more suited to applications where the energy(kWh): power(kW) ratio (which in this case is 12) is much lower. Where the VRFB is already deployed, the energy: power ratio is typically 2.5-4, which indicates that the VRFB is more suited to peaking applications. [81, 143]

The AQDS-HBr battery electrolytes also account for a high fraction of the overall capital cost (62%), and this is the only RFB with a significant cost associated with the supporting electrolyte (5%). So, overall, the electrolyte cost comes to 67%. Since the electrolytes are asymmetrical, crossover is a big issue which must be minimised as much as possible for viable long-term operation. As mentioned in the comments section above, the synthetic procedure for AQDS has a fairly low yield. Cost reductions could potentially be achieved by finding higher-yield synthetic routes, or in this particular case, by using the mixture of species produced as the electrolyte, provided that the electrochemical properties of species A, B, and C are similar. This could reduce the cost of the anolyte by as much as 60%.

The cost breakdown of the PMo_{12}/PV_{14} battery is similar to that of the all-vanadium cell, but the unit capital cost is about three times higher. The cost of anolyte and catholyte are 39% and 36%, respectively, which is attributed to the Mo and V centres in the POM being underutilised. Only four electrons are transferred per POM species. Cost savings could be achieved by utilising the metal centres more effectively, which would require the POMs to be reduced to a much larger degree. This was achieved in section 2.3.2 by altering the supporting electrolyte and pH. A similar investigation into PMo_{12} and PV_{14} may lead to a larger accessible capacity.

The anolyte dominates the cost of the SiW_{12}/Ferricyanide battery, which accounts for 87% of the total cost. As discussed, even if the accessible capacity of SiW_{12} is increased significantly, the cost of tungsten and the high molecular weight of the POM means that this species will almost certainly always contribute a significant amount to the overall cost of an RFB system.

The breakdown of costs for both POM systems indicates that research into POM-RFBs should focus on POMs primarily composed of cheap and widely available elements.

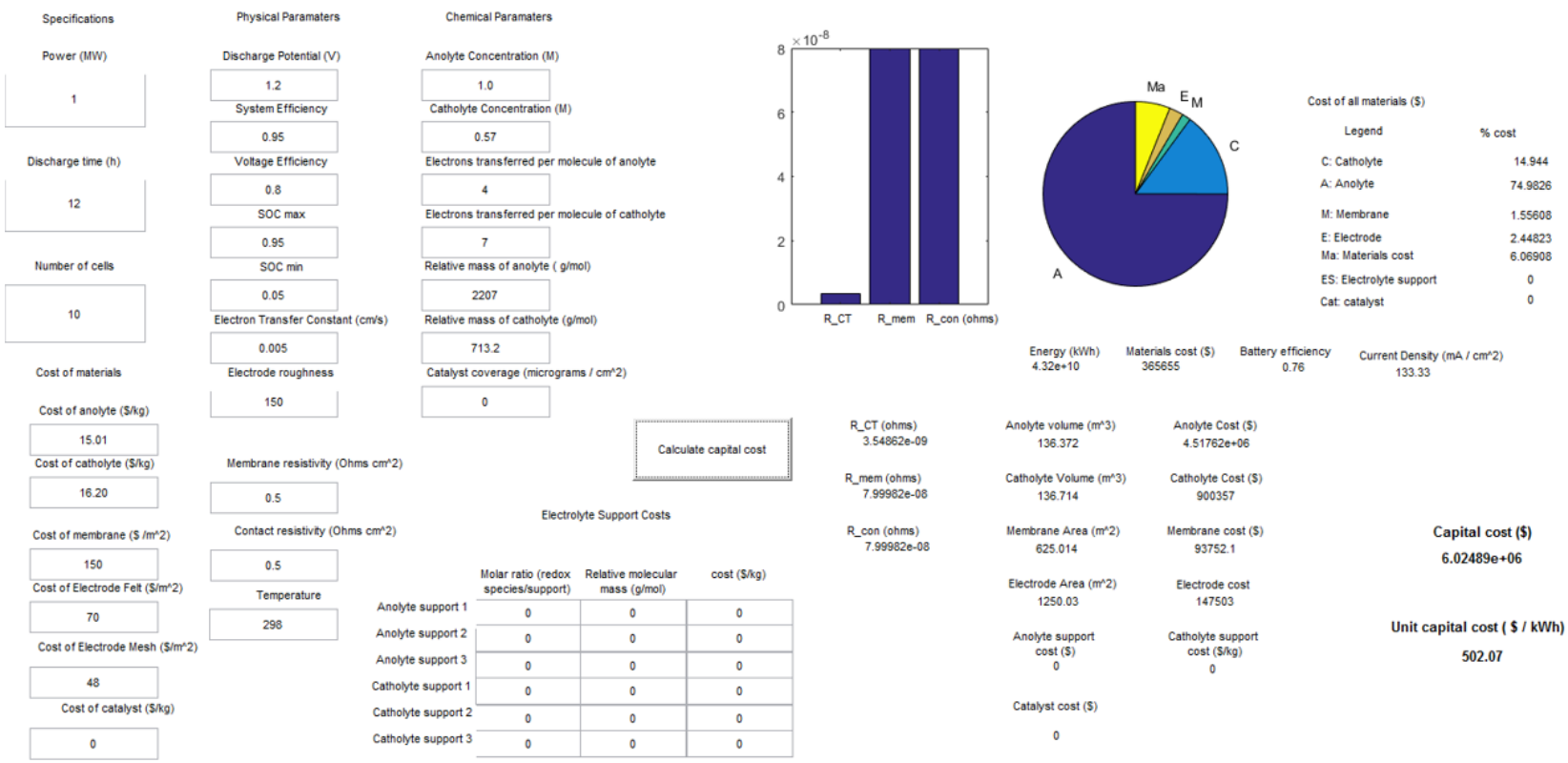

Figure 2.44: GUI of the capital cost calculator.

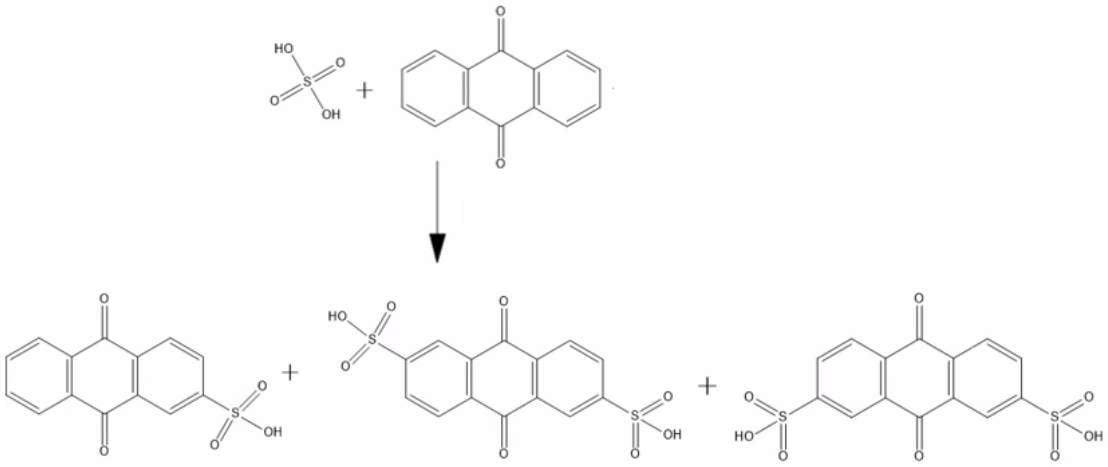

Figure 2.45: Formation of AQDS from anthroquinone

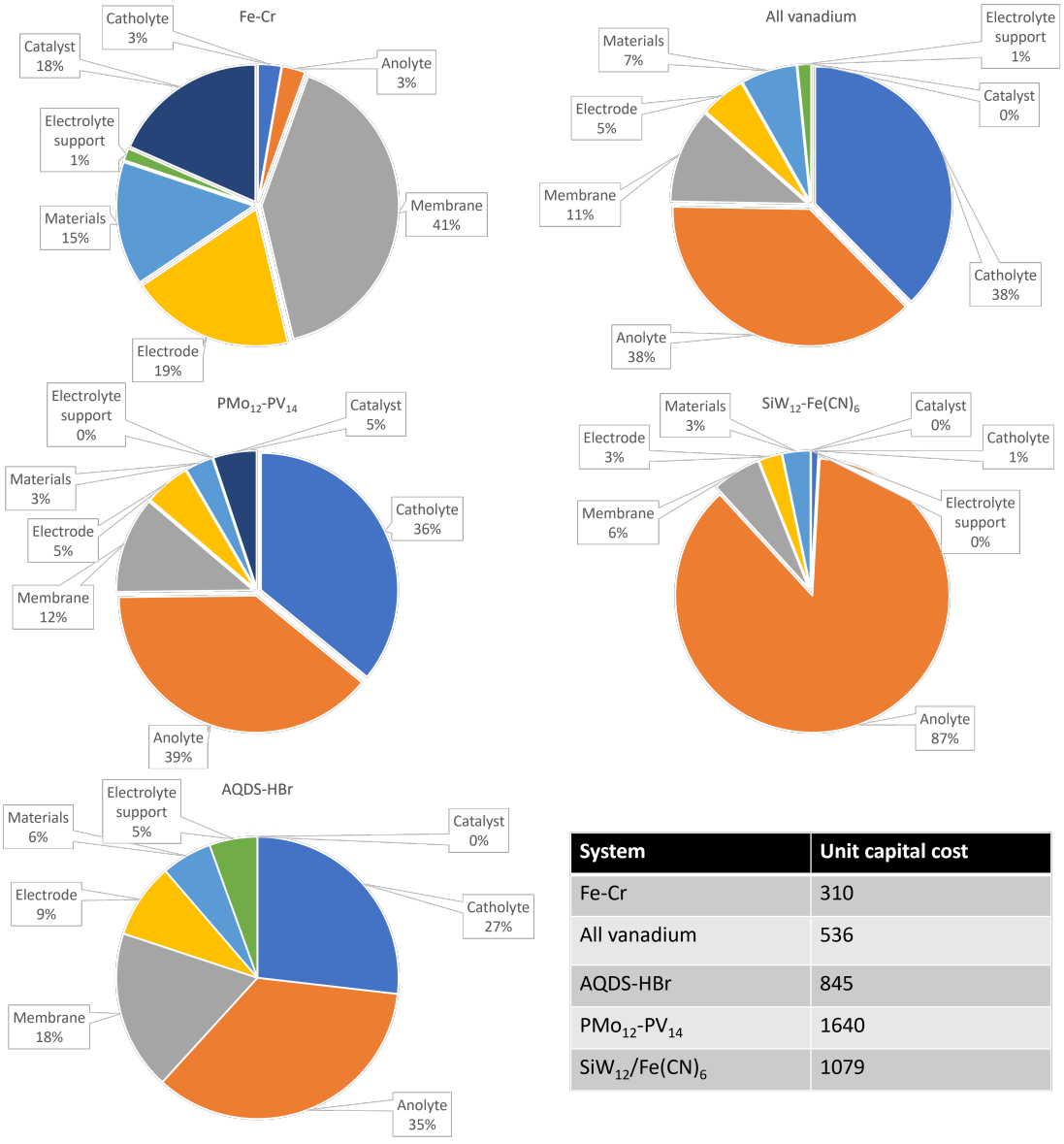

System	Unit capital cost
Fe-Cr	310
All vanadium	536
AQDS-HBr	845
PMo_{12}-PV_{14}	1640
SiW_{12}/$Fe(CN)_6$	1079

Figure 2.46: Percentage cost attributed to a system component for each RFB discussed, and a table listing the unit capital costs in \$ kWh^{-1}.

2.5 Conclusion

In this chapter, PMo_{12} was identified as a suitable redox flow battery anolyte which can undergo electrochemical oxidation and reduction at least several hundred times reversibly. This was confirmed through 3-electrode and 2-electrode flow battery experiments. The accessible capacity of PMo_{12} was shown to be at least 4 F mol^{-1}. However, the number of redox peaks in voltammograms of PMo_{12} samples would suggest that the accessible capacity of the POM is much higher.

It was shown that the accessible capacity of SiW_{12} is as high as 12 F mol^{-1} in 3-electrode experiments and that the reduction potential of the species is extremely low (when water is the solvent), which could give rise to high voltage cells when used with an appropriate catholyte. 3-electrode and flow cell two-electrode experiments showed that the POM could reversibly be reduced and oxidised by as much as 9 F mol^{-1} with a reasonably high coulombic efficiency for a newly developed RFB electrolyte. However, it is suspected that HER becomes an increasingly significant problem as the oxidation state of SiW_{12} decreases. Further study into this system may be warranted, but the capital cost calculator clearly shows that even a significant increase in accessible capacity will still yield a flow battery which is too expensive for commercial operation. Therefore, the findings of this study - that altering the supporting electrolyte and especially the pH significantly alters the behaviour of POMs in solution - may be put to better use by investigating the properties of cheaper POMs in various solvents, supporting electrolytes, and pH.

Finally, a capital cost calculator was presented that gives an approximate breakdown of costs for various flow battery systems. The findings also strongly suggest that if the POM-RFB is to be commercially successful, the development of cheaper electrolytes should be a key focus of any future investigation.

Chapter 3

Thermodynamics of species with multiple redox centres

Declaration

The following chapter is intended as a paper manuscript. It is the product of intensive collaboration between Jack Oliver Mitchinson and Felix Leon Pfanschilling. The underlying theoretical groundwork as well as the experimental verification were produced collaboratively and this resulting chapter appears in both authors' theses. The authors consider the work presented in this chapter to be of equal contribution.

3.1 Introduction

Being able to accurately simulate and predict the behaviour of a RFB is crucial for understanding, planning and implementation of this type of battery. The prediction of basic parameters, such as U, is of fundamental importance but poses a challenge for systems with more than two possible oxidation states. When describing the U of a redox-couple in solution as a function of the concentrations of reduced and oxidised species, the Nernst equation is usually employed. However, if the species in question can adopt a third oxidation state, this equation becomes insufficient and using individual Nernst equations for both redox couples fails to describe the transition regime between them adequately. Yet, this problem occurs frequently, e.g. when describing RFBs containing redox-active species with more than two

possible oxidation states, such as (POM)s. For precise modelling of this type of battery and active species with more than two possible oxidation states a concise description of U is strictly necessary.

Here we present an exact mathematical solution that directly relates U to the (S_{ox}) in a system with three possible oxidation states. The concentration profiles of all three species are modelled as well. We also show that finding the exact mathematical description for U for greater numbers of possible oxidation states is complex and of limited usefulness due to the challenges associated with solving higher order polynomials. Instead, a solution is presented that yields S_{ox} as a function of U (rather than vice versa) for any amount of possible oxidation states. For modelling purposes, these results can be calculated to a desired precision and used in the form of a lookup table. Experimental validation is provided for the predicted values of U.

Furthermore, the behaviour of the limiting currents for each involved redox reaction as well as the individual and total J_0 are predicted. Additionally, the (k^0) values for the involved reactions were measured using two independent techniques and from this data J_0 could be derived. Comparing these experimental values with the predictions showed good agreement.

Section 3.3 details the experimental setup for measuring U over a wide range of S_{ox} of a multi-oxidation state system. This data was also used to calculate kinetic parameters like k^0 and J_0. Impedance spectroscopy was employed, providing an independent experimental technique for verification of these parameters. Section 3.4 compares the measured values to the predicted ones. Reasons for minor deviations are discussed.

3.2 Relating reduction potential to oxidation state

3.2.1 Limitations of the Nernst equation when dealing with electrochemical species with more than two accessible redox states

In the case of a redox reaction accessing only two different redox states, the reduction potential can be described by the Nernst equation:

$$U = U^o + \frac{RT}{nF} \ln \frac{a_{Ox}}{a_{Red}} \tag{3.1}$$

where U = (half-cell) reduction potential, U^o = standard half-cell reduction potential, R = universal gas constant, T = temperature, n = number of electrons transferred in the reaction, F = Faraday constant, a_{Ox} = activity of the oxidised species and a_{Red} = activity of the reduced species.

At low concentrations, activity coefficients γ tend to unity, thus activity can be approximated as concentrations c_x. ($c_x \cdot \gamma_x = a_x$):

$$U = U^o + \frac{RT}{nF} \ln \frac{c_{Ox}}{c_{Red}} \tag{3.2}$$

The Nernst equation, however, covers only the case for two oxidation states. A hypothetical active species M with three accessible oxidation states M^{I+}, M^{II+} and M^{III+} constitutes two associated redox couples. We can formulate one Nernst equation for each of these redox couples. In order to reduce the number of sub- and superscripts and to improve clarity in the following equations, the concentrations of M^{I+}, M^{II+} and M^{III+} will be written as A, B and C, respectively:

$$U = U^o_{AB} + \frac{RT}{F} \ln \frac{B}{A} \tag{3.3}$$

$$U = U^o_{BC} + \frac{RT}{F} \ln \frac{C}{B} \tag{3.4}$$

where U^o_{AB} describes the standard reduction potential of the reaction $M^{I+} \rightleftharpoons M^{II+} + e^-$ (U^o_{BC} analogue). These equations describe the reduction potential reasonably well in the vicinity of the standard potentials but fail to describe the transition regime between the two equations, as shown in Figure 3.1. The underlying reason is that each equation takes only the concentrations of two species into account, whereas all three species will be present at any given potential in varying fractions.

This formulates the challenge to find a mathematical description of the reduction poten-

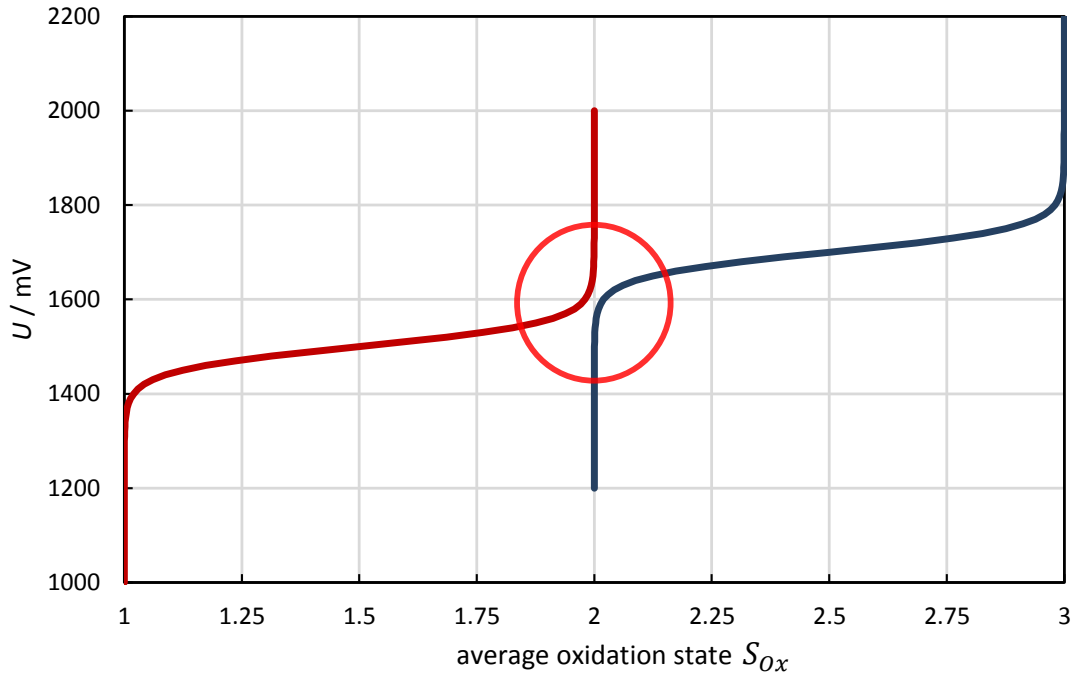

Figure 3.1: Graphical illustration of two individual Nernst equations. The red circle highlights the discrepancy at the transition. U^o_{AB} = 1500 mV, U^o_{BC} = 1700 mV.

tial as a function of the average oxidation state in a redox system with multiple redox states that includes the transition regime.

3.2.2 Calculating the reduction potential for a species with 3 possible oxidation states

The average oxidation state (S_{ox}) in our hypothetical system can be described by multiplying each concentration A, B and C with their associated oxidation state 1, 2 and 3, respectively, and dividing the sum of the above by the total concentration of $M(= A + B + C)$:

$$S_{ox} = \frac{A \cdot 1 + B \cdot 2 + C \cdot 3}{A + B + C} \tag{3.5}$$

In general, this variable can easily be determined from experimentation. For instance by coulomb counting for known concentrations of M, or by comparing spectroscopic data to known references, e.g. UV-Vis spectra of the various oxidation states. A homogeneous solution must have a single reduction potential; therefore, equations 3.3 and 3.4 can be set equal. The constants are separated from the concentrations and for simplicity will be defined

as k_1:

$$\exp\left(\frac{F}{RT}(U^o_{AB} - U^o_{BC})\right) = \frac{AC}{B^2} \tag{3.6}$$

$$k_1 = \frac{AC}{B^2} \tag{3.7}$$

Rearranging equation 3.5 for A gives:

$$A = \frac{2B + 3C - S_{ox}B - S_{ox}C}{S_{ox} - 1} \tag{3.8}$$

and substituting equation 3.8 into equation 3.7 gives:

$$k_1 = \frac{C}{B^2}\frac{2B + 3C - S_{ox}B - S_{ox}C}{S_{ox} - 1} \tag{3.9}$$

The result is a second-order polynomial. Solving this for the ratio $\frac{C}{B}$ yields:

$$\frac{C}{B} = \frac{2 - S_{ox}}{2(3 - S_{ox})} \pm \sqrt{\left(\frac{2 - S_{ox}}{2(3 - S_{ox}}\right)^2 + k_1\frac{S_{ox} - 1}{3 - S_{ox}}} \tag{3.10}$$

The negative solution is disregarded as a ratio of two concentrations cannot be negative. Inserting the positive solution into equation 3.4 yields the desired expression that describes the reduction potential as a function of the S_{ox}, implicitly taking into account the interdependence of the various ratios via the reduction potentials included in k_1:

$$U = U^o_{BC} + \frac{RT}{F}ln\left(-\frac{2 - S_{ox}}{2(3 - S_{ox})}\right) + \sqrt{\left(\frac{2 - S_{ox}}{2(3 - S_{ox})}\right)^2 + k_1\frac{S_{ox} - 1}{3 - S_{ox}}} \tag{3.11}$$

The graph shown in Figure 3.2 reflects experimental results reasonably well.

3.2.3 Calculating the reduction potential for a species with >3 possible oxidation states

In theory, this method can be applied to any number of oxidation states. However, with each additional oxidation state, the order of the polynomial will be incremented. When including a fourth oxidation state M^{IV+}, a third Nernst equation can be formulated:

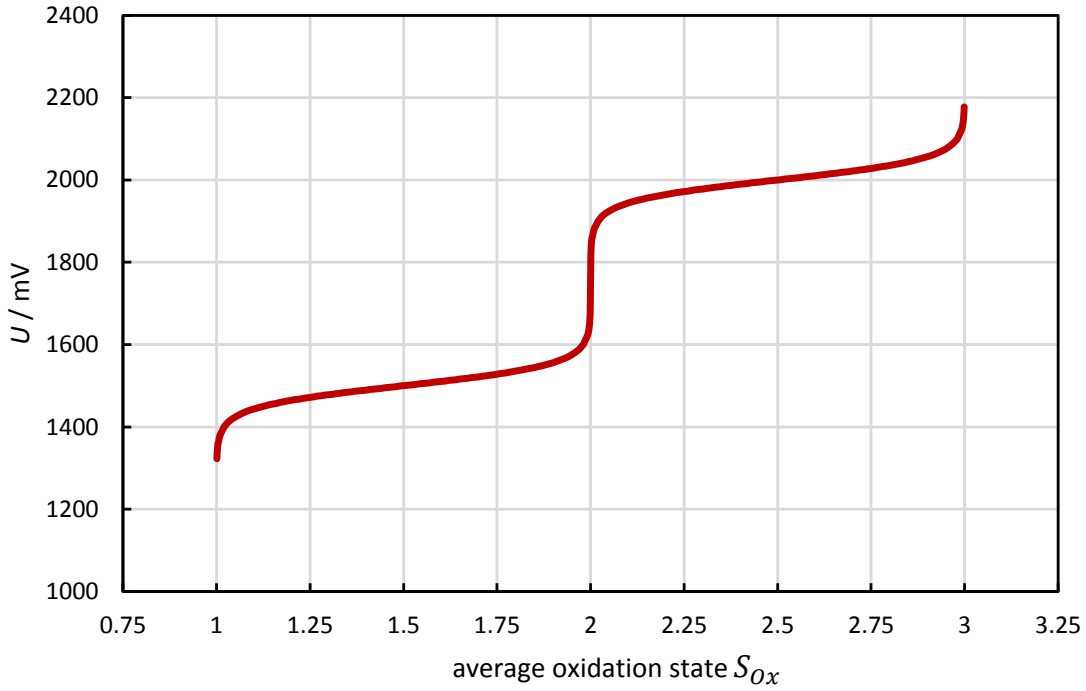

Figure 3.2: Plot of equation 3.11 using 1.5 V and 2.0 V as standard reduction potentials U^o_{AB} and U^o_{BC}, respectively.

$$U = U^o_{CD} + \frac{RT}{F} ln \frac{D}{C} \tag{3.12}$$

where $D = [M^{IV+}]$. Setting it equal to equation 3.4 and separating constants from concentrations, k_2 can be defined analogously to k_1:

$$\exp\left(\frac{F}{RT}(U^o_{BC} - U^o_{CD})\right) = \frac{BD}{C^2} \tag{3.13}$$

$$k_2 = \frac{BD}{C^2} \tag{3.14}$$

The S_{ox} in this system is also defined analogously:

$$S_{ox} = \frac{A + 2B + 3C + 4D}{A + B + C + D} \tag{3.15}$$

Combining equations 3.7, 3.14 and 3.15 yields:

$$Q_1^3 k_1^2 k_2 (S_{ox} - 4) + Q_1^2 k_1 (S_{ox} - 3) + Q_1 (S_{ox} - 2) + (S_{ox} - 1) = 0 \tag{3.16}$$

where $Q_1 = \frac{B}{A}$. Repeating the above procedure for five oxidation states yields:

$$Q_1^4 k_1^3 k_2^2 k_3 (S_{ox} - 5) + Q_1^3 k_1^3 k_2^2 k_3 (S_{ox} - 4) + Q_1^2 k_1 (S_{ox} - 3) + Q_1 (S_{ox} - 2) + (S_{ox} - 1)) = 0 \tag{3.17}$$

Comparing equations 3.16 and 3.17, a pattern can be discerned. However, solving higher order polynomials can be complex and computationally expensive. Particularly for general polynomial equations of fifth degree or higher, the Abel-Ruffini theorem states that there is no algebraic solution. To mitigate this, a different approach was chosen: the ratio B/A was calculated for the potential range of interest with increments of 1 mV for U, using a rearranged form of equation 3:

$$\frac{B}{A} = Q_1 = \exp\left(\frac{F}{RT}(U - U_{AB}^o)\right) \tag{3.18}$$

The results were then used to calculate the associated S_{ox} using equation 3.16 in a rearranged form:

$$S_{ox} = \frac{4Q_1^3 k_1^2 k_2 + 3Q_1^2 k_1 + 2Q_1 + 1}{Q_1^3 k_1^2 k_2 + Q_1^2 k_1 + Q_1 + 1} \tag{3.19}$$

The result can be regarded as a lookup table for correlating S_{ox} and U. Figure 3.3 shows the result plotted as U vs. S_{ox}. This approach can be used for any number of potential oxidation states and with smaller increments for U, if increased precision is desired.

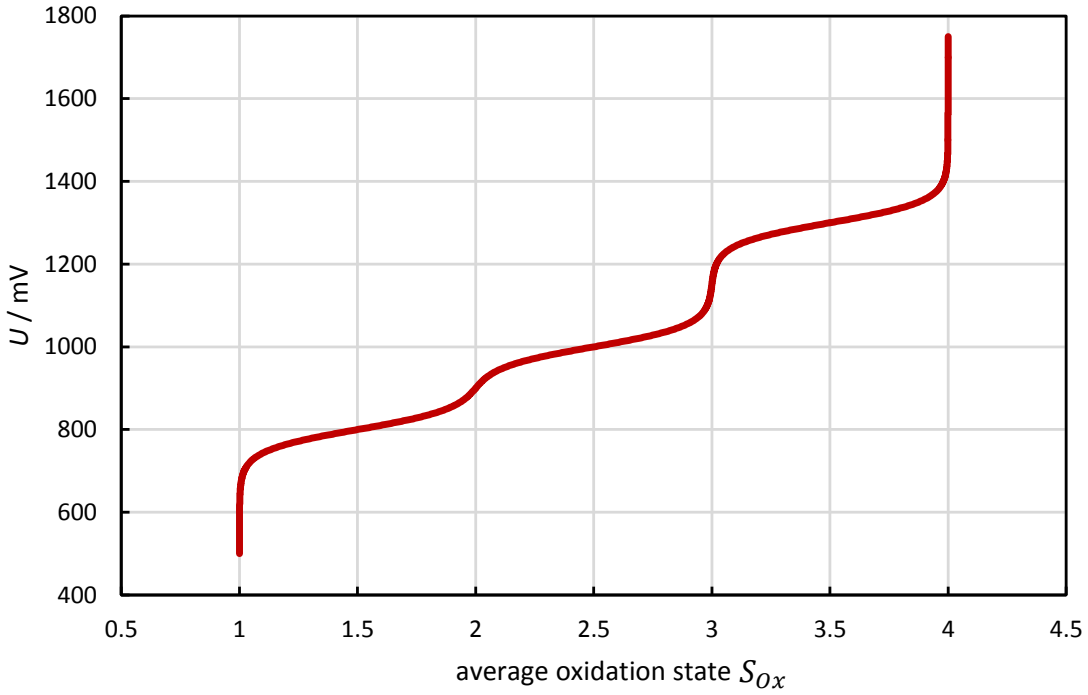

Figure 3.3: Plot of equation 3.19 using the results from equation 3.18 in the potential range from 0.5 V to 1.75 V with 1 mV increments. 0.8 V, 1.0 V and 1.3 V are used as standard reduction potentials U^o_{AB}, U^o_{BC} and U^o_{CD}, respectively.

3.2.4 SiW_{12} as an example case

As an illustrative example, we consider the first three reactions of SiW_{12}:

$$\mathrm{SiW_{12}(0) + e^- \rightleftharpoons SiW_{12}(-1)} \qquad U^o_{CD} \text{ vs SHE} = 0.00 \text{ V}$$
$$\mathrm{SiW_{12}(-1) + e^- \rightleftharpoons SiW_{12}(-2)} \qquad U^o_{BC} \text{ vs SHE} = -0.26 \text{ V}$$
$$\mathrm{SiW_{12}(-2) + 2\,e^- \rightleftharpoons SiW_{12}(-4)} \qquad U^o_{AB} \text{ vs SHE} = -0.40 \text{ V}$$

Since electrons are at least partially delocalised in POMs[1, 66], oxidation states cannot be assigned to individual atoms. We therefore give the oxidation state of the whole molecule in parenthesis as the deviation from the fully oxidised POM. U can be described by the rearranged Nernst equations 3.20-3.22:

$$\exp \frac{(U - U^o_{AB})2F}{RT} = \frac{B}{A} = Q_1 \tag{3.20}$$

$$\exp \frac{(U - U^o_{BC})F}{RT} = \frac{C}{B} = Q_2 \tag{3.21}$$

$$\exp \frac{(U - U^o_{CD})F}{RT} = \frac{D}{C} = Q_3 \tag{3.22}$$

As before, the concentration of the lowest oxidation state is assigned A, the second lowest oxidation state B, etc. with the standard reduction potential for the transition between two states marked with the respective subscript, i.e. U^o_{AB} for the transition from A to B. Hence, $[SiW_{12}(-4)] = A$, $[SiW_{12}(-2)] = B$, $[SiW_{12}(-1)] = C$ and $[SiW_{12}(0)] = D$. Therefore, for any given potential, the reaction quotients Q_i are known. Additionally, the total concentration of species is given by:

$$A + B + C + D = M \tag{3.23}$$

Substitution of the quotients defined by equations (3.20) - (3.22) into equation (3.23) yields expressions for the concentration of individual species:

$$A = \frac{M}{Q_1Q_2Q_3 + Q_1Q_2 + Q_1 + 1} \tag{3.24}$$

$$B = \frac{Q_1M}{Q_1Q_2Q_3 + Q_1Q_2 + Q_1 + 1} \tag{3.25}$$

$$C = \frac{Q_1Q_2M}{Q_1Q_2Q_3 + Q_1Q_2 + Q_1 + 1} \tag{3.26}$$

$$D = \frac{Q_1Q_2Q_3M}{Q_1Q_2Q_3 + Q_1Q_2 + Q_1 + 1} \tag{3.27}$$

Analagously to equation 3.5, the S_{ox} for any distribution of species is given by

$$S_{ox} = \frac{-4A - 2B - 1C - 0D}{A + B + C + D} = \frac{-4 - 2Q_1 - Q_1Q_2}{Q_1Q_2Q_3 + Q_1Q_2 + Q_1 + 1} \tag{3.28}$$

Since the reaction quotients Q_i only depend on constants and U, we can express S_{ox} for any given U. However, when simulating oxidation and reduction processes in a flow battery, the load profile or current regime is typically used as an input parameter. Since in such a case no direct information about U is given, it must be calculated from the change in S_{ox}. ΔS_{ox} is easily calculable from the amount of (Q) for a given (P) or current (I). However, as previously discussed, no explicit expression which relates U as a function of S_{ox} has been found for systems which are governed by more than two Nernst equations (i.e. more than 3 possible oxidation states).

Despite the lack of an explicit relationship, we can define U based on an implicit relationship with reasonably high accuracy. The procedure for relating S_{ox} to U is as follows:

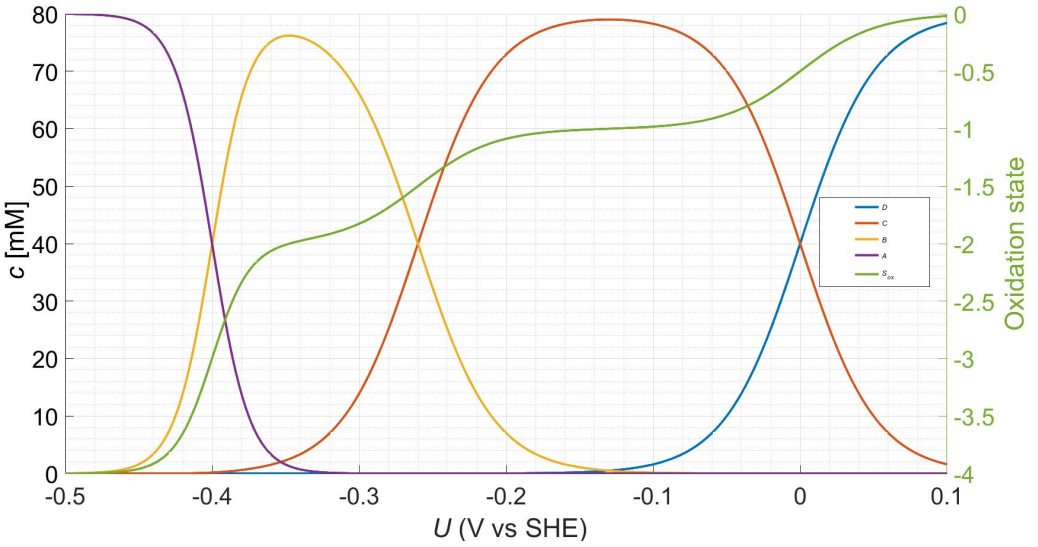

Figure 3.4: Portrayal of the concentration distribution and S_{ox} vs U for the species described by equations 3.20 - 3.22 where the total concentration is 80 mM.

1. The range of sensible values for U is defined according to the potential profile of the electrolyte.

   For our illustrative system it is unlikely that U will fall outside the range $-0.6 \leq U \leq 0.2$ V vs SHE.

2. An array of values ranging from $U(min) - U(max)$ is generated.

3. The arrayed values are used to calculate Q_1, Q_2 and Q_3 according to equations 3.20, 3.21 and 3.22, respectively.

4. A, B, C and D are then calculated from the values for Q_1, Q_2 and Q_3 according to equations 3.24, 3.25, 3.26 and 3.27.

5. S_{ox} can then be calculated from equation 3.28, essentially creating a lookup table for the distribution of species and S_{ox} over the defined potential range.

6. For a sufficiently dense array, the assumption can be made that for any small change in U the corresponding change in S_{ox} can be approximated as a linear change. Therefore, linear interpolation of the neighbouring points allows U for any value of S_{ox} to be determined.

3.2.5 pH dependence of the reduction potential

The situation becomes somewhat more complex when U is pH-dependent. In that case the concentration of the hydronium cation (H_3O^+) must be considered. For the general case of a proton-coupled electron transfer: $B + n_1\,e^- + z_1\,H_3O^+ \longrightarrow A + z_1\,H_2O$, where z is the stoichiometric coefficient, U is given by:

$$U = U^o_{AB} + \frac{RT}{n_1 F} \ln \frac{B[H_3O^+]^{z_1}}{A} \tag{3.29}$$

For the active species containing the redox states A, B and C, where
$B + n_1\,e^- + z_1\,H_3O^+ \rightleftharpoons A + z_1\,H_2O$ and
$C + n_2\,e^- + z_2\,H_3O^+ \rightleftharpoons B + z_2\,H_2O$,
following the same procedure as in section 3.2.4 yields

$$\exp \frac{(U - U^o_{AB})n_1 F}{RT} = \frac{B[H_3O^+]^{z_1}}{A} = Q_1 \tag{3.30}$$

$$\exp \frac{(U - U^o_{BC})n_2 F}{RT} = \frac{C[H_3O^+]^{z_2}}{B} = Q_2 \tag{3.31}$$

In order to determine the ratio of species, $\frac{B}{A}$ or $\frac{C}{B}$, the pH needs to be taken into consideration. Hence, a relationship between S_{ox} and pH is required. The precise relationship depends on the electrolyte in question and will be a function of the acid dissociation constants and concentration distribution of the species present in solution. However, if the electrolyte has multiple associated redox couples, then multiple polyprotic species would have to be considered to arrive at a reasonably accurate relationship. Information regarding acid dissociation constants for reduced POMs could not be found. Additionally, the situation is complicated further by the presence of supporting electrolytes, which are, in some cases, also polyprotic. It might, therefore, sometimes be necessary to resort to the use of empirical relationships which will be defined later for the respective systems.

With that established, it is possible to calculate the S_{ox} for any given pH and U combination. A reasonable range for U and pH is defined and the S_{ox} is calculated according to a procedure analogous to the one on page 161. The data can be represented as a Pourbaix diagram or surface plot, which can be used in a similar way as the lookup table described in section 3.2.2. If the relationship between pH and S_{ox} is established ($\text{pH} = f(S_{ox})$), the U for any S_{ox}/pH combination can simply be inferred from representations like Figure 3.5 and 3.6.

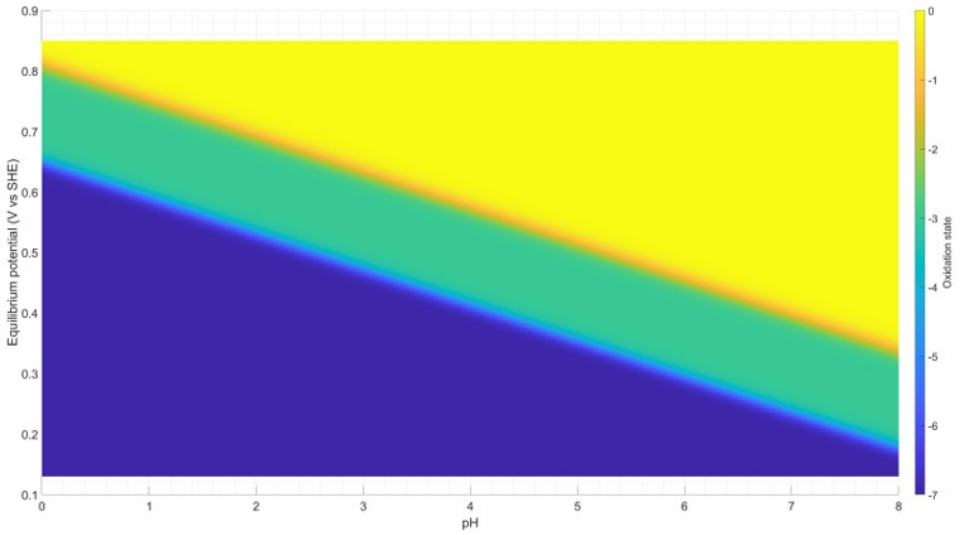

Figure 3.5: Pourbaix diagram for an electrolyte with oxidation states A, B and C, standard reduction potentials $U^o_{AB} = 0.59\text{V}$ and $U^o_{BC} = 0.81\text{V}$, and $z_1 = n_1 = 2$, and $z_2 = n_2 = 5$.

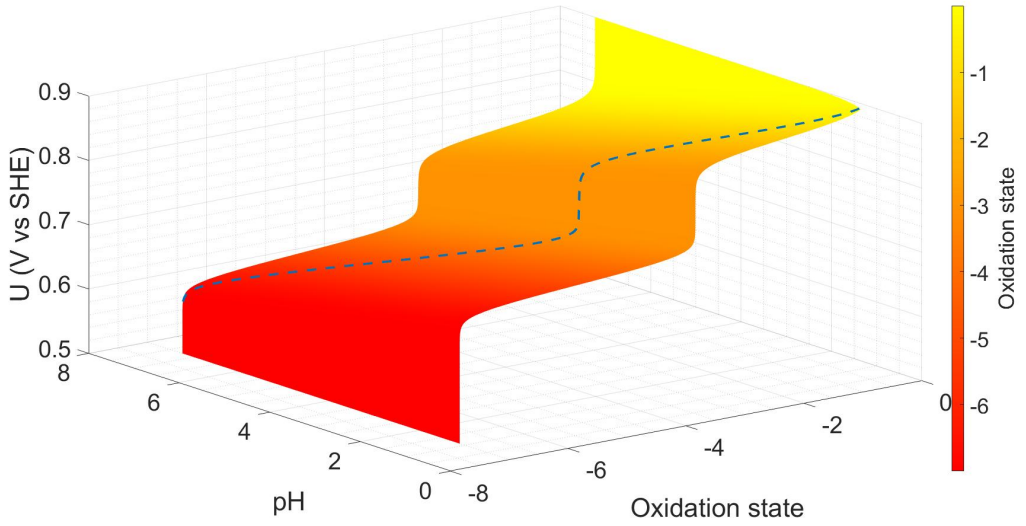

Figure 3.6: A surface plot with the same input parameters as in Figure 3.5 depicting the potential profile (blue dotted line) which an electrolyte adopts for the arbitrary relation: pH$= -0.89S_{ox} + 1.1$

3.3 Experimental

3.3.1 Stationary working electrode experiments

One of the simplest multi-redox couple species available to us, SiW_{12}, was investigated. The two most positive redox reactions are elementary one-electron reactions with no proton cou-

Table 3.1: Electrode specifications for the electrolysis cell (EC) and the reservoir (Res)

electrode	specification
EC working	GFD carbon felt (25 cm^2)
EC counter	GFD carbon felt (25 cm^2)
EC reference	Ag/AgCl in 1 M NaCl (0.200 V vs SHE)
Res working	Polished glassy carbon disk (7.07 mm^2)
Res counter	Au wire
Res reference	Ag/AgCl in 3 M NaCl (0.210 V vs SHE)

pling and (U^o)s 260 mV apart. [1]

The setup included a redox-flow cell (C-Tech INNOVATION C-Flow LAB 5x5, equipped with 5x5cm 4.6 GFD Sigracell carbon felt electrodes, heat treated for 3 h at 600 ºC in air) with the solution of interest (SiW_{12}, aq., 20 mM, 100 mL, at an initial pH of 4.0) in one half-cell and a NaCl solution (aq., 1 M, 1 L) in the other half-cell functioning as the counter electrode solution. The counter electrode half-cell also contained a silver wire coated in a layer of silver chloride, which acted as a reference electrode. The separator was a Nafion-117 membrane which, due to being a cation exchange membrane with a small pore size, does not permit significant crossover of POMs.[1]

As a consequence of bulk electrolysis, small amounts of chlorine are evolved and Na^+ crosses the separator. Over time, the change in sodium chloride concentration leads to reference electrode drift. Consequently, all experiments which utilised this setup had their counter electrode solution replaced on a daily basis.

Both half-cells were connected to separate reservoirs which were constantly purged with nitrogen gas (humidified to counter water evaporation). The reservoir containing the POM solution doubled as a three-electrode electrochemical cell. During electrochemical measurements, the pump was stopped and the reservoir solution was stagnant. Figure 3.7 shows a schematic of the setup and Table 3.1 details the electrode specifications.

Between electrochemical measurements, the flow was resumed so that the POM solution could be bulk-electrolysed in the flow cell to various extents. After each bulk-electrolysis step, the solution was continuously pumped for several minutes so that the S_{ox} throughout the RFB and reservoir was homogenised. The homogeneity was easily confirmed by comparing the open circuit potential of the two working electrodes.

The procedure for measuring the U involved polarising the electrode to a fixed potential until a steady state current was attained. This procedure is repeated for numerous applied potentials $\pm$ 10 mV vs OCP as shown in Figure 3.8. For small overpotentials the electro-

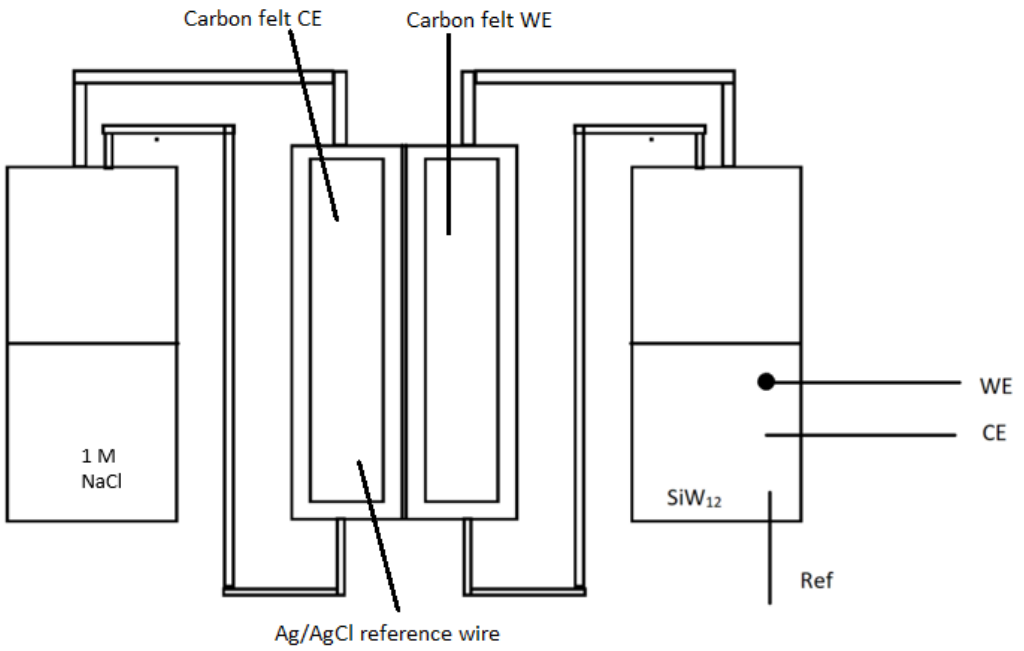

Figure 3.7: Schematic of the setup used for measuring reduction potential and kinetic properties at various oxidation states. The reference electrode for the bulk electrolysis cell is located inside of the cell and is not shown for clarity. There are two potentiostats connected in this experimental setup, one to WE, CE and RE in the electrolysis cell and one to the WE, CE and RE in the reservoir containing the SiW_{12} solution.

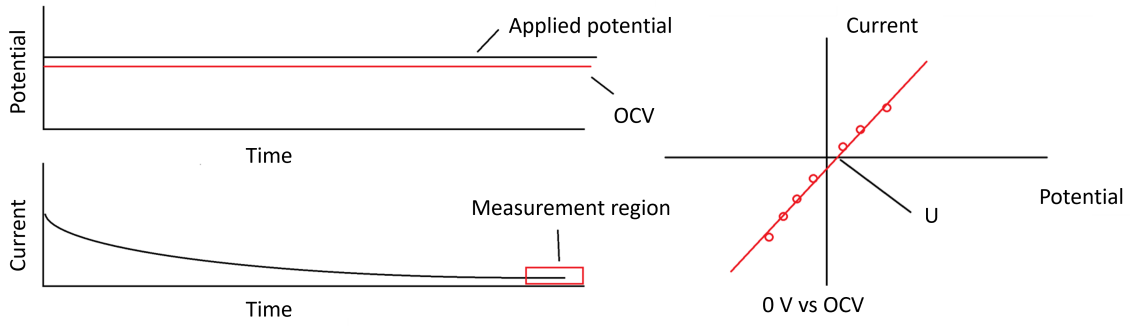

Figure 3.8: Graphical depiction of the experiment procedure (left). Typical plot of the steady state current vs potential (right)

chemical reaction is kinetically controlled and the current-overpotential relation is linear. The reduction potential can be extracted by interpolating the linear trendline to $I = 0$.

Potentiostatic electrochemical impedance spectroscopy was also carried out on solutions of SiW_{12} at varied oxidation state. This was done using the setup described in Table 3.1. The frequency range was 20 kHz-100 mHz and the excitation frequency was 10 mV with no underlying current. Prior to AC excitation, the potential was held at 0 V vs OCP for five minutes.

3.3.2 Rotating disk electrode experiments

As will be discussed in section 3.4.1, mass-transport limitations restrict the usefulness of the data collected in the stationary experiments. Therefore, the reservoir working electrode was replaced with a rotating glassy carbon disk (0.785 cm^2). The concentration of SiW_{12} was also increased to 20 mM to be in-line with previous measurements of kinetic parameters in our group.[1] The starting pH was 2.1, meaning that the third reduction of SiW_{12} (which at a pH < 2 is a two-electron process), is split into two one-electron processes as in Figure 3.9. The RDE was spinning at 5000 rpm throughout the experiment. Otherwise, the experimental parameters are identical to those listed in Table 3.1.

800 current vs potential (Tafel) plots with maximum overpotentials of $\pm$ 250 mV were recorded over the potential range -1.1 V to + 0.1 V vs SHE. This was achieved in the following way:

- A fixed potential was applied at the flow cell working electrode while the solution is

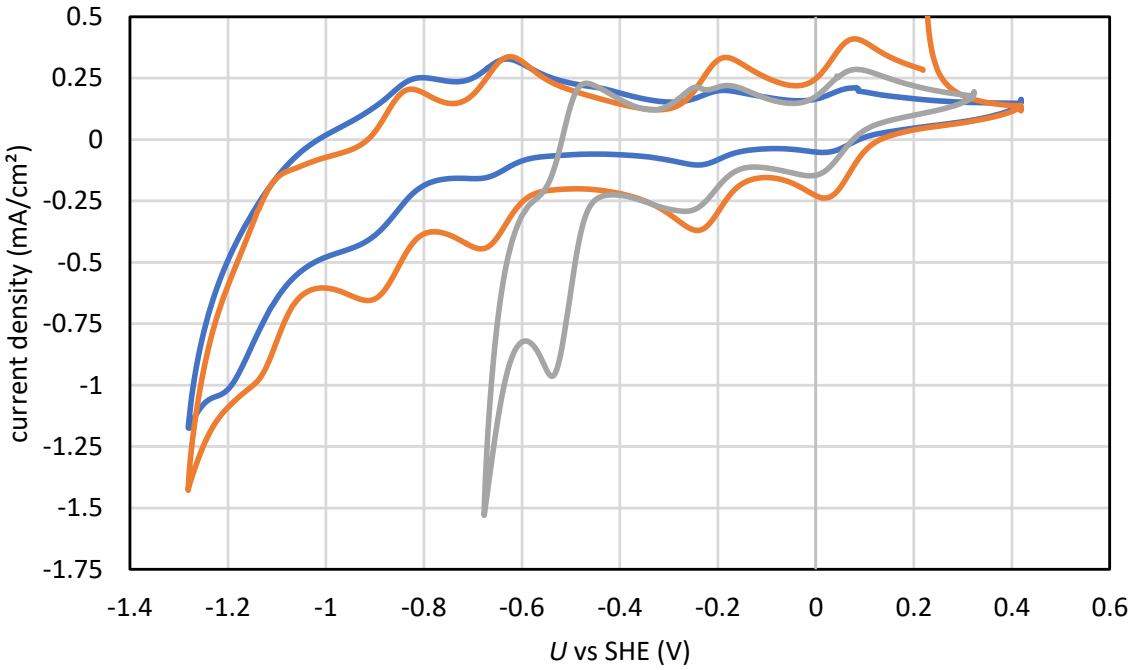

Figure 3.9: Cyclic voltammograms of 5 mM SiW_{12} in 1 M NaCl at varied pH. WE: glassy carbon disk, CE: Pt wire, RE: Ag/AgCl in 1 M NaCl (U = 220 mV vs SHE) for pH $>$ 2 and MSE in 1 M H_2SO_4 (U = 624 mV vs SHE) for pH $<$ 2. pH 1.7 (grey), pH 5.7 (orange), pH 6.0 (blue). This is a reproduction of figure 2.20.

constantly pumped until the current decreased to almost zero.

- A period of open circuit potential (minutes) ensures the solution is fully mixed.
- The current at the applied potential is recorded.
- A further period of OCP is applied to ensure no overlap in potentiostat operation.
- The process is repeated from the beginning for a series of potentials.

Throughout the multi-day experiment, the solutions were constantly purged with humidified nitrogen gas at a rate of ca. 0.5 L min^{-1}.

3.4 Results and discussion

3.4.1 Stationary working electrode experiment discussion

The initial set of experiments saw a solution of SiW_{12} (5.33 mM) in 1 M NaCl reduced from the fully oxidised state SiW_{12}(0) to various degrees up to SiW_{12}(-1.25). Thus, at all times the species distribution is dominated by three distinct oxidation states (0, -1 and -2). We therefore model this system using the equations described in section 3.2.2. The extent to which the species is reduced can be determined simply from coulomb counting and the reduction potentials for each unique S_{ox} are determined by the method described in section 3.3.1. Figure 3.10 depicts a typical dataset for the stationary cell experiment setup. Figure 3.11 depicts the experimental results and predicted values for the reduction potentials, showing good agreement between the two.

Furthermore, the difference between OCP and the reduction potential was measured for each dataset (Figure 3.12) and the difference was found to be small (< 2 mV) for approximately 87% of data sets. Discrepancies between OCP and the reduction potential typically arise due to competing redox reactions on the electrode surface (in this case from contaminants, e.g. airborne particles, impurities carried in via the nitrogen for purging, leaching from tubing and electrochemical cell, etc.) leading to the formation of a mixed potential. Due to the typically high standard rate constant for POM electron transfer, the possible contribution of contaminants' redox reactions towards a mixed potential is expected to be low. [1, 2, 66]

Since the OCP and U are in good agreement, an additional experiment was carried out: SiW_{12} was continuously electrolysed in the RFB with a 10 mA current until an S_{ox} of ca. -1.9 was achieved. During this time, the open circuit potential in the reservoir was continuously recorded. The low current resulted in extremely slow electrolysis, so the S_{ox} of the solution in the reservoir and the redox flow battery can be approximated as being homogeneous at any given time throughout the course of the measurement. This allows for direct comparisons of the open circuit potential recorded in the reservoir with the S_{ox} according to coulomb counting. It also allows for comparison with the predictions of equation 3.11, as in Figure 3.13.

It was observed that the highest discrepancy between the predicted and observed potential occurred when the oxidation state was close to zero. The exchange current of a redox reaction decreases rapidly when the ratio of the oxidised and reduced species approaches either very small or very large values. Given that this is the case at oxidation states near zero,

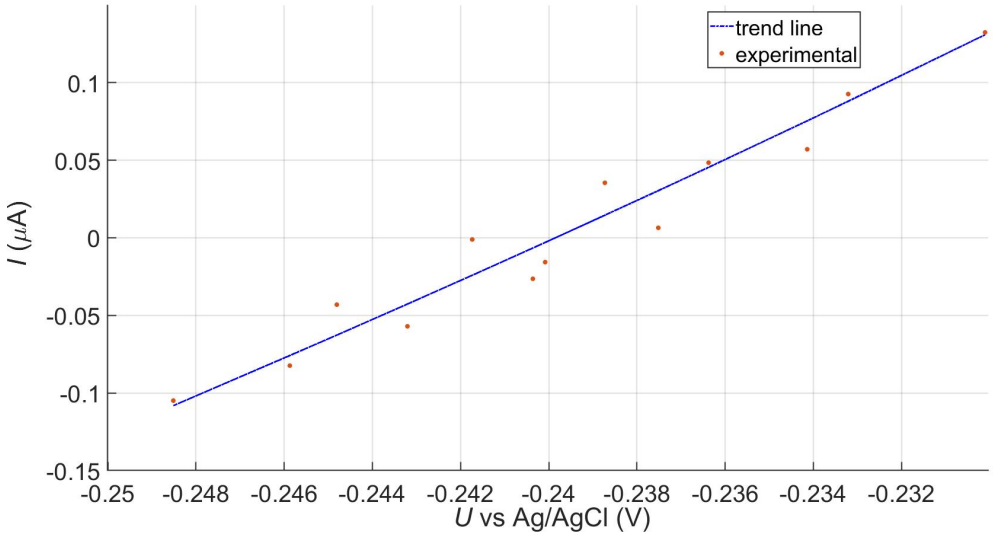

Figure 3.10: Typical results for the experimental procedure described in 3.3.1. steady state current vs potential of a partly reduced SiW_{12} in 1 M NaCl. The trend line (blue) is determined by the least squares method.

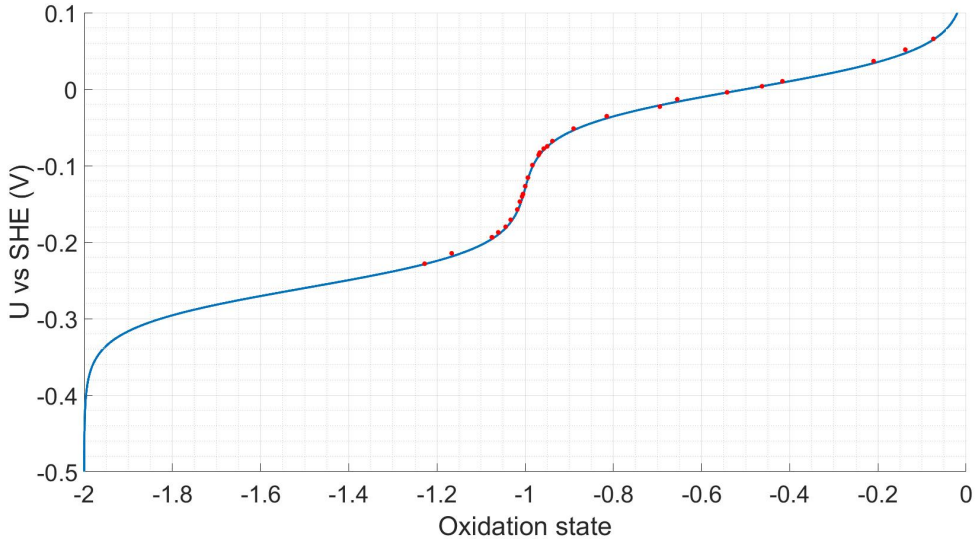

Figure 3.11: Comparison of the predicted reduction potential (blue line) and the experimentally observed results (red spots) vs S_{ox} of SiW_{12} in 1 M NaCl.

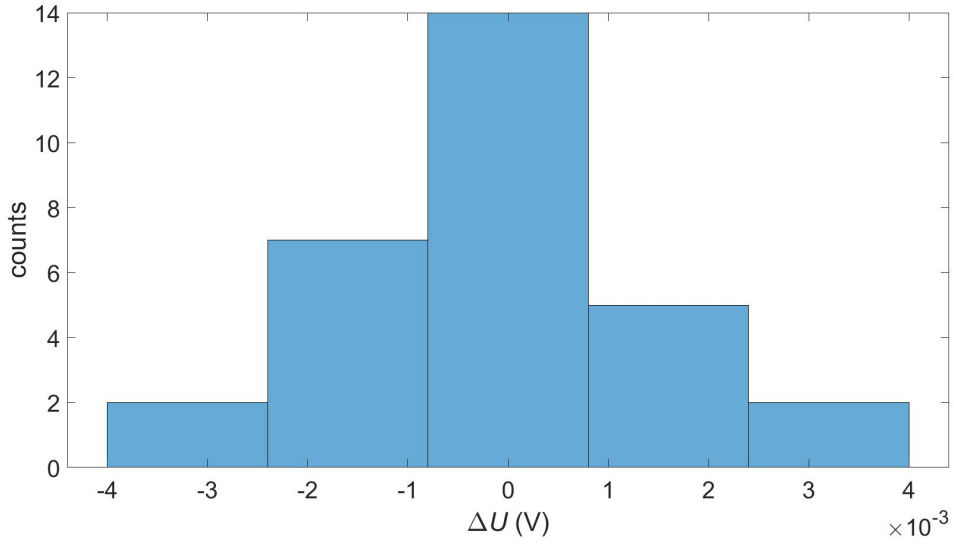

Figure 3.12: Histogram showing the discrepancy between the reduction potential and the open circuit potential for all datasets in this series. In this case, ΔU is defined as $\Delta U = OCP - U$.

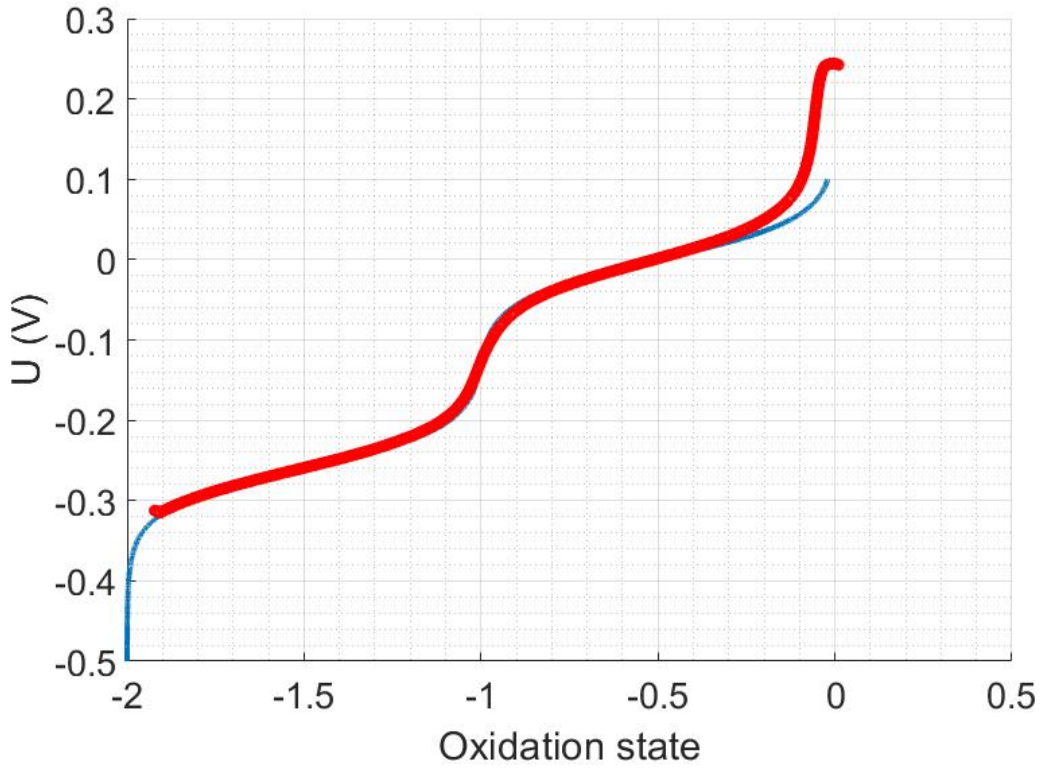

Figure 3.13: Comparison of the open circuit potential in the reservoir (red line) to the S_{ox} throughout the bulk electrolysis procedure.

the observed discrepancy is not unexpected. Additionally, the contribution of contaminants towards a mixed potential becomes more significant when the exchange current attributable to the contaminants rises with respect to the exchange current of the species of interest.

Another point of interest in Figure 3.13 is when the oxidation state is near -1. Close inspection shows that the experimental slope $\left(\frac{d(U)}{d(S_{ox})}\right)$ in this region is smaller than expected. The explanation for this is that in this region, the largest change in reduction potential relative to S_{ox} occurs. Therefore, the OCP measurement is more sensitive to inhomogeneity in the S_{ox}. A certain degree of inhomogeneity is expected and tolerated because perfect instantaneous mixing, even at high pump rates, is unattainable. Consequently, at any given time, it is expected that there is a slight local deviation in the S_{ox} at the reservoir working electrode interface, which is placed at the centre of the reservoir.

Despite the aforementioned points, we see that the recorded potential agrees very well with the predicted values of equation 3.11. Using two different experimental techniques, we have shown that the predicted reduction potential agrees very well with the experimentally observed reduction potential for a given S_{ox}.

With the relationship between S_{ox} and reduction potential established, we now demonstrate that the predicted concentration profile for this system (Figure 3.14) is also in line with experimental observations. However, experimentally differentiating between the discreet S_{ox} poses a challenge.

Fully oxidised solutions of SiW_{12} in its pure form are entirely colourless, or in some rare instances, a light shade of pink (as per our own observations). Reducing the SiW_{12} results in the formation of a deep blue solution. Indeed, this is perhaps the property for which tungsten and especially molybdenum POMs are best known, as this class of molecules is also described as heteropoly blues.[8] However, we have been unable to relate this property in a quantitative fashion and it is unclear if the two reduced forms of interest here have absorbtion profiles different enough for reliable distinction. The molar attenuation coefficient is so high that samples with a concentration of ≥ 1 mM have an absorbance too large to be measurable with the spectroscopy equipment available to us, even after reducing the path length to 1 mm. In addition, the reduced POMs are sensitive to air oxidation, which could not entirely be avoided when pumping samples between the cell to the spectroscopy equipment.

^{183}W is NMR active, but measurements suffer from its very low sensitivity, necessitating specialised equipment and time consuming measurements. Therefore, analysing a large amount of samples via NMR was not feasible.

Measuring the electrochemical kinetics of the solution seemed the most reasonable approach. Disregarding the contribution of possible contaminants to the solution, there are

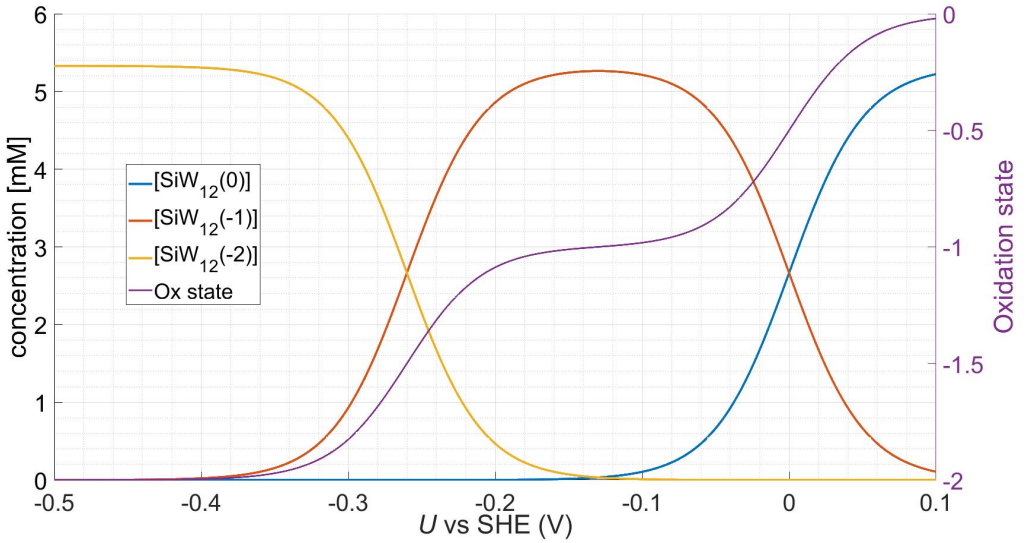

Figure 3.14: The concentration profile for SiW_{12} in the stationary cell experiments and the S_{ox} vs reduction potential.

two possible redox reactions which can occur to a significant extent:

$$SiW_{12}(0) + e^- \rightleftharpoons SiW_{12}(-1)$$
$$SiW_{12}(-1) + e^- \rightleftharpoons SiW_{12}(-2)$$

Provided that the rate limiting step is an elementary electron transfer from the POM to the electrode, the exchange current can be defined as:

$$J_0 = zFk^0(c_O^\alpha c_R^\beta) \tag{3.32}$$

where c_O and c_R are the concentrations of the reduced and oxidised species of interest, α and β are the anodic and cathodic charge transfer coefficients, which we assume to be 0.5, k^0 is the standard rate constant associated with the electron transfer.

Following the convention set out in section 3.2.4, i.e. associating letters to the species of interest starting from the lowest oxidation state, we define the concentration of the species of interest as: $[SiW_{12}(-2)] = A$, $[SiW_{12}(-1)] = B$ and $[SiW_{12}(0)] = C$. The absence of $SiW_{12}(-4)$ should be noted here, as it is only present in negligible quantities over the S_{ox} range being investigated. The total exchange current density can be defined as:

$$J_{0(AB)} = Fk^0_{(AB)}(B^\alpha A^\beta) \tag{3.33}$$

$$J_{0(BC)} = Fk^0_{(BC)}(C^\alpha B^\beta) \tag{3.34}$$

$$J_{0(tot)} = (J_{0(AB)} + J_{0(BC)}) \tag{3.35}$$

where j is the current density. Assuming $\alpha = \beta = 0.5$, equations 3.33 and 3.34 predict that the exchange current reaches a local maximum when the reduced and oxidised species are present in equal proportions, i.e. when $S_{ox} = -1.5, -0.5$. According to equation 3.35, a local minimum will be present at $S_{ox} = -1$. The datasets that were used to determine reduction potential can also be used to determine $J_{0(tot)}$. Under kinetically controlled conditions at small overpotentials, the slope depicted in Figure 3.10 is defined by:

$$J = J_0 \frac{zF}{RT} \Delta U \tag{3.36}$$

Hence, the slope is proportional to the exchange current. Figure 3.15 shows that, starting from $S_{ox} = 0$, the slope for each individual dataset increases until $S_{ox} = -0.5$ and then steadily decreases until the slope reaches a minimum at $S_{ox} = -1$ and then rises again. Qualitatively, this is in line with the prediction. However, for a quantitative comparison, we must first determine the standard rate constants.

Figure 3.14 depicts the modelled concentration profile with respect to potential. Therefore, if k^0 for each reaction can be determined, the expected value for $J_{0(tot)}$ at any given S_{ox} can be calculated. This value can then be compared with experimentally derived values of $J_{0(tot)}$ according to equation 3.36.

We see that at $S_{ox} = -0.5$, the concentration of species $SiW_{12}(-2)$ (A) is negligible and similarly, at $S_{ox} = -1.5$, the concentration of $SiW_{12}(0)$ (C) is negligible. Therefore, any measurement of the electrochemical kinetics carried out at these S_{ox} values can be fully attributed to the reactions $SiW_{12}(0) + e^- \rightleftharpoons SiW_{12}(-1)$ and $SiW_{12}(-1) + e^- \rightleftharpoons SiW_{12}(-2)$, respectively.

The k^0 for each reaction was determined using two independent techniques. Perturbing the potential by a small amount relative to the open circuit potential and recording the steady state current for different potential perturbations results in a slope which is defined by equation 3.36. Inserting the exchange current into equations 3.33 and 3.34 for $S_{ox} = -0.5$, where $B = C = 2.66$ mM and for $S_{ox} = -1.5$, where $A = B = 2.66$ mM. All transfer coefficients are assumed to be 0.5.

Additionally, electrochemical impedance spectra at both S_{ox} values were also recorded

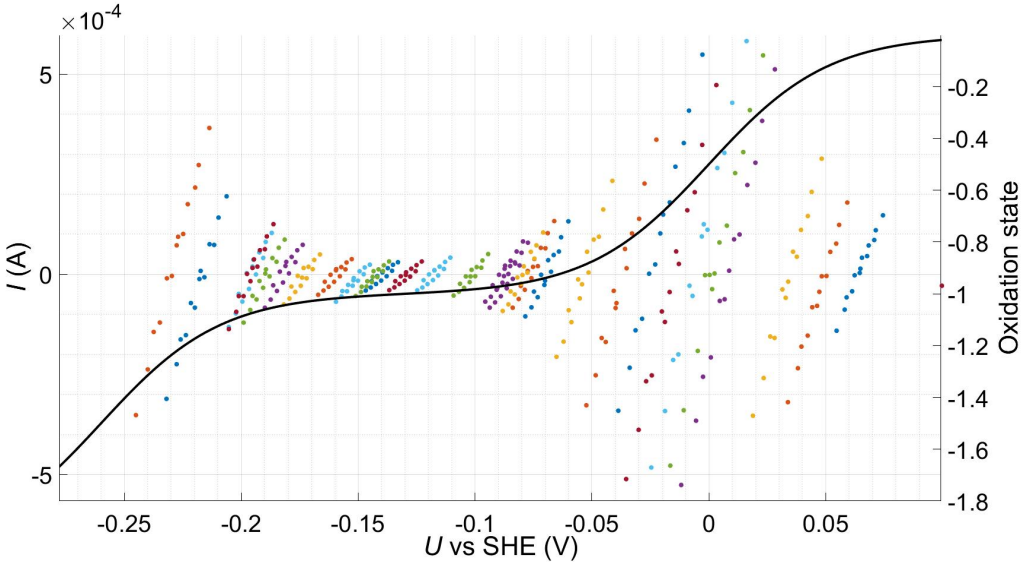

Figure 3.15: Current vs potential for SiW_{12} samples at varied S_{ox} (varied open circuit potential), where each of the coloured spots represents a different open circuit potential. For each dataset, the potential pertubation is equivalent. The black line is the S_{ox} vs reduction potential.

Table 3.2: EIS equivalent circuit element values

Element	$S = -0.5$	$S = -1.5$
R1	16.9 Ω	17.5 Ω
Q2	$4.057 * 10^{-6}$ F $s^{(a-1)}$	$4.057 * 10^{-6}$ F $s^{(a-1)}$
a1	0.7988	0.7988
R2	131.0 Ω	166.4 Ω
s1	2882 Ω $s^{-1/2}$	3014 Ω $s^{-1/2}$

in the reservoir under stationary conditions. The spectra and their fits are displayed in Figure 3.16 and the equivalent circuit used for the fit is displayed in Figure 3.17. Table 3.2 displays the fitted values for each circuit element. The value of interest here, is the charge transfer resistance R_{CT}, as this value, for an elementary single electron transfer, relates to the exchange current by equation 3.37:

$$R_{CT} = \frac{RT}{FI_0} \tag{3.37}$$

Substitution of J_0 into equations 3.33 and 3.34 allows the k^0 for each reaction to be determined (Table 3.3).

There is some variation between the calculated k^0 values depending on the technique

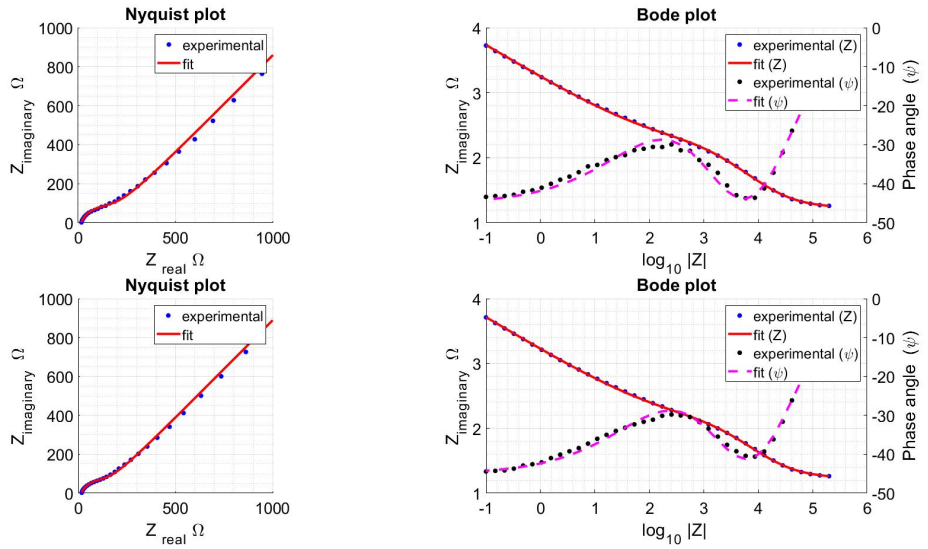

Figure 3.16: Nyquist and Bode plots for SiW_{12} in 1 M NaCl reduced to $S_{ox} = -1.5$ (top) and $S_{ox} = -0.5$ (bottom) on a glassy carbon disk electrode (stationary experiment setup). Nyquist plots display is limited to 1000 Ω for clarity of features.

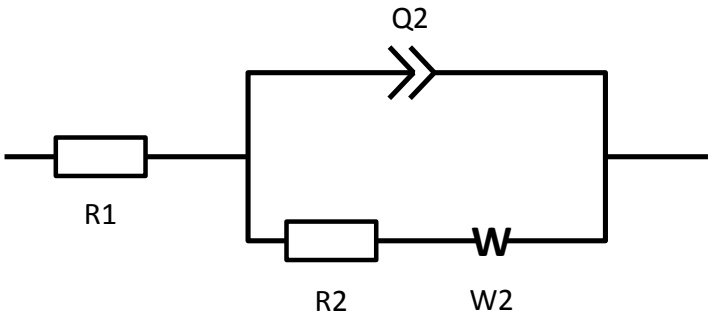

Figure 3.17: Equivalent circuit used for fitting the impedance spectra

Table 3.3: Measured k^0 values

Reaction	j vs U slope	PEIS
$SiW_{12}(0) + e^- \rightleftharpoons SiW_{12}(-1)$	$4.7 \cdot 10^{-3}$ cm s^{-1}	$5.39 \cdot 10^{-3}$ cm s^{-1}
$SiW_{12}(-1) + e^- \rightleftharpoons SiW_{12}(-2)$	$3.61 \cdot 10^{-3}$ cm s^{-1}	$4.25 \cdot 10^{-3}$ cm s^{-1}

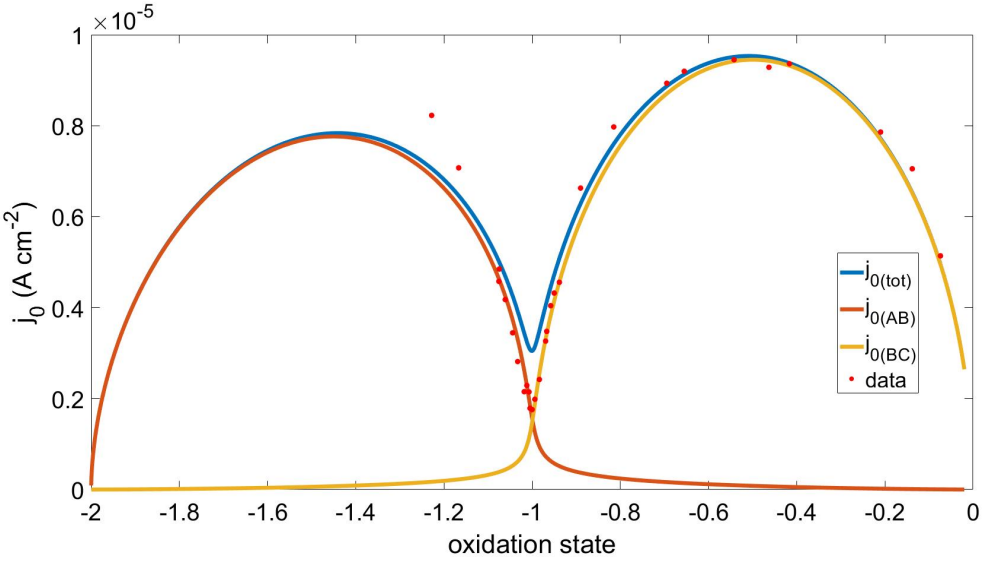

Figure 3.18: Exchange current density vs S_{ox}. Exchange current densities predicted by equations 3.33 (yellow), 3.34 (orange), 3.35 (blue) and the experimentally derived values (red dots). Fitted parameters: $k^0_{(BC)} = 5.2 \cdot 10^{-3}$ cm s^{-1} and $k^0_{(CD)} = 4.25 \cdot 10^{-3}$ cm s^{-1}

applied, but the values are reasonably close together.

Now that the standard rate constants are established, the expected total exchange current can be calculated from equations 3.33 - 3.35. The result of which is plotted in Figure 3.18 with the experimental values overlaid.

In general, the experimental results agree very well with the predicted values. However, we see that when $S_{ox} = -1$ (Figure 3.18) there is a small, but still significant deviation from the predicted value. The cause of this deviation becomes apparent when considering the combined effects of mass transport and significant depletion of species A and C when $S_{ox} \approx -1$.

There are numerous ways to determine the limiting current for a given system. Perhaps the simplest method is through observation of the maximum current in a Tafel plot which features a plateau. Figure 3.19 shows that the limiting current $j_{l_{a/c}} \approx 1.4$ µA when $S_{ox} = -0.5$ (The increasingly negative gradient at -200 mV is due to the onset of the AB reaction). Assuming that the limiting current is proportional to the concentration of species (A, B, and C), we can estimate the limiting anodic and cathodic currents for any given S_{ox} (Figure 3.20).

Qualitatively, it can now be seen that in the region where $S_{ox} = -1$, the limiting anodic current for the BC reaction and the limiting cathodic current for the AB reaction are low relative to the overall current. Equations 3.33 - 3.35 adequately describe the behaviour for a kinetically controlled system at low overpotential. However, since we have established that

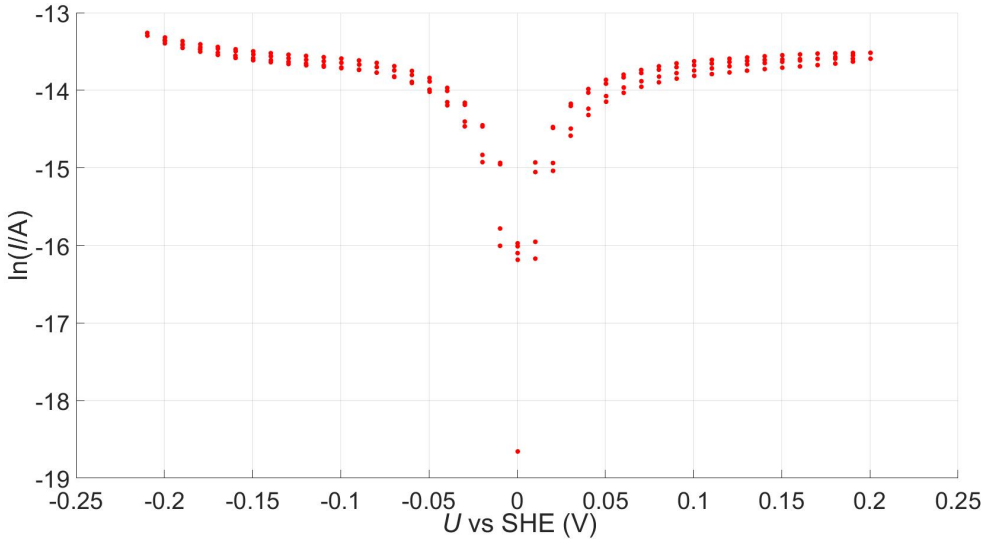

Figure 3.19: Tafel plot for SiW_{12} 5.33 mM in 1 M NaCl when $S_{ox} = -0.5$.

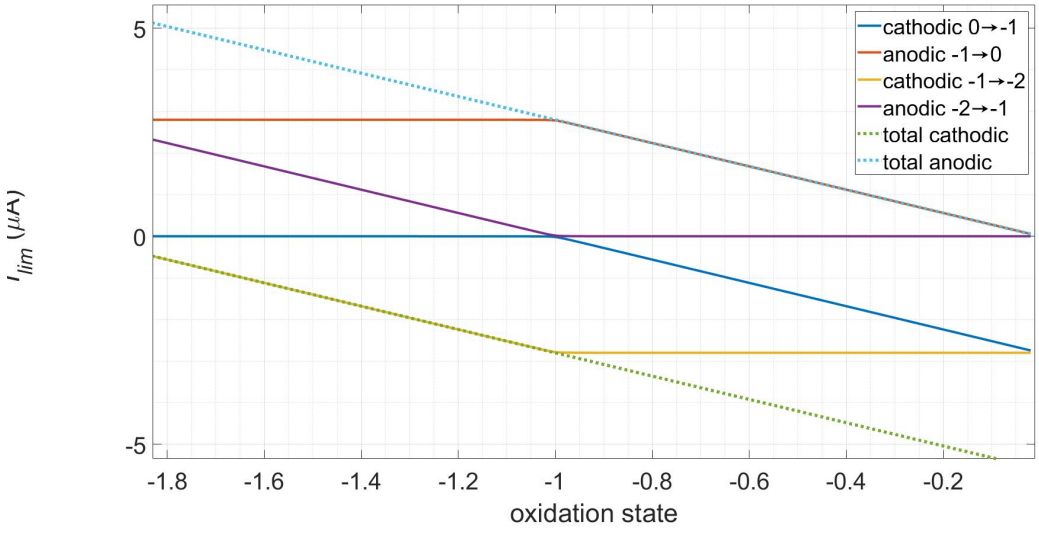

Figure 3.20: The limiting currents associated with each reaction.

mass transport has a considerable influence on this system, these equations are insufficient and the application of a more sophisticated model is necessary.

3.4.2 Rotating disk electrode experiment discussion

There are multiple advantages of using an RDE to record current vs potential plots, such as:

- The time required to attain a steady state current (depicted in Figure 3.8) is less than 1 second at 5000 rpm. Therefore, data for a given S_{ox} can be produced in 1-2 minutes (as thorough mixing is still necessary), ensuring that the effects of O_2 ingress are minimised. Additionally, the small timeframe allows many datasets over a large range of S_{ox} to be collected in a timely fashion.
- The material flux in the vicinity of the RDE (the reservoir) is high enough that the flux from pumping to the flow cell can be ignored during measurement. Therefore, the procedure for measuring over different S_{ox} can be easily automated.
- The applied potential range can be extended to high values ($\pm 250\text{mV}$) with little effect on data collection time. We can then analyse the kinetic and mass transport properties at a given S_{ox}.
- As can be seen in figures 3.10 and 3.19, there is significant hysteresis when a stationary electrode is used. This probably occurs as a result of small differences in the density: It was observed that on reduction of SiW_{12} the newly generated blue material sank to the bottom of the reaction vessel, hardly mixing with the surrounding liquid. This induced uncontrolled convection in the vicinity of the working electrode. With the RDE at 5000 rpm, these effects are mitigated by forced convection in the vicinity of the working electrode surface.

Assuming that the rate limiting step is an elementary electron transfer process from the POM to the electrode and vice versa, the processes at the electrode can be adequately described by the extended current-overpotential relationship:[144]

$$J = J_0 \left[\left(1 - \frac{J}{J_{l,a}} \right) e^{\alpha f \eta} - \left(1 - \frac{J}{J_{l,c}} \right) e^{-\beta f \eta} \right] \tag{3.38}$$

Which can be rearranged for j:

$$J = \frac{J_0 (e^{\alpha f \eta} - e^{-\beta f \eta})}{J_0 (\frac{e^{\alpha f \eta}}{J_{l,a}} - \frac{e^{-\beta f \eta}}{J_{l,c}}) + 1} \tag{3.39}$$

Over the potential range studied in this experiment, there are four associated redox couples (Figure 3.9). Consequently, there are five possible oxidation states, since the third reduction reaction of SiW_{12}, a two-electron reaction, is split into two one-electron reactions at this pH. According to the previous conventions, the concentrations of the various states are assigned A, B, C, D, E, starting from the lowest oxidation state, e.g. $[SiW_{12}(-4)] = A$. The redox reactions are as follows:

$SiW_{12}(0) + e^- \rightleftharpoons SiW_{12}(-1)$ $\quad U^o$ vs SHE = 0.00 V

$SiW_{12}(-1) + e^- \rightleftharpoons SiW_{12}(-2)$ $\quad U^o$ vs SHE = -0.26 V

$SiW_{12}(-2) + e^- \rightleftharpoons SiW_{12}(-3)$ $\quad U^o$ vs SHE = -0.65 V

$SiW_{12}(-3) + e^- \rightleftharpoons SiW_{12}(-4)$ $\quad U^o$ vs SHE = -0.87 V

Equation 3.39 gives the current at a given overpotential for a single redox couple, so the total current will be the sum of the currents according to equation 3.39 for all associated redox couples:

$$j_{tot} = j_{AB} + j_{BC} + j_{CD} + j_{DE} \tag{3.40}$$

Typically, the kinetic parameters for an electrochemical system are determined through analysing a Tafel plot. A typical analysis involves extrapolating along the linear regions in the $\log(j)$ vs U plot of the anodic and cathodic branch to zero overpotential. The value of the () at the abscissa intercept is taken to be the exchange current density and from this the rate constant can be calculated. The challenge here is that the onset of the linear region is very rarely clear-cut in experimental data, leaving the analysis of the data very much up to the interpretation of the individual researcher. Consciously or otherwise, this can lead to the researcher forming conclusions which support a preferred narrative. Moreover, this type of analysis would be insufficient to explain the kinetics arising from equation 3.40.

Given the wide availability of fitting tools in commonly used software (Excel, MATLAB etc.), it seems preferable to fit the experimental data directly to equation 3.40. If the system obeys the equation then a good fit will be achieved and the parameters will be calculated with much less ambiguity. If no good fit can be found, then this can potentially indicate that the underlying chemistry is more complex and/or different than anticipated. Furthermore, the application of a model to a series of Tafel plots taken over a large S_{ox} range allows for a rich understanding of the kinetic and mass-transport parameters.

Equation term	Contained variables
j_{AB}	$[SiW_{12}(-4)]$, $[SiW_{12}(-3)]$, α_{AB}, β_{AB}, k^0_{AB}, $j_{l,a_{(AB)}}$ $j_{l,c_{(AB)}}$
j_{BC}	$[SiW_{12}(-3)]$, $[SiW_{12}(-2)]$, α_{BC}, β_{BC}, k^0_{BC}, $j_{l,a_{(BC)}}$ $j_{l,c_{(BC)}}$
j_{CD}	$[SiW_{12}(-2)]$, $[SiW_{12}(-1)]$, α_{CD}, β_{CD}, k^0_{CD}, $j_{l,a_{(CD)}}$ $j_{l,c_{(CD)}}$
j_{DE}	$[SiW_{12}(-1)]$, $[SiW_{12}(0)]$, α_{DE}, β_{DE}, k^0_{DE}, $j_{l,a_{(DE)}}$ $j_{l,c_{(DE)}}$

Table 3.4: Variables to be fitted.

Data processing methodology

There are four associated redox couples of interest within the potential range studied in this experiment. Assuming that all four follow Butler-Volmer kinetics then equation 3.40 should describe the system. The expanded form of equation 3.40 is not displayed here for the sake of brevity, but it can be seen from equation 3.39 that there are a large number of variables (24 in total) which need to be fitted if an exact solution is to be found (Table 3.4).

A number of approaches were taken in order to fit this data. The first and largely unsuccessful attempt was to fit all variables listed in Table 3.4 to equation 3.40. This is achieved using the built-in MATLAB fitting function which, by default, uses the non-linear least squares method to fit a dataset to a pre-defined model. Major problems arose due to both the large number of variables involved and the range of their respective impacts to the overall current for a given S_{ox}. For example, when $S_{ox} < -3$, the contribution of the j_{DE} is essentially 0.

We also encountered the obstacle that such fitting programs are generally unable to overcome the problem of localised minima. The fitting procedure works by changing the starting value in an iterative process until a decrease in the residual squares is no longer achievable. This can be problematic when both local and global minima are present. Hence, it is advisable to test a wide variety of starting values over a sensible range. However, for multivariant problems, the fitting procedure becomes computationally exhaustive very fast. If 10 starting values are tried for every variable, then there are 10^{24} possible combinations which need to be calculated and tracked.

The model is therefore simplified in the following ways:

- In section 3.4.1 we showed that the SiW_{12} example case is verifiable, in the sense that the reduction potential accurately behaves as predicted and that we can calculate the distribution of species for any given S_{ox}. We therefore treat the concentrations of species as constants for a given S_{ox} based on a modified form of equation 3.28 that includes five oxidation states.

- In section 3.4.1 we also presented two different ways of calculating the standard rate

constant for each redox reaction. We use this data as starting values in the least squares fitting procedure.

- From a Tafel plot at $S_{ox} = -0.5$ it was found that the limiting current density can be approximated as 0.567 mA cm^{-2} mM^{-1}. Since no significant changes in molecule size or solvation shell are expected [145] and since the total concentration of SiW_{12} is small, the limiting current is assumed to be directly proportional to the concentration for all oxidation states. Hence, we apply this relation to all limiting current variables listed in Table 3.4. For instance, if A = 1 mM, prior to fitting $j_{l,c(AB)} = 0.567$ mA cm^{-2}.

- As the SiW_{12} redox couples are well separated and because the potential range of the Tafel plots studied herein do not obviously exhibit characteristics associated with more than two redox reactions occurring simultaneously, we simplify equation 3.40 to include only the two most relevant redox reactions for a given S_{ox}. This is achieved using the following conditions:

  - If $A+B+C > B+C+D$ and $A+B+C > C+D+E \Rightarrow j \approx j_{AB}+j_{BC}$
  - If $B+C+D > A+B+C$ and $B+C+D > C+D+E \Rightarrow j \approx j_{BC}+j_{CD}$
  - If $C+D+E > A+B+C$ and $C+D+E > B+C+D \Rightarrow j \approx j_{CD}+j_{DE}$

- Sensible bounds were placed on all variables. We know, for instance, that the limiting anodic current cannot be negative and is also probably not more than twice the value calculated from the Tafel plot (as described above), i.e. not more than $2 \cdot 0.567$ mA cm^{-2}mM^{-1}. Likewise, the limiting cathodic current is likely between 0 and $-2 \cdot 0.567$ mA cm^{-2}mM^{-1} and the transfer coefficients are likely between 0 and 1. All of the standard rate constants are likely between 10^{-1} cm s^{-1} and 10^{-5} cm s^{-1}.

Determination of the kinetic and mass transport parameters of SiW_{12} over a wide range of reduction potentials

The total data collected amounts to 800 Tafel plots, which for obvious reasons cannot be displayed here, but an illustrative sample of the data is displayed in Figure 3.21. Each of the Tafel plots exhibits features which justify our approach over a typical Tafel plot analysis:

- $U = -0.75$ V vs SHE: The cathodic branch profile does not exhibit typical behaviour for a single-electron reaction. On the anodic branch, the limiting current is reached

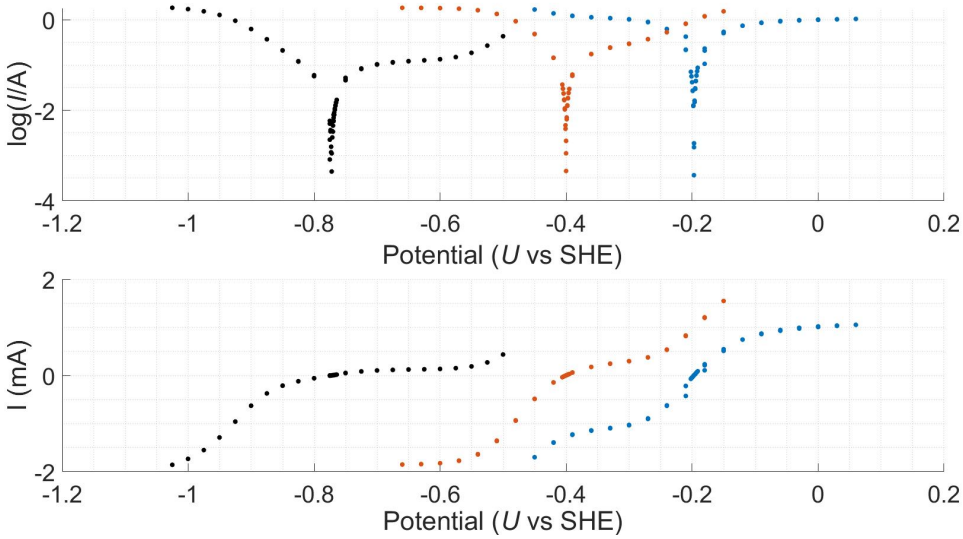

Figure 3.21: Selected Tafel plots of a SiW_{12} solution with different potentials. The top and bottom graphs are the same data in semi-log and non-logarithmic representations, respectively.

at very low overpotential due to the low concentration of $SiW_{12}(-2)$. A typical Tafel analysis would be prone to error in this case, because the region in which the reaction is purely under kinetic control is very small. Additionally, at high overpotential the contribution of j_{BC} becomes significant.

- $U = -0.40$ V vs SHE: The anodic branch exhibits behaviour of two reactions with different standard reduction potentials.

- $U = -0.20$ V vs SHE: The cathodic branch exhibits behaviour of two reactions with different standard reduction potentials.

In each of these cases, the potential range of the segment that would be analysed in a typical Tafel analysis is small and therefore evaluation of the kinetic parameters is prone to error. Figures 3.22 - 3.24 show kinetic and mass transport parameters derived from the 800 Tafel plots generated throughout the experiment. As anticipated, Figure 3.22 shows that the spread of values for k^0 for any given redox reaction is quite small. There are several outliers, which are likely due to erroneous fitting. However, other values which are inconsistent with the trend, such as the increase in k^0 for the $E \rightleftharpoons D$ at an S_{ox} of around -0.9, could be due to the effect of slight temperature changes in the system. Even though the temperature was not controlled in this experimental setup, the results are remarkably consistent to themselves

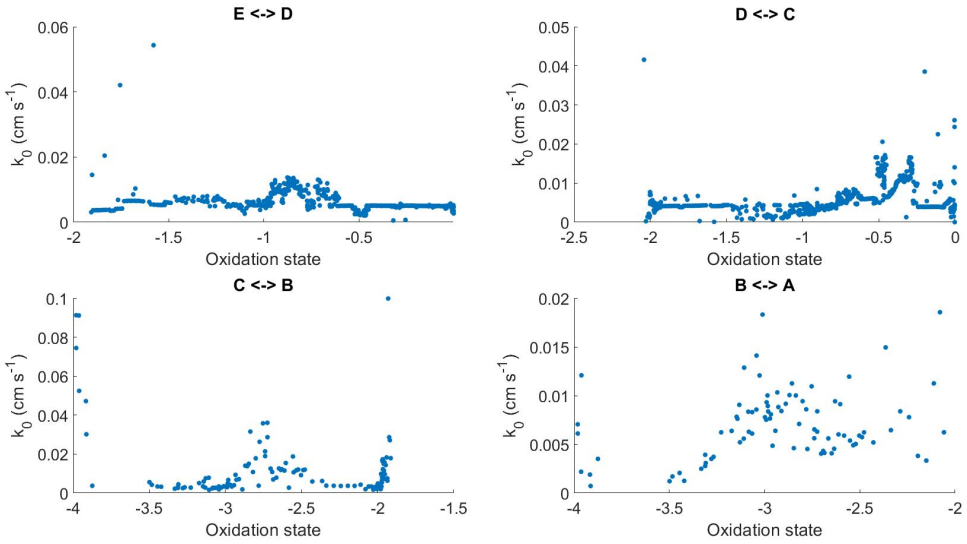

Figure 3.22: Fitted values for the standard rate constant of each reaction.

and to results reported in the literature [1, 2]. The intention here is to illustrate that useful information about an electrochemical system with multiple associated redox couples can be easily and accurately determined using the methods described in this chapter.

It is apparent that as the S_{ox} decreases, the data is generally more scattered. This is especially true for the values of the electron transfer constant for the $B \rightleftharpoons A$ reaction. One possible explanation for this is that oxygen ingress leads to reoxidation of the POM as the Tafel plots are being recorded. This seems likely, given that the purge gas used in this experiment was provided from an in-house system, generated through a pressure swing absorption method, which leads to a relatively low purity compared to distillation. Furthermore, it is expected that oxygen from the lab atmosphere permeates the Norprene tubing leading to and from the flow cell to a certain extent. Additionally, at certain points U of the solution is in the region of -1 V vs SHE, so the thermodynamic driving force for oxidation is significant.

Another possible explanation is that at such low potentials at least some hydrogen was generated at both the rotating disk electrode surface and the flow cell electrode surface. As a consequence of the competing reaction, the data at low potentials may be erroneous. Data for the $B \rightleftharpoons A$ reaction at S_{ox}s < -3.0 supports this hypothesis. At this point, with decreasing S_{ox}, the limiting cathodic current increases much faster than anticipated (Figure 3.23). The peak (most negative) values associated with the $B \rightleftharpoons A$ reaction are also much higher than that observed for the other reactions.

The limiting current generally behaves as expected, as shown in Figure 3.23. For example,

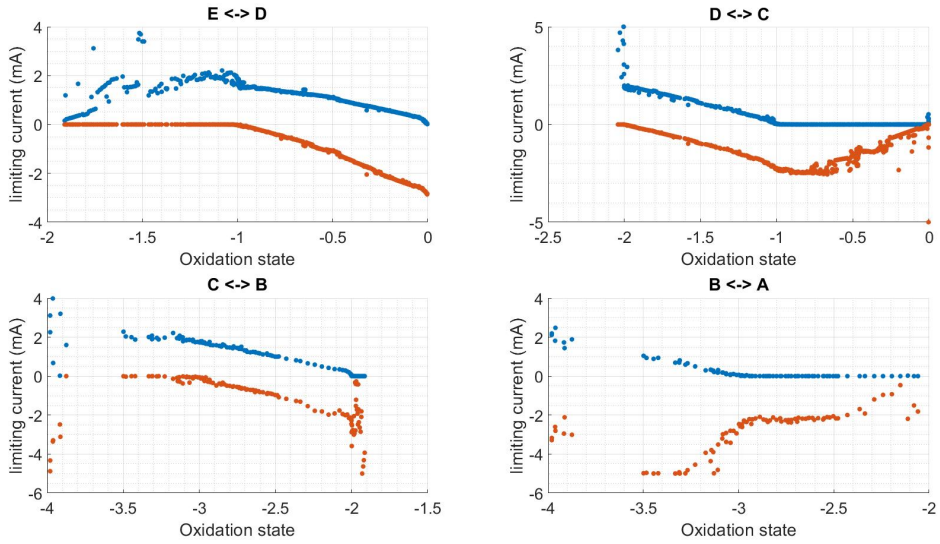

Figure 3.23: Fitted cathodic (orange) and anodic (blue) limiting currents for each reaction.

at $S_{ox} = 0$, the limiting current for the anodic process of the $D \rightleftharpoons E$ reaction is essentially 0. As the S_{ox} decreases, the magnitude of the limiting currents for both the anodic and cathode processes increases linearly. They are roughly equal when $S_{ox} = -0.5$ and the limiting current for the cathodic process drops to 0 when $S_{ox} = -1$ and the limiting current for the cathodic process is at a maximum. At this point the concentration of species $SiW_{12}(0)$ (E) in solution is basically zero, so the limiting cathodic current for the $D \rightleftharpoons E$ remains at zero. Also, the concentration of species SiW_{12}(-1) (D) decreases as the S_{ox} decreases to $S_{ox} = -2$, meaning that the limiting current of the anodic process also decreases (roughly) linearly towards 0. The main outlier is the cathodic process for the $D \rightleftharpoons E$ reaction. Given that these values were generated using a least squares approach, the values presented in Figure 3.23 provide evidence that supports our interpretation of the electrochemical system.

The transfer coefficients were derived as part of the procedure and are shown in Figure 3.24. There is no clear trend or pattern to the reported values. The values associated with the $D \rightleftharpoons E$ and $C \rightleftharpoons D$ reactions have a reasonably low spread and show that the reaction is approximately symmetrical regardless of S_{ox}. The values for the $C \rightleftharpoons B$ reaction are less consistent and the sum of the transfer coefficients for any given S_{ox} is less than one. This potentially indicates that the rate limiting step for the $C \rightleftharpoons B$ reaction is not an elementary electron transfer reaction.

The transfer coefficient values for the $B \rightleftharpoons A$ seem to diverge as the decreases (α_{AB} increases while β_{AB} decreases). As can be seen in Figure 3.9, the standard potential for this

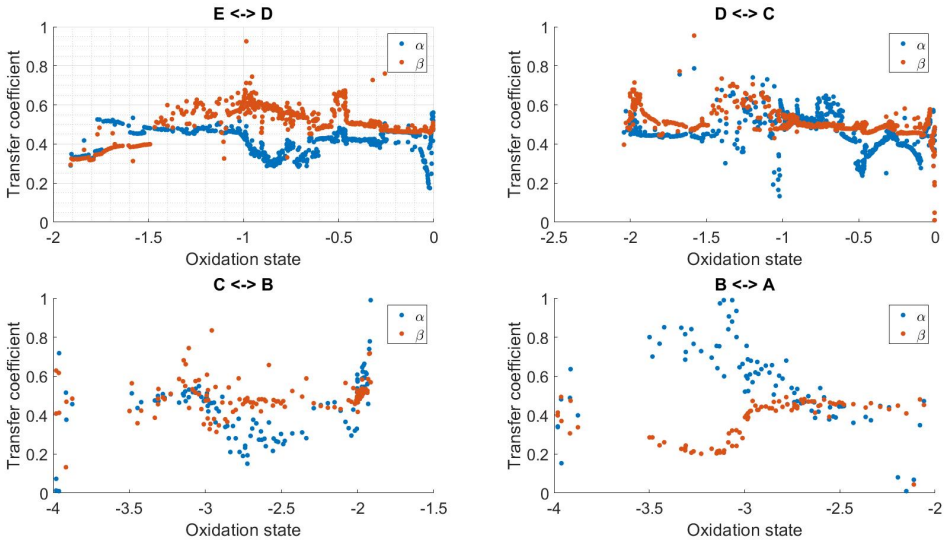

Figure 3.24: Anodic (blue) and cathodic (orange) charge transfer coefficients for each reaction.

reaction is -0.85 V vs SHE. Additionally, there is a plateau present on the cathodic sweep at -1.15 V vs SHE and a corresponding plateau on the anodic sweep at approximately -1.1 V vs SHE, indicating that this reaction is reversible (to some extent). The plateau is attributed to either the adsorption of hydrogen onto the electrode, or a reduction of SiW_{12}(-4) to SiW_{12}(-5). A further unresolved feature forming at -1.25 V vs SHE (without a corresponding anodic peak/plateau) is attributed to hydrogen evolution, since this process is irreversible under the experimental conditions described in the caption of Figure 3.9.

The reactions which are accounted for to fit the data are SiW_{12}(-4) $\rightleftharpoons$ SiW_{12}(-3) and SiW_{12}(-3) $\rightleftharpoons$ SiW_{12}(-2). However, the processes occurring at -1.15 V and -1.1 V vs SHE are not. At an of $\sim$ -3.5 ($U \leq$ -0.85 V vs SHE) this is problematic because the data accumulated on the cathodic branch of the Tafel plot will be influenced by the reactions centred around at -1.15 V and -1.1 V vs SHE.

In other words, the fitting procedure is attempting to find the best fit for a process which involves three or four reactions to the equation $I = I_{AB} + I_{BC}$. In this case, the Tafel plot is asymmetrical, with the current response being more pronounced on the anodic branch. This manifests as a decrease in the cathodic transfer coefficient and an increase in the anodic transfer coefficient, as this leads to the best fit. .

3.5 Conclusion and outlook

A description of the reduction potential and distribution of species at any given oxidation state for species with multiple associated redox couples has been detailed. An explicit solution was presented for species with two associated redox couples (i.e. three possible oxidation states), which allows for direct calculation of S_{ox} and the concentration of species in different oxidation states from the reduction potential and vice versa.

For species with more than two redox couples, the situation is more complex. No general solution for any number of redox couples was found that relates the S_{ox} to the reduction potential. An alternative solution was presented instead, which involves calculating the concentration of species and the S_{ox} for a defined potential window and using the results as a lookup table.

Solutions of SiW_{12} in NaCl (aq., 1 M) were gradually reduced in an electrochemical cell and the reduction potential was measured at various different S_{ox}s. In addition, current-overpotential measurements were recorded in a stationary solution and on a rotating disk electrode. The data from these experiments shows that the kinetic parameters (i.e. the exchange current density and limiting currents) as well as the reduction potential are consistent with the values predicted by our description of the underlying thermodynamics.

Furthermore, useful electrochemical information (e.g. electron transfer constants, limiting currents and transfer coefficients) about the investigated system was extracted by rigorous application of thermodynamic principles. This also provides insight into how these variables may evolve as the S_{ox} changes.

The next steps might involve testing various other electrochemical systems with two or more redox couples with increasing complexity. This can include closer spacing of standard reduction potentials, species with proton coupled electron transfers, etc. Results could then be compared to elucidate if the concepts described here yield similarly accurate predictions for more complex systems.

Chapter 4

A redox flow battery electrochemical model

Author's note

The model described here was intended to be a significant improvement upon the capital cost calculator described in chapter 2. The driving force for this decision was to demonstrate further that the theory developed in chapter 3 could be used to accurately simulate the operation of a redox flow battery containing active species with multiple redox couples. The model was developed during the first and second lockdowns of the COVID-19 pandemic, and access to on-site university resources was either wholly unavailable or severely restricted.

Regretfully, there was not enough time to properly verify the predictions of this model against experimental results in the laboratory. I decided that the best solution would be to attempt to verify the model against data that our group had already published.[2] The impact of this unanticipated situation means that several assumptions about the nature of the flow battery had to be made.

Despite these limitations, I felt it might be helpful to include a full description here so that anyone attempting a similar project can use this as a point of reference.

4.1 Introduction

As the demand for renewable energy generation increases, the need for cost-effective, large-scale energy storage solutions rises. This requirement results directly from the intermittent nature of renewable energy sources such as solar and wind energy. Of the electrochemical energy storage devices available, RFBs are a competitive contender for energy storage options; in many cases, they are already being commercialised on a large scale. The most well-known RFB is undoubtedly the ($VRFB$), but many chemistries are reported in the literature.[59] Examples of systems that employ highly soluble large metal-oxide clusters, fullerenes, organic molecules, and numerous transition metal complexes are available in the literature and discussed to some extent in chapter 2.[1, 2, 20, 78, 125, 126, 146, 147]

The $VRFB$ is by far the most investigated system, and there is no shortage of literature data about almost every aspect of the system. Likewise, the vast majority of RFB models published to date are for the $VRFB$. The variety and scope of $VRFB$ models in the literature are enormous. For example, Knehr *et al.* produced a highly sophisticated model of the membrane-electrolyte interface, incorporating the effects of crossover of all species, including water, due to convection, diffusion and migration.[148] They were able to predict the ΔU of a charge/discharge cycle with a 1.83% error and the capacity loss over 45 cycles with an error of 4.2%. Shah *et al.* produced a model with the specific intention of describing the (HER) at a $VRFB$ anode during charge. Describing the anode as a 2D object, they calculated the volume of H_2 evolution with respect to the distance from the current collector and the inlet, including the formation of bubbles and the effect on the flowfield and efficiency.[149] Highly detailed component-specific modelling is suitable for assisting research of the specific components which are modelled, but due to their complexity, they are computationally expensive and often do not describe the overall system properties. Consequently, they are generally unsuited to the investigation of large RFB cell/stack performance over a long period.

As several authors point out, the error in their models typically arises from not accounting for one or more loss mechanisms. Barton and Brushett published a one-dimensional $VRFB$ stack model, which evaluates most of the loss mechanisms typically associated with the $VRFB$. These include shunt currents, hydraulic pressure losses, membrane crossover, mass transport, and kinetic effects.[150] They also provide a publically available graphical interface to their model so that virtually all parameters can be changed as seen fit by a prospective user in order to aid their research. Importantly, they note that, given the conflicting data in the literature, it is challenging to model many of the parameters associated with RFBs

in a meaningful way. Perhaps this is primarily due to the use of electrochemical techniques, which are not entirely suitable for the investigation of RFB properties. For instance, due to the improper analysis of cyclic voltammograms, the reported k^0 for the V^{II}/V^{III} reaction vary by at least three orders of magnitude.[151]

Viswanathan et al. published a comparative analysis of the different generations of the $VRFB$ with the Fe-Cr RFB and Fe-V RFB.[123, 152] Their model accounts for electrochemical, pumping, and shunt current losses; however, as with many capital cost models, they do not provide a significant amount of detail regarding the electrochemical calculations, choosing instead to focus heavily on the economic aspects of the system.[122, 124]

Despite the many models presented in the literature, we are unaware of any models that describe multi-redox centre electrolytes, such as POM or modified fullerene RFBs. This is partly due to the use of multi-redox centre species in RFBs being somewhat uncommon, but also potentially due to the added complexity of describing a system which necessitates the use of the theory described in chapter 3 to be implemented. Also, multiple Butler-Volmer (current-overpotential) expressions per electrode appropriately describe these systems' thermodynamic, kinetic, and mass transport properties.

Herein a one-dimensional segmented transient model which allows for comparison of a variety of RFB chemistries, including multi-redox centre species, is described. The model assesses the performance of RFB systems based on the thermodynamic, kinetic, mass transport parameters, and capacity loss mechanisms.

4.2 Model Description

4.2.1 Reduction potential

The reduction potential is desribed by the Nernst equation, or by the series of Nernst equations and the theory desribed in 3 where appropriate.

4.2.2 Calculation of the operational Parameters

Ohmic overpotential

Ohmic losses are easily calculated assuming that (U_{int}) is homogenous across the entire electrode and that there is an ohmic drop between the electrode and the terminal (point of contact to the external circuit). In reality, an ohmic drop would occur within the felt and depend on its conductivity and the distance from the current collector. However, given that carbon felt usually has reasonably high conductivity and that the current collector connects to the felt across the entirety of the geometric area, this is assumed to be negligible. The ohmic overpotential η_Ω is related to the (R_Ω) by

$$\eta_\Omega = IR_\Omega \tag{4.1}$$

Kinetic overpotential

The kinetic overpotential is calculated by solving the Butler-Volmer equation(BVE) for each electrochemical reaction at the electrode interface. For an electrochemical reaction where the rate-determining step is an elementary electron transfer process, the kinetic current overpotential relationship is described by:

$$I = I_0(e^{\alpha f\eta} - e^{-\beta f\eta}) \tag{4.2}$$

where $f = nF/RT$, $\eta = (U_{int} - U)$, and α and β are the anodic and cathodic charge transfer coefficients respectively.

Both the exchange current, I_0 and U are subject to change throughout RFB operation depending on the S_{ox}. For a reaction with an elementary charge transfer process as the limiting step I_0 is given by:

$$I_0 = nFk^0(C_O^\alpha C_R^\beta) \tag{4.3}$$

where C_O and C_R are the concentrations of species in the oxidised and reduced state, respectively, k^0 is the standard rate constant for the rate-determining step.[76, 153]

When the electrolyte has multiple redox centres, the BVEs for each reaction are solved independently, and it is assumed that for a given (η), the resulting current from each possible electrochemical reaction does not interfere with the resulting current for any other reaction on the same surface. Therefore, the total current at the electrode is calculated by the sum of all individual currents. For example, for an electrolyte with three accessible redox states (A, B, C) where

$A + e^- \longrightarrow B$

$B + e^- \longrightarrow C$

The (I) - η relation be described by:

$$I_{AB} = n_{AB} F k^0_{AB} (C_b^{\alpha_{AB}} C_a^{\beta_{AB}})(e^{\alpha_{AB} f\eta} - e^{-\beta_{AB} f\eta}) \tag{4.4}$$

and:

$$I_{BC} = n_{BC} F k^0_{BC} (C_c^{\alpha_{BC}} C_b^{\beta_{BC}})(e^{\alpha_{BC} f\eta} - e^{-\beta_{BC} f\eta}) \tag{4.5}$$

The total current is then:

$$I = I_{AB} + I_{BC} \tag{4.6}$$

There are two main operational modes depending on the context in which the RFB is being used. Firstly, on the lab scale, researchers will often cycle RFBs galvanostatically between an upper and lower cut-off potential. Secondly, in a real-world application, the load on the RFB will depend on the supply/demand of power, meaning that the power and current may fluctuate with time. For both of these scenarios, varied power and galvanostatic operation, it is not possible to rearrange equation 4.6 such that η can be described as a function of I. Moreover, it is not possible to directly calculate the individual contributions of I_{AB} and/or I_{BC} for a given total current/power requirement. A brute-force search approach is employed:

1. The user defines a suitable range for the electrode potential e.g. $\{U_{int} \in \Re : -0.3V \leq U \leq +0.3V\}$

2. An array of discrete values which satisfies the range is generated, the values of which are inputted into equations 4.4 and 4.5 to generate a lookup table for $\eta = f(I)$.

3. The value of η which satisfies the input value i or P can then be easily interpolated, and the individual contributions of i_{AB} and i_{BC} determined by inputting η into equations 4.4 and 4.5.

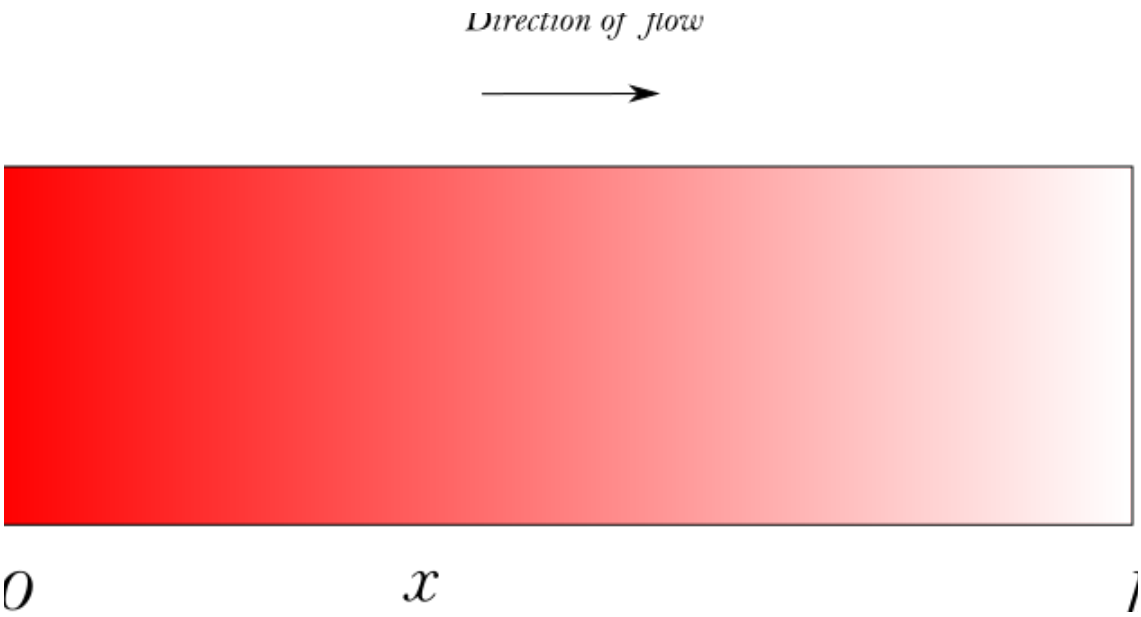

Figure 4.1: Qualitiative depiction of the concentration profile in a cell, where 0 is the position of the inlet, and l is the position of the outlet. The fading colour represents a decrease in active species due to an electrochemical reaction

When the input parameter is P, the calculation must satisfy the requirement:

$$P = I(U + \eta_{kin} + \eta_{MT} + \eta_{\Omega} + \eta_{Mem}) \tag{4.7}$$

Where $\eta_{(kin,\, MT,\, Mem)}$ are the overpotentials associated with the kinetics, mass-transport, and membrane conductivity, respectively.

Mass transport: forced convection

For a cell of length l, the concentration at a given point (x) is a function of the inlet concentration at time t of the active-species C_{in}, (n_V), and I. Schematically this is represented by Figure 4.1. Especially in the case of low flow rates and high current density, the concentration at any given point along the length of the electrode $C_i(x)$ will be lower than C_{in}. An accurate description of the concentration profile across the cell is necessary for understanding the mass transport overpotential.

A plug flow approach is used to model the flow and concentration profile throughout the cell.[154, 155]

1. The electrode is split up into evenly distributed segments of uniform fixed volume V_s (Figure 4.2).

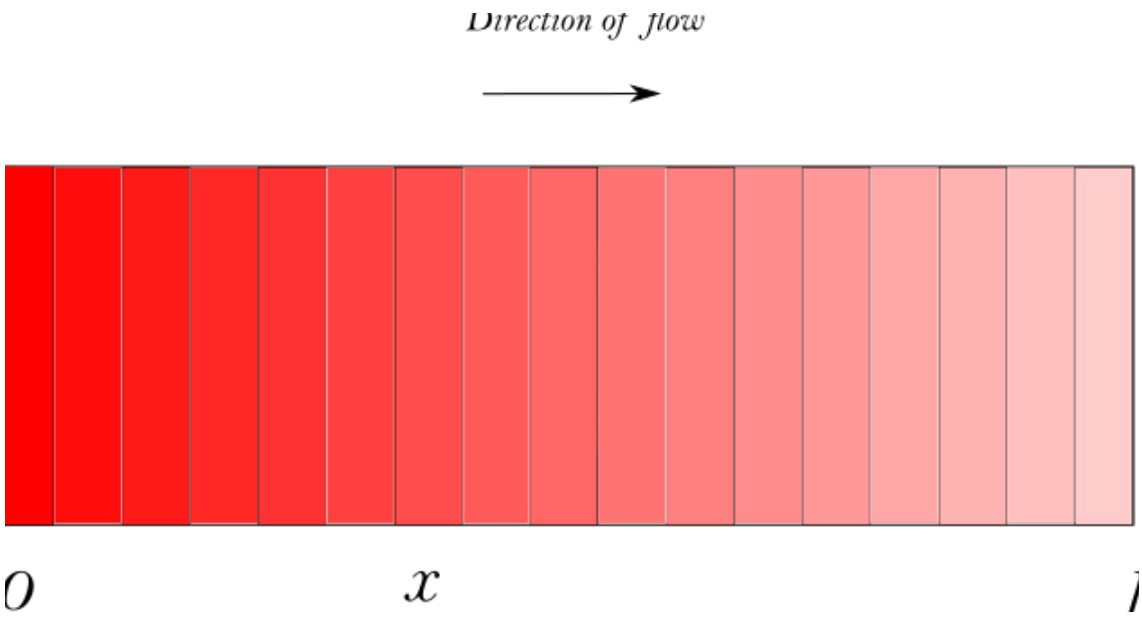

Figure 4.2: depiction of the concentration of active material in a segmented cell. As the electrolyte progresses through the active material is diminished.

2. For every increment of time (tick) that passes (t_r), the electrolyte from the tank enters the cell as a discrete volume (plug) equal in size and shape to the electrode segment. The electrolyte resides in the segment for t = t_r.

3. Equations 4.4, 4.5, and 4.6 are solved for each segment and tick.

4. On the next tick, the plug moves to the consecutive segment and the corresponding Q transferred is used to update S_{ox}.

5. The updated S_{ox} is used to calculate U and the distribution of species according to the procedure described in chapter 3.

6. The process is repeated until a cut-off condition is met.

This model assumes no axial mixing (segment to segment), but there is perfect mixing within a segment and, therefore, uniform current density.

The flow rate depends on (t_r) according to:

$$n_V = \frac{V_s}{t_r} \tag{4.8}$$

Where V_s is the volume of each segment. Plug flow is generally used to describe the laminar flow of material through a tubular reactor, and for that application, the model is

a reasonably good approximation. Application of the plug flow model to flow through a compressed carbon felt electrode can only be valid if the flow is laminar and n_V is even over the entire cross-section. There are many circumstances in which this may not be the case; for instance, the phenomenon of channelling in porous electrodes, potentially leading to preferential flow paths within the porous structure, has also been well documented.[146] The effects of bubble formation from gassing reactions could block certain flow paths, and the uneven pore distribution could also lead to the formation of preferential flow paths. Despite these effects on the flow path, several authors have shown that the plug-flow model can be used to approximate flow in a carbon-felt electrode.[156, 157]. Furthermore, numerous models employ the use of Darcy's Law, or the Kozeny-Carmen equation to describe flow through carbon felt, both of which are only valid under the condition of laminar flow.[149, 150, 158–162]

Additionally, this approach has been shown to have validity in an experimental setting. Typically this is achieved by using a printed circuit board with a segmented current collector placed in an RFB to record the local current density for a given η. If the assumption is made that the electrode properties (i.e. surface properties, contact pressure, electrolyte penetration) are constant across the entire electrode, then the resulting localised current density can be used to infer differences in concentration throughout the electrode. There are a handful of studies which have been conducted on this topic. Gerber et al. measured the deviation from average current across a $VRFB$ cathode for differing state of charge (SOC) at normalised flow rates between $0.5 - 2.5$ mL min^{-1} cm^{-2} and found that, in general, the current density distribution is high and does not seem to correlate to a gradient characteristic of the cell.[163]. However, they note that the tested felts original width varied between $4.8mm - 5.4mm$, leading to an ununiform local compression of $72\% - 81\%$ of the original thickness inside of their test cell, to which they attribute the non-uniform distribution of current density. When the flow rate and current are increased, the distribution of current density across the cell, whilst more pronounced due to the higher overall current, is indeed more uniform. Clement et al. conducted a similar study which focused primarily on carbon paper. However, they also conduct high current density experiments on carbon felt 400 and 450 mA cm^{-2} for felt compressed to 75% and 25% of its original thickness and observed a current distribution which varies uniformly with distance from the inlet, thus indicating a concentration gradient with the same characteristic. The flowfield for the felt compressed to 25% original thickness shows a less uniform deviation in current. However, this compression level makes little difference on the limiting current and would lead to a pressure drop far too high for use in a commercialised RFB. [162] The plug flow model presented above reason-

ably approximates macroscopic flow through an electrode when the compression is evenly distributed.

Mass transport: electrode-electrolyte interface

To model the mass-transport characteristics of the electrode-electrolyte interface, the shortened form of the Butler-Volmer equation (4.2) is replaced by the complete form, which includes terms for the time-dependent interface concentration $C_i(0,t)$

$$I(t) = I_0 \left(\frac{C_R(0,t)}{C_R^*(t)} e^{\alpha f \eta} - \frac{C_O(0,t)}{C_O^*(t)} e^{-\beta f \eta} \right) \tag{4.9}$$

where the notation (x,t) indicates the distance from the electrode interface and the dependence on time. $C_i^*(t)$ is the bulk concentration of species i at time t. Whilst complete, this form needs to be modified further due to the difficulties associated with defining $C_i^*(t)$ and $C_i(0,t)$ in the void spaces of a 3-dimensional electrode with a large distribution of pore sizes. It is, therefore, useful to relate the bulk and interface concentration terms to the mass-transport limiting current, which is considerably easier to determine experimentally.

The current at an electrode interface under steady-state mass transport conditions can be described by:

$$\frac{I}{nFA_{el}} = m_i[C_i^*(t) - C_i(0,t)] \tag{4.10}$$

where m_i is the mass transfer coefficient for the species i, and A_{el} is the geometric area of the electrode. The limiting steady-state current is obtained when the interface concentration is 0 and is therefore given by:

$$I_l = nFA_{el} m_i C_i^* \tag{4.11}$$

Equations 4.10 and 4.11 can be combined to give:

$$\frac{C_i(0,t)}{C_i^*} = 1 - \frac{I}{I_l} \tag{4.12}$$

Substitution of 4.12 into 4.9 gives:

$$I = I_0 \left[\left(1 - \frac{I}{I_{l,a}} \right) e^{\alpha f \eta} - \left(1 - \frac{I}{I_{l,c}} \right) e^{-\beta f \eta} \right] \tag{4.13}$$

Where the subscripts a, c indicate the current associated with the anodic and cathodic pro-

cesses, respectively. Equation 4.13 can be rearranged for I:[76]

$$I = \frac{I_0(e^{\alpha f \eta} - e^{-\beta f \eta})}{I_0(\frac{e^{\alpha f \eta}}{I_{l,a}} - \frac{e^{-\beta f \eta}}{I_{l,c}}) + 1} \tag{4.14}$$

Analogously, the same procedure is applied to equations 4.4, 4.5. Modifying equation 4.6 to include the mass-transport overpotential, and for an electrolyte with an arbitrary number of redox centres, the total current can be calculated as:

$$I = I_{AB} + I_{BC} + ... = \sum_k I_k \tag{4.15}$$

Where I_k is calculated by equations of the same form as equation 4.14, and according to the procedure in section 4.2.2.

Mass transport: limiting current

The limiting current for a porous electrode in an RFB is a function of numerous parameters. For a complete understanding of the mass transport processes, one must account for the individual fluxes as described by the Nernst-Planck equation:

- Forced convection through the electrode due to pumping
- Natural convection within the electrode due to temperature differences and electrolyte density
- Migration as a function of electrode potential and mobility
- Diffusion as a function of concentration gradients and diffusivity

Deconvolution of these parameters is beyond the scope of this model; therefore, several simplifications are made. Firstly, since it is assumed that the electrode potential is homogenous at any given point in time, migration within the void space of the electrode from one region to another is considered negligible. Secondly, due to the presence of large amounts of supporting electrolyte, we assume that the effect of migration of the active species from the bulk phase to the electrode surface is negligible. The solution is also considered to be isothermal and isochoric.

The $(\boldsymbol{J}_i)$ to the electrode surface as a function of diffusion and forced convection can be estimated in terms of a mass-transfer coefficient:

$$\boldsymbol{J}_i(x,t) = m_i C_i^*(x,t) \tag{4.16}$$

Under limiting mass-transport conditions (i.e. for a fast reaction or high overpotential), the 'instantaneous' limiting current (I_l) can be related to the flux by:

$$I_l = nF\boldsymbol{J}_i A_s = nFm_i C_i^*(x,t) \tag{4.17}$$

where A_s is the electrode's specific electrochemically active surface area. Note the specification of 'instantaneous' limiting current in order to distinguish it from the steady-state limiting current, which can be derived from equation 4.17.[76]

$$I_l = nFm_i C_i(0,t) A_s e^{\left(-\frac{m_i c_i(x,t)A}{\nu}x\right)} \tag{4.18}$$

Whilst equation 4.18 is valid at the steady-state limit of mass-transport, for cases where the $I < I_l$, it predicts a concentration profile which is not representative of the real system. This model calculates the limiting current on the segment level per tick according to equation 4.17. Provided that the segments and t_r are sufficiently small, the analogous physical system would not exhibit an appreciable change in C_i, and therefore I_l would also not change appreciably over this time/length scale.

The mass-transfer coefficient for a species can be empirically determined by recording the limiting current under a given set of conditions. Schmal *et al.* measured the limiting current of 10 mM Ferricyanide solutions on a single fibre over a range of flow rates and related the (Sh) and (Re):[156]

$$Sh = \frac{m_i d}{D_i} \tag{4.19}$$

where d is the average fibre diameter.

$$Re = \frac{n_s d}{\nu} \tag{4.20}$$

The empirical relationship which they establish is:

$$Sh = 7Re^{0.4} (0.004 \leq Re \leq 0.2) \tag{4.21}$$

Higher flow rates were tested, but turbulent flow leads to fibre movement and thus higher limiting currents than predicted by equation 4.21.[156]. The single fibre and a carbon felt electrode are compared according to their respective characteristic lengths λ for a given flow

rate (n_s):

$$\lambda = \frac{n_s}{m_i A_s} \tag{4.22}$$

where A_s is the specific surface area.

λ is defined as the distance over which the concentration of reactant is lowered by $c_i(0)/e$. They find that the characteristic lengths for the felt electrode ($10 * 2 * 0.5$ cm^3) and single fibre are in good agreement: $\lambda_{fibre}/\lambda_{felt} = 0.9$.

Vatistas *et al.* conducted similar experiments and compared their results to that of others.[157] It seems that a logarithmic plot of Sherwood vs Reynolds numbers for carbon felt electrodes yields results with a similar slope, which can be well defined for a given system, but the spread of results over several systems is relatively large. Undoubtedly this is caused by a lack of standardised equipment and, according to Schmal, differing interpretations of how one calculates the Sherwood number for a given system.[156] Moreover, these studies have generally been conducted on electrolytes with rather low concentrations, on the order of 10 mM, which is not representative of a typical redox flow battery electrolyte.

More recently, Xu and Zhao determined a pore-level mass-transfer coefficient for a $VRFB$ with vanadium ion concentrations varied between $0.125\text{M} - 1.5\text{M}$.[159] They initially establish a means of calculating the effective diffusion coefficient for a porous felt electrode as an alternative to the widely used Bruggermann correlation.[148, 149, 158, 164] They, unfortunately, do not report the thickness of the felt used for determining the mass-transfer coefficient, and the provided diagram would indicate that it is substantially thinner than what is typically used in an RFB. It is assumed that this factor is accounted for in the correlation which they establish for determining the mass-transport coefficient:

$$Sh = 2 + 1.534Re^{0.912} (0.3 < Re < 2.4) \tag{4.23}$$

Membrane conductivity

Membrane conductivity is calculated based on the effects of diffusion and migration. Mass transport due to convection through the membrane can be assumed negligible due to the boundary layer condition observed for laminar flow. The flux through the membrane can be determined by the modified Nernst-Planck equation:

$$J_i(x) = -D_i \frac{\partial C_i(x)}{\partial x} - \frac{n_i F}{RT} D_i C_i(x) \frac{\partial \phi(x)}{\partial x} \tag{4.24}$$

For linear concentration and diffusion gradients across the membrane, equation 4.24 simplifies to:

$$J_i(x) = \frac{D_i \Delta C_i^*(x)}{l} - \frac{n_i F}{RT} D_i C_i^*(x) \frac{\Delta U_{sol}^*(x)}{l} \tag{4.25}$$

Where $\Delta U_{sol}^*(x) = U_{eq,c}^*(x) - U_{eq,a}^*(x)$

For the specific case where ($\Delta U = 0$), the flux across the membrane is due to diffusion only. The principle of electroneutrality forbids the build-up of net electric charge in either electrode compartment. Therefore, diffusion of a cation with charge z from the catholyte compartment to the anolyte compartment will be counter-balanced by a cation or cations with equal charge passing from the anolyte compartment to the catholyte compartment (for cation exchange membranes, the assumption is made that anion crossover is negligible). When $\Delta U \neq 0$, the diffusion of a cation through the membrane can be counter-balanced by the passage of $n\ e^-$ through the external circuit, under this condition, the net current through the membrane due to diffusion only may be non-zero.

Furthermore, electroneutrality dictates that the net current through the membrane is equal to the net current through the external cell. The net flux is the sum of the fluxes of all species in solution and is related to the net current by:

$$I_{mem} = \overbrace{-FA_{mem}\frac{\Delta U_{sol}}{l_{mem}}\sum_k z_k \mu_k C_k}^{I_{mig}} - \overbrace{F\frac{A_{mem}}{l_{mem}}\sum_k z_k D_k \Delta C_k}^{I_{diff}} \tag{4.26}$$

Where μ_i is the mobility of species i, and z_i is the charge on species i.

The migration term in equation 4.26 can be used to calculate the membrane conductance L_{mem}

$$L_{mem} = \frac{1}{R} = \frac{I_{mig}}{\Delta U_{sol}} = \frac{FA}{l}\sum_k |z_k| \mu_k C_k \tag{4.27}$$

Where I_{mig} is the through-membrane current due to migration, $I_{mig} = I - I_{diff}$.

The overpotential due to the membrane transport processes η_{mem} is then easily calculated using Ohm's Law.

Calculation of transference numbers t_i allows for the calculation of current due to migration of individual species in the solution.

$$t_i = \frac{I_{i,mig}}{I_{k,mig}} = \frac{|z_i| \mu_i C_i}{\sum_k |z_k| \mu_k C_k} \tag{4.28}$$

The mobility is calculated based on observed diffusion coefficients for various cations in Nafion 117 membranes as reported by Stenina *et al.*[84]

$$\mu_i = \frac{|z_i| F D_i}{RT} \tag{4.29}$$

Transferrence numbers of anions through Nafion membranes are sufficiently low to be ignored.

Determination of t_i provides the basis for analysing the effects of a changing pH during cycling on the cell's performance. Due to active-species crossover, it also allows self-discharge processes to be evaluated, which are observed in some RFB chemistries.

As discussed, the magnitude of active-species crossover is determined by equation 4.25. A linear concentration gradient across the membrane is assumed. If an active species crosses the membrane, it is generally the case that this will lead to a chemical reaction resulting in depletion of species i once crossover is complete. For example, for a species, i, which crosses from the catholyte to the anolyte compartment, $\Delta C_i = C_i(ca) - C_i(an)$, since $C_i(an) = 0$, $\Delta C_i = C_i(ca)$. It is assumed that the resulting chemical reaction is instantaneous once crossover has occurred. Luo *et al.* describe the self-discharge reactions which occur in a $VRFB$ as:[83]
At the catholyte cell compartment:

$$V^{2+} + 2\,VO_2^{+} + 2\,H^{+} \longrightarrow 3\,VO^{2+} + H_2O$$
$$V^{3+} + VO_2^{+} \longrightarrow 2\,VO^{2+}$$

and at the anolyte cell compartment:

$$VO^{2+} + V^{2+} + 2\,H^{+} \longrightarrow 2\,V^{3+} + H_2O$$
$$VO_2^{+} + V^{3+} \longrightarrow 2\,VO^{2+}$$

This model assumes that the volume of electrolytes in each tank remains constant throughout operation. In the case of RFBs, which has a very low pH, Diffusion coefficients for electroactive species through Nafion membranes can be found in the literature.[105, 165]

Hydrogen evolution reaction

Hydrogen evolution is an essential parasitic side reaction that occurs primarily in RFBs with acidic electrolytes on the anode during charge. A rigorous treatment of hydrogen evolution

in the $VRFB$ is given by Shah *et al.*[149] Comparatively, this model makes several simplifications. We assume that the HER accounts for a small amount of the total current at the electrolyte-electrode interface and can be described without mass transport considerations. The formation of bubbles is not considered. We also assume that HER is only significant on the anode and only during the charge. The Volmer-Tafel mechanism[153] is also assumed, meaning that the rate of hydrogen evolution can be accurately represented by the Butler-Volmer equation and therefore estimated by the Tafel equation for an insignificant anodic reaction:

$$I_{H_2} = I_{0,H_2} e^{\beta_{H_2} F \frac{\eta_{H_2}}{RT}} \tag{4.30}$$

Equation 4.30 is then considered in terms of equation 4.15 for the total current evaluation.

Symmetric electrolyte remixing

The key benefit of symmetric electrolytes, such as in the $VRFB$, is the ability to easily remix the electrolytes to reverse the effects of unwanted crossover through the membrane. To model this effect, we assume the presence of a specialised mixing chamber which perfectly mixes the anolyte and catholyte. Therefore, the resulting oxidation state of the anolyte and catholyte is the average of the individual electrolytes prior to mixing. Thus, for the anolyte/catholyte on remixing ($S_{an,ca}(R)$) is given by:

$$S_{an/ca,}(R) = \frac{S_{an} + S_{ca}}{2} \tag{4.31}$$

The oxidation state is calculated analogously to equation S_{ox} for the relevant active species. The R notation indicates that the electrolyte is remixed. The electrolyte may then require rebalancing to return the electrolytes to their initial S_{ox} values.

Rebalance mechanisms

Over long periods of operation, loss mechanisms such as oxidation by air ingress, HER, OER, or degradation of the electrolyte can affect the catholyte/anolyte disproportionately such that the accessible state of charge range ΔSOC decreases. For example, if one considers HER in isolation, the effect of the parasitic current is to decrease the SOC_{max} of the anolyte slightly over every cycle. On discharge, this imbalance leads to an increase in the SOC_{min} of the catholyte. Thus, not only does the capacity decrease, but the accessible SOC of the anolyte

decreases, and the accessible SOC of the catholyte increases, which encourages further HER and potentially OER. After some time, the imbalance of electrolytes needs to be addressed. The method of rebalancing is beyond the scope of most publications dealing with RFBs on the lab scale because they generally do not operate for a long enough period for this to become an issue or because the electrolyte balance is not of interest for the particular investigation.

The simplest way to address this problem in most systems is to use a rebalance cell. Acevedo and Stalnaker described a rebalance cell for the Fe-Cr RFB in 1983; however, the general principle of the design is extendable to all RFBs with aqueous acidic electrolytes.[166] In addition to the RFB stack, a cell with a hydrogen electrode is placed in parallel to the catholyte half cell. In their system, the catholyte becomes over-oxidised with cycling. To compensate, a hydrogen stream is supplied to the rebalance cell, where it is oxidised, thus reducing the catholyte solution.

The question of when a rebalance cell would be used in an RFB is somewhat tricky to answer. If it is used continuously, the rated power will not be as large, and the accessible capacity of the RFB would remain more consistent throughout its operation. However, since the rebalance cell is separated from the main electrolyte by a membrane, crossover of the electrolyte would occur continuously and lead to poisoning of the hydrogen electrode.[166] Conversely, if the rebalance cell is infrequently used, it would have to be larger so that rebalancing does not take an unreasonable time to complete. Attempting to model this behaviour would add a level of complexity which is not particularly useful for this investigation, so the assumption is made that, despite the importance of this element to long-term operation, the effects on RFB performance and the costs associated with a rebalance cell are small enough to be ignored.

It is therefore assumed that when a symmetric RFB electrolyte is remixed, as described above, the SOC of the anolyte and catholyte are returned to their initial values in the fully discharged state. For asymmetric electrolytes, the same effect occurs when the accessed states of charge deviate by some critical margin which will be defined for each system.

4.3 Verification

As discussed at the start of this chapter, there was not enough time to properly verify the model against experimental results in the laboratory. Since other experiments on flow batteries in this text have primarily focused on increasing the accessible capacity of various POMs, a complete electrochemical characterisation of those cells was not carried out. Using these cells as a reference to verify the model against would lead to a large number of assumptions

Species	catholyte concentration (M)	anolyte concentration (M)
$H_4PV_{14}{}^{5-}$	0.08	0
$SIW_{12}{}^{4-}$	0	0.088
Na^+	1.12	0
Li^+	0.60	1.336
Cl^-	1.005	1.000
$H_2PO_4{}^-$	0.32	0
H_3O^+	0.005	0.016

Table 4.1: Cyclic voltammetry cell details

being made about several key parameters (ohmic, kinetic, and mass transport parameters). Conversely, the 1400 cm^{-2} (referred to as the large cell) SiW_{12}/PV_{14} presented by Friedl et al. is comparatively well characterised.[2] This is because the work is the result of an ongoing investigation into the POMs under a specific set of conditions that are well understood. Therefore, the decision was made to verify the model against this cell to minimise the number of assumptions.

Comments on the description and conditions of the experiment used for model verification

The concentration of chloride in the catholyte and lithium in the anolyte are estimated, as an unknown amount of hydrochloric acid and lithium hydroxide were added to alter the pH to their starting values. The initial oxidation state is also heavily dependent on the effectiveness of nitrogen purging, and the age of the hydrazine solution, as the concentration of hydrazine in solution decreases over time due to evaporation. Therefore, the initial oxidation state of PV_{14} is estimated to be -1.5, as this provides the best fit.

From experimental observation, it is known that when PV_{14} is reduced as the pH rises. The reduction is proton-coupled. i.e. PV_{14} accepts a proton when reduced. Table 4.1 shows that the concentration of protons is much lower than the concentration of PV_{14}. We also know that the pH of the anolyte does not change appreciablly when cycling. Hence, we conclude that PV_{14} acts as a buffer.

Since the empirical relationship between S_{ox} and pH is known, but the acid dissociation constants for reduced PV_{14} are not, we calculate the ratio $H_4PV_{14}{}^{5-}/H_5PV_{14}{}^{4-}$ from charge balancing.

PV_{14} can be reduced by a maximum of 7 electrons from its initial state before becoming unstable. Provided that the empirical relationship $pH = -0.89S_{ox} + 1.1$ holds, the maximum possible pH for the catholyte is 7.33. However, the literature data shows that the

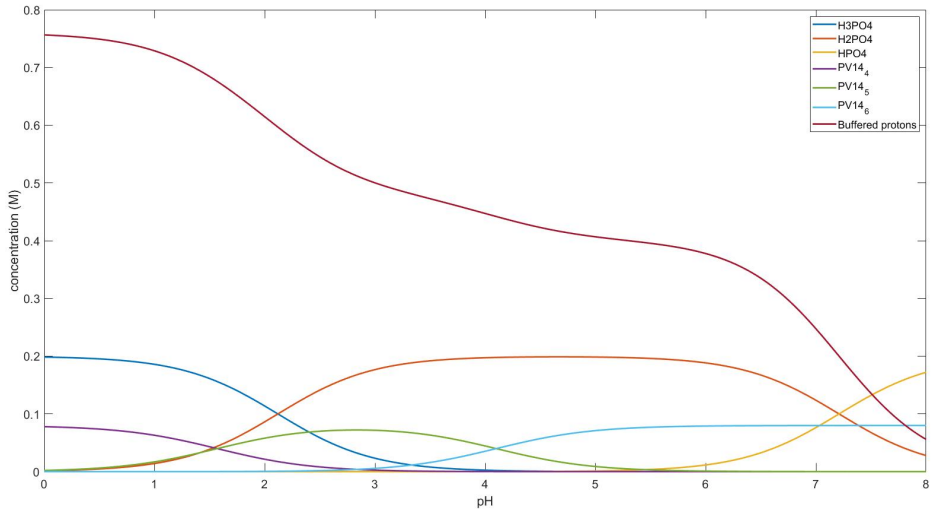

Figure 4.3: phosphate ion fraction over the pH range 0-8

lowest oxidation state reaches around -1.5. Hence, the maximum pH is around 2.5. Over this pH range, phosphoric acid can be accurately modelled as a diprotic acid. Hence, for any given $[H_3O^+]$, the fraction of H_3PO_4, $H_2PO_4^-$, and HPO_4^{2-} are shown in Figure 4.3 and are calculated according to:

$$f_{H_3PO_4} = \frac{[H^+]^2}{[H^+]^2 + K_{a1}[H^+] + K_{a1}K_{a2}} \tag{4.32}$$

$$f_{H_2PO_4^-} = \frac{K_{a1}[H^+]}{[H^+]^2 + K_{a1}[H^+] + K_{a1}K_{a2}} \tag{4.33}$$

$$f_{HPO_4^{2-}} = \frac{K_{a1}K_{a2}}{[H^+]^2 + K_{a1}[H^+] + K_{a1}K_{a2}} \tag{4.34}$$

where $K_{a1} = 10^{-1.772}$ and $K_{a2} = 10^{-6.418}$. [3]

The reactions and standard potentials for the anolyte are as follows:

$SiW_{12}(0) + e^- \longrightarrow SiW_{12}(-1)$ $\qquad U^o_{01}$ vs SHE = 0.05 V

$SiW_{12}(-1) + e^- \longrightarrow SiW_{12}(-2)$ $\qquad U^o_{12}$ vs SHE = -0.26 V

The reactions and standard potentials for the catholyte are as follows:

$PV_{14}(0) + 2\,e^- \longrightarrow PV_{14}(-2)$ $\qquad U^o_{02}$ vs SHE = 0.8 V

$PV_{14}(-2) + 5\,e^- \longrightarrow PV_{14}(-7)$ $\qquad U^o_{25}$ vs SHE = -0.6 V

Variable	value
I	11.2 A
A	1400 cm^{-2}
U_{max}	1.4 V
U_{min}	0.1 V
R_{Ω}	0.38
α (all reactions)	0.5
β (all reactions)	0.5
$k^0_{SiW_{12}}$ (all reactions)	10^{-2} cm s^{-1}
k^0_{PV14} (all reactions)	10^{-4} cm s^{-1}
t_r	2.0741 s
n_V	1350 mL min^{-1}
m_i (anolyte and catholyte)	5.86*10^{-4} m s^{-1}
L_{mem}	3.3258*10^3 S

Table 4.2: Standard variables for the SiW_{12}/PV_{14} RFB used in the model calculations.

Species	Diffusion coefficient (cm^2s^{-1})
Na^+	$1.31 * 10^{-6}$[84]
Li^+	$1.58 * 10^{-6}$[84]
H_3O^+	$5.3 * 10^{-6}$[84]

Table 4.3: Diffusion coefficients of various cations through a Nafion 117 membrane.

Information regarding standard variables is detailed in Table 4.2.

The diffusion coefficients of relevant cations through Nafion 117 are given in Table 4.3.

Figure 4.4 shows a voltage vs time plot for a typical cycle of the experimental cell vs the modelled cell. Given that various assumptions had to be made about the cell and electrolyte properties modelled and experimental data are in reasonably good agreement.

The significant difference between modelled and experimental results is that the model predicts that the battery will have flatter plateaus than it actually does. This is likely due to the established empirical relationship between pH and the oxidation state of PV_{14} being only a general estimate. In other words, it is suspected that the pH changes more than predicted by the model, which would cause a greater rate of change in the potential of the catholyte, and, therefore the voltage.

Another difference between the modelled and experimental data is the lack of an initial sharp decrease in voltage at the beginning of the discharge procedure. However, this difference is easily explained. The model immediately switches to the discharge procedure at the end of the charging procedure with no intervening rest period. So, the available material for

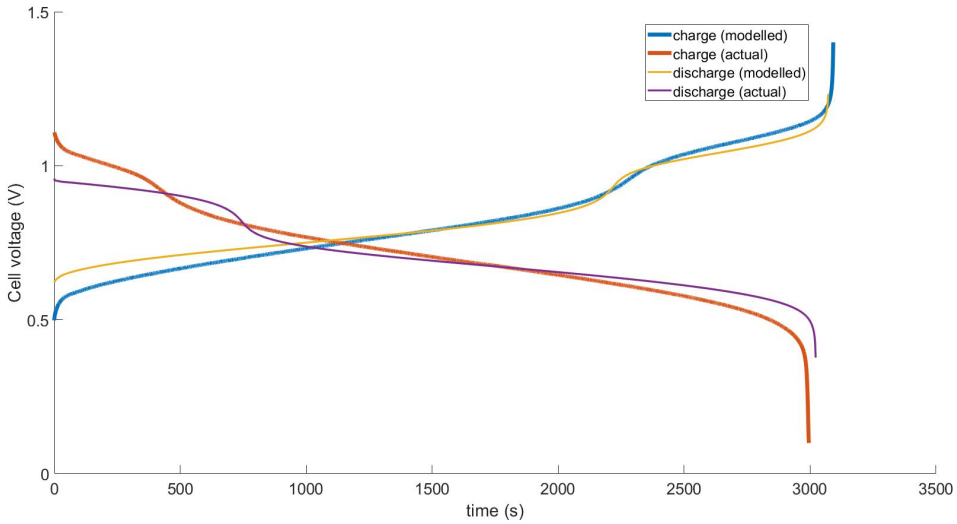

Figure 4.4: Charge/discharge voltage vs time for a typical cycle.

the discharge step is relatively high. However, there was a rest period in the experimental cell, so the starting conditions were different.

This is most easily seen in Figure 4.5. In this particular simulation, the current density is 80 mA cm^{-2} to exaggerate the phenomenon. On the top right plot, it can easily be seen that at the end of the charging procedure, the amount of PV_{14}(-2), and SiW_{12}(-2). Therefore, the overpotential is relatively low on the respective oxidation and reduction of those species.

A timelapse video of a typical cycle for modelling of the experimental cell is available here: `https://1drv.ms/v/s!AmTZRnAUzjfJhqlSy_wKXxFb4yNREw?e=GEbOkU`. The video details similar information to that in 4.5, but is representative of a typical cycle with a current density of 4 mA cm^{-2}.

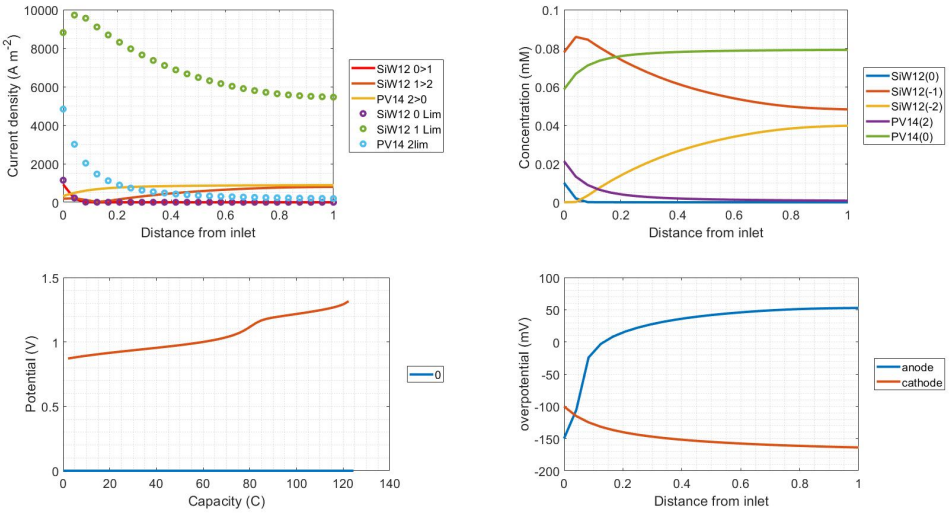

Figure 4.5: Top left: current density associated with a particular reaction (see legend) vs distance from the inlet. Top right: concentration of species vs distance from the inlet. Bottom lefr: Potential of the battery vs capacity (the legend indicates the number of seconds since the beginning of the charge (or discharge) step. Bottom right: Overpotential vs distance from the inlet. In this instance, overpotential refers to the potential difference between the electrode and the solution potential (determined by the oxidation state of reactants, which changes throughout the electrode).

4.4 Conclusion

An electrochemical model which accounts for the ohmic, kinetic, and mass transport characteristics of flow batteries was described and verified against the experimental results of a flow battery described in the literature.

The model is novel in that it can describe the behaviour of electrochemical species with more than two accessible oxidation states and shows how the electrolyte properties change as it passes through the cell. Provided that the electrolytes are described adequately, the model is agnostic towards redox flow battery chemistry, so it can be used to compare different electrolytes and make predictions about the effects that changes in programmable parameters would have on the operation and performance of the cell.

Conclusion

The primary objectives of this thesis were to contribute towards the understanding and development of POM mediated biomass fuel cells and POM redox flow batteries. In chapter 1, a method for characterising the kinetics of biomass oxidation by polyoxometalates was developed. The utilisation of this method showed that PMo_{12} is a reasonably good oxidation catalyst for biomass when the biomass is fully oxidised. However, it was also shown that as the biomass becomes progressively more oxidised, the effectiveness of the POM as a catalyst decreases significantly. This results in a solution which contains a difficult to separate mixture of partially oxidised biomass and POMs.

At present, the only strategy for fully oxidising the biomass is to leave the solution under aerobic conditions for an extended period of time. This process is not only time consuming, but is also an inefficient use of biomass as the chemical energy cannot be effectively utilised during this step. The utilisation of expensive catalysts (POMs) is also inefficient. An important step in the development of POM mediated biomass fuel cells is therefore an investigation into the mechanism of biomass oxidation by POMs. A better understanding in this area would allow the cause for the reduced rate of biomass oxidation to be identified and hopefully addressed.

An alternative route would be to test the effectiveness of other POMs as oxidation catalysts on the partially oxidised biomass. Isolation of the biomass from the POM could be achieved through addition of a TBA salt to the solution. After which the organic products could be isolated and characterised. Additional POMs could be introduced to the solution, and their effectiveness as oxidation catalysts could then be determined using the CP-OCV procedure developed in chapter 1. If a suitable catalyst is found, testing mixtures of different POMs would be the logical next step.

Employing the CP-OCV procedure on a wide variety of POM-biomass mixtures could help to identify suitable biomass oxidation catalysts. The technique is useful in that it can be largely automated using standard potentiostat software, and the required equipment should be available in any standard electrochemical lab. If multiple potentiostat channels and electrochemical cells are available then the utilisation of this technique should allow for a relatively quick screening of POM candidates.

The possiblity of utilising heterogenous catalysts for biomass oxidation was also briefly explored in chapter 1. As part of this effort, POMs were immobilised on a carbon felt electrode surface using a very simple procedure. Although the electrodes were not stable at elevated temperature (a requirement for biomass oxidation catalysis), it was shown that

the POMs were confined to the electrode surface and remained there over several hundred voltammetric cycles at room temperature. Due to the relative ease and success of this technique, further investigation is warranted. Optimisation of the technique should be a relatively straightforward process (at least initially), and the prospective researcher could investigate the effects of POM concentration, drying time, cation type, electrode type, and even various other POM species. The relevance of POM modified surfaces extends well beyond biomass fuel cells. There are potential applications in medicine, sensors, energy storage, catalysis and other areas.

In chapter 2, it was shown that the supporting electrolyte properties have a remarkable impact on the ability of POMs to undergo electrochemical oxidation and reduction reactions reversibly. This ultimately led to significant increases in the accessible capacity of SiW_{12} relative to previously published results. However, it is also clear that the POMs under investigation undergo isomerisation (and possibly other chemical changes) when reduced to a significant extent. The effect of this isomerisation on the long term operation of the RFBs remains unknown.

It was also shown that PMo_{12} can undergo electrochemical oxidation and reduction reactions for at least 100 cycles, and that the POM has good stability towards high temperature.

A capital cost calculator was used to show that the use of expensive metals such as tungsten, molybdenum, and vanadium should be minimised to reduce the capital cost of POM RFBs. The capital cost calculator could be used by researchers to identify how feasible it would be to commercialise the chemistry which they are working on, and potentially be used to help secure funding for new projects.

The rationale for using POMs such as SiW_{12} as an active material in flow batteries is that it is well behaved, very well understood, and easy to obtain/synthesise. However, it is unclear if further investigation into the POMs discussed in this thesis (SiW_{12}, PMo_{12}, and PV_{14}) as RFB active materials is warranted. A large variety of POM RFBs have now been reported in the literature, and it is well established that many POMs exhibit properties which are desirable in RFBs (such as excellent stability toward repeated cycling, high coulombic efficiency, and multiple accessible redox states). When considering new candidates for redox flow battery electrolytes, researchers should confront the etchical, moral, and societal impacts of obtaining and using non-abundant materials, especially conflict minerals such as tungsten, in their research. It is important to consider whether the intended outcomes of the project outweigh the consequences of acquiring these materials.

Further investigation in this area should focus on POMs which are composed of largely Earth abundant and inexpensive elements that can potentially be cost competitive to tradi-

tional RFBs. The capital cost calculator described in chapter 2 shows that POM RFBs have a long way to go before they are cost competitive, and unless a solid case can be made for cost competitiveness of a POM RFB can be made, then research efforts should be directed elsewhere.

The theory described in 3 builds on the Nernst equation, which describes the relationship between the oxidation state and equilibrium potential for a species with two accessible oxidation states, and extends it to any number of states.

To this author's knowledge, this is the first time a description of the equilibrium potentials of multi-redox species has been described. Such a description is important because it allows for a richer understanding of the fundamental properties of polyoxometalates and similar species which can undergo multiple redox reactions that have standard potentials (especially when the standard reduction potentials are very similar). Using the theory developed in chapter 3, researchers could more accurately model the properties of POMs undergoing electrochemical reactions in a variety of settings. As an example, voltammograms of POMs could be fitted to an electrochemical model which varies the standard potential until a good fit is achieved. As has been shown in this thesis and in other work, standard analysis of voltammetric data of POMs can be difficult or impossible due to overlapping redox processes. Utilising such a model could help determine the standard reduction potentials of the overlapping processes.

This theory was then used in conjunction with Tafel plots recorded on a rotating disk electrode to characterise the kinetic and mass transport characteristics of SiW_{12}. The method for analysing the collected data is superior to a typical Tafel analysis, as the data is fitted directly to the Butler-Volmer equation(s), removing a great deal of ambiguity. Additionally, because we have a more complete understanding of the amount of species in a given oxidation state, we can easily attribute certain features in the collected data to one redox couple over another. Assuming the reaction is Nernstian, we can model the electrochemical behaviour of the system very well using the Butler-Volmer equation. In fact, if the system cannot be modelled accurately using similar principles as those described in section 3.4.2, this is a good indication that the process is more complicated than a simple electron transfer reaction. Using alternative forms of the current-overpotential equation (e.g. those described by Bard), it may be possible to determine the type of reaction(s) which are occurring at the electrode by comparing actual data against modelled predictions.

In chapter 4, a redox flow battery model is presented which is agnostic towards the active species and takes into account a large variety of electrochemical parameters. To the author's knowledge, it is the first model to describe the behaviour of polyoxometalate elec-

trochemistry and the first to describe the behaviour of species with more than two accessible oxidation states. Although the model could not be appropriately verified due to time constraints and limited access to the lab as a result of the COVID-19 pandemic and subsequent lockdowns, it may nonetheless be a good starting point (or at least a point of reference) for anyone attempting to model these kinds of batteries/reactions.

One finding of particular interest which arose due to the compartmentalised nature of the model described in the section titled "Mass transport: forced convection" and displayed in figure 4.5 is that there is an unexpected relationship between the concentration of reactant and distance from the outlet. In the cell that was modelled, the prediction is that the vast majority of available reactant is depleted very close to the inlet, meaning most of the cell area is not effectively utilised. If true, optimisation of the cell geometry could lead to significant improvements. Of course, experimental verification of the model would be the next logical step in this project.

Overall, the broad body of work explored within the scope of this project builds on the existing body of research on POM mediated biomass fuel cells and RFBs. In addition, meaningful contributions towards characterising fundamental polyoxometalate electrochemical properties have been made.

Glossary

D_i	diffusion coefficienct of species i
E_{pump}	pump energy (J)
E	energy
F	Faraday constant
I_0	exchange current
I	current
J	current density
OCP	open circuit potential
OCV	open-circuit voltage
PMo_{12}	$H_3PMo_{12}O_{40}$,
PV_{14}	$H_xPV_{14}O_{42}{}^{9-x}$, (x = 3-5)
P	power
Q	charge
RFB	redox flow battery plural
R_Ω	ohmic resistance
R_{mem}	membrane resistance
Re	Reynolds number
R	gas constant
R	resistance
SOC	state of charge
S_{ox}	oxidation state
Sh	Sherwood number
T	temperature
U^o	standard reduction potential
U^o_{AB}	standard potential for the reaction $A + z\,e^- \longrightarrow B$

U^o_{BC}	standard potential for the reaction $\mathrm{B} + z\,\mathrm{e}^- \longrightarrow \mathrm{C}$
U_{int}	potential of the electrode interface
Uan	anode reduction potential
Uca	cathode reduction potential
U	reduction potential
$VRFB$	vanadium redox flow battery
$\boldsymbol{J}_i$	flux of species i
η_{mem}	membrane overpotential
η_{pump}	pump efficiency
η	overpotential
μ	mobility
ν	viscosity
a_{Ox}	activity of the oxidised species
a_{Red}	activity of the reduced species
c_{Ox}	concentration of the oxidised species
c_{Red}	concentration of the reduced species
j_0	exchange current density
k^0	standard rate constant
l_{mem}	membrane thickness
n_V	volumetric flow rate
n_s	superficial flow rate
n	number of electrons exchanged
t_r	residence time/tick duration (s)
SiW_{12}	$\mathrm{SiW_{12}O_{40}}^{4-}$
HER	hydrogen evolution reaction
POM	polyoxometalate

Bibliography

(1) J. Friedl, M. V. Holland-Cunz, F. Cording, F. L. Pfanschilling, C. Wills, W. McFarlane, B. Schricker, R. Fleck, H. Wolfschmidt and U. Stimming, *Energy and Environmental Science*, 2018, **11**, 3010–3018.

(2) J. Friedl, F. L. Pfanschilling, M. V. Holland-Cunz, R. Fleck, B. Schricker, H. Wolfschmidt and U. Stimming, *Clean Energy*, 2019, **3**, 1–10.

(3) A. Selling, I. Andersson, L. Pettersson, C. M. Schramm, S. L. Downey and J. H. Grate, *Inorganic Chemistry*, 1994, **33**, 3141–3150.

(4) A. Selling, I. Andersson, J. H. Grate and L. Pettersson, *European Journal of Inorganic Chemistry*, 2000, 1509–1521.

(5) A. Brückner, G. Scholz, D. Heidemann, M. Schneider, D. Herein, U. Bentrup and M. Kant, 2007, **245**, 369–380.

(6) A. Linz, *Industrial and Engineering Chemistry - Analytical Edition*, 1943, **15**, 459.

(7) M. Ammam, *Journal of Materials Chemistry A*, 2013, **1**, 6291–6312.

(8) M. Pope, *Heteropoly and Isopoly Oxometalates*, Springer-Verlag Berlin Heidelberg, Berlin, 1st edn., 1983, pp. 101–116.

(9) C. Streb, *Dalton Transactions*, 2012, **41**, 1651–1659.

(10) S. Shigeta, S. Mori, E. Kodama, J. Kodama, K. Takahashi and T. Yamase, *Antivir Res*, 2003, **58**, 265–271.

(11) Y. R. Wang, L. Gong, J. K. Jiang, Z. G. Chen, H. Q. Yu and Y. Mu, *Electrochimica Acta*, 2017, **258**, 1304–1310.

(12) S. Wang, W. Sun, Q. Hu, H. Yan and Y. Zeng, *Bioorg Med Chem Lett*, 2017, **27**, 2357–2359.

(13) X. Wang, S. Wei, C. Zhao, X. Li, J. Jin, X. Shi, Z. Su, J. Li and J. Wang, *Journal of Biological Inorganic Chemistry*, 2022, **27**, 405–419.

(14) K. Azmani, M. Besora, J. Soriano-López, M. Landolsi, A. L. Teillout, P. de Oliveira, I. M. Mbomekallé, J. M. Poblet and J. R. Galán-Mascarós, *Chemical Science*, 2021, **12**, 8755–8766.

(15) K. Kamata and K. Sugahara, *Catalysts 2017, Vol. 7, Page 345*, 2017, **7**, 345.

(16) W. Liu, W. Mu, M. Liu, X. Zhang, H. Cai and Y. Deng, *Nature communications*, 2014, **5**, 3208.

(17) W. Liu, W. Mu and Y. Deng, *Angewandte Chemie - International Edition*, 2014, **53**, 13776–13780.

(18) B. Huang, D. H. Yang and B. H. Han, *Journal of Materials Chemistry A*, 2020, **8**, 4593–4628.

(19) M. R. Horn, A. Singh, S. Alomari, S. Goberna-Ferrón, R. Benages-Vilau, N. Chodankar, N. Motta, K. Ostrikov, J. Macleod, P. Sonar, P. Gomez-Romero and D. Dubal, *Energy & Environmental Science*, 2021, **14**, 1652–1700.

(20) J. Friedl, M. A. Lebedeva, K. Porfyrakis, U. Stimming and T. W. Chamberlain, *Journal of the American Chemical Society*, 2018, **140**, 401–405.

(21) M. Langholtz, B. Stokes and L. Eaton, *2016 billion-ton report: Advancing domestic resources for a thriving bioeconomy (Executive Summary)*, tech. rep., 2016.

(22) P. W. Gerbens-Leenes, A. Y. Hoekstra and T. van der Meer, *Ecological Economics*, 2009, **68**, 1052–1060.

(23) N. H. Ravindranath, C. Sita Lakshmi, R. Manuvie and P. Balachandra, *Energy Policy*, 2011, **39**, 5737–5745.

(24) D. Pimentel and T. W. Patzek, *Natural Resources Research*, 2005, **14**, 65–76.

(25) *G.B. National Grid Status*, 2021.

(26) S. J. Yoon, Y. C. Choi, Y. I. Son, S. H. Lee and J. G. Lee, *Bioresource Technology*, 2010, **101**, 1227–1232.

(27) B. Dou, V. Dupont, P. T. Williams, H. Chen and Y. Ding, *Bioresource Technology*, 2009, **100**, 2613–2620.

(28) F. Yang, M. A. Hanna and R. Sun, *Biotechnology for Biofuels*, 2012, **5**, 1–10.

(29) *INSIGHT: Europe glycerine spot prices post triple-digit rises on fears of further biodiesel output cuts*, 2020.

(30) C. Charles and R. Bridle, *Biofuels—At What Cost?*, tech. rep. April, The International Institute for Sustainable Development, 2013.

(31) *Ambient air pollution: A global assessment of exposure and burden of disease*, tech. rep., 2016.

(32) N. Kongprasert, P. Wangphanich and A. Jutilarptavorn, *Procedia Manufacturing*, 2019, **30**, 128–135.

(33) *Knowledge sharing with the Green Reach Trust - WasteAid*, 2018.

(34) *Charcoal: a burning issue*, 2019.

(35) R. A. Villazón Montalván, M. de Medeiros Machado, R. M. Pacheco, T. M. P. Nogueira, C. R. S. de Carvalho Pinto and A. C. Fantini, *Environment, Development and Sustainability*, 2019, **21**, 3093–3119.

(36) A. Ayodele, P. Oguntunde, A. Joseph and M. d. S. Dias Junior, *Revista Brasileira de Ciencia do Solo*, 2009, **33**, 137–145.

(37) E. N. Chidumayo and D. J. Gumbo, *The environmental impacts of charcoal production in tropical ecosystems of the world: A synthesis*, 2013.

(38) *Clean Energy — Department of Energy*.

(39) *Renewables Beating Coal Competitors on Cost — UNFCCC*.

(40) *Workbook: IRENA RE Time Series*.

(41) *Data and Statistics*, 2021.

(42) H. Government, *Energy White Paper*, tech. rep.

(43) E. Great Britain. Department for Business and I. Strategy., 122.

(44) Y. Ding, B. Du, X. Zhao, J. Y. Zhu and D. Liu, 2017, DOI: `10.1016/j.biortech.2016.12.109`.

(45) X. Zhao and J. Y. Zhu, *ChemSusChem*, 2016, **9**, 197–207.

(46) C. Liu, Z. Zhang, W. Liu, D. Xu, H. Guo, G. He, X. Li and Y. Deng, *Clean Energy*, 2018, 1–9.

(47) W. Wu, W. Liu, W. Mu and Y. Deng, 2016, DOI: `10.1016/j.jpowsour.2016.03.074`.

(48) X. Zhao, Y. Ding, B. Du, J. Y. Zhu and D. Liu, *Energy Technology*, 2017, **53726**, 1–7.

(49) Z. Zhang, C. Liu, W. Liu, Y. Cui, X. Du, D. Xu, H. Guo and Y. Deng, *Applied Energy*, 2017, **200**, 226–236.

(50) F. Xu, H. Li, Y. Liu and Q. Jing, *Scientific Reports*, 2017, DOI: 10.1038/s41598-017-05535-2.

(51) M. Sadakane and E. Steckhan, *Chemical Reviews*, 1998, **98**, 219–238.

(52) N. Mizuno and M. Misono, *Chemical Reviews*, 1998, **98**, 199–218.

(53) I. V. Kozhevnikov, *Chemical Reviews*, 1998, **98**, 171–198.

(54) J. W. Agger, P. J. Nilsen, V. G. Eijsink and S. J. Horn, *Bioenergy Research*, 2014, **7**, 442–449.

(55) H. Zhang, Y. Tan, J. Li and B. Xue, *Electrochimica Acta*, 2017, DOI: 10.1016/j.electacta.2017.08.016.

(56) W. Liu, W. Mu and Y. Deng, *Angewandte Chemie*, 2014, **126**, 13776–13780.

(57) H. Y. Chen, G. Wee, R. AlOweini, J. Friedl, K. Soon Tan, Y. Wang, C. Ling Wong, U. Kortz, U. Stimming, M. Srinivasan, R. Al-Oweini, J. Friedl, K. S. Tan, Y. Wang, C. L. Wong, U. Kortz, U. Stimming, M. Srinivasan, C. Han-Yi, W. Grace, R. Al-Oweini, F. Jochen, K. S. Tan, Y. Wang, W. C. Ling, U. Kortz, S. Ulrich and S. Madhavi, *ChemPhysChem*, 2014, **15**, 2162–2169.

(58) H.-Y. Chen, J. Friedl, C.-J. Pan, A. Haider, R. Al-Oweini, Y. L. Cheah, M.-H. Lin, U. Kortz, B.-j. Hwang, M. Srinivasan, U. Stimming, H.-Y. Chen, J. Friedl, C.-J. Pan, A. Haider, R. Al-Oweini, Y. L. Cheah, M.-H. Lin, U. Kortz, B.-j. Hwang, M. Srinivasan, U. Stimming, H.-Y. Chen, J. Friedl, C.-J. Pan, A. Haider, R. Al-Oweini, Y. L. Cheah, M.-H. Lin, U. Kortz, B.-j. Hwang, M. Srinivasan and U. Stimming, *Phys. Chem. Chem. Phys.*, 2017, **19**, 3358–3365.

(59) J. Noack, N. Roznyatovskaya, T. Herr and P. Fischer, *Angewandte Chemie - International Edition*, 2015, **54**, 9776–9809.

(60) J. Friedl, R. Al-Oweini, M. Herpich, B. Keita, U. Kortz and U. Stimming, *Electrochimica Acta*, 2014, **141**, 357–366.

(61) M. Genovese, Y. W. Foong and K. Lian, *Journal of the Electrochemical Society*, 2015, **162**, A5041–A5046.

(62) T. Feng, H. Wang, Y. Liu, J. Zhang, Y. Xiang and S. Lu, *Journal of Power Sources*, 2019, **436**, 226831.

(63) J. D. Strickland, *Journal of the American Chemical Society*, 1952, **74**, 862–867.

(64) J. D. Strickland, *Journal of the American Chemical Society*, 1952, **74**, 872–876.

(65) M. Holland-Cunz, J. Friedl and U. Stimming, *Journal of elect*, 2017, DOI: 10.1016/j.jelechem.2017.10.061.

(66) E. Falbo and T. J. Penfold, 2020, DOI: 10.1021/acs.jpcc.0c04169.

(67) J. P. Launay, R. Massart and P. Souchay, *Journal of The Less-Common Metals*, 1974, **36**, 139–150.

(68) J. Clayden, N. Greeves and S. Warren, *Organic chemistry*, Oxford university press, 2012.

(69) T. Yamase, *Chem. Rev.*, 1998, **98**, 307–326.

(70) D. Sloboda-Rozner, K. Neimann and R. Neumann, *Journal of Molecular Catalysis A: Chemical*, 2007, **262**, 109–113.

(71) R. Neumann and A. M. Khenkin, *Chemical Communications*, 2006, 2529–2538.

(72) Z. Zhang, C. Liu, W. Liu, X. Du, Y. Cui, J. Gong, H. Guo and Y. Deng, 2017, **141**, 1019–1026.

(73) B. B. Sarma and R. Neumann, *Nature Communications 2014 5:1*, 2014, **5**, 1–6.

(74) R. Banerjee, N. Bevilacqua, L. Eifert and R. Zeis, *Journal of Energy Storage*, 2019, **21**, 163–171.

(75) A. Misra, K. Kozma, C. Streb and M. Nyman, *Angewandte Chemie - International Edition*, 2020, **59**, 596–612.

(76) A. J. Bard, L. R. Faulkner and J. Wiley, 2001, 1–33.

(77) NASA, *Nasa Tm-83469*, 1983, **1**.

(78) G. P. Corey, *An Assessment of the State of the Zinc-Bromine Battery Development Effort*, tech. rep., 2010, pp. 1–14.

(79) A. Parasuraman, T. M. Lim, C. Menictas and M. Skyllas-Kazacos, *Electrochimica Acta*, 2013, **101**, 27–40.

(80) J. Rubio-Garcia, A. Kucernak, D. Zhao, D. Li, K. Fahy, V. Yufit, N. Brandon and M. Gomez-Gonzalez, *JPhys Energy*, 2019, **1**, DOI: 10.1088/2515-7655/aaee17.

(81) *World's largest battery: 200MW/800MWh vanadium flow battery - site work ongoing — Electrek*.

(82) E. H. Kirk, F. Fenini, S. N. Oreiro and A. Bentien, *Batteries*, 2021, **7**, DOI: 10.3390/batteries7040087.

(83) Q. Luo, L. Li, W. Wang, Z. Nie, X. Wei, B. Li, B. Chen, Z. Yang and V. Sprenkle, *ChemSusChem*, 2013, DOI: 10.1002/cssc.201200730.

(84) I. A. Stenina, P. Sistat, A. I. Rebrov, G. Pourcelly and A. B. Yaroslavtsev, *Desalination*, 2004, **170**, 49–57.

(85) P. L. Domingo, B. Garcia and J. M. Leal, *Canadian Journal of Chemistry*, 1990, **68**, 228–235.

(86) *Battery felts for redox flow batteries — SGL Carbon*.

(87) G. HERVÉ, Annales de chimie, Masson., 1971, vol. 6, p. 219.

(88) H. D. Pratt, N. S. Hudak, X. Fang and T. M. Anderson, *Journal of Power Sources*, 2013, **236**, 259–264.

(89) U. National Minerals Information Center, 2011.

(90) • *Tungsten price 2021 — Statista*.

(91) W. Chen, L. Huang, J. Hu, T. Li, F. Jia and Y.-F. Song, *Physical chemistry chemical physics : PCCP*, 2014, **16**, 19668–73.

(92) D. A. C. Brownson and C. E. Banks, *Interpreting Electrochemistry*, 2014.

(93) H.-y. Chen, R. Al-oweini, J. Friedl, Y. Lee, L. Li, C. Y. Lee, L. Li, U. Kortz, U. Stimming and M. Srinivasan, *Nanoscale*, 2015, **7**, 7934–7941.

(94) F. Li, L. E. Vangelder, W. W. Brennessel and E. M. Matson, *Inorganic Chemistry*, 2016, **55**, 7332–7334.

(95) Y. Liu, S. Lu, H. Wang, C. Yang, X. Su and Y. Xiang, *Advanced Energy Materials*, 2017, **7**, DOI: 10.1002/aenm.201601224.

(96) H. D. Pratt, W. R. Pratt, X. Fang, N. S. Hudak and T. M. Anderson, *Electrochimica Acta*, 2014, **138**, 210–214.

(97) N. Elgrishi, K. J. Rountree, B. D. McCarthy, E. S. Rountree, T. T. Eisenhart and J. L. Dempsey, *Journal of Chemical Education*, 2018, **95**, 197–206.

(98) A. Selling, 1996.

(99) M. Grabau, J. Forster, K. Heussner and C. Streb, *European Journal of Inorganic Chemistry*, 2011, 1719–1724.

(100) *Molybdenum - 2022 Data - 2005-2021 Historical - 2023 Forecast - Price - Quote - Chart*.

(101) P. C. H. Mitchell, *Speciation of molybdenum compounds in water Ultraviolet spectra and REACH read across*, tech. rep., 2009, pp. 1–28.

(102) S. Mallik, S. S. Dash, K. M. Parida and B. K. Mohapatra, *Journal of Colloid and Interface Science*, 2006, **300**, 237–243.

(103) *NFS Membrane*.

(104) P. Schwendt, J. Tatiersky, L. Krivosudský and M. Šimuneková, *Coordination Chemistry Reviews*, 2016, **318**, 135–157.

(105) C. Sun, J. Chen, H. Zhang, X. Han and Q. Luo, *Journal of Power Sources*, 2010, **195**, 890–897.

(106) K. Marques, J. Marschewski, N. Ebejer, P. Ruch, R. Machado, B. Michel and D. Poulikakos, 2017, **359**, 322–331.

(107) N. Aristov and A. Habekost, *World Journal of Chemical Education*, 2015, **3**, 115–119.

(108) X. Ke, J. M. Prahl, J. I. D. Alexander and R. F. Savinell, 1–48.

(109) G. G. Wildgoose, D. Giovanelli, N. S. Lawrence and R. G. Compton, 2004, 421–433.

(110) J. Chai, X. Wang, A. Lashgari, C. K. Williams and J. Jiang, *ChemSusChem*, 2020, **13**, 4069–4077.

(111) Y. Long, Z. Xu, G. Wang, H. Xu, M. Yang, M. Ding, D. Yuan, C. Yan, Q. Sun, M. Liu and C. Jia, *iScience*, 2021, **24**, 103157.

(112) W. Lee, A. Permatasari and Y. Kwon, *Journal of Materials Chemistry C*, 2020, **8**, 5727–5731.

(113) G. Wang, H. Zou, Z. Xu, A. Tang, F. Zhong, X. Zhu, C. Qin, M. Ding, W. You and C. Jia, *Materials Today Energy*, 2022, **28**, 101061.

(114) S. Uematsu, Z. Quan, Y. Suganuma and N. Sonoyama, *Journal of Power Sources*, 2012, **217**, 13–20.

(115) K. Nomiya, K. Kato and M. Miwa, *Polyhedron*, 1986, **5**, 811–813.

(116) W. Seichter, H.-J. Mögel, P. Brand and D. Salah, *European Journal of Inorganic Chemistry*, 2002, **1998**, 795–797.

(117) O. Sadeghi, M. Amiri, E. W. Reinheimer and M. Nyman, 2018, **77381**, 6247–6250.

(118) R. Gupta, I. Khan, F. Hussain, A. M. Bossoh, I. M. Mbomekallé, P. De Oliveira, M. Sadakane, C. Kato, K. Ichihashi, K. Inoue and S. Nishihara, *Inorganic Chemistry*, 2017, **56**, 8759–8767.

(119) M. Abdul Aziz, K. Oh and S. Shanmugam, *Chem. Commun.*, 2017, **53**, 917–920.

(120) M. E. Rinc, *Synthesis*, 2007, **53**, 91–95.

(121) K. Gong, X. Ma, K. M. Conforti, K. J. Kuttler, J. B. Grunewald, K. L. Yeager, M. Z. Bazant, S. Gu and Y. Yan.

(122) M. Zhang, M. Moore, J. S. Watson, T. A. Zawodzinski and R. M. Counce, *Journal of the Electrochemical Society*, 2012, **159**, A1183–A1188.

(123) V. Viswanathan, A. Crawford, D. Stephenson, S. Kim, W. Wang, B. Li, G. Coffey, E. Thomsen, G. Graff, P. Balducci, M. Kintner-Meyer and V. Sprenkle, *Journal of Power Sources*, 2014, **247**, 1040–1051.

(124) K. E. Rodby, T. J. Carney, Y. Ashraf Gandomi, J. L. Barton, R. M. Darling and F. R. Brushett, *Journal of Power Sources*, 2020, **460**, 227958.

(125) N. H. Haegedorn, *NASA redox storage system development project. Final Report.* Tech. rep., National Aeronautics and Space Administration, Cleveland, OH (USA). Lewis Research Center, 1984.

(126) K. Gong, X. Ma, K. M. Conforti, K. J. Kuttler, J. B. Grunewald, K. L. Yeager, M. Z. Bazant, S. Gu and Y. Yan, *Energy Environ. Sci. Energy Environ. Sci*, 2015, **8**, 2941–2945.

(127) Q. Luo, H. Zhang, J. Chen, D. You, C. Sun and Y. Zhang, *Journal of Membrane Science*, 2008, DOI: 10.1016/j.memsci.2008.08.025.

(128) P. Zhao, H. Zhang, H. Zhou, J. Chen, S. Gao and B. Yi, *Journal of Power Sources*, 2006, **162**, 1416–1420.

(129) J. Friedl and U. Stimming, *Electrochimica Acta*, 2017, **227**, 235–245.

(130) B. Huskinson, M. P. Marshak, C. Suh, S. Er, M. R. Gerhardt, C. J. Galvin, X. Chen, A. Aspuru-Guzik, R. G. Gordon and M. J. Aziz, DOI: 10.1038/nature12909.

(131) R. F. Gahn and N. H. Hagedorn, 1983.

(132) USGS, *USGS science for a changing world*, 2018, 1–67.

(133) D. M. Kabtamu, J. Y. Chen, Y. C. Chang and C. H. Wang, *Journal of Power Sources*, 2017, **341**, 270–279.

(134) J. Friedl, C. M. Bauer, A. Rinaldi and U. Stimming, *Carbon*, 2013, **63**, 228–239.

(135) I. Derr, D. Przyrembel, J. Schweer, A. Fetyan, J. Langner, J. Melke, M. Weinelt and C. Roth, *Electrochimica Acta*, 2017, **246**, 783–793.

(136) I. Derr, A. Fetyan, K. Schutjajew and C. Roth, *Electrochimica Acta*, 2017, **224**, 9–16.

(137) B. Satola, L. Komsiyska and G. Wittstock, *Journal of The Electrochemical Society*, 2017, **164**, A2566–A2572.

(138) R. Schweiss, A. Pritzl and C. Meiser, *Journal of The Electrochemical Society*, 2016, **163**, A2089–A2094.

(139) G. Oriji, Y. Katayama and T. Miura, *Journal of Power Sources*, 2005, **139**, 321–324.

(140) *Potassium Ferricyanide - K3(Fe(CN)6) Latest Price, Manufacturers & Suppliers*.

(141) *Potassium Ferrocyanide - 14459-95-1 Latest Price, Manufacturers & Suppliers*.

(142) *China Sodium Ferrocyanide, Sodium Ferrocyanide Manufacturers, Suppliers, Price — Made-in-China.com*.

(143) *Energy Superhub Oxford - Invinity Energy Systems*.

(144) A. J. Bard and L. R. Faulkner, *Electrochemical Methods Fundamentals and Applications*, John Wiley & Sons, Inc., 2001.

(145) H. Wang, S. Hamanaka, Y. Nishimoto, S. Irle, T. Yokoyama, H. Yoshikawa, K. Awaga, H. Wang, S. Hamanaka, Y. Nishimoto, S. Irle, T. Yokoyama, H. Yoshikawa and K. Awaga, *Journal of the American Chemical Society*, 2012, **134**, 4918–4924.

(146) L. D. Brown, T. P. Neville, R. Jervis, T. J. Mason, P. R. Shearing and D. J. Brett, *Journal of Energy Storage*, 2016, **8**, 91–98.

(147) E. S. Beh, D. De Porcellinis, R. L. Gracia, K. T. Xia, R. G. Gordon and M. J. Aziz, *ACS Energy Letters*, 2017, **2**, 639–644.

(148) K. W. Knehr, E. Agar, C. R. Dennison, A. R. Kalidindi and E. C. Kumbur, *Journal of the Electrochemical Society*, 2012, **159**, A1446–A1459.

(149) A. A. Shah, H. Al-Fetlawi and F. C. Walsh, *Electrochimica Acta*, 2010, **55**, 1125–1139.

(150) J. L. Barton and F. R. Brushett, *Batteries*, 2019, **5**, 1–26.

(151) H. Fink, J. Friedl and U. Stimming, *The Journal of Physical Chemistry C*, 2016, **120**, 15893–15901.

(152) A. Crawford, V. Viswanathan, D. Stephenson, W. Wang, E. Thomsen, D. Reed, B. Li, P. Balducci, M. Kintner-Meyer and V. Sprenkle, *Journal of Power Sources*, 2015, **293**, 388–399.

(153) J. Newman and K. E. Thomas-Alyea, *Electrochemical systems*, John Wiley & Sons, 2012.

(154) S. König, M. R. Suriyah and T. Leibfried, *Journal of Power Sources*, 2017, **360**, 221–231.

(155) Y. Li, M. Skyllas-Kazacos and J. Bao, *Journal of Power Sources*, 2016, **311**, 57–67.

(156) D. Schmal, J. Van Erkel and P. J. Van Duin, *Journal of Applied Electrochemistry*, 1986, **16**, 422–430.

(157) N. Vatistas, P. F. Marconi and M. Bartolozzi, *Electrochimica Acta*, 1991, **36**, 339–343.

(158) N. Gurie, D. F. Keogh, M. Baldry, V. Timchenko, D. Green, I. Koskinen and C. Menictas, 2006.

(159) Q. Xu and T. S. Zhao, *Physical Chemistry Chemical Physics*, 2013, **15**, 10841–10848.

(160) J. González-García, P. Bonete, E. Expósito, V. Montiel, A. Aldaz and R. Torregrosa-Maciá, *Journal of Materials Chemistry*, 1999, **9**, 419–426.

(161) N. Gurieff, D. F. Keogh, M. Baldry, V. Timchenko, D. Green, I. Koskinen and C. Menictas, *Applied Sciences*, 2020, **10**, 2801.

(162) Y. Li, Ph.D. Thesis, The University of New South Wales Sydney, Australia, 2018.

(163) T. Gerber, P. Fischer, K. Pinkwart and J. Tübke, *Batteries*, 2019, **5**, DOI: `10.3390/batteries5020038`.

(164) J. Fu, T. Wang, X. Wang, J. Sun and M. Zheng, *Energy Procedia*, 2017, **105**, 4482–4491.

(165) T. Yamamura, N. Watanabe, T. Yano and Y. Shiokawa, *Journal of The Electrochemical Society*, 2005, **152**, A830.

(166) J. C. Acevedo and D. K. Stalnaker, *Nasa-Tm-83363*, 1983.